Gas-phase synthesis of graphene in a microwave plasma reactor

Von der Fakultät für Ingenieurwissenschaften,
Abteilung Maschinenbau und Verfahrenstechnik der
Universität Duisburg-Essen

zur Erlangung des akademischen Grades
eines
Doktors der Ingenieurwissenschaften
Dr.-Ing.

genehmigte Dissertation

von

Paolo Fortugno
aus
Duisburg

Gutachter: Prof. Dr. Hartmut Wiggers
Prof. Dr. Ferdi Schüth
Tag der mündlichen Prüfung: 15. Juli 2024

Abstract

The present work investigates the growth of carbon nanoparticles – mainly few-layer graphene (FLG) – produced from gaseous hydrocarbons in a microwave plasma reactor. In addition to the analysis of the produced carbon particles, different *in situ* and inline methods are applied to characterize the synthesis process. The plasma is analyzed using optical emission spectroscopy (OES) and the concentration of molecular products formed in the exhaust gas is analyzed quantitatively and semi-quantitatively using infrared absorption and gas chromatography. The methods are additionally compared with reaction kinetic and equilibrium simulations of gas phase chemistry based on combustion mechanisms for interpretation. The growth of carbon particles for FLG is investigated using spatially-resolved thermophoretic sampling.

The first part of this work examines the structure and morphology formation of the growing carbon particles along the reactor via thermophoretic sampling. It is observed that the particles change their morphology along the reactor axis. In accordance with the general theory for the growth of carbon particles, the formation of monolayer graphene for the present process is demonstrated by microscopic analysis. The first FLG particles obtained close to the plasma are almost flat. A comparison of samples taken at different points along the reactor shows that the FLG particles fold more strongly along the reactor axis and form denser structures. This process is confirmed by time-resolved laser induced incandescence and explains the typical morphology of the obtained samples of crumpled FLG sheets.

The second part of the work deals with the investigation of the influence of different precursor mixtures and concentrations on the formed carbon particle product. The precursors used are ethanol, ethylene, and various ethylene-water mixtures. In particular, the influence of oxygen in the mixture and the resulting C/O ratio is considered and discussed. The results show in accordance with literature that low C/O ratios are favorable for the formation of FLG, whereas higher ratios lead to mixtures with graphitic or soot-like particles. At the same time, oxygen-free precursors show the same trend when their applied concentration is reduced. The yield of carbon particles scales with the concentration of precursor used and the amount of water added. The addition of less precursor or more water decreases the particle yield. OES results indicate that the plasma temperatures in the process are the same for all experimental cases and thus different temperature conditions for particle formation can probably be excluded. The recorded FTIR spectra semi-quantitatively show changes in the concentrations of the gas molecules formed when water is added. With increasing water content, more and more CO is formed and the amount of small hydrocarbons such as C_2H_2 decreases. These observed trends can be reproduced with reaction kinetics simulations. Based on the results of the applied *in situ* methods and simulation, the influence of oxygen can be explained by a change in concentration. The oxygen present reacts with carbon to form CO and thus reduces the concentration of growth species available for the formation of carbon particles.

The third part of the work attempts to transfer the knowledge gained for water to other oxygen carriers. Water is substituted by nitrous oxide (N_2O), carbon dioxide (CO_2) and molecular oxygen (O_2). Based on simulations, a comparable reduction of particle formation is expected for all oxygen carriers. A validation of the simulations using gas chromatography shows a maximum relative deviation of ~20% for CO and C_2H_2. The yield of carbon particles is reduced for all oxygen carriers in line with expectations. However, the analysis of the produced particles shows that not all oxygen carriers suppress the formation of soot-like particles. Experiments

with low C/O ratios with the addition of CO_2 continue to lead to the formation of different carbon particles other than FLG. Samples obtained with thermophoretic sampling already show partial differences in composition close to the plasma, i.e., close to the onset of particle formation and growth. Distinctive decomposition products of the oxygen carriers are detected using OES. In contrast to N_2O and O_2, CO_2 spectra are characterized by the unexpected formation of C_2 and C. The temperature determined from C_2 luminescence is significantly higher than the other estimated temperatures and therefore indicates thermal non-equilibrium for this species. These additional carbon species may be able to influence the first nucleation of solid particles, leading to the formation of additional soot-like particles.

Kurzzusammenfassung

Die vorliegende Arbeit untersucht das Wachstum von Kohlenstoff-Nanopartikeln, hauptsächlich Few-Layer Graphen (FLG), hergestellt aus gasförmigen Kohlenwasserstoffen in einem Mikrowellenplasmareaktor. Neben der Analyse der hergestellten Kohlenstoffpartikel werden zu diesem Zweck unterschiedliche *in situ* und inline Methoden angewandt, um den Syntheseprozess zu charakterisieren. Das Plasma wird mithilfe der optischen Emissionspektroskopie (OES) und die Konzentration gebildeter molekularer Produkte quantitativ und semiquantitativ mit Infrarot-Absorptionsspektrometrie und Gaschromatographie untersucht. Die Methoden werden zur Interpretation zusätzlich mit Reaktionskinetischen- und Gleichgewichtssimulationen der Gasphasenchemie auf Basis von Verbrennungsmechanismen verglichen. Das Wachstum der FLG-Partikel wird durch ortsaufgelöste thermophoretische Probennahme untersucht.

Der erste Teil der Arbeit untersucht die Strukturbildung und Morphologie der wachsenden Kohlenstoffpartikel entlang des Reaktors durch thermophoretische Probennahme. Die Partikel ändern entlang der Reaktorachse ihre Morphologie. Die ersten nah am Plasma gewonnene FLG-Partikel sind flach. Über mikroskopische Analyse kann hier, im Einklang mit der allgemeinen Theorie für das Wachstum von Kohlenstoffpartikeln, die Bildung von Monolagengraphen für den vorliegenden Prozess nachgewiesen werden. Durch den Vergleich von Proben, die an unterschiedlichen Stellen entlang des Reaktors entnommen werden, zeigt sich, dass sich sie FLG-Partikel der Reaktorachse zunehmend falten und kompaktere Strukturen bilden. Dieser Vorgang wird durch Messungen der zeitaufgelösten laserinduzierten Inkandeszenz bestätigt und erklärt die typische Morphologie der gewonnenen Proben.

Der zweite Teil der Arbeit beschäftigt sich mit der Untersuchung des Einflusses von unterschiedlichen Präkursormischungen und Konzentrationen auf das gebildete Kohlenstoffpartikelprodukt. Bei den eingesetzten Präkursoren handelt es sich dabei um Ethanol, Ethen und verschiedene Ethen/Wasser-Gemische. Insbesondere der Einfluss von Sauerstoff in der Mischung und das dadurch resultierende C/O-Verhältnis wird betrachtet und diskutiert. Die Ergebnisse zeigen im Einklang mit der Literatur, dass niedrige C/O-Verhältnisse vorteilhaft für die Bildung von FLG sind, wohingegen größere Verhältnisse zu Mischungen mit graphitischen oder rußartigen Partikeln führen. Sauerstofffreie Präkursoren zeigen bei Verringerung ihrer eingesetzten Konzentration ebenfalls den Trend einer bevorzugten Erzeugung von FLG. Die Ausbeute an Kohlenstoffpartikeln skaliert dabei mit der Konzentration an eingesetzten Präkursor und der Menge an zugegebenem Wasser. Die Zugabe von geringeren Präkursor- oder höheren Wasserkonzentrationen lässt die Ausbeute sinken. OES-Ergebnisse deuten darauf hin, dass die Plasmatemperaturen für alle untersuchten Fälle gleich sind und somit unterschiedliche Temperaturbedingungen für die Partikelbildung wahrscheinlich ausgeschlossen werden können. Die aufgenommenen FTIR-Spektren zeigen semiquantitativ, dass die Zugabe von Wasser Konzentrationsänderungen der gebildeten Gasspezies verursacht. Mit steigendem Wasseranteil wird zunehmend mehr CO gebildet und die Menge einfacher Kohlenwasserstoffe wie C_2H_2 nimmt ab. Diese beobachteten Trends lassen sich mit reaktionskinetischen Simulationen reproduzieren. Auf Basis der Ergebnisse der angewandten In-situ-Methoden und Simulation, lässt sich der Einfluss von Sauerstoff über einen Konzentrationsänderung erklären. Der vorhandene Sauerstoff reagiert dabei mit Kohlenstoff zu CO und reduziert so die zu Verfügung stehende Konzentration an Wachstumsspezies für die Bildung von Kohlenstoffpartikeln.

Der dritte Teil der Arbeit hat das Ziel, die für Wasser gewonnenen Erkenntnisse auf weitere Sauerstoffträger zu übertragen. Wasser wird dabei durch Lachgas (N_2O), Kohlenstoffdioxid (CO_2) und molekularen Sauerstoff (O_2) substituiert. Anhand von Simulation wird für alle Sauerstoffträger eine vergleichbare Reduktion der Partikelbildung erwartet. Eine Validierung der Simulationen mittels Gaschromatographie zeigt für CO und C_2H_2 eine relative Abweichung von maximal ~20 %. Die Ausbeute an Kohlenstoffpartikeln wird für alle Sauerstoffträger entsprechend der Erwartung reduziert. In der Analyse der hergestellten Partikel lässt sich aber erkennen, dass nicht alle Sauerstoffträger die Bildung rußartiger Partikel unterbinden. Experimente mit niedrigen C/O-Verhältnissen bei der Zugabe von CO_2 führen weiterhin zu der Bildung andersartiger Kohlenstoffpartikel. Proben, die mit thermophoretischer Probennahme gewonnen werden, zeigen bereits nah am Plasma, d.h. nah am Beginn des Partikelwachstums, Unterschiede der Zusammensetzung. Anhand von OES-Spektren können markante Zerfallsprodukte der Sauerstoffträger nachgewiesen werden. Die CO_2-Spektren zeichnen sich im Gegensatz zu N_2O und O_2 durch die unerwartete Bildung von C_2- und C aus. Die ermittelte Temperatur der C_2-Lumineszenz ist deutlich höher als die sonstigen bestimmten Temperaturen und lässt deshalb wahrscheinlich auf die Bildung durch einen Nichtgleichgewichtseffekt schließen. Diese zusätzlichen Kohlenstoffspezies sind dann möglicherweise in der Lage, die Nukleation von festen Partikeln zu beeinflussen, was zu der Bildung zusätzlicher rußartiger Partikel führt.

Statement of contributions

Paolo Fortugno is the sole author for the Sections 1–3 and 7–9, which were specifically written for this thesis. All the research presented in Sections 4–6 has been published previously in collaboration with different coworkers. To present the published results in this thesis, parts of the results are rearranged and partly expanded. Repeating contents, e.g., referring to measurement techniques, are removed and now reference to the location of the first mention.

In all the presented research papers, with the exception of Section 4, I performed work that can be described by the CRediT system as conceptualization, methodology, validation, formal analysis, investigation, writing – original draft, writing – review & editing, and visualization. The contribution to Section 4 is mentioned separately.

The research presented in Section 4 has been published as in

> C.-F. López-Cámara, P. Fortugno, M. Asif, S. Musikhin, C. Prindler, H. Wiggers, T. Endres, N. Eaves, K.J. Daun, C. Schulz, Evolution of particle size and morphology in plasma synthesis of few-layer graphene and soot, Combustion and Flame 258 (2023) 112713.
>
> C.-F. López-Cámara, P. Fortugno, M. Heidelmann, H. Wiggers, C. Schulz, Graphene self-folding: Evolution of free-standing few-layer graphene in plasma synthesis, Carbon 218 (2024) 118732.

C.-F. López-Cámara is the lead author of both manuscripts. I contributed to the first manuscript (2023) in the conceptualization, methodology, validation, formal analysis, investigation, writing – review & editing, and visualization. I performed the experimental part for synthesizing and sampling the carbon nanomaterials and aided in the process description and the sample analysis and interpretation. For the second manuscript (2024), my contribution is restricted to investigation and writing – review & editing.

The research presented in Section 5 has been published as:

> P. Fortugno, S. Musikhin, X. Shi, H. Wang, H. Wiggers, C. Schulz, Synthesis of free-standing few-layer graphene in microwave plasma: The role of oxygen, Carbon 186 (2022) 560-573.

Technical support with acquiring part of the results has been provided by Markus Heidelmann (TEM), Sascha Apazeller (TGA), Beate Endres (BET), and Md Yusuf Ali and Alexander Tarasov (XPS).

The research presented in Section 6 has been published as:

> P. Fortugno, C.-F. López-Cámara, F. Hagen, H. Wiggers, C. Schulz, Relevance of C/O ratios in the gas-phase synthesis of freestanding few-layer graphene, Applications in Energy and Combustion Science 15 (2023) 100180.

Technical support with acquiring part of the results has been again provided by Markus Heidelmann (TEM), Sascha Apazeller (TGA), Beate Endres (BET), and Md Yusuf Ali (XPS). GC/MS measurements were performed by Jürgen Herzler. Support on the software Chemkin-Pro has been provided by Sebastian Peukert.

Table of Contents

ABSTRACT ..... **I**

KURZZUSAMMENFASSUNG ..... **III**

STATEMENT OF CONTRIBUTIONS ..... **V**

1 INTRODUCTION **1**

2 FUNDAMENTALS AND METHODS **3**

2.1 PLASMA PROPERTIES 3
2.2 THEORY AND MODELS FOR SOLID CARBON GROWTH 4
2.2.1 Studies on graphene growth in plasmas *8*
2.3 *EX SITU* MEASUREMENT TECHNIQUES FOR THE ANALYSIS OF CARBON NANOMATERIALS 9
2.3.1 Raman spectroscopy *9*
2.3.2 Transmission electron microscopy *12*
2.3.3 Thermogravimetric analysis *13*
2.3.4 Gas adsorption isotherm *15*
2.3.5 X-ray photoelectron spectroscopy *15*
2.4 *IN SITU*, INLINE, AND PARTICLE SAMPLING TECHNIQUES APPLIED IN THIS THESIS 17
2.4.1 Optical spectroscopy *17*
2.4.2 Thermophoretic sampling of particles *20*
2.4.3 Gas chromatography *22*
2.5 NUMERICAL SIMULATIONS WITH CHEMKIN 23

3 EXPERIMENTAL SETUPS **25**

3.1 EXPERIMENTAL SETUP FOR INFRARED ABSORPTION MEASUREMENTS 29
3.2 EXPERIMENTAL SETUP FOR OPTICAL EMISSION SPECTROMETRY 31
3.3 EQUIPMENT FOR THERMOPHORETIC SAMPLING 32

4 STRUCTURE EVOLUTION OF GRAPHENE FLAKES DURING SYNTHESIS **34**

4.1 INTRODUCTION 34
4.2 STRUCTURAL PROPERTIES OF THE FIRST FORMED FLG MATERIALS 35
4.3 STRUCTURAL EVOLUTION OF FLG ALONG THE REACTOR 38
4.4 SUMMARY 41

5 IMPACT OF WATER ON CARBON PARTICLE GROWTH **42**

5.1 INTRODUCTION 42
5.2 RESULTS OF *EX SITU* MATERIALS ANALYSIS 43
5.3 APPLICATION OF *IN SITU* TECHNIQUES 50
5.3.1 OES *50*
5.3.2 FTIR *53*
5.4 REACTION KINETICS MODELING 55
5.5 CONCLUSIONS 59

6 EFFECT OF DIFFERENT OXYGEN CARRIERS ON GRAPHENE SYNTHESIS **62**

6.1 Introduction 62
6.2 Reaction kinetics modeling and experimental comparison 62
6.3 Experimental results: Powder analysis 65
6.4 Optical emission spectroscopy 71
6.5 Summary 73

7 SUMMARY 75

7.1 Outlook 77

8 REFERENCES 79

9 APPENDIX 92

9.1 Thermogravimetric analysis of particle samples and reference measurements 92
9.2 IR absorption measurements of ethanol vapor 94
9.3 OES measurements 95
9.3.1 Constraints by process stability and spectrometer system properties 95
9.3.2 Details on the temperature determination from OES 96
9.3.1 Limitation of hydrogen concentration measurements 97
9.4 Discussion on quantitative differences particle composition between Cases 2 and 8 98
9.5 Additional material on section 5 100
9.5.1 Hydrogen addition as reactant 100
9.5.2 Complete set of measured TGA QMS data 103
9.5.3 XPS measurements performed on Cases 1–7 104
9.5.4 Simulation of chemical equilibrium compositions and gas species profiles 107
9.6 Additional material on Section 6 110
9.6.1 Chemkin simulations of the gas-phase species 110
9.6.2 TEM images of all discussed experimental cases 116
9.6.3 GC/MS validation measurements of the effluent gas composition 117
9.6.4 Raman spectra obtained from synthesis and their analysis 118
9.6.5 TGA measurement results for Cases 8–16 120
9.6.6 XPS measurements of the synthesized nanopowders 121

10 ACKNOWLEDGMENT 125

1 Introduction

Plasma processes are promising to achieve electrification of industrial processes as they can be employed to synthesize a wide variety of different chemical compounds or perform specific tasks [1, 2]. Examples include the plasma treatment of liquids [3] for, e.g., the removal of pollutants [4], gas reforming [5, 6], nitrogen fixation [7, 8], plasma-assisted catalysis [9, 10], the synthesis of functional nanomaterials [11, 12], or the simultaneous generation of hydrogen and carbon black from pyrolysis of methane [13-16]. Plasma dissociation processes are not only able to produce carbon black but can also be used for the synthesis of more valuable carbon structures while using identical hydrocarbon reactants. Plasmas are commonly employed to synthesize e.g., carbon nanotubes [17-19]. Approximately fifteen years ago, work of Dato et al. showed that continuous gas-phase plasma processes are able to reform hydrocarbon reactants towards few-layer graphene flakes (FLG) [20]. Major byproducts of the process include – depending on the process conditions – H_2, CO, C_2H_2, and HCN [21-23]. Graphene is an interesting material for many applications as it possesses unique and versatile properties. These include its electrical and thermal conductivity which make it great for being used as a functional material or as a filler material for composites [24-27], its inertness which allows it to be used for, e.g., electrochemistry [28-30], and its highly anisotropic structure and mechanical strength which lead to varying use cases including membranes for water desalination [31], or pressure and gas sensing [32, 33]. Hence, investigating the growth process via plasma may allow in the future to upscale its production to relevant scales while producing relevant byproducts in, e.g., H_2 and CO. Similarly, understanding the graphene formation may benefit the general understanding of carbon growth towards cleaner combustion processes [34].

The goal of this thesis is to gain fundamental knowledge about the growth of different carbon allotropes in gas-borne particles with a special focus on obtaining freestanding graphene in a microwave plasma reactor. The two main questions that are addressed in this work are first, how the morphology and structure of the growing graphene flakes evolves, and second, which effect oxygen has on the synthesis process for the formation of FLG. To address both questions, different *in situ*, inline, and particle sampling techniques with *ex situ* analysis are applied to the synthesis process and the generated materials.

The investigation is motivated by the fact that FLG particles harvested from similar plasma reactors typically show a crumpled and folded multilayer structure. However, the formation of this crumpled and folded structure has been unclear because conceptually, graphene monolayers can be considered as large (flat) PAH molecules that should only grow at their edges. Therefore, the transformation from a graphene monolayer to the observed multi-layered structures had to be investigated. Thermophoretic sampling is used to sample particles from a reaction zone in a spatially resolved manner which are then analyzed by microscopic techniques. Thus, thermophoretic sampling provides information about the residence-time dependent structure formation. For this thesis, carbon particles were sampled at different axial reactor positions and analyzed by transmission electron microscopy (TEM). The experimental conditions are chosen to only lead to the formation of FLG as particle phase, to only probe growing graphene sheets and not mixed particle allotropes. TEM images are then qualitatively analyzed and the size of the FLG flakes is quantified by measuring their size distributions. The results by TEM are compared to *in situ* time-resolved laser-induced incandescence (TiRe LII)

measurements performed by Stanislav Musikhin and Muhammad Asif that probe the available surface area of the aerosolized flakes at different axial positions in the reactor.

The motivation to study the effect of oxygen on the particle synthesis is based on literature reports that suggest a direct link between the employed reactant (mixture) and the produced carbon particle composition. Specific C/O ratios, such as in ethanol (C/O = 2), are reported to be favorable to obtain FLG [35-37], while larger C/O ratios or other oxygen carriers (specifically carbon dioxide) tend to form particle mixtures containing soot-like or graphitic particles. Here, the effect of the C/O ratio and the oxygen carrier type is investigated in two parts by employing different reactant compositions, reactant concentrations, and characterizing the grown carbon particles. In the first approach, the reactants used are ethanol, ethylene, and various ethylene/water mixtures. Reactant mixtures of ethylene and water allow to alter the C/O ratio freely, while also being able to reproduce the elemental composition of ethanol. In experiments that follow up on the obtained results generated by the first approach, water is substituted by other oxygen carriers, namely nitrous oxide (N_2O), carbon dioxide (CO_2) and molecular oxygen (O_2).

The synthesized carbon particles are analyzed with different characterization methods, such as Raman spectroscopy, thermal analysis, X-ray photoelectron spectroscopy, and TEM to qualitatively and quantitatively assess their respective allotrope composition and possible correlation with reaction conditions. To improve the process understanding, various techniques are employed to determine gas temperatures in the reactor and observe changes in the effluent gas composition. A gas-temperature profile for the reactor is estimated based on spectroscopic techniques and thermocouple measurements. The concentration of formed gas molecules in the effluent is – depending on the specific experiment – assessed by infrared absorption and gas chromatography. Infrared absorption spectroscopy is thereby used to observe qualitative trends of the formed gaseous compounds while gas chromatography gives quantitative information. The results are interpreted with the help of reaction kinetics simulations with the aim to reproduce the observed qualitative and quantitative trends of species concentrations and gain further insight into the synthesis process.

The thesis is organized as described in the following. The relevant fundamentals and methods are introduced in Section 2. The section is separated in specific information about the plasma environment and a broad overview of the theory of carbon growth and previous studies reported in literature (Sections 2.1 and 2.2). It is followed up by the introduction of the different *ex situ* methods for material characterization (Section 2.3), the applied *in situ* and inline methods (Section 2.4) to analyze the plasma process, and a description of the simulation methods employed (Section 2.5). Section 3 addresses the experimental setups used for the synthesis process and the assembly for the applied *in situ* and inline methods. Sections 4–6 show and discuss results related to the structure formation of FLG in the plasma reactor (Section 4) and the effect of oxygen on the carbon particle synthesis (Sections 5–6). Section 7 summarizes and discusses the presented results, extracts the main findings, and provides suggested directions for further research based on remaining open questions and experimental shortcomings.

2 Fundamentals and methods

2.1 Plasma properties

In the universe, plasmas are the most abundant physical phenomenon fulfilling the originally postulated conditions by Langmuir [38]. On the macroscale, plasmas are considered to be electrically neutral as the number of positive and negatively charged species are balanced (first condition). Yet plasmas possess free charged species that make the plasma conductive, internally interactive, and highly susceptible to electromagnetic fields. Thus, the plasmas behavior is governed by the interaction of charged species (collective behavior, second condition) and charges are electrically screened on the microscale (Debye shielding, third condition). As an example, the movement of charge carriers on the microscale is influenced by ambipolar diffusion, i.e., a collective movement of positively and negatively charged species. Plasmas can be characterized by multiple parameters including their degree of ionization, their temperature, and density. Because plasmas can consist of multiple species – electrons, ions, molecules, and atoms – they are usually described by a separate temperature for their respective degrees of freedom. Depending on the respective values, plasmas can be considered to be in chemical equilibrium or having non-equilibrium properties. In an equilibrium plasma, all temperatures have the same value and knowing or determining one of them allows to calculate, e.g., the ionization degree by using the Saha equation. In non-equilibrium plasmas, the miscellaneous temperatures can be different and more complex descriptions for the excitation of the involved species are necessary. A similar distinction is to characterizes plasmas as thermal and non-thermal. Most thermal plasmas are equilibrium plasmas while most non-thermal plasmas are non-equilibrium plasmas.

For the experimental work in this thesis, a plasma excited and maintained by microwave radiation (2.45 GHz) is employed. The electrons are accelerated in the electric field and lose their energy by collisions with other electrons or heavier species. Depending on how much energy the electrons are able to attain before they collide with, e.g., an atom, the collisions can lead to processes such as impact ionization or momentum transfer. The energy of the electrons can thereby be described in a first approximation by a distribution (e.g., Maxwell-Boltzmann or Druyvesteyn) and an average electron temperature which are the result of the different collisional processes. In many low-pressure plasmas, the electron energy is much larger than the characteristic species temperatures as the mean free path is large, leading to a low number of collisions in each excitation/acceleration cycle. Such plasmas have the ability to selectively excite molecules, atoms, or induce reactions and, thus, engineering the electron energy can determine the interaction with other collision partners for e.g., the production of reactive species. When the pressure is increased towards atmospheric pressure, the heavy species temperature and the electron temperature can become more similar as Joule heating becomes more efficient and more energy is spent on heating up the gas (Figure 2-1). In such a case, the plasmas become less selective and the effect on chemistry can become purely thermal. There are, however, atmospheric pressure plasmas (especially for medical or coating applications) which show strong non-equilibrium and only possess gas temperatures close to room temperature as they work with specific geometries and low power consumption.

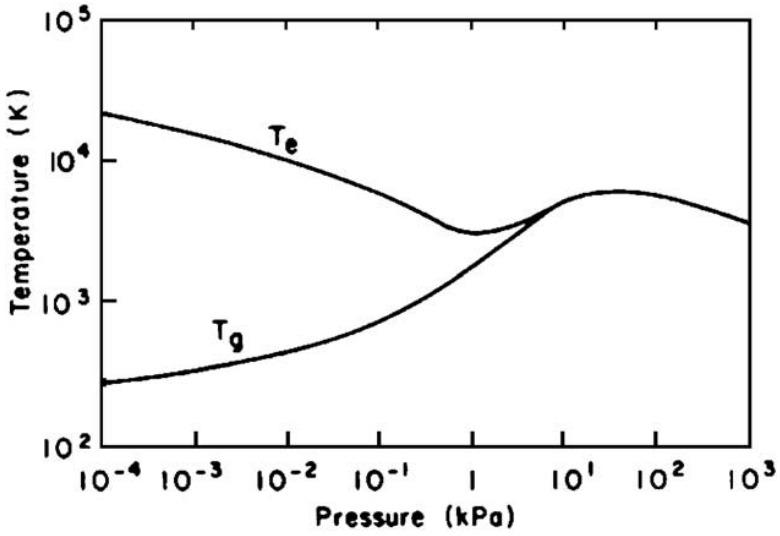

Figure 2-1:Pressure dependent electron and gas temperature for a mercury arc plasma. Reprinted with permission of Elsevier [39].

Microwave plasmas at atmospheric pressure are usually considered to be non-equilibrium plasmas but not necessarily non-thermal. Instead, they are often called warm plasmas as they don't reach values form classical thermal plasmas such as arcs (~10,000 K) but can still significantly heat up a gas stream. Electron temperatures up to ~1 eV (≈ 11,604 K) and gas temperatures in the range of 1000–6000 K are commonly reported [40-44] which are sufficient to dissociate a large fraction of the molecules.

2.2 Theory and models for solid carbon growth

Carbon can be created in the form of different pure allotropes such as diamond and graphene. In their most idealized (defect-free) form, one characteristic which allows to distinguish between these allotropes is their bond configuration. In diamond, carbon atoms bond to four neighboring atoms (sp^3-hybridization) tetrahedrally, i.e., three-dimensional. Graphene shows only three bonds (sp^2-hybridization) that are located within one plane, thus, a two-dimensional structure is generated. Unlike these ideal systems, allotropes showing a mixture of different bonding configurations are also possible, for example in soot or carbon black.

Most of the work that investigates the growth of carbon particles is performed to study soot or carbon black formation in the context of combustion processes e.g., internal combustion engines, jet engines, and sooting flames. Therefore, and because in-depth studies concerning the gas-phase formation of graphene in similar pyrolysis processes are rare, the carbon growth is only described in a broad conceptualized manner based on work which is performed on the formation of soot and carbon black. This section therefore focuses on a brief description of the fundamental processes that lead to the formation of soot and how the processes should proceed in case graphene is formed. Before focusing on the carbon particle formation, classical aerosol particle growth described via nucleation theory is introduced.

In idealized aerosols the formation of particles can be described as a bottom-up process with a gas-to-particle conversion. Thus, the first stages of the growth can be conceptually discussed by classical (homogeneous) nucleation theory for aerosol processes.

At the start, a gaseous compound containing the element of interest is decomposed and releases the growth species. In case the partial pressure of the growth species exceeds the temperature-dependent saturation vapor pressure, it will start to condense. The overall Gibbs free energy of a potential spherical particle possesses contributions of the volume and surface energy (Figure 2-2). An energy barrier needs to be overcome that leads to a state of supersaturation prior to condensation. Larger clusters can form by random collisions but they are not thermodynamically stable and can directly evaporate again, as they are below the critical cluster radius *r**. Only when a sufficiently large supersaturation is present, the clusters may become large enough in size to be stable and grow as the negative volume energy becomes large enough to overcome the positive term for the surface energy.

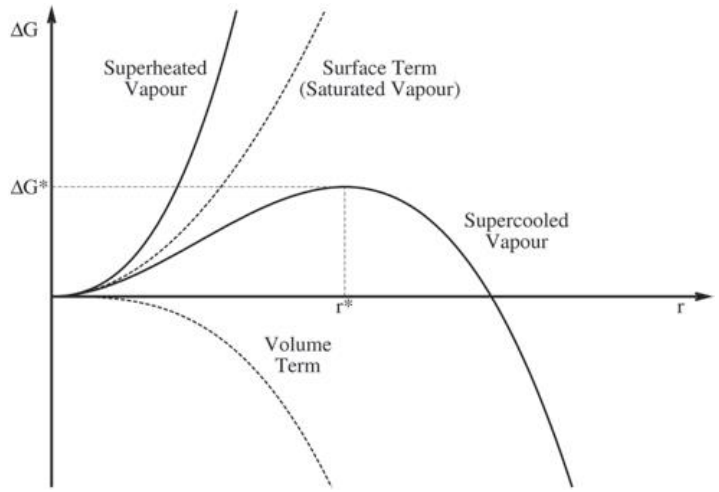

Figure 2-2: Schematic [45] showing the Gibbs free energy in relation to the size of a spherical cluster and the critical radius *r** for an idealized chemical compound. Reprinted with permission by Sage Publications.

When now coming from the idealized aerosol picture to growing carbon particles in the form of soot or carbon black, some differences have to be noted as such particles consist of interconnected aromatic rings and not condensed carbon atoms. Figure 2-3 depicts a sketch for the different processes occurring during the formation of soot-like particles. At first, the hydrocarbon reactant is decomposed into small fragments which then start to reassemble into small aromatic rings and further fuse and grow into larger polycyclic aromatic hydrocarbons (PAH). As can also be seen in Figure 2-3, the exemplary shown molecular clusters aggregate or agglomerate which then transforms them into three-dimensional soot-like particles. The growth of clusters and particles can be partly described by HACA-like (HACA: hydrogen abstraction acetylene addition) surface growth [46], in which hydrogen containing surface sites are activated and start to bond with acetylene or other reactant species. The particles will show a characteristic inner structure which is linked to the type of PAHs grown, i.e., the specific pyrolysis or combustion conditions [47]. Following their first formation, the particles will agglomerate and/or aggregate into larger particle aggregates with a morphology and fractal dimension depending on their characteristic collision and sintering times [48-50]. In case oxygen is also present, parallel oxidation of the particles in form of reverse surface growth can also occur, which will reduce their size or fully remove them.

The transition (condensation) from gaseous PAH molecular clusters towards a solid or liquid particle is ill defined but usually assumed to happen for clusters exceeding four to five aromatic

rings. In an idealized image, the clustering of PAH molecules towards particles is driven by different (partly reversible) physical and chemical processes that can occur simultaneously but are still highly debated [51-55]. For a more detailed discussion on debated mechanisms for soot inception, see the extensive review of Martin et al. [56].

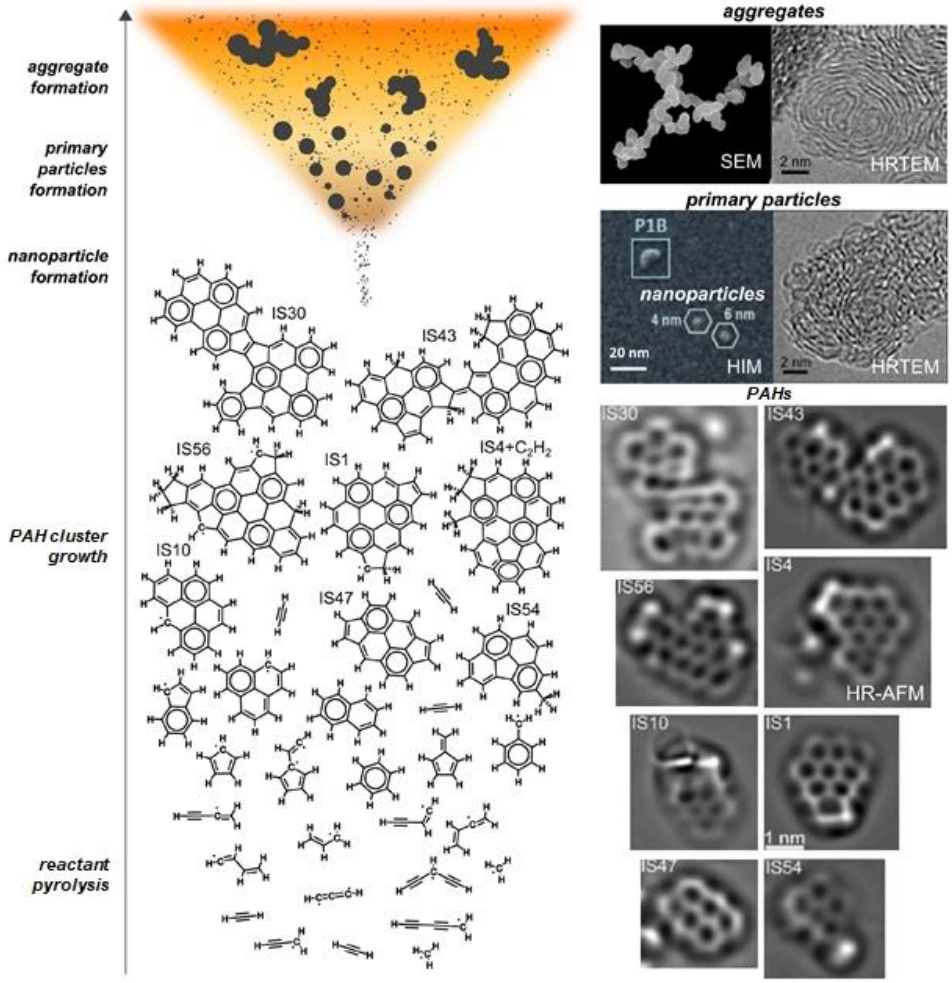

Figure 2-3: Different stages of solid carbon growth starting from reactant pyrolysis up to the agglomeration of formed solid carbon structures. Reprinted and altered with permission by Elsevier [56].

When now distinguishing between graphene and soot-like particles with graphene being a monolayer of sp^2 hybridized hexagonal carbon rings, it is clear that graphene represents an ideal large PAH molecule that does not cluster in the different growth stages. Instead, if it forms by the same processes as soot-like particles, it most likely forms by ordered continuous growth at its edge by adding small carbon fragments and clusters to the overall structure. Figure 2-4 visualizes an example for the distribution of different PAH fragments in dependence of their hydrogen-to-carbon ratio (H/C) and their number of carbon atoms extracted from a sooting flame. As a comparison, a bold line depicting fully fused (pericondensed) aromatics is shown. The bold line can be considered to represent an ideal growing graphene monolayer. It can be seen that the combustion sampled PAH fragments vary drastically in size and deviate largely from the idealized pericondensed curve.

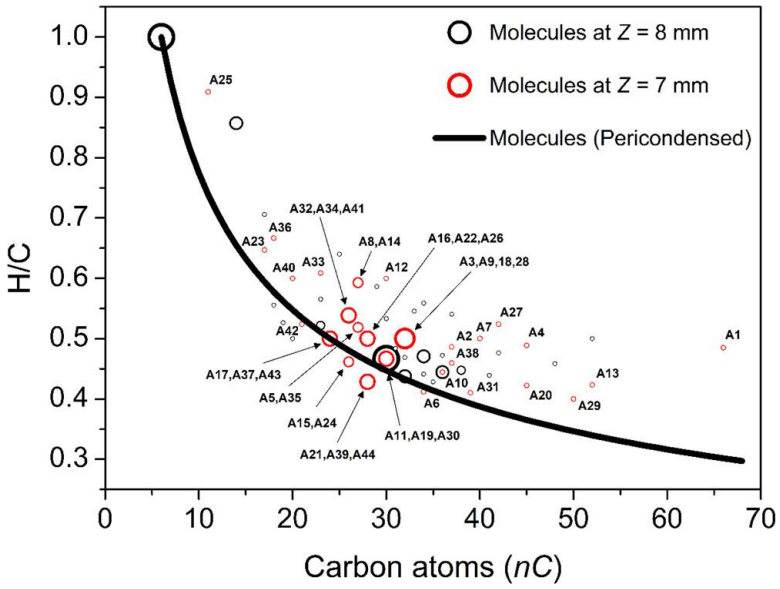

Figure 2-4: Different aromatic carbon fragments sampled from a sooting flame at two positions *Z* above a burner [57]. The black line refers to fully pericondensed aromatics, i.e., ideal graphene structures.

One reason for these deviations can be crosslinking between different PAHs and the inclusion of defects such as five- and seven-membered rings in the structure (compare to structures in Figure 2-3). The inclusion of such non six-membered rings can enhance the crumpling and growth into three-dimensional structures [58, 59] and result in strong contortions of the structure which may further increase the formation of three-dimensional structures. Examples for highly strained and contorted PAH molecules are well known in chemical synthesis (e.g., [60, 61]), are predicted by molecular dynamics simulations [62, 63], and can be observed in sooting flames [64].

When looking at their formation pathway in aerosol processes, the formation of five- and seven-membered rings has been theoretically proposed in the past by Whitesides to be temperature sensitive [65]. Five- and seven-membered rings become unstable at temperatures above 2000 K leading to their removal which results in only flat six-membered ring containing PAHs. More recently, authors such as Leon et al. and others showed that such structures can be stabilized at similar temperatures in larger PAH structures by specific reactions [66, 67], thus the quantitative effect of temperature on the inclusion of non six-membered rings is still up to debate as there also exist other proposed pathways which transform five-membered rings to six-membered rings [68]. In general, it is known that the amount of soot generated in flames depends on the temperature and does show a characteristic bell-shaped curve, i.e., at too high temperatures, the volume fraction of solid carbon becomes smaller [69, 70]. A commonly used explanation in accordance with Whitesides is that at high temperatures, a large fraction of the required precursor molecules become unstable. Additionally, experiments performed in high-temperature flames by Dasappa et al. showed the formation of graphitized and graphenic structures when the temperature of the flames is increased [71-73]. Therefore, high temperatures seem to favor the formation of larger sized ordered PAHs.

Another aspect that has been considered important is parallel oxidation of the growing carbon clusters. It was shown theoretically that the oxidation of PAH molecules depends on their structure and the oxidant used [74, 75]. Consecutive theoretical studies revealed that the oxidation of five-membered rings is faster when atomic oxygen is the oxidant compared to molecular

oxygen or OH [76]. Based on these considerations, Leon et al. proposed a model in which the type of carbon nanostructures obtained only depends on the partial pressure of either molecular or atomic oxygen as oxidizer in typical flame conditions [77]. Detonation experiments with acetylene/O_2 mixtures have also shown the formation of graphene-like materials, but also reach larger temperatures (>2500 K) [78, 79].

To summarize, solid carbon is formed by the formation of growing molecular PAHs. Depending on the growth conditions, the interaction between these clusters and their own properties can change. Graphene monolayers can be considered as a single large PAH, which indicates that their growth is not governed by the agglomeration or aggregation of PAH clusters but instead by controlled edge growth. In the following Section 2.2.1 a short overview of studies concerned with the growth of freestanding graphene is presented.

2.2.1 Studies on graphene growth in plasmas

The catalyst-free gas-phase growth of freestanding graphene-like materials is experimentally investigated in a large variety of different plasma systems including inductively coupled plasmas, gliding arcs, and microwave plasmas. Most of the studies are phenomenological in nature and are not as detailed as some of the studies on the formation of soot presented in the previous section. Yet, some interdependencies between the reactants and specific grow conditions have been revealed. As an example, Dato et al. [36], Münzer [35] and Fronzcak et al. [37, 80] varied the (oxygen-containing) reactants supplied in their respective plasmas to investigate the effect of the reactant's elemental composition on the grown carbon nanomaterials. In all three cases the conclusion is that a specific elemental composition of the reactant has an impact on the growing carbon materials in which 2:1 carbon-to-oxygen ratios such as in ethanol are favorable. Increasing the C/O ratio leads to an increasingly larger fraction of soot-like particles being formed. The absolute reactant concentration [81-83] and the residence time [36, 84, 85] are also observed to impact the grown carbon materials. Experiments with varying reactant concentrations show that under otherwise identical conditions, lower reactant concentrations favor the formation of freestanding graphene while larger concentrations lead to mixed carbon materials. When the residence time is varied, it is shown that longer residence times can lead to a shift from the formation of freestanding graphene towards thicker stacks of layers [85] or graphitic particles [36, 84]. Other authors are able to show that the specific time-temperature profile in the reactor affects the growth conditions leading to the formation of different types of carbon materials [86-90]. Pristavita et al. [86] and Toman et al. [88] altered the reactor dimensions, Wang et al. [89] changed the reactant input position, and Tartarova et al. artificially controlled the downstream wall temperature [87]. In all cases differences in the grown carbon material are noted. Some authors also argue that high temperatures (>2500 K) and the presence of C2 species are pivotal to generate ordered carbon structures [89-92]. Additionally, the influence of hydrogen on the growth process has been investigated and the results suggest that hydrogen addition can be beneficial to favor the formation of a specific carbon material such as freestanding graphene [93-96]. The common argument used for the effect of molecular hydrogen is that it passivates/inactivates the surface of growing PAH molecules and therefore prevents and slows further growth or reactive assembly into three dimensional structures.

As a specific example and similar to the fundamental studies for the growth of soot, the work of Toman et al. [90] used an atmospheric microwave plasma torch and analyzed the growing PAH clusters when synthesizing solid carbon particles from ethanol vapor under varying

conditions. For analysis, they sampled molecular species grown in the plasma reactor by proton-transfer-reaction time-of-flight mass spectrometry (PTR-TOF-MS) and tried to link it to the grown carbon nanostructures. Their results show the presence of evenly spaced PAH molecules up to 229 u with step sizes of 50 u (+1 six-membered ring) and intermediate separations of 24/26 u suggesting the growth of PAHs by acetylene addition. They measured both even ($C_{2n}H_x$) and odd ($C_{2n+1}H_x$) sized clusters, i.e., pericondensed PAHs and PAHs containing defects such as pentagons. When the input microwave power was increased, they observed an increase in (rotational) gas temperature and the relative fraction of even-numbered carbon clusters increased leading to less defective carbon materials, i.e., again giving evidence that higher temperatures are favorable for the synthesis of freestanding graphene.

Based on the fundamental description of carbon growth and the aforementioned different investigations there are two major question which will be addressed in this thesis.

First, when graphene materials only grow by edge growth, it should be possible to sample and observe perfect monolayers in the early growth stages. Additionally, this might give insight into the morphology and structure generation as the materials harvested are usually highly crumpled and vary drastically from perfect round monolayer graphene.

Second, what is the effect which makes specific C/O ratios favorable for the synthesis of graphene? The primary goal in this context is to rationalize the empiric studies as performed by Dato et al., Münzer et al., and Fronzcak et al. by eluding the effect of oxygen on the process.

2.3 *Ex situ* measurement techniques for the analysis of carbon nanomaterials

2.3.1 Raman spectroscopy

Raman spectroscopy is commonly employed to characterize carbon materials as it is very sensitive to their microstructural properties The method is based on the inelastic scattering of light with a sample which is probed (Figure 2-5). For the measurements, the sample is illuminated by a laser beam with a fixed frequency ν_L which either interacts elastically (Rayleigh scattering) or inelastically with the sample (Raman scattering).

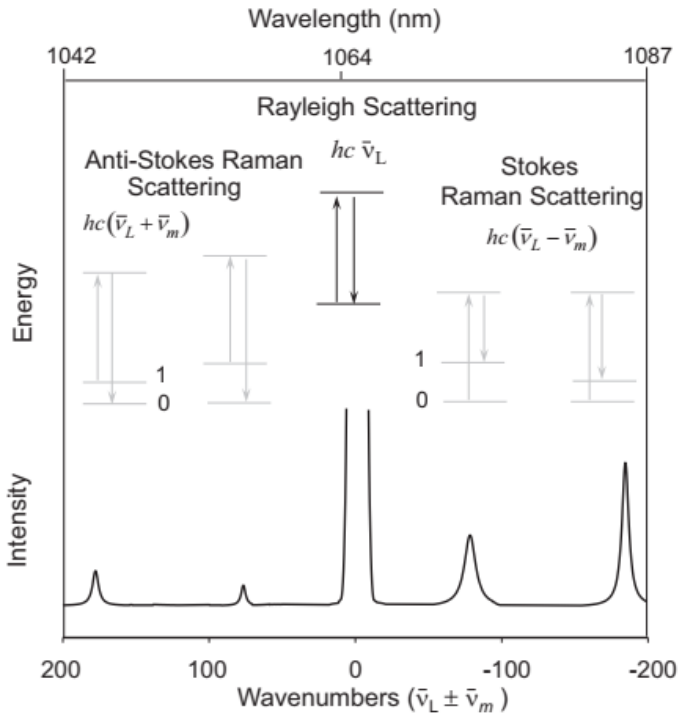

Figure 2-5: Sketch depicting the elastic (Rayleigh) and inelastic (Raman) scattering of radiation (Reprinted with permission by Elsevier [97] p.17).

Depending on whether the frequency of the inelastically scattered light is shifted to higher or lower values, it is referred to as Anti-Stokes and Stokes scattering. The light used for excitation couples to the vibrational modes of the sample. In solids the vibrational modes are a result of a collective atom motion which depend on the crystal structure and are called phonons. When the frequency of the emitted light (in relation to the excitation beam) decreases, the energy difference is attributed to the excitation of a phonon with the energy ν_M. When the frequency increases, the increase is attributed to the obliteration of a phonon. Not all vibrational modes are Raman active but they have to obey and fulfill specific selection rules. For vibrations that are Raman active, the selection rules require the polarizability α to change in respect to a change of the amplitude Q of the vibrational motion.

$$\frac{\partial \alpha}{\partial Q} \neq 0 \qquad \text{Eq. 2-1}$$

In case of solid carbon materials, the Raman active vibrational modes refer to oscillations of the six-membered ring structure and specific bonds. In the following the focus is on the interpretation of the measured G (~1350 cm^{-1}), D (~1850 cm^{-1}), and 2D (~2695 cm^{-1}) Raman bands and not on the detailed theory of their generation. Thus, only a short summary is presented. More details on their origin and their behavior can be found in the book of Jorio et al. [98] or several review articles, e.g. [99-101]. As a short summary, the D band is activated by elastic electron scattering defects in the sample. The G band represents an oscillation of sp^2-bonded carbon, so it is also observed in highly disordered carbons but sensitive to sample properties such as strain and doping. The 2D band is second order overtone of the D band and its intensity is sensitive to the band structure and structural order of the carbon materials.

2.3.1.1 Raman bands of ordered and disordered carbon materials

In general, the Raman bands of graphene are directly linked to fundamental interactions between generated charge carriers and the band structure of the material. Thus, the Raman bands are commonly employed to analyze graphene samples and infer their properties. The number concentration of structural defects and the crystallite size are two quantities which can be extracted from the D and G band [102, 103]. The 2D band is commonly employed to probe the number of stacked graphene layers (e.g., for Bernal stacked layers [104]). Other information such as the level of strain or doping can also be inferred from the position of the 2D and G bands in monolayer samples [105]. Figure 2-6 shows an example for two Raman spectra recorded for two carbon materials synthesized during this work in which all the discussed bands are present and clear differences between their intensities and widths are observable.

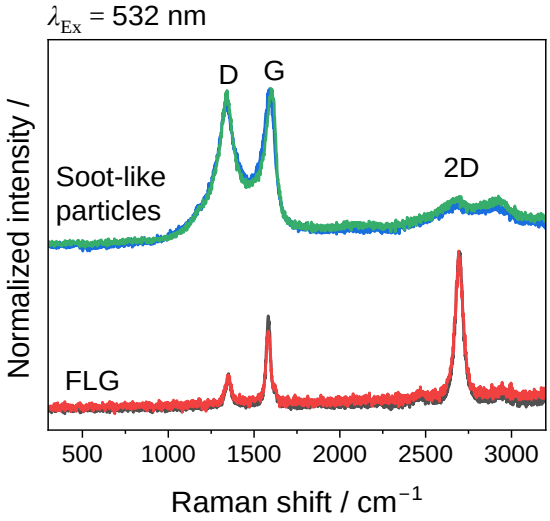

Figure 2-6: Raman spectra recorded of soot-like particles and FLG prepared in the plasma reactor.

The calculation of the layer number employs a model which is based on the induced changes of the band structure by the addition of more layers. This criterion is used on graphene materials which have been either grown by CVD or were prepared by exfoliation techniques as the stacking order of such materials is known. In case of the gas-phase synthesized materials prepared in this work, the stacking order is not automatically known and not necessarily homogeneous. Instead, usually an arbitrary stacking and folding in the generated flakes is observed. The measured intensity and width of the 2D band in the Raman spectra do not match to the expectations of Bernal stacked layers. A possible explanation might be that the random folding of layers leads to the formation of turbostratic stacking. It is known that turbostratic stacking produces a different evolution of the band structure which still results in a single Lorentzian band instead of the combination of multiple bands which generate the analyzed broadening [106-109]. A proof for the observation of such stacking order can be the specific combinational modes in the range of ~1750–2200 cm^{-1} [110-112]. However, bands in this region are not consistently observed for every measurement, so they are not used for analysis.

The models used to predict the crystallite size or defect density require to fit the different bands to extract the ratio of integrated areas of the D and G band (A_D/A_G) and the width of the G band. The models are developed for the application in monolayer graphene, so an application to multilayer structures which also might contain strain and dopants is not straightforward and

requires careful examination [102]. Another aspect affecting the measured Raman spectra is the specific morphology of the graphene flakes generated in plasma synthesis. Compared to flakes generated by CVD and, e.g., mechanical exfoliation, the flakes are quite small in size with ~200–300 nm of equivalent diameter. Therefore, the excitation laser beam will always measure the edges of the flakes which in case of a (symmetry-breaking) armchair configuration will contribute to the detected D band intensity [113, 114]. Other works suggest that scattering promoting a D band can also be generated at folds [115, 116].

When analyzing highly defective carbon materials such as specific soot's, the crystallite sizes and defect concentrations can also be estimated based on the D and G bands. In case of soot-like particles, the presence of additional bands is observed in the region between 1100–1650 cm^{-1} with some of them being characteristic for defective sp^3-carbon structures [117, 118]. Dependent on the degree of crystallinity, the separation of D and G band disappears and is instead filled up with another defect induced band [119]. Another important difference compared to graphene-like materials is the weakened 2D band intensity.

To conclude, for simple homogeneous carbon samples models exist that based on their respective assumptions have limited applicability. Therefore, it is not possible to directly extract quantitative information about, e.g., specific layer numbers or defect densities from the synthesized carbon samples. Additional problems arise when the samples analyzed are heterogeneous as in this work in which the samples are rarely consisting of just one carbon phase. As an example, it may not be clear which part (width, intensity) of e.g., the D band belongs to which phase. Still, it is possible to qualitatively distinguish between disordered and ordered carbon materials. In cases where the Raman bands in the region of 1100–1650 cm^{-1} are not well separated and a shoulder in the range of 1100–1250 cm^{-1} can be observed, the presence of disordered carbon structures such as soot-like particles is likely, especially when the 2D band is not as pronounced as for pure graphene samples.

For the measurements, a small amount of a sample is transferred onto a glass plate and compacted with a spatula. The measurements are performed at room temperature under ambient atmosphere at wavenumbers between 300 and 3200 cm^{-1}. A Renishaw inVia confocal Raman microscope is operated with a 532 nm frequency-doubled continuous-wave Nd:YAG laser and a diffraction grating of 1800 lines/mm. During measurement, the laser power was set to ~0.07 mW with a spot size of 10–15 µm in diameter. These conditions (<100 W/cm^2) are chosen to prevent any sample heating or induced reactions [120] during the measurements. The measurements were performed at two or more separate locations for each sample, as the prepared powder bed does not fulfill the necessary requirements for Raman maps.

2.3.2 Transmission electron microscopy

Transmission electron microscopy (TEM) is employed to image and analyze the generated carbon materials. Explicit details on the instrumentation and imaging can be found in the books of, e.g., Leng [121] and Brydson [122]. For such measurements an electron beam with acceleration voltages up to ~400 kV is generated and both focused and guided with the help of magnetic and electrostatic lenses. The theoretically obtainable resolution is depending on the electron energy because the de Broglie wavelength of an electron scales with its energy. Hence, because of the high acceleration voltage, the electron beam allows for imaging with a high resolution (<1 nm) when aberrations are corrected. The elastic or inelastic interaction of

the electron beam with the samples is driven by different mechanisms, which allow to infer different corresponding properties of the sample.

Some electrons are elastically scattered while passing the sample, which modulates the detected electron beam intensity and generates an image. Diffracted electrons are excluded from reaching the detector. When the contrast is generated by such interactions (mass-density contrast and diffraction contrast), it is called an amplitude contrast. When high-resolution TEM (HRTEM) images are generated, both the diffracted and non-diffracted transmitted electrons are analyzed which together generate an interference pattern based on their phase shifts (phase contrast).

Additionally, electrons can inelastically scatter with the sample. They can collide with other electrons of the atoms in the sample and kick them out leading to core level ionization. These states are refilled by electrons of higher energy which can then lead to the emission of (elemental) characteristic X-ray photons or Auger electrons. The ratio of emitted Auger electrons to X-ray photons is depending on the mass of the atom. Light elements tend to emit a larger fraction of Auger electrons while heavy atoms emit relatively more X-rays. An emission spectroscopy method analyzing the emitted characteristic X-ray photons is the energy dispersive X-ray spectroscopy (EDX). It allows to determine the elemental composition of the sample locally resolved to, e.g., visualize the presence and distribution of contaminants. A separate absorption spectroscopy method is the electron energy loss spectroscopy (EELS). For this analysis method, the kinetic energy of transmitted electrons is measured and analyzed. EELS spectra can be separated based on processes involved in the inelastic electron scattering in low loss (<50 eV) and high loss region (>50 eV). The high loss region maps the ionization edges of the different elements but also allows to analyze its fine structure. In carbon materials, the fine structure can give information about the present chemical bonds [20, 123, 124].

TEM and HRTEM measurements are performed with a Cs-corrected JEOL Jem 2200FS using 200 kV acceleration voltage. The samples which are harvested from the filter (compare to Figure 3-5) are prepared by dispersing a small amount of the sample powder in absolute ethanol (≥99.8 % purity) followed by ultrasonication for 20 min. A few droplets of the dispersion are drop-casted on lacey copper TEM grids and dried under a fume hood. Contrary, the samples collected with the thermophoretic sampling system (see. Sections 2.4.2 and 3.3) are measured without further sample preparation as they are directly deposited on TEM grids.

2.3.3 Thermogravimetric analysis

Thermogravimetric analysis (TGA) describes a method in which the mass of a sample is recorded in relation to an applied temperature program. The measurements are called dynamic when a constant heating rate is applied or isothermal when the temperature is held constant, but custom heating programs are also possible. For the measurement the atmosphere (inert, reactive) can be adjusted to look at reactions of interest. The temperature-resolved mass changes then allow to deduct information about chemical reactions like oxidation or decomposition occurring in the measured sample. Additionally, the differential thermogravimetric (DTG) curve is complementarily displayed to show the rate of mass change. The method can be combined with the simultaneous measurement of heat flow (Simultaneous thermal analysis) or the measurement of the evolving gases by, e.g., a mass spectrometer. In his work, TGA measurements are in all cases combined with quadrupole mass spectrometer (QMS)

measurements of the released gases. More details on instrumentation and calibration procedures can be found in the books of, e.g., Laye et al. or Gabbot et al. [125, 126].

For characterizing the microstructure of carbon materials, a common approach to is to measure the mass loss by combustion. The oxidation reaction is heterogeneous and will depend on the transport processes of the oxidizer to the surface of the carbon material and on the number of available active sites. The transport phenomena involve the diffusion of the oxidizer to the surface of the carbon material, its adsorption and chemical reaction, followed by the desorption and removal of products (Figure 2-7). The active sites and the corresponding reaction rates depend on the specific edge site and the oxidizer used [74, 76]. Because the oxidation process possesses such dependencies, it proceeds differently when the carbon materials have varying properties such as graphene compared to more amorphous soot-like particles.

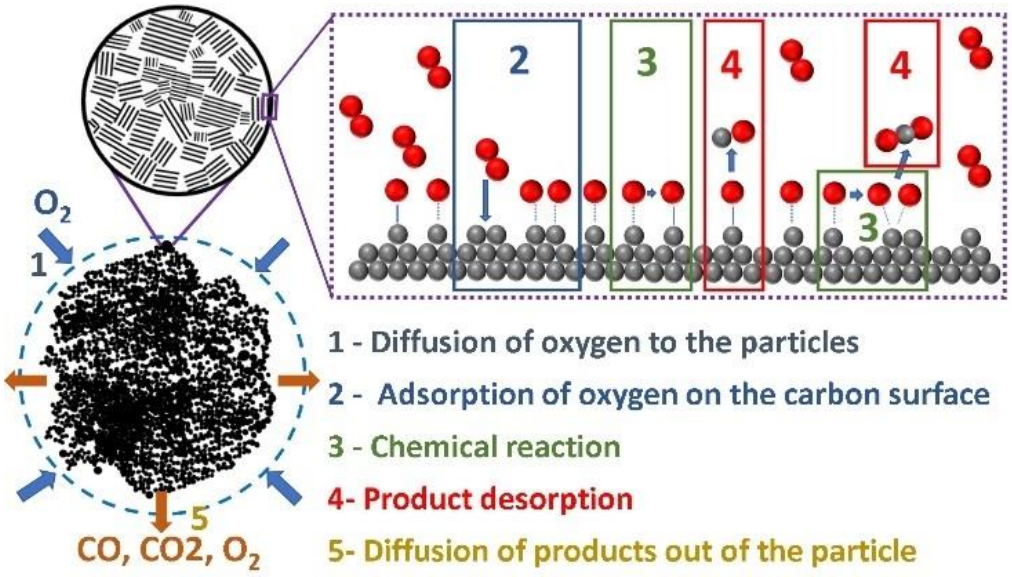

Figure 2-7: Transport processes involved in the oxidation of carbonaceous materials [127].

It is known that the oxidation onset and speed can vary dramatically when more or less graphitic soot types are analyzed by thermogravimetry (400–900 °C) [128-131]. For graphene-like materials, similar observations are reported and the DTG profiles can be employed to distinguish between graphene oxide, reduced graphene oxide, few-layer graphene, and graphite [132, 133]. Interlaboratory comparisons have shown that thermogravimetry does perform well in terms of reproducibility and confidence, therefore, the method is considered to be implemented in the International Organization for Standardization (ISO 229) and International Electrotechnical Commission (IEC 133) standard for the chemical characterization of graphene-like materials [134]. Additionally, it can be employed to detect metal contaminants which are able to catalyze the oxidation reaction [135].

The carbon samples prepared in this work mostly contain soot-like particles and FLG. In case the oxidation of the soot-like particles (depending on how graphitic they are) does not overlap with the oxidation of FLG, the different carbon phases can be quantified. The analysis is performed based on a calibration procedure which also involves the CO_2 evolution measured by the QMS and is described in more detail in the Appendix Section 9.1. For the measurements, a Netzsch STA 4491 F1 Jupiter connected to a Netzsch QMS 403 D Aëolos for simultaneous mass spectroscopic measurements is employed. For all these measurements, O_2 (17 % or

25 %) diluted in Ar was introduced into the sample chamber, in which materials are thermally treated from 40 to 1000 °C at a heating rate of 5 °C/min. The mass spectrometer was set up to monitor the mass to charge (m/z) ratios for the TG combustion products and reactants, i.e., water and CO_2 fragments, O_2, and Ar.

2.3.4 Gas adsorption isotherm

Gas adsorption describes the fundamental physical process of a gaseous species becoming attached to a solid material by the means of physical or chemical forces. There exists a large number of practical applications and characterization methods utilizing adsorption processes in, e.g., thermal separation processing or for characterization of materials. One analysis method based on physisorption is the determination of e.g., pore volume, type of porosity, and the specific surface area (SSA) by measuring adsorption isotherms. More details on relevant adsorption processes can be found in corresponding books, e.g., [136, 137].

Adsorption isotherms can be recorded for the adsorption of any gaseous species and are classified by the International Union of Pure and Applied Chemistry (IUPAC) based on their specific shape into six different categories [138]. Its shape can give insights into whether the measured sample possesses micro- (<2 nm), meso- (2–50 nm), or macropores (>50 nm) and whether other physical processes such as cavitation are occurring. A way to perform the measurements is to dose specific amounts of adsorbent species to the sample and to monitor the equilibrium pressure at which the rate of adsorption and desorption is equal. When repeating the process multiple times, an adsorption isotherm displaying the number of adsorbed species in relation to its partial pressure is generated. To extract the specific surface area of a sample, a standard approach is to apply the model developed by Brunauer, Emmett, and Teller (BET) [139]. The BET model describes multilayer adsorption on a surface while requiring some fundamental assumptions. As an example, one assumption is that no interactions between neighboring adsorbed species occur and that the surface has homogeneous adsorption sites. Therefore, its applicability is limited by, e.g., the type of observed isotherm or which type of porosity is present in the sample. The linearized version of the BET equation is shown in Eq. 2-2. The equation describes the amount of adsorbed species $n(p)$ in dependence of the measured equilibrium pressure p. C describes an empirical constant, n_m the monolayer capacity of the adsorption, and p^0 is the saturation pressure of the used adsorbent.

$$\frac{p/p^0}{n(p)(1-p/p^0)} = \frac{1}{n_m C} + \frac{C-1}{n_m C}\left(p/p^0\right) \qquad \text{Eq. 2-2}$$

To determine the surface area, the obtained datapoints have to be converted in a BET plot format by plotting $[p/n(p)(p^0–p)]$ against p/p^0 and the values for n_m and C can be extracted from the slope and intercept. When n_m is known, the surface area can be calculated. The BET analysis is usually restricted to datapoints recorded in the range of ~0.05–0.3 p/p^0 but can be altered to different ranges when care is taken.

2.3.5 X-ray photoelectron spectroscopy

X-ray photoelectron spectroscopy (XPS) allows to probe the composition and bonding state of measured materials in a surface sensitive manner by determining the kinetic energy of emitted electrons. The electrons can thereby be created by two processes shown in Figure 2-8.

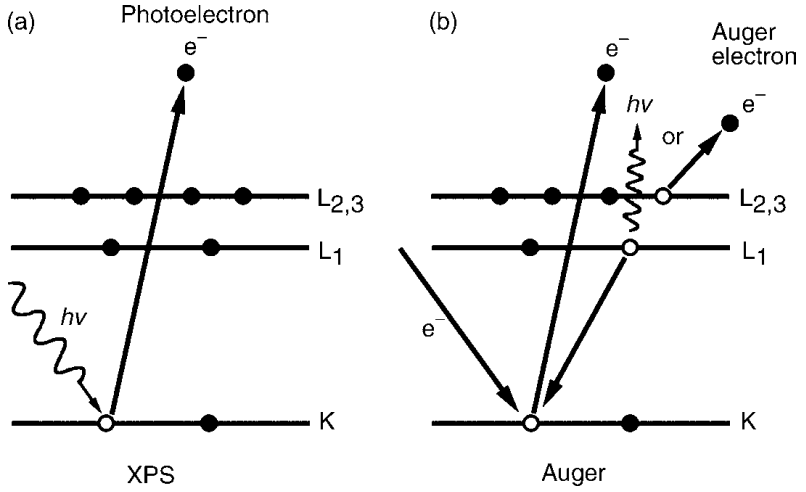

Figure 2-8: Generation of a) photoelectrons or b) Auger electrons. Reprinted with permission by John Wiley & Sons [140].

Core level electrons can be directly excited by the absorption of an X-ray photon with the energy $h\nu$ when the energy surpasses the binding energy and the work function for the electron. As already mentioned when describing TEM in Section 2.3.2, secondary emission can occur when the now unoccupied level is repopulated by electrons from outer shells. Either an X-ray photon or an Auger electron is emitted. The process is surface sensitive because the generated photoelectrons can scatter in the material and reabsorb. Therefore, only electrons are detected which are excited near the surface within their kinetic energy dependent escape depth, which is usually below 10 nm (Figure 2-9). The energy of the emitted electrons is characteristic for the core level of its parent atom. Hence, it can be used to identify the (surface) elemental composition of materials. Furthermore, the kinetic energy is sensitive to the "environment" of the involved atoms (chemical shift), so it is used to analyze the atomic bonds.

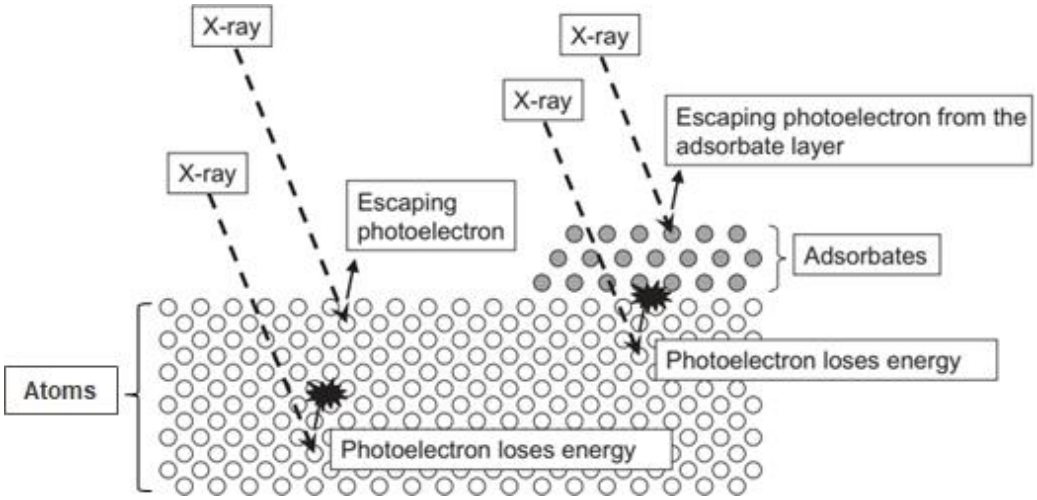

Figure 2-9: Losses of generated photoelectrons leading to surface sensitivity of XPS measurements. Reprinted and modified with permission by John Wiley & Sons [141]

Measurements of carbon materials directly allow to analyze the type of bonding and the presence of impurities or dopants. Figure 2-10 displays the comparison of typical measured spectra of FLG and soot-like particles (both contain ≤1 at.% oxygen) for a high-resolution scan of the C_{1s} spectrum. The line shape and position of the carbon signal depends on the carbon

structure, i.e., the hybridization state. Carbon materials possessing sp^2 hybridization show an asymmetric line shape while sp^3 hybridization generates a symmetric line shape and their line positions are different at 284.3–284.6 eV and ~285 eV respectively [142, 143]. Additionally, sp^2 carbon materials show a characteristic π–π^* shakeup feature at ~290 eV. Because soot-like particles contain a different sp^2/sp^3-bond ratio than FLG, the C–C bond line is slightly shifted to larger binding energies and the line is broader and more symmetric. Based on the shift in line position and shape, Münzer [35] developed an empirical model to fit the carbon line for heterogeneous samples (containing both soot-like particles and FLG) and infer their concentrations. The same approach is used within this work as well.

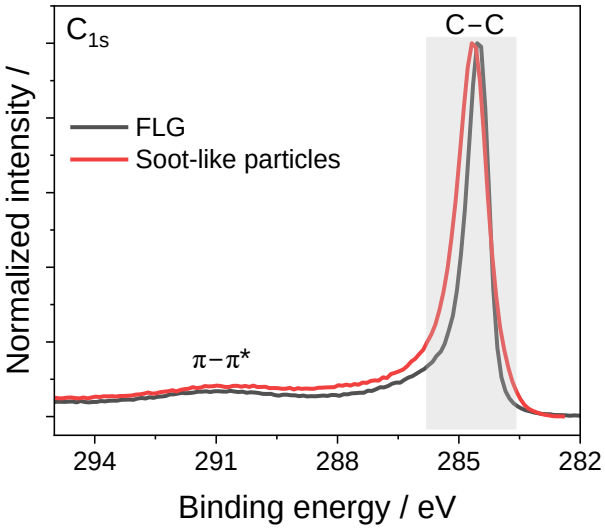

Figure 2-10: High-resolution XPS scans of the C_{1s} carbon line obtained from measuring FLG and soot-like particles.

The instrument used for the measurements is a PHI 5000 Versaprobe II microfocus X-ray spectrometer. Powder samples are mounted on a double-sided 3M Scotch tape onto the sample holder. An influence of the sample preparation on the measurements has not been observed [144]. For all measurements, the angle between specimen and analyzer is fixed at 45° and an Al-Kα source ($h\nu$ = 1486.6 eV) is used for excitation. All spectra are attained using 11.75 eV pass energy, and shifted relative using a 360 s etched Cu-foil surface as reference. The spectra are analyzed using Casa XPS [145].

2.4 *In situ*, inline, and particle sampling techniques applied in this thesis

2.4.1 Optical spectroscopy

In the context of this work, optical emission spectroscopy (OES) and infrared absorption spectroscopy are utilized to identify molecular and atomic species in and near the plasma and stable pyrolysis products in the effluent of the reactor. In both cases, the measurements are influenced by the properties of the molecular and atomic species as the absorbed or emitted light is characteristic and represents specific energy transitions. In the following a brief description of the involved energy levels and their analysis is given, while more elaborate explanations and details can be found in the books of, e.g., Herzberg, Hanson, or Bernath [146-148]. Raman spectroscopy on gas molecules is explicitly neglected, albeit it was used as a *ex situ* analysis

technique on the obtained carbon particles (Section 2.3.1). Simple examples for the energy level structure for atoms and molecules are depicted in Figure 2-11.

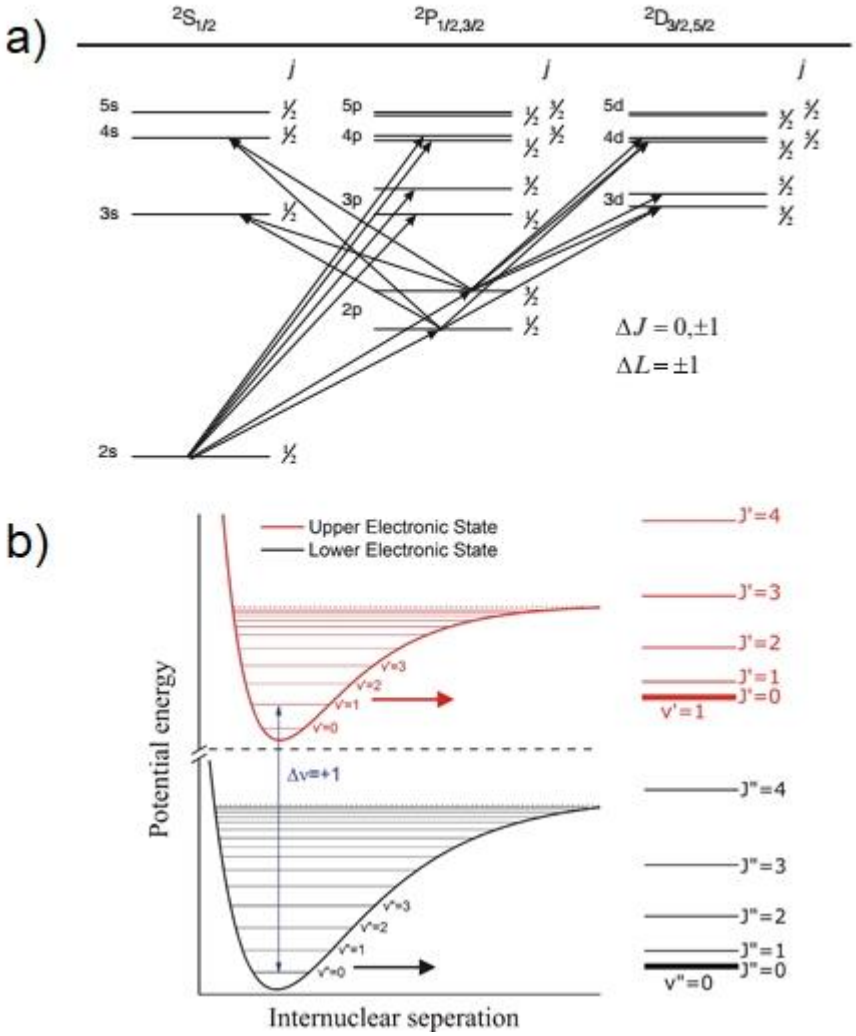

Figure 2-11: Examples for the energy levels of atoms (a) and molecules (b) including their energy splitting. For (a), some of the low-lying lithium energy levels are shown (Reprinted with permission by Springer Nature [149]), while (b) shows an arbitrary molecule (taken from [150]).

It can be seen that both atoms and molecules possess characteristic energy levels. The transition between the different levels is restricted by specific selection rules, i.e., not every energy level can transition into another energy level. In atoms the energy levels are related to the electron quantum numbers while in molecules these energy levels can be split into electronic, vibrational, and rotational contributions. When either the emission or absorption is measured, the intensity of the different observed bands will depend on characteristic factors describing the specific transitions like, e.g., the occupation of the respective states and transition probabilities. Therefore, in both cases information of the probed/observed molecules or atoms can be obtained. For molecules it is common, e.g., to extract information about the gas-phase temperature. For such purpose, different approaches can be used, but in all cases the relative line intensities are related to the temperature dependent equilibrium occupation of excited states (Boltzmann distribution). Care has to be taken though to not misinterpret some of the occupied energy states as some of them may be generated by, e.g., reactions and not by the equilibrium temperature.

Another aspect is the analysis of the line shape as the width of the lines is not infinitesimal small but determined by different broadening mechanism. The line shape can be described by a Voigt profile which consists of Gaussian and Lorentzian contributions. The Gaussian profile/shape contributions include the instrument function of the measurement system and Doppler broadening generated by the movement of the species relative to the detection system. The Lorentzian contributions can be distinguished between effects caused by pressure broadening and natural line width broadening. The latter refers to the natural lifetime of an excited state before it decays or recombines which when related to the uncertainty principle leads to a small spread of energies. Pressure broadening then refers to processes which perturb either the energy state itself or the lifetime of the excited state. Effects that change the lifetime of the excited states are usually collisional processes, e.g., collisions with alike species (resonance broadening) and collisions with different neutral perturbers (Van der Waals broadening). In plasmas, Stark broadening is observed as well, which is generated by nearby ions or electrons that alter the energy state of the excited species via electric microfields (Coulomb interaction) [151-153]. Because the broadening mechanisms depend on parameters such as the gas temperature and the number density of the perturbing species, the line shape can be deconvoluted to gain corresponding information.

2.4.1.1 Optical emission spectroscopy

OES utilizes the emission of light to determine properties of the light emitting system. In a plasma this may yield information about, e.g., concentration of electrons or the temperature of different present species. The intensity of an emission line in energy per second from a state *n* to *m* can be defined following the definition by Herzberg ([146] p. 20) as:

$$I_{nm} = N_n h c\, \tilde{\nu}_{nm} A_{nm} \qquad \text{Eq. 2-3}$$

The emission intensity is proportional to the number of species in the initial state N_n and their effective transition probability A_{nm} in addition to the energy of each emitted photon of energy $hc\tilde{\nu}_{nm}$. Assuming that the number of species in the initial state is only occupied based on the equilibrium temperature, it can be substituted with the Boltzmann distribution leading to Eq. 2-4. E_n is the energy of the transition, g_n the degeneracy of the energy level, and $Z(T)$ the partition function.

$$I_{nm} = hc\tilde{\nu}_{nm} A_{nm} N_0 g_n \frac{\exp\left[{}^{-E_n}/_{k_B T}\right]}{Z(T)} \qquad \text{Eq. 2-4}$$

Rearranging the equation and taking the logarithm on both sights yields the general form (Eq. 2-5) used for the Boltzmann plot method. Plotting the logarithm against the energy level of the upper state will – in case of equilibrium – lead to a straight line which slope can be used to calculate the characteristic temperature *T*.

$$\ln \frac{I_{nm}}{\tilde{\nu}_{nm} A_{nm} g_n} = \text{const.} - \frac{E_n}{k_B T} \qquad \text{Eq. 2-5}$$

There exist a number of different more specific formulations for the Boltzmann plot formula depending on the temperature which is analyzed and whether the lines are observed as emission or absorption. As an example, atomic emission lines such as Ar are commonly used to estimate excitation or electron temperatures in plasmas while the molecular lines allow one to

obtain information about rotational and vibrational temperatures of the corresponding molecule. Within the thesis (Sections 5 and 6), the emission lines of OH and C_2 are used to obtain rotational temperatures after simplifying Eq. 2-5 with some assumptions (details of the employed formulations are given in Section 9.3 of the appendix). Thus, as a second approach, the measured C_2 spectra are also fitted by comparing them to simulated spectra with the software PGOPHER [154]. The program can simulate emission and absorption spectra for a wide range of small molecules. For further information the online documentation is suggested [155].

Another common approach in plasmas is to use specific lines of the emission of atomic hydrogen (Balmer series) to estimate electron concentrations. Thereby the line width is deconvoluted into different contributions including the Stark shift, which gives information on the electron concentrations near the emitter. However, a full calculation and analysis of the Stark shift was not possible during this work and the reasons are discussed in more detail in the appendix Section 9.3.

2.4.1.2 Infrared absorption spectroscopy

As mentioned in the previous section, molecules possess vibrational and rotational energy levels. Infrared radiation is able to excite the vibrational levels when specific selection rules are fulfilled. Gaseous molecules will also show a complex rotational fine structure. The amount of light a molecular species absorbs depends on its concentration, absorption cross section and the absorption length. Eq. 2-6 describes the expected attenuation of light in form of the Beer-Lambert law ([147] p.125). L describes the path length for the absorption, n is the number density and σ_v is the absorption cross section.

$$\frac{I}{I_0} = \exp(-n\sigma_v L) \qquad \text{Eq. 2-6}$$

The absorption measurements are not performed with narrow wavelength IR light but instead by using wideband IR light analyzed by Fourier transformed infrared spectroscopy (FTIR). In FTIR, a Michelson interferometer is employed which produces an interferogram. The interferogram contains the intensity of light in relation to the optical path difference which is changed with a movable mirror. Fourier transforming the interferogram then generates the absorption spectrum showing characteristic lines for the different active molecular species [156]. Analyzing the fine structure of molecular lines can then be used to employ the Boltzmann plot method and determine the rotational temperature.

2.4.2 Thermophoretic sampling of particles

Particles generated in aerosol processes typically show a distribution of their particle size. The distribution poses a problem for the collection of particles, as most deposition mechanisms are a function of the particle size. Hence, collecting particles in a way that represents their particle size distribution in the aerosol is challenging. As an example, gravitational settling does directly depend on the particle mass, i.e., smaller particles can take magnitudes longer to collect ([157] pp. 407–409) leading to larger particles being overrepresented compared to the particle distribution in the aerosol. Similarly, depositing particles by exposing them to an electric force depends on the acquired charges of the particles, which is strongly size dependent [158] and again leads to an overrepresentation of large particles.

For sampling of hot carbon particles during formation and growth in the aerosol, thermophoretic deposition is employed in Sections 6 and 4. Thermophoretic forces generate particle motion in a temperature gradient. In a microscopic picture, the particle motion is generated by collisions with more energetic molecules from the hot side, which transfer momentum to the particle leading to a net flow towards the cold surface. Unlike both previously mentioned examples, gravitational settling and electrical precipitation, thermophoretic particle deposition is almost independent of particle size for Knudsen numbers in the free-molecular regime ($Kn > 1$). The Knudsen number is defined as the ratio of twice the mean free path of the gas molecules (l_g) to the particle diameter (d_p). Figure 2-12 shows a plot depicting the dependence of the dimensionless thermal settling velocity on the Knudsen number (the mean free path uses the index p). As can be seen, the dimensionless thermal settling velocity in the region $Kn > 1$ is almost constant while the region $Kn < 1$ shows strong variations in the settling velocity, which also depend on the ratio of thermal conductivity of the considered particle (k_p) and the gas (k_g). The mean free path l_g for the experiments described in this thesis is estimated with Eq. 2-7 ([157] p.399). For the calculation values for the gas viscosity μ_g, gas pressure p_g, molecular mass Mg, and gas temperature T_g are required. Values for the gas viscosity are taken from literature (~5.5×10^{-5} and ~12×10^{-5} Pa s) [159] based on the estimated gas-phase temperature at the sampling position of ~1000 and 2600 K (temperatures are based on a temperature profile which was generated during the work for this dissertation, see. Figure 5-13).

$$l_g = \frac{2\mu_g}{p_g\sqrt{\frac{8M_g}{\pi RT_g}}} \qquad \text{Eq. 2-7}$$

Based on these assumptions, values of ~314 nm (1000 K) and ~1 µm (2600 K) are obtained. As most of the generated single FLG flakes and soot aggregates are in the range of 100–300 nm, the sampling is therefore considered to be representative for the aerosol particle size distribution.

An aspect which is neglected in the aforementioned considerations is that the thermophoretic force in the described and plotted model only applies to spherical particles. More advanced models which described thermophoresis on non-spherical particles exist (e.g., [160]) but are limited to theoretical descriptions. More details on aerosol behavior and dynamics can be found in the books of Seinfeld and Friedlander [157, 161].

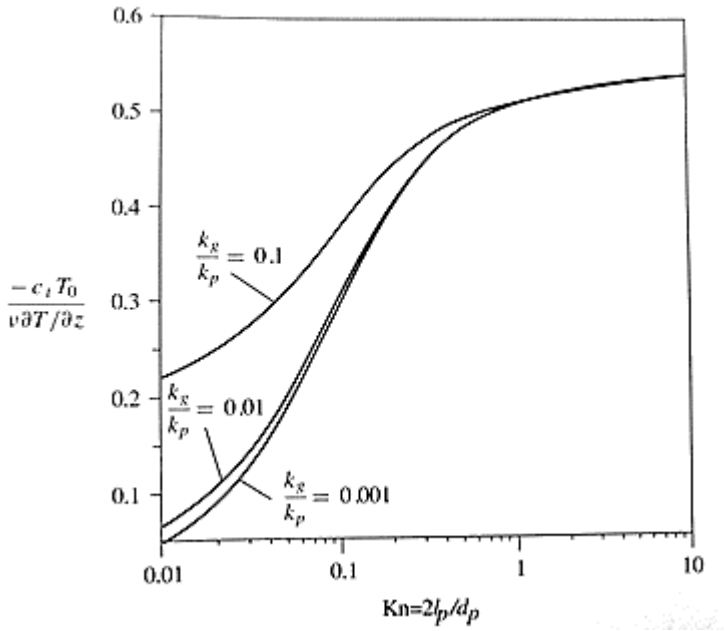

Figure 2-12: Dependence of the dimensionless thermal settling velocity on the Knudsen number and the thermal conductivity ratio k_g/k_p of the gas molecules compared to the considered particle ([161] p. 51). Reprinted with permission by Oxford Publishing Limited.

2.4.3 Gas chromatography

Chromatography is a separation technique used to segregate single components of a multi-component mixture. The working principle of chromatography is based on the interaction of the mobile phase – a gas or liquid sample – and the stationary phase that can be either liquid or solid. When the stationary phase is liquid, the process is called partition chromatography, while using a solid is classified as adsorption chromatography [162]. In Section 6, gas–solid chromatography coupled to mass spectrometry (GC/MS) is employed to measure the concentration of gaseous products which are generated in the plasma reactor during the carbon synthesis. Depending on the interaction (adsorption/desorption), the gas sample needs a specific amount of time to travel through a capillary filled with the adsorbent and reach a detector. The time required is called the retention time and is characteristic for the used measurement conditions. To identify the species which show a specific retention time, the process can be coupled to a mass spectrometer. In mass spectrometry, the species are ionized and then separated based on their mass-to-charge ratio by employing electric or magnetic fields. Depending on the employed ionization technique, characteristic fragment patterns of the parent species are generated and can be analyzed with the aid of databases [163].

The GC/MS measurements are performed in Section 6 with an Agilent 7890A/ Agilent 5975C combination to probe the gas species concentrations downstream of the plasma at a distance of ~0.8 m height above nozzle (HAN). A Plot-Q column is used to separate the test-gas species. Samples are taken during reactor operation by extracting gas samples into 3 l volume vacuum containers (<10^{-3} mbar l/s leak rate) through a vacuum lock. Prior to sampling, the containers are purged with nitrogen and evacuated multiple times. Then, the containers are filled with the gaseous sample up to ~800 mbar (absolute pressure). Afterwards, the containers are transported and measured at the GC/MS system.

2.5 Numerical simulations with Chemkin

The software Chemkin is employed to perform chemical equilibrium calculations and calculate molecular species concentration profiles in the reactor during the synthesis (for both Sections 5 and 6). It contains several modules specific for a problem or topic such as a 1D plug-flow reactor calculations. In all cases the modules are coupled to a chemistry set which contains the reactions of interest and needs to be defined prior to the calculations. The chemistry set consists of three different files which include information about the chemical kinetics, the fundamental thermodynamic data, and transport data for each species. In the following some details about the methodology for these calculations are given, while more information on Chemkin can be found in literature such as the book of Kee et al. [164].

To calculate the molecular species concentration profiles, simple 1D kinetics simulations are performed. The reactor geometry does allow for fast and simple computation of the desired species profiles, while more elaborate 2D/3D models require more precise boundary conditions, which are partly unknown. Three different widely accepted and validated combustion reaction mechanisms are combined for the calculations. As a base, the USC Mech Version II [165] mechanism with the addition of thermal ethanol decomposition taken from the CRECK modelling group (CRECK_2003_TPRF_HT_LT_ALC) [166] is employed. For including nitrogen chemistry, the respective reactions from the GRI-Mech 3 [167] mechanism are added. Reactions driven by plasma chemistry are not accounted for in the resulting reaction scheme. This assumption can be justified by the fact that the plasma is mostly confined to the resonator and no plasma torch reaching into the effluent is observed. Therefore, from distances of HAN > 0.12 m, there is not a significant fraction of charged species expected and the process is mainly thermal. The largest species considered in the mechanism are C6 and C7 species and the formation of solid carbon particles is neglected. The simplification to not include carbon growth can be justified by two aspects. First, there are no models available for gas-phase graphene growth and other models (CRECK) for soot do not predict particle formation for the employed assumptions and experimental conditions. Secondly, the yield of carbon particles is for relevant experiments below 10 wt.%, thus, the effect on the concentrations is considered negligible.

Simulations are performed with the 1D plug-flow module in Chemkin. The plug-flow reactor module requires the input of several parameters including a temperature profile, species concentrations and the overall flowrate of the reactant mixture, the reactor dimensions, pressure, inlet gas viscosity, and an estimation of the normalized internal and external surface area for the implementation of surface reactions and heat transfer. Surface reactions and heat transfer are ignored as the mechanism does not include them and the reactor walls are assumed to be isothermal. The reactor dimensions are simplified by assuming that the complete domain (up to 0.5 m) only consists of the quartz tube with an inner diameter of 70 mm. The reactor is longer, but already at a distance of ~0.3 m and a temperature of <1000 K, stable species concentrations are predicted. The pressure is assumed to be 1000 mbar as this is the reactor pressure during synthesis and for the inlet gas viscosity the value for Ar at the assumed temperature is chosen. A temperature profile is generated during this thesis based on the temperature extracted from the OES and IR-absorption measurements. It is further refined by thermocouple and pyrometry measurements [168]. As a result, the temperature is assumed to drop from 3700 K at 0.09 m HAN to 600 K at 0.35 m HAN. The overall reactant flowrates and species concentrations are put into the model as supplied into the reactor.

Chemical equilibrium calculations are performed employing the same combustion mechanism with the chemical and phase equilibrium calculations module. Calculations are performed for 1 bar input pressure and specific gas compositions. A step size of 10 K in the range of 300–8000 K for constant temperature and volume is chosen. The reliability of the chemical equilibrium calculations is limited to typical combustion temperatures, because the utilized combustion mechanisms only contain a small number of species and some of the species' properties are estimated.

3 Experimental setups

For the work in this thesis, two similar microwave plasma reactors are employed to synthesize carbon particles when being fed with hydrocarbon reactants. Previous work has shown that such reactors are well suited for generating carbon particles as they also allow control on the type of allotrope formed. Depending on the specific experiments and the *in situ* or inline methods applied, one or the other reactor is operated. Both reactors share the same characteristics in the plasma generation and reaction zone, while the geometry of the reactor housing in which the post-plasma gas is released to differs in diameter, length, and ports (windows and flanges). In the following the working principle and design of the plasma reactor for the carbon particle synthesis is explained. Afterwards, Sections 3.1–3.3 describe the different configurations for the employed *in situ* methods and the equipment used.

To ignite and maintain the plasma, microwave radiation with a frequency of 2.45 GHz is transported via waveguides (WR340) to a resonant cavity in which the plasma is formed. The resonant cavity used is for both reactors a CYRANNUS® (CYlindrical Resonator with ANNular Slots) from iplas GmbH. It consists of an outer ring resonator which focuses microwave radiation homogeneously through multiple annular slots into an inner cylindrical resonator. The inner cylindrical resonator thereby acts as a TM_{012} cavity enhancing the electrical fields in three different regions: the center and two rings in the upper and lower resonator (see e.g., simulations in the work of Münzer [35] p. 22). TM thereby means transversal-magnetic i.e., the magnetic fields are perpendicular to the wave propagation direction. In the normal use case, a quartz tube of 70 mm inner diameter is placed in the cylindrical inner resonator which is transmissive for the microwave radiation and wavelengths in the UV-VIS region, while it seals the reactor against the outer atmosphere with two O-rings. Hence, the quartz tube acts as a reaction tube for the complete vacuum vessel. For igniting the plasma, the reactor is pumped down to vacuum at approx. 10–20 mbar absolute pressure and microwave radiation is supplied. Because of the installed quartz tube, the regions which can potentially show increased electric field strength which are not in the middle of the resonator, are open to ambient air, so the plasma ignition is hindered as the required breakdown voltage is larger than in the middle. Instead, after supplying enough microwave power to ionize molecular and atomic species, a plasma is only formed and maintained in the middle of the cylindrical cavity. Figure 3-1 depicts a sketch of the microwave coupling, the resulting electrical field distribution, and a picture taken of an Ar/H_2 plasma at atmospheric pressure from above. The resonator has the advantage that it generates a homogeneous plasma in its center which can be operated in a wide pressure range from vacuum to – at least as reported – 1.5 bar and can be adapted for different processes such as chemical vapor deposition, gas-phase synthesis of nanoparticles, or gas reforming [169-172].

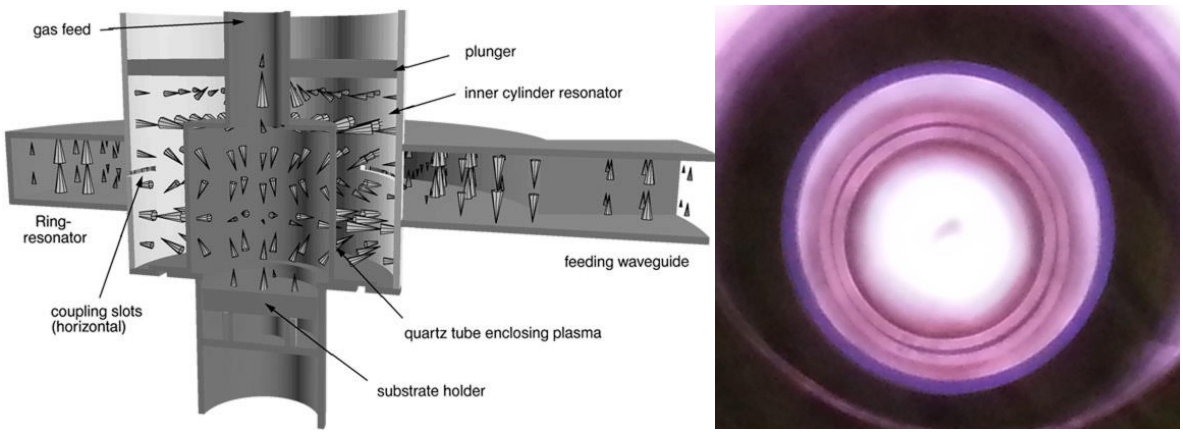

Figure 3-1: The microwave coupling into the CYRANNUS® resonator and the resulting electrical field distribution is shown on the left [173] (reprinted with permission by IOP publishing Ltd). On the right a picture taken of the plasma containing Ar and H_2 from above at atmospheric pressure is shown.

The two reactors are supplied by magnetrons that can deliver up to 2 kW of microwave power. To optimize the energy input into the plasma, two more components are added along the waveguide transmission lines. The microwave transmission from the magnetron to the CYRANNUS® device can be described by an equivalent electronic circuit model. Thus, the concept of impedance matching can be employed to maximize the transferred power into the circuits load, the plasma. Three-stub or EH-tuners are used to optimize and deploy most of the energy into the plasma by influencing the coupling to the slots of the ring resonator. Microwave radiation which does not travel through the slots into the inner cylindrical resonator is reflected back in the direction of the magnetron. For measuring the reflected microwave power, i.e., the power that is not deposited in the plasma, circulators are installed. The circulators prevent back reflection of microwave radiation into the magnetron, which might otherwise cause damage. Instead, the radiation is guided towards a water load that absorbs it. The circulator also contains a diode which generates a voltage signal proportional to the reflected microwave power. Monitoring the diode voltage signal then allows to optimize the energy input into the plasma when altering the three-stub or EH-tuner positions. The components for generation and transfer of the microwave radiation are shown exemplarily for Reactor B in Figure 3-2 and summarized for both reactors in Table 3-1. The components vary for both reactors but should not affect the plasma properties when similar conditions are used. Circulator, magnetron, and most parts in the vicinity of the plasma are air or water cooled.

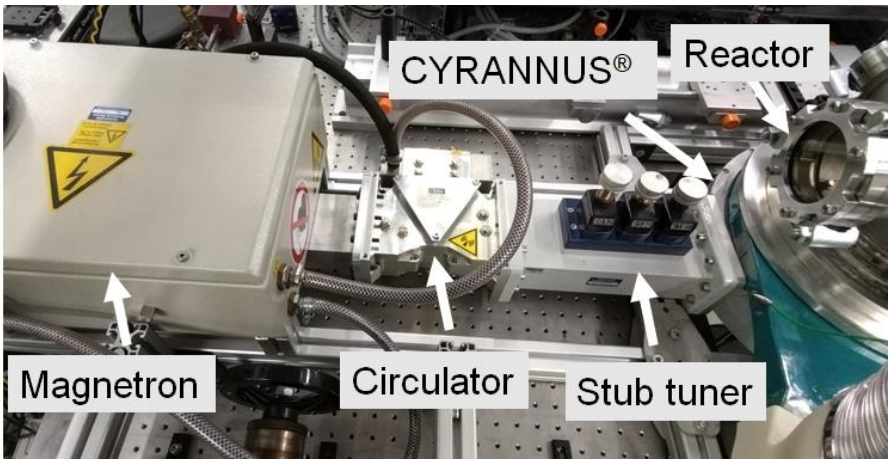

Figure 3-2: Components used to generate and transfer microwave radiation into the resonator to ignite and sustain the plasma.

Table 3-1: Components of both the employed microwave plasma reactors used to generate and transmit the microwave radiation into the respective iplas resonators.

Setup	Magnetron head	Circulator	Impedance matching
Reactor A	Muegge MH2000S-213BA	Muegge MW1003A-210EC	iplas EH Tuner: T202-0310/003
Reactor B	Fricke&Mallah: FMG 1×2.0 kW, 2.45 GHz	Fricke&Mallah: 2722 162 12431	Muegge 3-stub tuner: MW201A-260EF

The working gases are introduced through a set of two nozzles. A central nozzle introduces the reactants (hydrocarbons and eventually oxygen carriers) diluted in argon, while a second nozzle generates a tangential sheath-gas stream [170, 174]. The sheath-gas volume flow is set to 30 slm of Ar (5.0) and 1 slm of H_2 (5.0) if not mentioned otherwise, while the gas flow through the central nozzle is varied as described in each chapter. Both nozzles are visualized in the cross-sectional drawing in Figure 3-3.

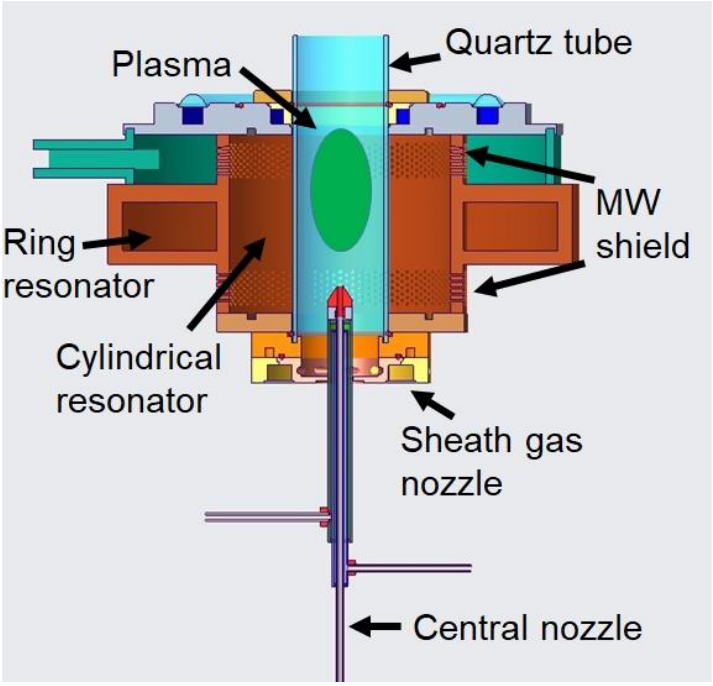

Figure 3-3: Cross-sectional drawing of the plasma reactor. The image shows the two different gas inlets and the region of plasma generation.

The reactant gas mixture supplied through the central gas nozzle can be generated by a combination of evaporating a single liquid reactant source or by mixing different reactant gases. Both options are schematically shown in Figure 3-4.

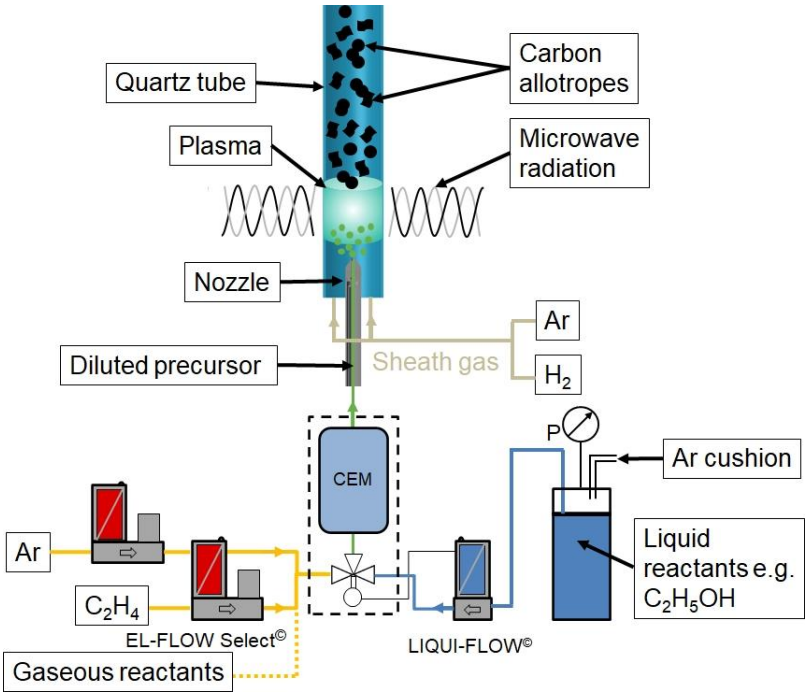

Figure 3-4: Schematics of the different options for the reactant supply to the reactor. For the supplied gaseous reactants, C_2H_4 is shown as example, for an evaporated reactant, ethanol is shown.

For the liquid reactant, a stainless-steel vessel is filled with the respective liquid. An argon gas cushion is applied on the vessel that pushes the liquid out and transports it through a Liqui-

Flow™ (L1-FAC-22-0, Bronkhorst®) to the mixing valve of a controlled evaporation and mixing system (CEM, W-209-333-P, Bronkhorst®). The valve actuation is controlled by the flow that is measured in the Liqui-Flow™. The liquid is then dispersed together with the added gases and evaporated in a heated chamber (180 °C). For the supply of different gaseous reactants, mass-flow controllers (MFCs, Bronkhorst®) are employed. The gases are premixed and then sent either directly into the central nozzle or through the CEM. Because the gaseous reactants are usually a mixture containing a large volume flow of Ar (~5 slm) and a small volume flow of hydrocarbon and eventually, an oxygen carrier (~0.285 slm in total), homogenization is required. Otherwise, pulsating flows are observed. When sending the gas mixture through the CEM, homogenization is automatically achieved.

The gaseous components are heated and decomposed in the hot plasma. Solid carbon particles and gaseous byproducts then form during cooling in the downstream region. To harvest carbon particles, an industry-grade fiber-fabric filter is installed at the reactor exit. Because carbon particles are deposited on the filter, a pressure drop is caused by the filter that increases with reaction time. Therefore, without further control, the reactor pressure continuously increases due to the fixed gas flows. In order to prevent such a pressure increase, prior to the synthesis of particles, a secondary N_2 gas flow as fed into the reactor between the filter and a bellow-sealed angle valve that leads to the vacuum pump and acts as an additional gas ballast. The MFC of this secondary nitrogen flow is controlled by an PID controller connected to the measure pressure, i.e., the flowrate is automatically reduced when a pressure increase due to filter clocking/particle deposition is detected. For most experiments a pressure of 1000 mbar abs. is used. Only the experiments described in Section 4 are performed at 700 mbar.

As mentioned in the second paragraph, the plasma in the reactor system as described here is only ignited at reduced pressure. A procedure to initiate the experiments is repeated every time. Each experiment starts by evacuating the reactor to ~20 mbar, followed by plasma ignition in a pure argon flow with a magnetron output power of 600 W with the sheath gas running. Hydrogen is then added to the system and the pressure and microwave power are stepwise increased and stabilized at 1000 mbar and 1400 W, respectively. Once stable plasma operation is established at 1000 mbar, various reactants are introduced depending on the exact experimental conditions.

3.1 Experimental setup for infrared absorption measurements

Infrared absorption measurements are performed to measure and monitor the formation of pyrolysis product gases generated in the plasma reactor during the synthesis of solid carbon particles and to estimate gas-phase temperatures in the plasma effluent. To perform *in situ* line-of-sight infrared absorption measurements, flushed cells are constructed to guide an IR beam through a straight tube located in the reactor off-gas. The cells are equipped with KBr windows (diameter: 25 mm, thickness: 5 mm, Korth Kristalle GmbH) and mounted before the particle collection filter. To achieve a high sensitivity when monitoring the formation of pyrolysis products, the length of the absorption path was selected as ~0.6 m. Figure 3-5 shows the schematics and a photo of this arrangement.

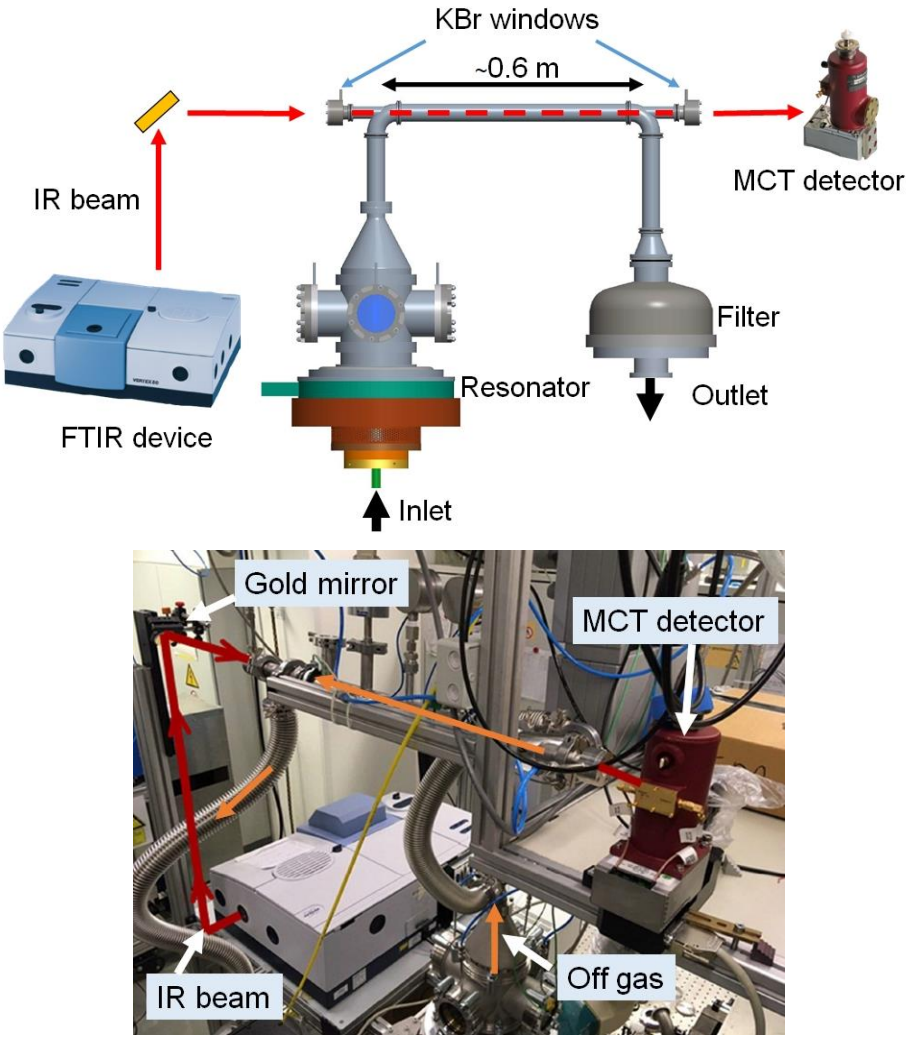

Figure 3-5: Schematics [175] and photo of the arrangement for IR absorption measurements in the reactor off-gas.

The IR beam is coupled out of a Brucker Vertex 80 FTIR spectrometer through the side window. Then the beam is deflected and guided by gold-coated mirrors to the optical cells and through the straight tube in the effluent. After exiting, the beam is directed onto an external liquid-nitrogen cooled mercury cadmium telluride (MCT) detector belonging to the FTIR spectrometer. To decrease the influence of varying CO_2 and H_2O concentrations in the lab air on the measurements, part of the IR-beam path is housed (not shown) and continuously flushed with dry N_2.

As for the measurement procedure, several different spectra are recorded. The resolution of the spectra is varied depending on the exact purpose of the measurements. Measurements of the rotational fine structure of, e.g., CO for temperature measurements are carried out with a spectral resolution of 0.1 cm^{-1}. For the other measurements and if not mentioned otherwise, the resolution is set to 0.5 cm^{-1}. Usually, transmission spectra of the (N_2-flushed) laboratory air and the pristine/undoped (Ar + H_2) plasma are used as reference. Then, the reactants are added and the absorption was measured. The absorbance or transmittance is afterwards calculated via post processing of the transmission spectra. Examples for transmission spectra for ethanol as reactant with and without plasma (with and without ethanol decomposition) are shown in the appendix in Section 9.2.

3.2 Experimental setup for optical emission spectrometry

OES is performed to measure excited intermediate species in or near the plasma and to extract estimated values for the gas temperature in the reaction zone. To perform OES measurements, a spectrometer system was assembled consisting of the components displayed in Figure 3-6. The light originating from an arbitrary source (e.g., the plasma) connected by a fiber to a SMA fiber connector is guided into the spectrometer system by two planoconvex silica lenses (f_1 = 50 mm, f_2 = 150 mm, diameter: 2.54 cm) that focus the light onto the entrance slit of a SPEX 1704 Czerny-Turner monochromator (1 m pathlength). Inside the monochromator, the light is reflected onto a blazed grating with 1200 lines/mm and a blaze wavelength of 400 nm. The diffracted light then travels through the outlet slit and is collected by a Hamamatsu R995 photomultiplier tube (PMT, 160–900 nm spectral response). The PMT signal is transformed by an A/D-converter (National instruments USB 6001) and read out by a LabVIEW program. Because the monochromator control is analog, only the time-resolved voltage signal is measured. Thus, time needs to be converted to wavelength in post-processing of the recorded data, which can introduce some errors. The spectrometer is scanned by rotating the grating resulting in a wavelength tuning of e.g., ~0.05 nm/s (40 nm in 800 s) and constant rotation rates are assumed.

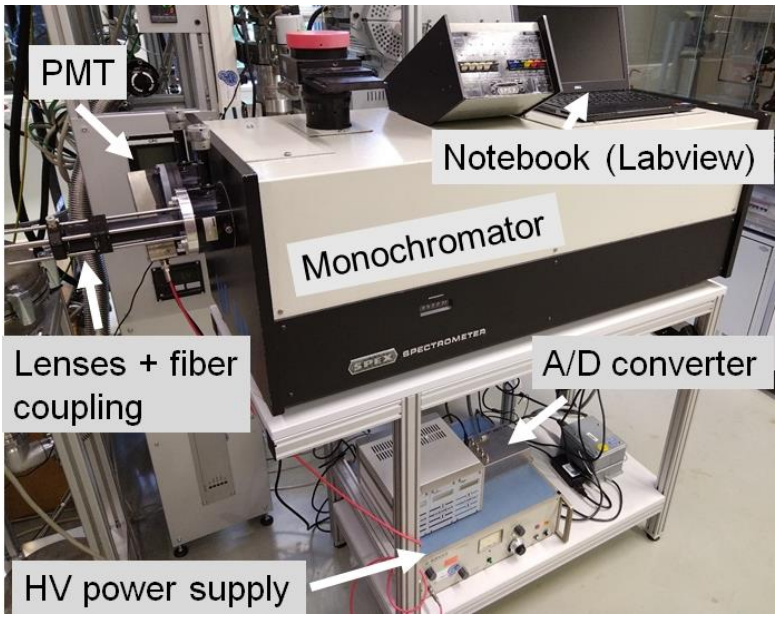

Figure 3-6: Spectrometer system for optical emission measurements indicating the major components.

The light originating from the plasma reactor is collected by an open ended SMA connector from a multimode optical fiber with 0.6 mm diameter in the region where part of the microwave shield in the downstream region is installed. The installation is sketched in Figure 3-7. The spectrometer system including the fiber is calibrated with light from a Hg/Ar lamp (LOT QuantumDesign). The spectral resolution of the OES system is measured to be about 0.03 nm (full-width-half-maximum; FWHM) when a slit width of 40 µm is used. The instrument function of the spectrometer system (i.e., the wavelength-dependent detection efficiency) is measured and corrected by using a calibrated spectrum of a laser-driven light source (Energetiq LDLS EQ-99X) as reference. The comparison between the measured and know spectrum together with the instrument function correction is shown in the Appendix, Figure 9-6.

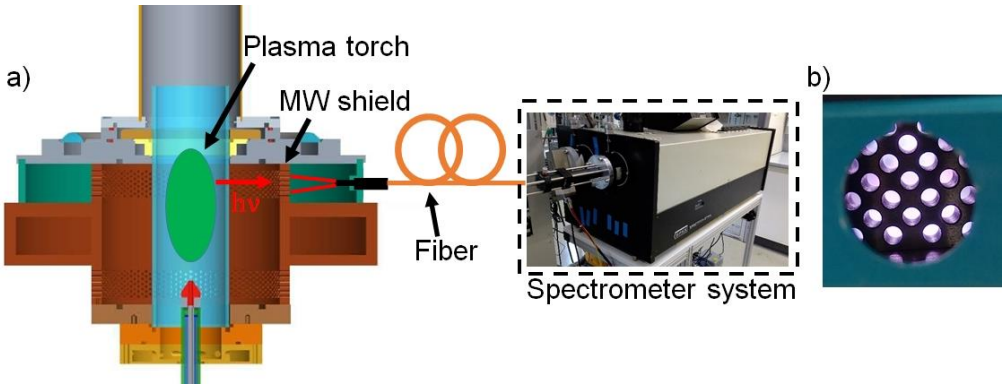

Figure 3-7: Sketch depicting how the optical fiber is installed to capture the emitted light of the plasma in a), and b), view of the plasma from the side from which the fiber collects the radiated emission.

For the measurements, the Hα Balmer line is selected to properly align the fiber with the plasma reactor microwave shield by adjusting it for the maximum intensity. Taking on a first assumption geometrical considerations into account (numerical aperture: 0.22, fiber core diameter: 0.6 mm, distance of ~5 cm to the hole), this reflects a field of view of the fiber, which represents approximately one hole in the microwave shield.

3.3 Equipment for thermophoretic sampling

The general reactor assembly used for thermophoretic sampling is shown in Figure 3-8. It consists of (i), the microwave reactor to synthesize the carbon nanomaterials, (ii), the thermophoretic sampling system, and (iii), the fiber filter which is always installed to harvest the synthesized materials in the effluent. The piston driving the thermophoretic sampling system is separated from the main reactor by a ball valve and a purging system. The purging system is adjustable in height by 10 cm and enables – in combination with the ball valve – to safely repeat the sampling multiple times without the need to stop the synthesis process. Additionally, it also ensures that the reactor is not exposed to air. To collect the samples, a pneumatic cylinder operated with inert gas (either Ar or N_2) is actuated. At the front on the thread of the cylinder, the actual spring-loaded sampling unit is installed (Figure 3-9).

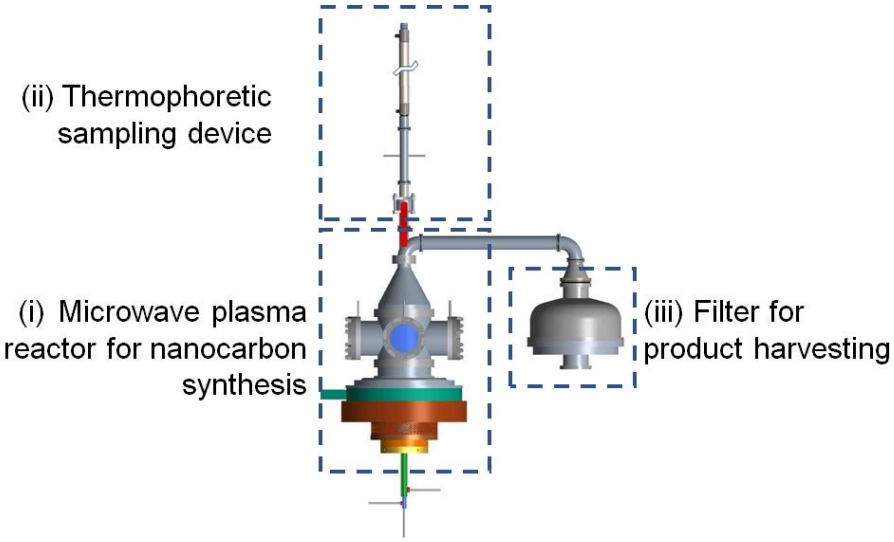

Figure 3-8: Sketch depicting the reactor assembly used for experiments in which thermophoretic sampling of material along the reactor axis is performed [168].

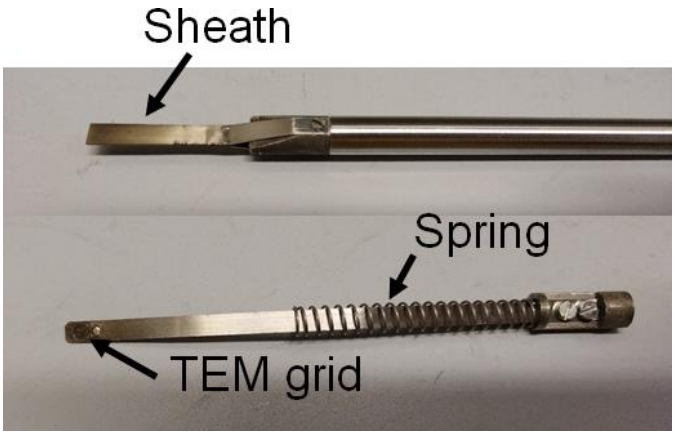

Figure 3-9: Spring-loaded sampling unit for thermophoretic sampling installed on the thread at the front of the piston.

The sampling unit was developed by Frederik Kunze (IUTA) and has been utilized in the past for similar tasks [174, 176]. It consists of a tube with a slit-shaped sheath at the front (left). The sheath shields the inner parts and prevents undesired premature particle collection. The inner part consists of two metal plates which are welded together. At the front of the metal plates is a small hole which fits a TEM grid. The grid is pushed into the hole from the side through both metal plates. To prevent the movement of the TEM grid along the metal plates, a welding spot is placed next to it a as physical barrier as it connects both plates. After the rod at the end of the pneumatic piston is accelerated, it will hit the inner end of the pneumatic piston. When hitting the end, the inertia of the rod will drive out the sampling unit out of the sheath and material will be collected. To alter the acceleration of the TEM grid part, multiple weights can be added into the hollow tube. A spring is installed to pull the metal plates back into the sheath and the hollow tube. By varying gas pressure (piston acceleration), used weights, and spring constant, the TEM grid exposure time can be changed between 5–30 ms [177].

To verify the time which the TEM grids are exposed during the pneumatic actuation cycle, high-speed camera measurements are performed. Based on these measurements, thermophoretic sampling was set to expose the TEM grid for approximately 10–15 ms to the aerosol. Depending on the aerosol concentration, the actuation has to be performed multiple times (~20) to sample sufficient amounts of material. To enable thermophoretic sampling at different axial HAN sampling positions, the geometry of the purge system and/or the length of the pneumatically operated piston are optionally varied.

4 Structure evolution of graphene flakes during synthesis

4.1 Introduction

A recurring question when analyzing FLG flakes generated in the plasma reactors is how their shape and morphology is formed as the flakes typically show strongly folded or crumpled structures. Based on the considerations of carbon growth (Section 2.2), it would be expected that the first carbon nuclei are just PAH molecules that later grow into larger two-dimensional flat sheets. Hence, any kind of induced curvature after the first inception of solid carbon should result in further bending and out-of-plane attachment of other growing carbon nuclei, ultimately forming three-dimensional structures. On the other hand, nucleation of PAH molecules and processes that lead to morphological changes are considered crucial for the creation of soot-like particles; in this case, the growing PAHs start to randomly agglomerate and attach to each other. So, the transformation from a potential monolayer flat sheet to crumpled stacked layers as they are obtained from the downstream installed filter is unclear. It is generally accepted that large monolayer graphene flakes can become unstable and form wrinkles, ripples, and other kinds of mechanical deformations [178-180]. However, it is yet to be studied how the formation of mechanical deformations influences the structure of the obtained flakes in similar gas-phase processes i.e., whether folding and crumpling are pivotal for the resulting (multi-layered) structure.

To investigate the morphology evolution of carbon particles (mainly FLG), thermophoretic sampling along the centerline of reactor B (Table 3-1) together with Claudia López-Cámara was performed. To further support the results and to probe the structural evolution, spatially resolved optical diagnostic measurements by time-resolved laser induced incandescence (TiRe-LII) were performed by Muhammad Asif and Stanislav Musikhin. TiRe-LII is a commonly employed laser-based *in situ* diagnostic technique to characterize different aerosol particles about, e.g., their particle size and is especially common for carbon particles [181]. Unlike the experiments which are presented in Sections 5 and 6, the experiments with the thermophoretic sampling along the reactor axis are performed at 700 mbar since these conditions lead to a more stable particle torch, which is more favorable for the TiRe-LII measurements. For the same reason, the overall experimental conditions (Table 4-1) are slightly different than the parameters described in Section 3.

Table 4-1: Experimental parameters used on the study of the FLG morphology evolution.

Precursor	Ethanol
H_2 / slm	0.88
Swirl Ar / slm	39.42
Nozzle Ar / slm	4.95
Flush N_2 / slm	16.47
Reactor pressure / mbar	700
Precursor / slm	0.16
Microwave plasma power / W	1600

Figure 4-1 displays an image of the particle torch and the positions probed with the employed methods (both thermophoretic TEM sampling and TiRe-LII). The visible particle torch is a result of black body radiation from the generated hot carbon particles, as without reactant addition no particle torch is observable. Samples are taken at several spatial positions between HAN = 24.4 and 12.4 cm. Because of geometrical limitations, the lowest measurement point for the TiRe-LII measurements is at HAN = 17 cm. The points at which the different measurements are performed are marked with a color-coded cross, indicating whether both methods (purple) or only TiRe-LII measurements or thermophoretic sampling (red or blue, respectively) are employed.

In the following, two aspects are the main points of interest. At first, the structure of the earliest nuclei or clusters is investigated. The goal is to proof or refute the presence of monolayer graphene sheets that are expected to form initially from PAH molecules. Afterwards, the growth and structural evolution of these nuclei along the reactor centerline is analyzed and discussed.

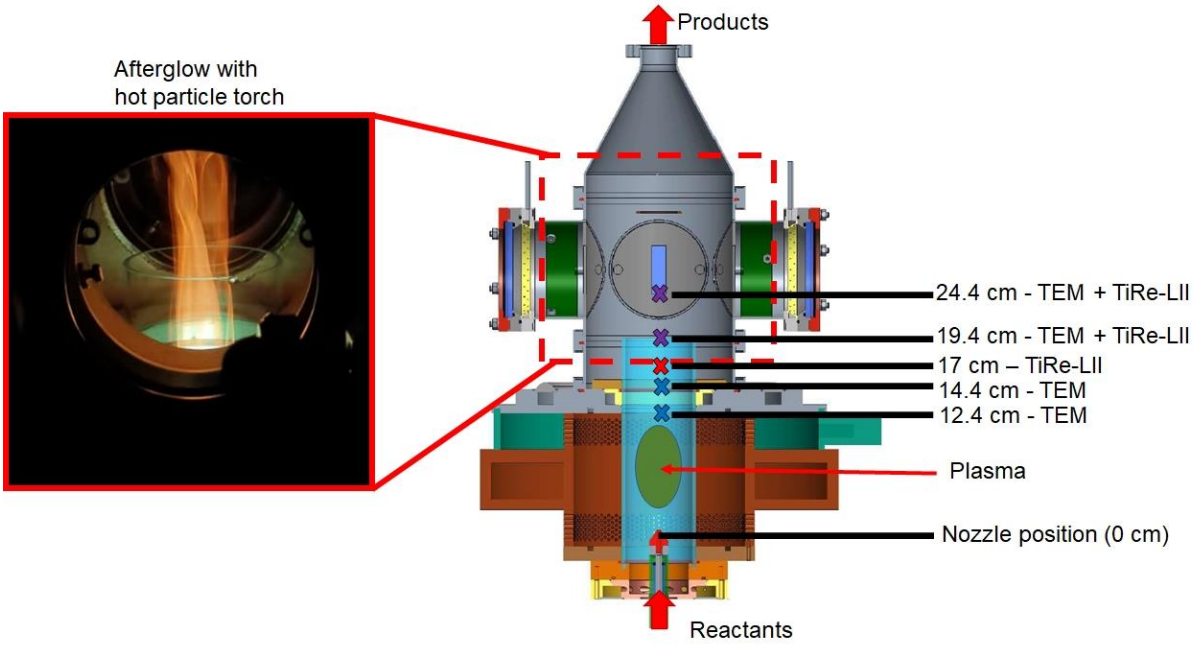

Figure 4-1: Sketch depicting the spatial positions probed for studying the morphology evolution of the generated FLG materials and a photographic image of the generated particle torch.

4.2 Structural properties of the first formed FLG materials

Figure 4-2 displays TEM images of FLG obtained at different spatial positions showcasing the structural transformation of FLG flakes in the reactor. Figure 4-2a displays FLG sampled at HAN = 12.4 cm in a qualitative comparison to Figure 4-2b which shows FLG harvested from the filter installed downstream (Figure 3-8 for details).

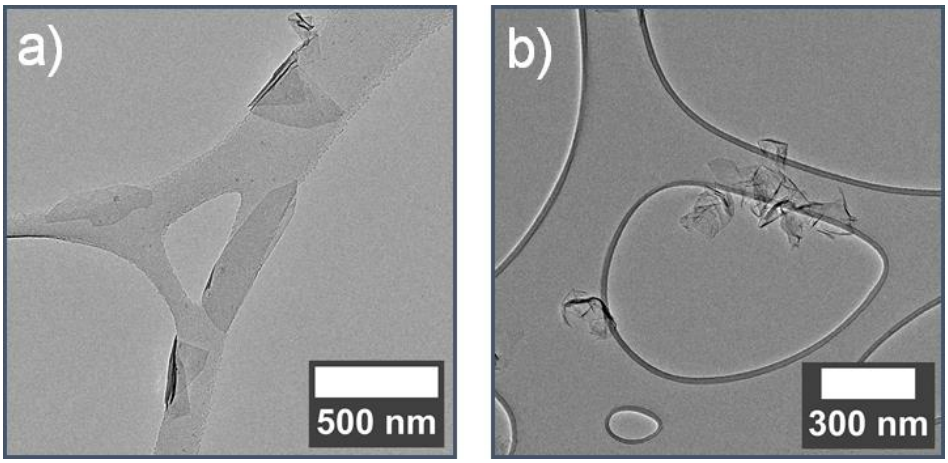

Figure 4-2: TEM images obtained from materials a) collected via thermophoretic sampling at HAN = 12.4 cm and b) at the downstream fiber filter.

When looking at the FLG material obtained at the filter, it is evident that it contains folded and partly agglomerated flakes. On the contrary, the materials sampled at HAN = 12.4 cm show mostly flat and weak crumpled/folded flakes. In many cases, the observed flakes are larger than 100 nm in one lateral dimension, and either round or showing shapes produced by folding or rolling round sheets. The presence of flakes at HAN = 12.4 cm indicates that the formation of solid carbon materials starts at a lower HAN, in regions which are only accessible by OES in the current experimental setup. Furthermore, the flatness of the flakes suggests that the morphology of the first grown/born FLG sheets is indeed close to ideal two-dimensionally growing PAH molecules, as discussed in Section 2.2. Many of the observed flakes show structures which can be generated by a low number of folds indicating that self-folding is important for the formation of the typically observed multi-layered structure. Nonetheless, the observations are qualitative and the FLG flakes show varying degrees of folding and crumpling. Most are large in size and weakly folded or crumpled but show in some cases also <100 nm round flakes and strongly crumpled flakes.

To further confirm the expectation that the first formed carbon flakes are related to large PAHs, the number of stacked layers needs to be determined. That is because perfect graphene monolayers are likely to be formed by growing PAH molecules. Figure 4-3a shows an example of a large collected round carbon flake. As seen, the deposited flake is mostly supported by the underlying carbon film and it shows some folding at the freestanding section (region indicated by the blue circle). Focusing on the fold in the unsupported region, Figure 4-3b confirms the low number of stacked layers as no stacked layers can be observed at the edge of the flake. Using the Fast-Fourier-Transform on Figure 4-3b, it generates Figure 4-3c, showing twelve separate points for a lattice spacing of 0.21 nm (1 0 0). Six points would be expected for a perfect monolayer, i.e., twelve points indicate the presence of a graphene bilayer in the folded region of Figure 4-3b [182, 183]. This indirectly confirms that the unfolded pristine flake consists of a graphene monolayer and links it to the theory of solid carbon growth via growing (two-dimensional) PAH clusters.

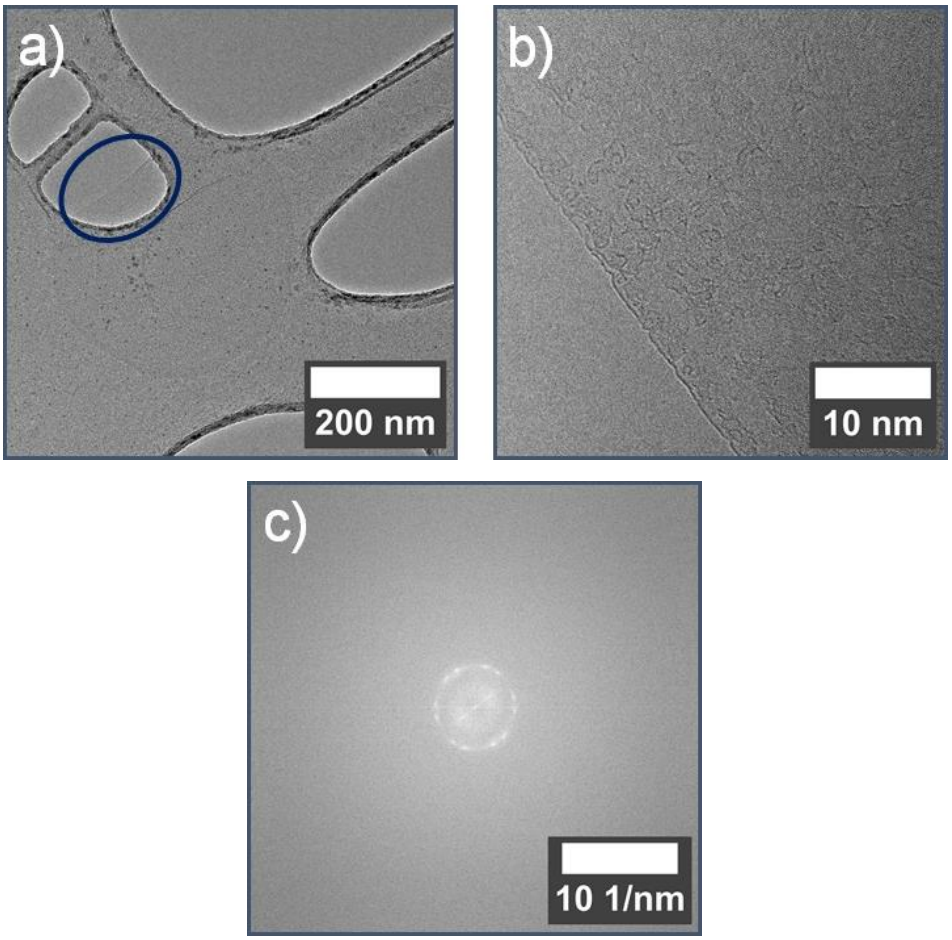

Figure 4-3: Images characterizing a sampled FLG flake [184]. a) overview of the flake showcasing wrinkles and a single fold (blue circle) in the unsupported area; b) rotated zoomed-in of the folded region. c) Fast-Fourier Transformation (FFT) image generated from (b).

Figure 4-4 shows an example containing both more- and less-crumpled flakes in close vicinity to each other. Carbon flakes sampled on TEM grids with a continuous carbon film instead of lacey or holey carbon films also shows similar structures (both weakly folded and on occasions more strongly crumpled). Thus, the type of grid is not expected to influence the degree of crumpling or folding leading to measurement artifacts. The observed weakly folded flake indicates that the structure formation should continue further downstream. One indication may come from the typically observed BET SSAs from filter obtained materials in this work which are in the range of 300–400 m^2/g, i.e., much lower than what would be expected for a bilayer flake (~1337 m^2/g). The estimated temperature at the sample position should be sufficiently high (~2600 K) with abundant concentration of reactants (such as C_2H_2) for further growth to take place. Following the conceptual model in which FLG only consists of a perfect PAH mono--layer and adsorption on its surface is not considered to contribute to growth, only the flake edges are reactive sites that allow further growth. Hence this can occur even when flakes are highly crumpled and/or stacked. At the same time further folding and crumpling can also occur. The FLG structure evolution along the reactor axis will be revisited in Section 4.3.

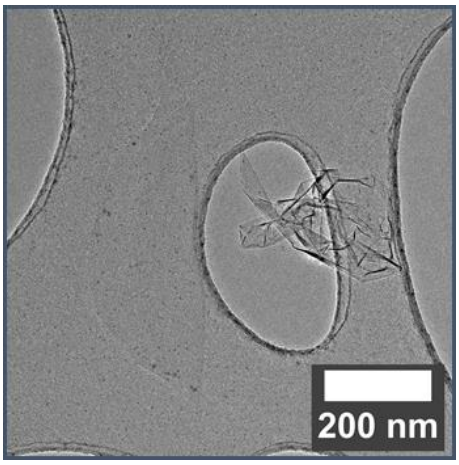

Figure 4-4: TEM image from particles sampled via thermophoresis from the hot plasma off-gas showcasing the difference in carbon flake structures (HAN = 12.4 cm).

The TEM observation provides experimental proof that prior to crumpling and agglomerating, a certain fraction of the graphene flakes can be considered to be flat monolayer graphene. The TEM observations also show that folding of these sheets is an important process in the overall structure formation. Because this is only based on qualitative information, it is unclear how representative the observation of monolayer graphene is for all sampled carbon materials and what fraction of the produced carbon material tends to agglomerate or crumple earlier in the growth process. Yet, the transformation of PAH molecules towards monolayer graphene is evident.

4.3 Structural evolution of FLG along the reactor

Following the discussion of FLG flakes formed in the early stages of the reactors, the transformation of these towards the morphologies observed from the filter collected materials is nebulous. One possible criterion to characterize the different observed carbon particle morphologies is their dimension or size, as folding of single flakes or the agglomeration of multiple sheets may lead to more compact structures. Thus, the structure evolution is examined by determining the particle size distributions for the carbon flakes observed from TEM images and TiRe-LII measurements.

For the TEM images analysis, the maximum Feret diameter of single flakes was determined. The Feret diameter, also called caliper diameter, represents the dimension of an arbitrarily-shaped particle between two parallel planes as could be measured with a caliper. The maximum Feret diameter, is the largest diameter that can be measured this way for a given particle. To perform such analysis on the sampled carbon flakes, ellipsoids are drawn around the sheets in the TEM images to determine their major axis diameter. After obtaining the corresponding Feret diameter, size distributions are constructed to compare the carbon particles sampled at different HAN positions. A comparison between the different spatial positions for thermophoretic sampling shows that the collected FLG sheets become smaller along the reactor axis in downstream direction. Figure 4-5 shows the measured distributions of Feret diameters including a fit with a lognormal distribution and the cumulative fraction.

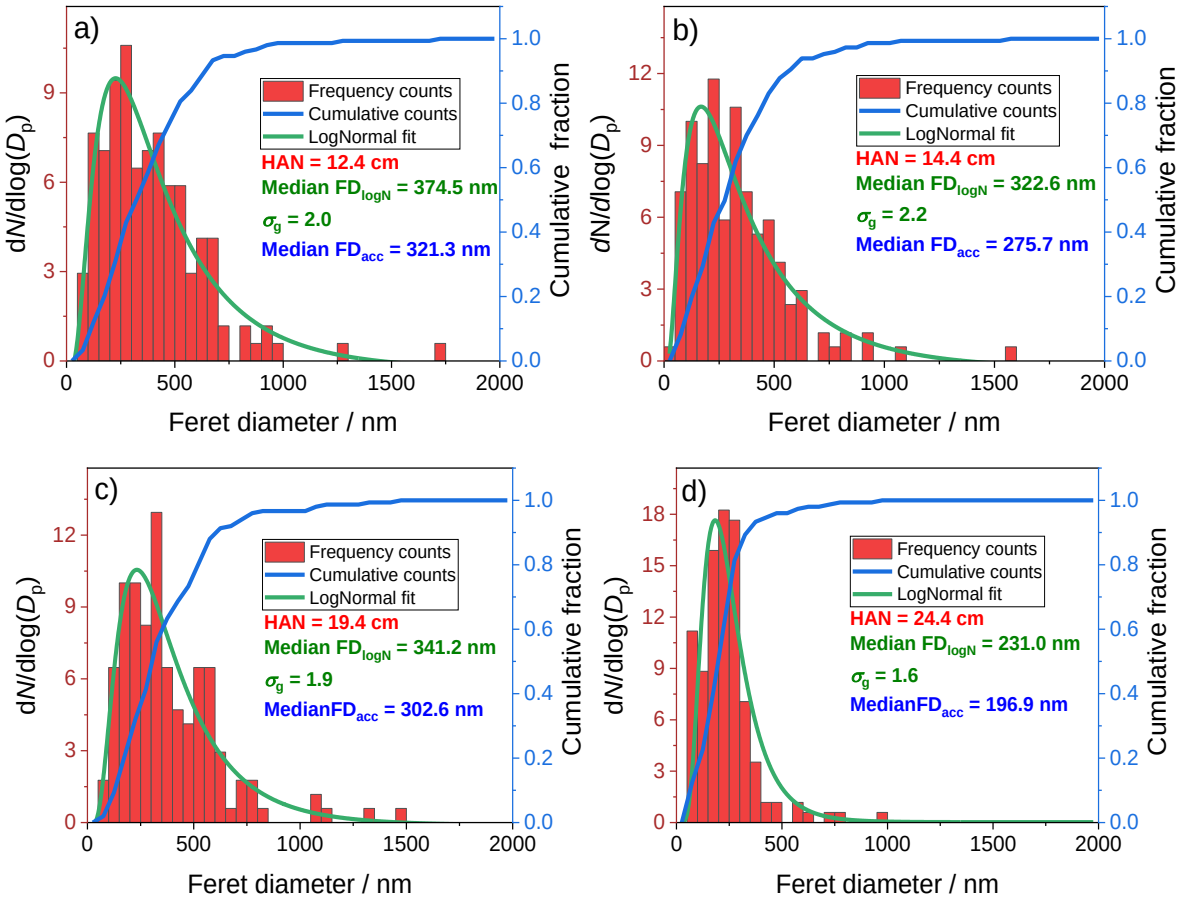

Figure 4-5: Feret diameter distributions from thermophoretically sampled carbon particles at different HAN a)–d) [168]. For each distribution 150 flakes are counted.

As shown, the sheets have a wide distribution of Feret diameters, ranging from 50 to > 1000 nm at HAN = 12.4 cm. When describing the distribution with a lognormal function, the count median diameter (CMD) is 375 nm. The distribution is wide, with a geometric standard deviation $\sigma_g \approx 2$. Comparing these values to the ones obtained for carbon flakes harvested further downstream, it is revealed that both the CMD and the geometric standard deviation decrease (as for HAN = 24.4 cm, the CMD is 231 nm with $\sigma_g \approx 1.6$). Although the median Feret diameter obtained by the cumulative plot slightly deviates from the CMD which is extracted by the lognormal fit, it shows a similar general trend. Thus, based on the TEM image analysis, the average sheet dimension becomes smaller as the FLG flake moves further from the plasma zone, which is a qualitative indicator for having more crumpled and compact structures further from the plasma region despite the potential for further growth of the carbon flakes between HAN = 12.4 cm and HAN = 24.4 cm. A qualitative comparison for the increasingly crumpled nature of the FLG particles is shown in Figure 4-6.

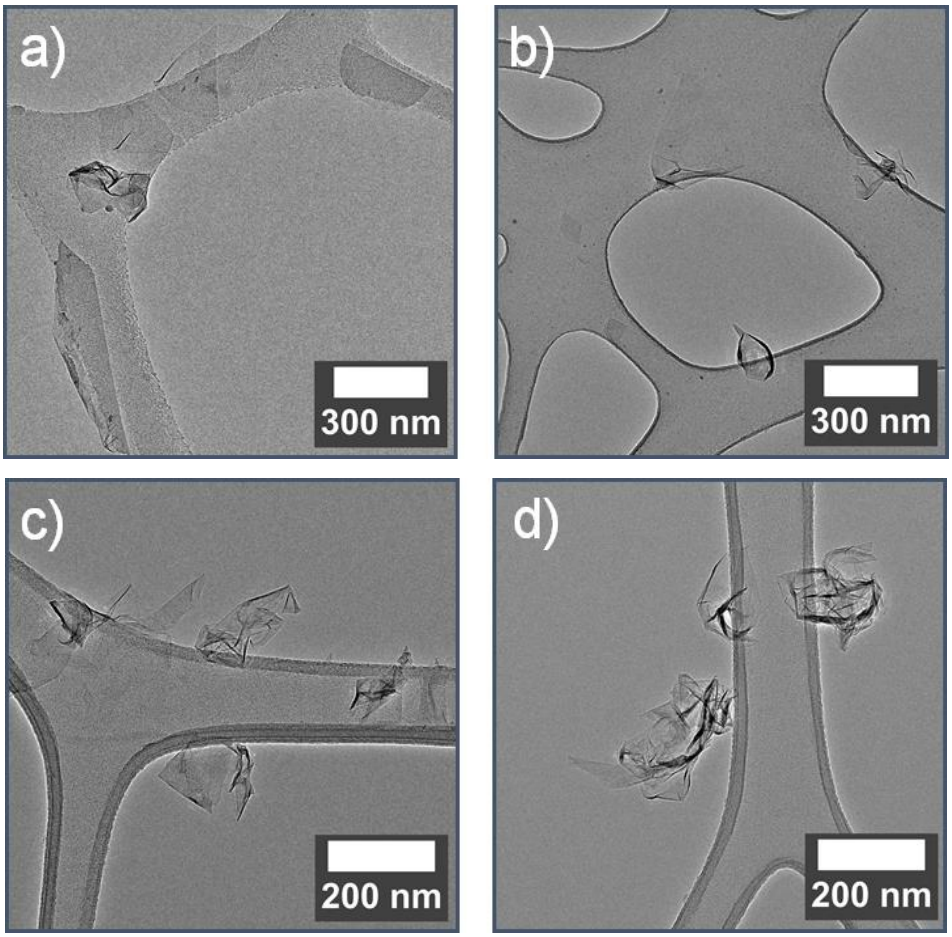

Figure 4-6: Qualitative comparison of exemplary TEM images of samples collected at different HAN distances. a) = 12.4 cm, b) = 14.4 cm, c) = 19.4 cm, and d) = 24.4 cm.

The observation that FLG particles become more compact while passing the reactor is compared to spatially resolved TiRe-LII measurements and displayed in Figure 4-7. The measurements are performed and analyzed by Muhammad Asif, Stanislav Musikhin. In general, TiRe-LII uses a laser beam to thermally excite aerosol particles in the gas-phase and subsequently detects the emitted light (blackbody radiation) of the hot aerosol particles. After an initial phase in which high peak temperatures might lead to the evaporation of parts of the solid or liquid particles, the energy balance and heat loss of the particles is mostly determined by the conductive heat transfer with the surrounding gas. This heat transfer is determined and limited by the 'active' surface area accessible. Therefore, in the context of crumpling and folding carbon sheets, the accessible surface directly relates to the crumpledness/wrinkledness of the flakes. This method has been applied to the produced carbon aerosols at three different HAN positions, as defined in Figure 4-1. Details on the measurement procedure and the employed models can be found in the joint publication [168].

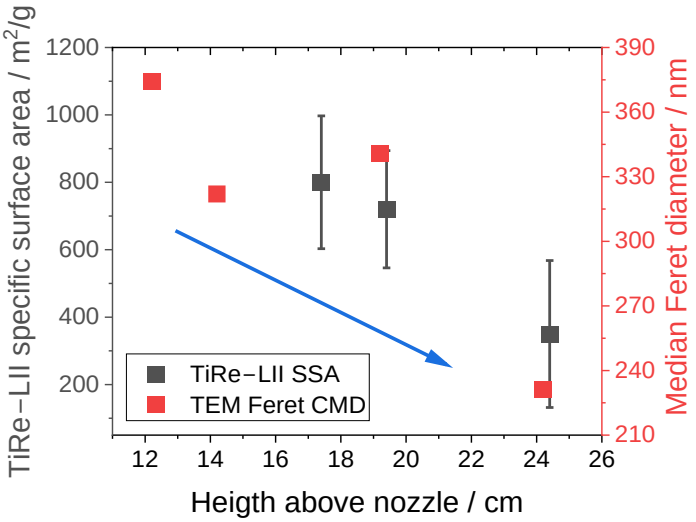

Figure 4-7: Comparison of TiRe-LII-determined specific surface areas and the median Feret diameters from the thermophoretically sampled materials [168].

Comparing the obtained equivalent specific surface are values from TiRe-LII, a trend similar to the TEM observations is obtained. At HAN = 17 cm, the equivalent SSA obtained by TiRe-LII is ~800 m^2/g, which drops to ~350 m^2/g at HAN = 24.4 cm. The first value of ~800 m^2/g suggest the average presence of 3–4 stacked layers, which can be created by folding a monolayer graphene sheet twice. The latter value agrees with the obtained BET value of 337 m^2/g; however, the error bars are large (±150 m^2/g) and limited by the data quality. Still, the reduction of apparent specific surface area confirms the TEM observations of smaller and because of crumpling/folding denser structures being formed along the reactor axis in the effluent.

4.4 Summary

Summarizing the results of this section, the TEM results obtained through thermophoretic sampling close to the plasma at the lowest HAN distance possible show that the first formed graphene sheets are weakly folded and crumpled. Analyzing their thickness indirectly via FFT reveals that the flakes can be monolayer graphene. The formation of monolayer graphene can be linked to the fundamentals of carbon growth by PAH molecules, it in general would be expected for such FLG materials, but has not been observed before. Evaluating the morphology transformation further downstream at larger HAN distances shows that the graphene sheets become more compact as they fold, crumple or agglomerate into denser structures. Additionally, the formation of denser structures is successfully probed via TiRe-LII measurements which shows a reduction in effective surface are for heat conduction. Thus, it has been possible to for the first time probe the structure evolution of graphene in a gas-phase synthesis process starting from single monolayer sheets.

5 Impact of water on carbon particle growth

5.1 Introduction

As briefly mentioned while discussing different studies of the growth of graphene in Section 2.2.1, previous phenomenological comparisons of carbon nanoparticle formation from multiple reactants showed that the C/O ratio is an important factor, which has been correlated with the type of carbon particles generated [36, 37, 80]. In these studies, ethanol (C_2H_5OH) is shown to be a suitable reactant for the synthesis of FLG while reactants with larger C/O ratios start to form other allotropes such as soot-like particles as well. It is important to stress that the comparison is done with the same supply of carbon atoms as the pure reactant concentration also affects the formed carbon nanoparticles. Increasing the ethanol concentration can also lead to the formation of carbon particles other than FLG [23, 83].

A question which arises from these results is how the produced carbon allotropes are linked to the employed reactants and the specific number of carbon, oxygen, and hydrogen atoms, as the plasma would be suspected to fully break down the reactants. Hence, experiments including a model system of ethylene (C_2H_4, ≥ 99.9 %) and water (H_2O, milli Q, 18.2 MΩ) are performed (partly reported by Münzer [35]) to mimic the elemental composition of ethanol. It could be shown in the experiments reported by Münzer that the increasing addition of water (decreasing C/O ratio) can guide the synthesis to preferentially generate FLG, while without water addition only mixtures of nanoscale carbon allotropes – soot-like particles, graphitic particles, and FLG – are generated from C_2H_4. Compared to experiments with pure C_2H_5OH, more water has to be added in case of ethylene/water to generate the same carbon allotrope, and the carbon yield decreases consistently with the addition of more water, but it partly shows that reactants resulting in arbitrary C/O ratios can be mixed to obtain similar results to singular reactants.

Table 5-1: Experimental cases investigated for the effect of water addition on the synthesis of nanoscale carbon allotropes.

Case	Reactant	Flow rate / slm	Ar flow rate / slm	H_2O_g / slm	C/O ratio	Experimantal observations
1	Ethanol	0.19	5	0	2:1	FLG
2	Ethylene	0.19	5	0	∞	(less) FLG/ (more) soot mix
3	Ethylene	0.095	5.095	0	∞	(more) FLG/ (less) soot mix
4	Ethylene	0.38	4.62	0	∞	soot mix
5	Ethylene	0.19	4.905	0.095	4:1	(less) FLG/ (more) soot mix
6	Ethylene	0.19	4.81	0.19	2:1	(more) FLG / (less) soot mix
7	Ethylene	0.19	4.715	0.285	1.33:1	FLG

However, a detailed explanation for this observation is missing. Therefore, the experiments of Münzer are revisited here with the use of different *in situ* measurement techniques (OES and FTIR) to investigate the underlying processes in more detail by determining temperatures in the plasma/effluent, identifying light emitting species in the plasma, and semiquantitative comparison of the effluent gas composition. The focus is thereby on how oxygen affects the carbon growth in order to rationalize the previous and here newly generated results. For additional data analysis, chemical kinetic simulations and equilibrium calculations are performed. The in the following discussed experiments are summarized in Table 5-1, including the general experimental observation. The experiments contain pure C_2H_5OH as a reference material (Case 1) and C_2H_4 (Case 2) for comparison synthesized with the same flowrate. Other experiments are variations for the C_2H_4 flowrate and thus carbon concentration, and the addition of water to C_2H_4 to adjust the corresponding C/O ratio.

5.2 Results of *ex situ* materials analysis

At first, experiments with either pure C_2H_5OH (Case 1) or C_2H_4 (Case 2) are performed (190 sccm flowrate) and the respective obtained materials are analyzed. A comparison of the Raman spectra and TGA results is shown in Figure 5-1. In Raman measurements it was found that both samples contain the specific carbon bands of D (~1340 cm^{-1}), G (~1580 cm^{-1}), and 2D (~2685 cm^{-1}), in addition to some specific overtones (D+D'' and D+D'). However, their relative intensities do vary. Similarly, the TGA results show characteristic features that vary between the samples.

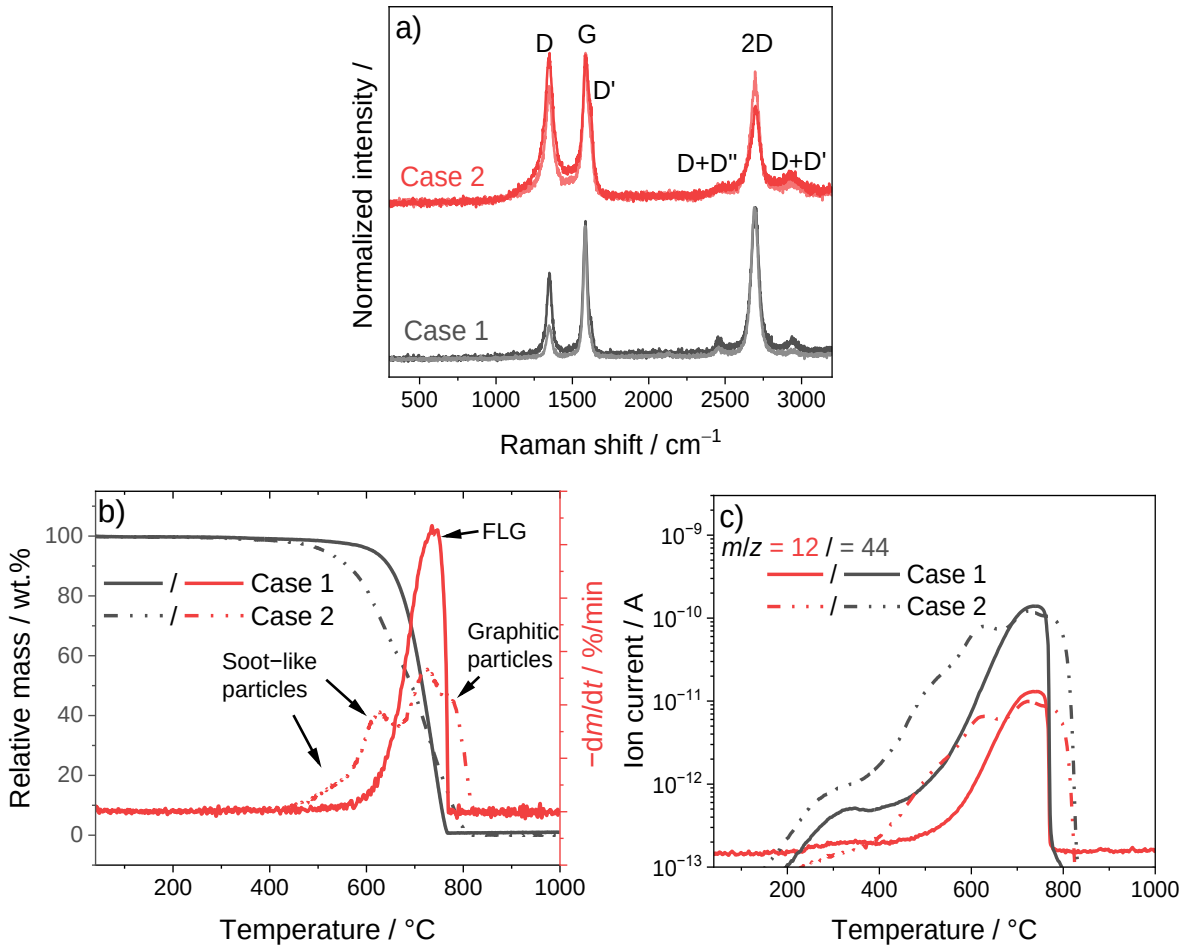

Figure 5-1: Raman spectra (a) [175], TGA/DTG data (b), and TGA QMS data (c) obtained from samples prepared by Case 1 and Case 2. The arrows in b) indicate the onset of oxidation of different carbon allotropes.

Figure 5-1a displays the results of the Raman measurements. Comparing the band intensities of the ethanol-made sample, the 2D band possesses a larger intensity than the G band and the D band. Its FWHM is ~55 cm^{-1}. The combination of FWHM and the relative intensity implies that the sample does not follow the conventional Bernal stacking order that is commonly found in graphite, but that it possesses some rotational disorder originating from turbostratic stacking. Such a combination is not possible based on the evolution of the electronic bands in Bernal-stacked graphene [101]. Furthermore, the reported specific weak overtone bands in the range of 1700–2150 cm^{-1}, which would allow to distinguish between different types of graphene-like materials (stacking order and layer number) [110-112], are not observed consistently. The presence of turbostratic stacking between the graphene layers may be explained by the structure formation studied in Section 4 as the self-folding, crumpling, and agglomeration of flakes is most likely random. The D band intensity can theoretically be compared to the G band to infer information about defect densities and crystallite sizes, but is not applied here because the flakes are too small relative to the laser beam, meaning that always a larger number of surface defects are detected which influence the results substantially (see section 2.3.1.1). Comparing the ethanol-made sample now to the one prepared with ethylene, the 2D band is less pronounced. The lower relative intensity of the 2D band in the ethylene-made sample can be a sign for the presence of soot-like, graphitic particles, or a combination of both,

as such materials usually show weak 2D bands. It can also be observed that the D band has a larger relative intensity and shows a weak shoulder at lower Raman shifts (~1250 cm^{-1}). Such a shoulder is usually assigned to the presence of amorphous carbons [119].

The TG and DTG plots in Figure 5-1b for the ethylene-made sample show multiple peaks that can be assigned to different carbon allotropes. The structure of the multiple peaks is also evident when looking at the simultaneously measured QMS data in Figure 5-1c for m/z = 44 (CO_2) and 12 (C). For better visibility only two signals are shown while the complete QMS data is shown in Figure 9-13. As explained in the comparative study in the Appendix, Section 9.1, the peaks in the DTG and the measured QMS signal can be assigned to different carbon allotropes. The low temperature peak at ~630 °C can be assigned to the presence of soot-like particles, while the large peak at ~730 °C matches with the temperature required for the oxidation of FLG. Additionally, a small shoulder at ~770 °C can be seen which might originate from the presence of graphitic particles, because graphitic structures (graphite compared to graphene) are known to be more resistant to oxidation. The ethanol-made sample only consist of the peak which can be assigned to FLG and does not show any further peaks in the DTG or QMS plot.

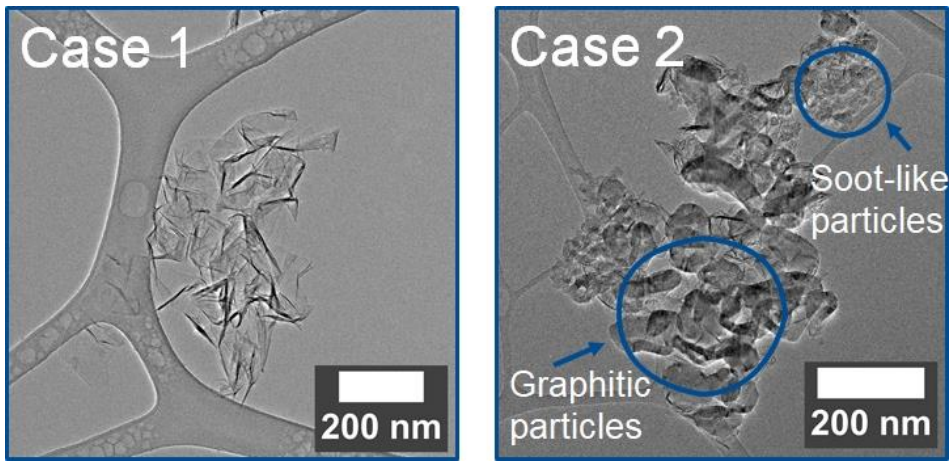

Figure 5-2: TEM measurements taken from samples prepared by Case 1 and Case 2.

TEM images are taken to further confirm the TGA and Raman observations. Figure 5-2 displays TEM images for the comparison of Case 1 and 2. When comparing the two cases, it is evident that the sample prepared with ethanol as reactant is consisting of FLG, while C_2H_4 generates a mix of several different carbon allotropes. These mixed allotropes include small (~30 nm) soot-like particles, large (>80 nm) graphitic particles, and FLG sheets. Hence, confirming the assignment that Case 1 forms FLG while Case 2 generates a mixture of different carbon allotropes.

For investigating how the type of the generated carbon particles changes in dependance of the C/O ratio of the supplied reactant mixture, different amounts of water are premixed with C_2H_4 (Case 5: 95 sccm, C/O ratio :4:1; Case 6: 190 sccm, C/O ratio: 2:1; Case 7: 285 sccm, C/O ratio: 1.33:1). When comparing the yield of carbon particles harvested from the filter, a gradual decrease to ~1.5 wt.% (Case 7, 0.15 g/h) from ~6.5 wt.% (Case 2, 0.8 g/h) is observed when the amount of added water increases. Case 1 using ethanol as a reactant generates a yield of~1.8 wt.% (0.24 g/h). The comparative Raman spectra and DTG/QMS plots shown in Figure 5-3 reveal changes in the formed carbon particles.

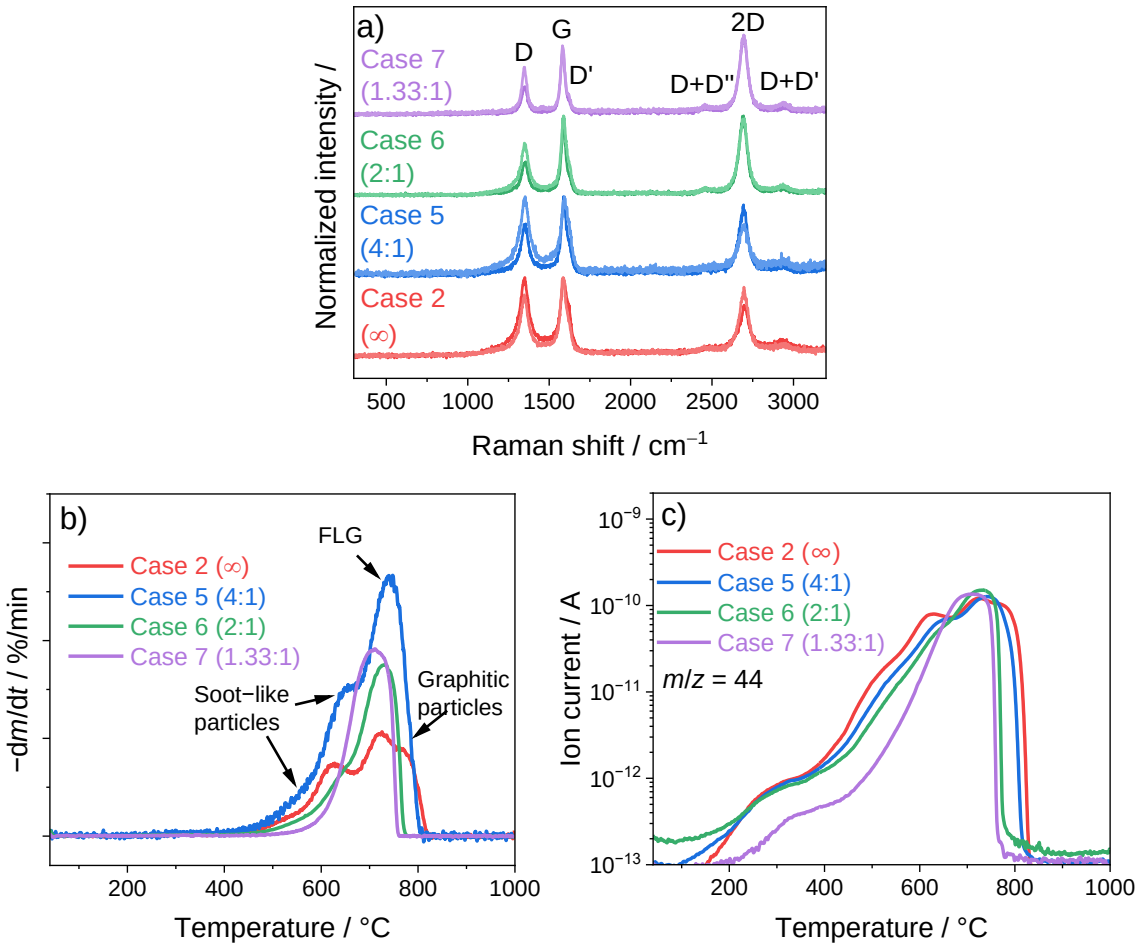

Figure 5-3: Raman spectra (a), DTG data (b), and TG/QMS data (c) obtained from samples prepared by Case 2 and Cases 5–7.

The Raman spectra in Figure 5-3a reveal an increase of the relative intensity of the 2D band while the shoulder of the D band at ~1250 cm^{-1} vanishes for Cases 5–7. Such a transformation can be a sign of a larger FLG content in the respective samples. The DTG and TG/QMS plots in Figure 5-3b and c show that the peaks assigned to soot-like or graphitic particles vanish, while only the one assigned to FLG remains. More evidence for the transformation can be observed when looking at comparative TEM images as shown in Figure 5-4.

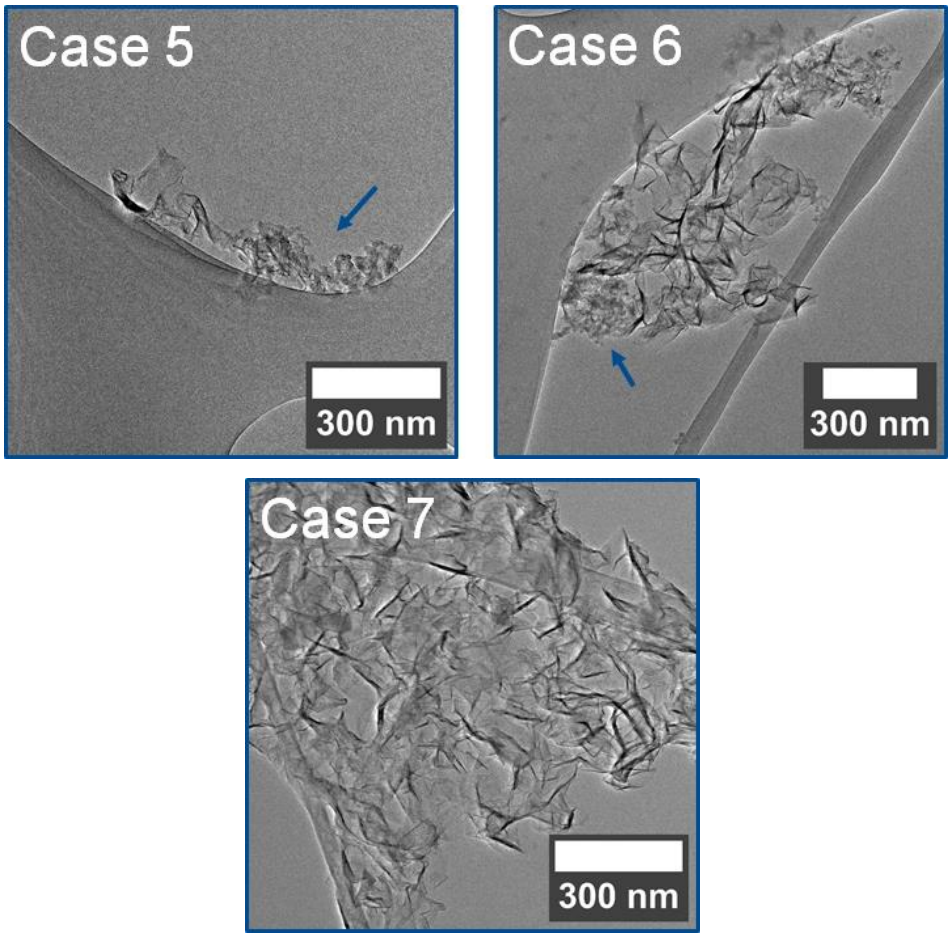

Figure 5-4: TEM images obtained from samples prepared with Cases 5–7 (C/O ratios 4:1–1.33:1) [175]. The blue arrows indicate soot-like particles.

Case 5 (C/O ratio of 4:1) shows the presence of a large number of soot-like particles. When the amount of water is increased while keeping the mass flow of ethylene constant (Case 6, C/O ratio of 2:1), the number of soot-like particles further decreases. For Case 7 (C/O ratio of 1.33:1), only FLG flakes can be found by TEM. Comparing the BET SSA values, it can be observed that an increase in (input) C/O ratio also increases the SSA value (Figure 5-5).

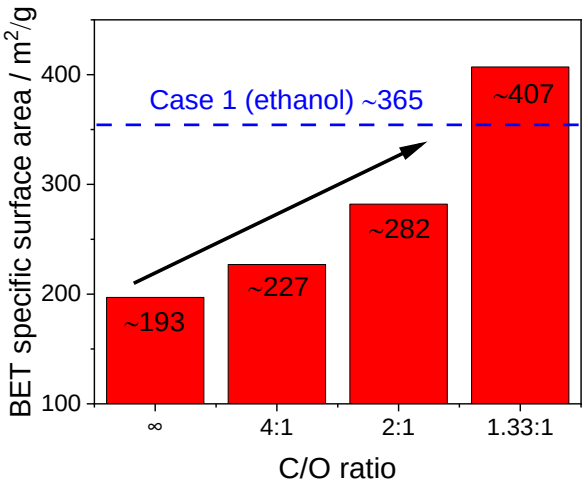

Figure 5-5: BET SSA values comparing material from Case 2 with the Cases 5–7 [175]. As a reference, the result for Case 1 is plotted as dashed line.

The SSA increases for Case 5 (4:1) to 227 m^2/g, for Case 6 (2:1) to 282 m^2/g, and for Case 7 (1.33:1) to 407 m^2/g. The latter value for Case 7 does exceed the values measured for Case 1 (C_2H_5OH). Taking into account that the generated soot-like particles are usually in the size range of ~20 to 30 nm and have (compared to FLG) a lower SSA, an increase in SSA might indicate the removal or absence of the low-SSA component and imply purer FLG samples, thus, reinforcing the impression by the TEM, TGA, and Raman results.

To further investigate which formation processes might influence the carbon structure, the C_2H_4 concentration was varied by either increasing (380 sccm, Case 4) or decreasing (95 sccm, Case 3) the flow rate by a factor of two and thus the ethylene concentration compared to the base flow rate of Case 2 (190 sccm). The results are again compared by TEM, Raman and TGA in Figure 5-6. Looking at the yield of harvested particles from the filter, the yield slightly decreases for Case 3 to ~6 wt.% (0.35 g/h) while for Case 4 it becomes ~13 wt.% (2.4 g/h) compared to ~6.5 wt.% (0.8 g/h) for Case 2. A comparison of the Raman spectra in Figure 5-6a reveals that in comparison to Case 2, the relative intensity of the 2D band for Case 3 increases, while its intensity for Case 4 decreases. Data by TGA (Figure 5-6b and c) shows similar trends by either an increase or decrease of the carbon fraction oxidized at low temperatures (~630 °C) and high temperatures (~730 °C). Both results by Raman and TGA lead to the interpretation that the relative fraction of FLG is correlated to the concentration of C_2H_4 supplied into the reactor.

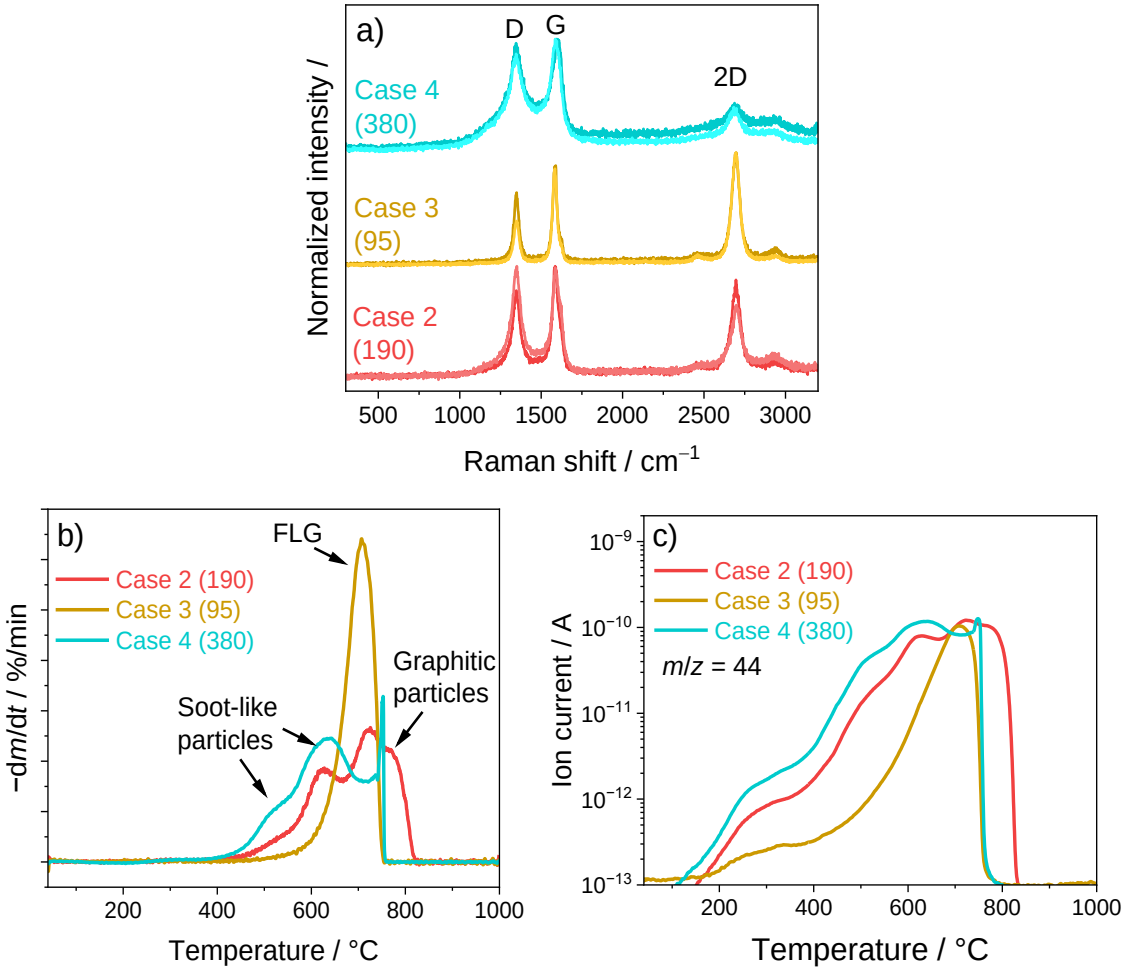

Figure 5-6: Raman spectra [175] and DTG/QMS plots for Cases 2–4 with different C_2H_4 concentrations indicated in the brackets.

Figure 5-7 displays comparative TEM images. Comparing the TEM images for Cases 2–4, Case 3 shows the smallest number of soot-like particles present and mostly consists of FLG. Contrary, Case 4 mostly consists of soot-like or graphitic particles, confirming the trend observed by TGA and Raman. Additionally, the obtained SSA values do either increase or decrease relative to Case 2. For Case 3 it increases to 311 m^2/g, while for Case 4 a decrease to 158 m^2/g is observed. Using the same argument as in the comparison for Case 5–7, the SSA change can be an indicator for less or more abundant FLG in the particle mixtures.

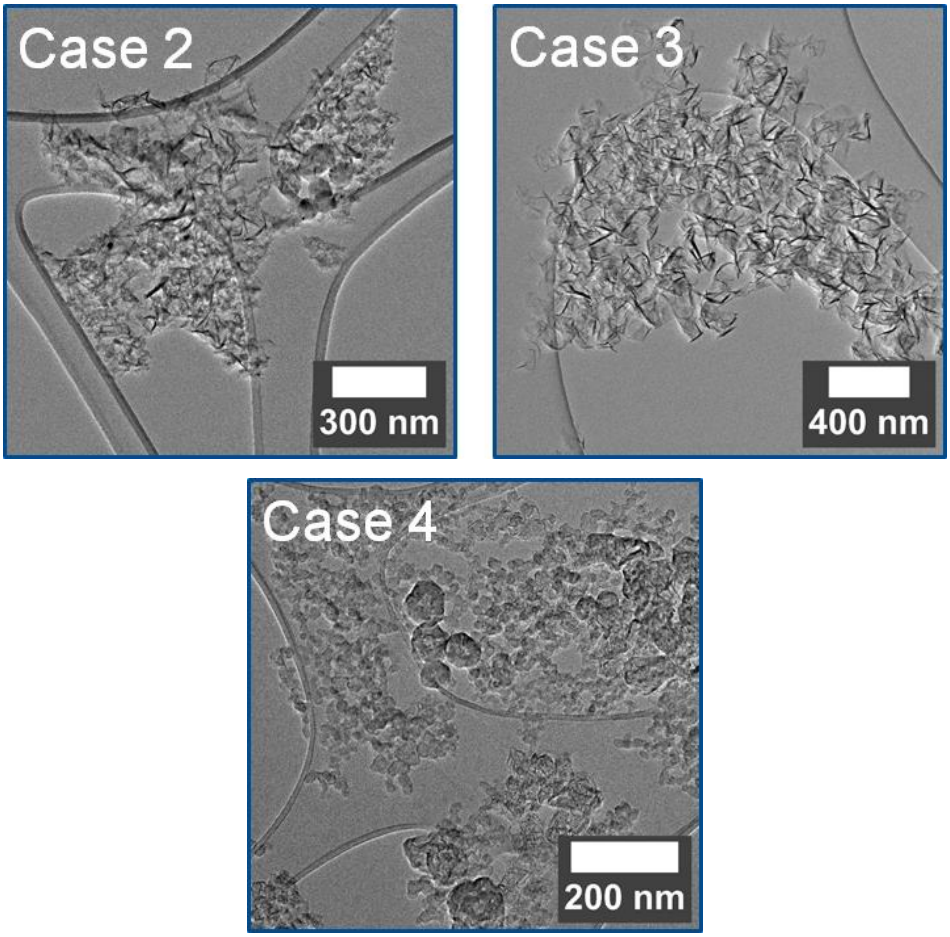

Figure 5-7: TEM images taken from samples prepared from Cases 2–4.

Summarizing the obtained information by *ex situ* analysis techniques for the different carbon particle mixtures synthesized for Cases 1–7, different dependencies of the input flowrates of water, C_2H_4, and the used reactant are found. When comparing two different reactant which are supplied with the same flowrate but possess different C/O ratios (Case 1 and 2), lower C/O ratios lead to lower yields and a different carbon allotrope mixture. Case 1 generates pure FLG while Case 2 forms a mixture of three carbon particles types. When decoupling the input C/O ratio from the used single reactants by employing reactant mixtures of C_2H_4 and H_2O (Cases 5–7), a trend is observed. Lowering the C/O ratio by adding more H_2O, reduces the yield but leads to purer FLG samples. However, more water needs to be added to obtain a pure FLG sample. Lastly, instead of adding water and influencing the C/O ratio, modifying the C_2H_4 reactant flowrate also alters the carbon particle mixture and its yield (Cases 2–4). Lower flowrates favor the formation of FLG-rich mixtures with reduced yield while larger flowrates generate large yields of FLG-depleted carbon particle mixtures.

5.3 Application of *in situ* techniques

5.3.1 OES

As discussed in chapter 2.2, the gas temperature is an important factor during the growth of carbon particles and may influence the formation pathways of PAHs and their growth towards

larger molecular clusters. However, the peak temperature of the plasma and the temperature profile in the post-plasma zone is not known sufficiently well. Therefore, it is not clear so far, whether part of the observed experimental results are influenced by variation in gas temperature. To improve the understanding of temperatures, OES measurements are performed to observe which molecular and atomic species emit light. In case of small molecules, their rotationally resolved emission can be used to calculate their respective rotational temperature. Because the plasma process is operated at atmospheric pressure, fast collisional energy transfer will promote equilibration of rotation excitation with the gas temperature. Further discussion and constraints/limitations on the OES measurements and explanations on which information can be extracted is presented in Section 9.3. Figure 5-8 displays example OES spectra obtained for different plasma conditions.

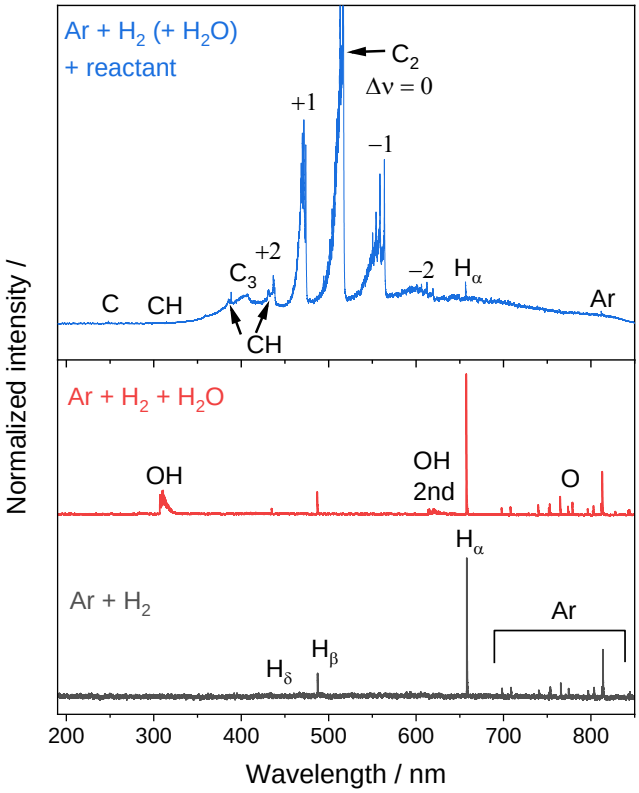

Figure 5-8: Example OES spectra measured for different plasma conditions [175]. The lower half shows the pristine and H_2O doped plasma, while the upper half displays the emission after a hydrocarbon reactant is introduced.

The pristine plasma spectrum – prior to the injection of either H_2O or any hydrocarbon reactant – only consists of emissions from hydrogen and argon. The emitted lines can be assigned to the Balmer series of H and metastable Ar states above ~670 nm [185]. When the plasma is doped with water, atomic oxygen lines (~777, ~833 nm) [185, 186] and OH (~310 nm) [187, 188] emission becomes visible. Upon the addition of hydrocarbon reactants (either C_2H_5OH or C_2H_4), the plasma shows emission of the C_2 swan band system [189, 190] centered at 516 nm and several other hydrocarbon fragments such as CH (~430, ~390, and ~314 nm [43, 191]), atomic carbon (~250 nm [192]), and C_3 (~405 nm [193]). One of the CH lines might overlap with the C_2 Deslandres-d'Azambuja system at ~385 nm [194]. When adding C_2H_4 to plasmas

doped with water, the OH emission vanishes and only CH is detected in the corresponding wavelength region of 300–320 nm. Similarly, atomic oxygen is not observed anymore.

The OH and C_2 emission observed is compared between the different experimental cases to judge whether first, the temperature is changing by injecting different hydrocarbon reactants (Case 1 and 2) with different concentrations (Cases 2–4), and second, whether the apparent rotational temperatures are affected by non-equilibrium effects such as chemiluminescence which is reported to occur in, e.g., methane/hydrogen plasmas [195]. In case of chemiluminescence, the rotational temperatures of OH and C_2 could deviate due to excess energy as result of exothermal chemical reactions, and the determination of the gas temperature is not possible. For all experimental cases – with the exception of Case 7 – 2–3 spectra for the C_2 emission in the wavelength range of 510–520 nm are recorded. For Cases 5–7 in which water is added to the Ar+H_2 plasma, one spectrum for the OH emission at 300–320 nm is recorded. Figure 5-9 shows results for the rotational temperature obtained by analyzing the C_2 emission with the Boltzmann plot method for Case 2.

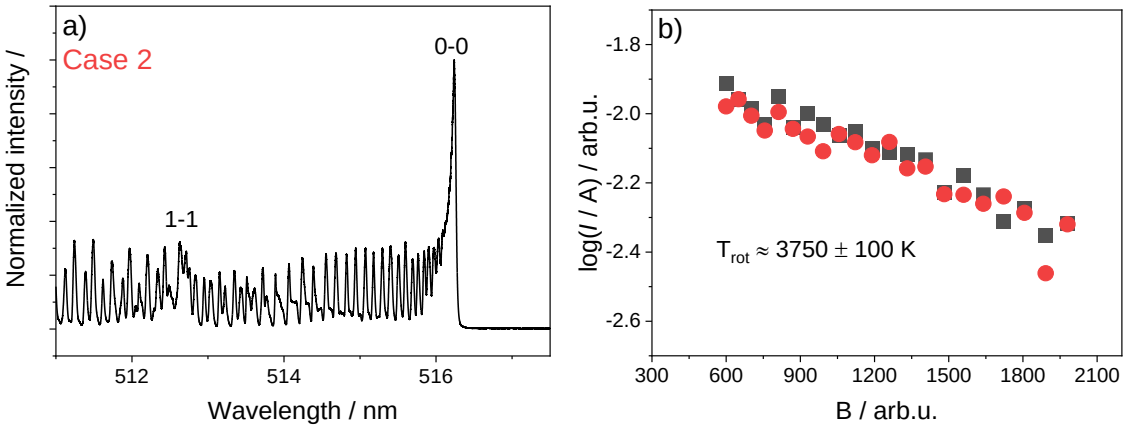

Figure 5-9: a) High-resolution OES spectrum of the C_2 (0-0) bandhead at ~516 nm for Case 2. b) Boltzmann plot for the rotational lines (of two measurements) with the resulting temperature [175].

Using the Boltzmann plot method and comparing Case 1 with Case 2, both experimental Cases show a similar rotational temperature of T = 3830 ± 200 K (Case 1) and T = 3750 ± 100 K (Case 2). These two values are within the experimental error and similar to values which have been reported for other microwave plasma systems during the synthesis of FLG in literature [22, 88]. To judge whether these values are realistic for the reactor used, simulations of the spectra with PGOPHER are performed. The simulation and fitting results (~3800 K for Case 1) also match the result by the Boltzmann plot method. Figure 5-10 shows the overall comparison of temperatures obtained by the Boltzmann plot method for C_2 and OH for the experimental Cases 1–7. The C_2 obtained temperature for Case 7 does not show an error bar because the plasma became less table at such high H_2O flowrates, i.e., the C_2 spectra are noisy.

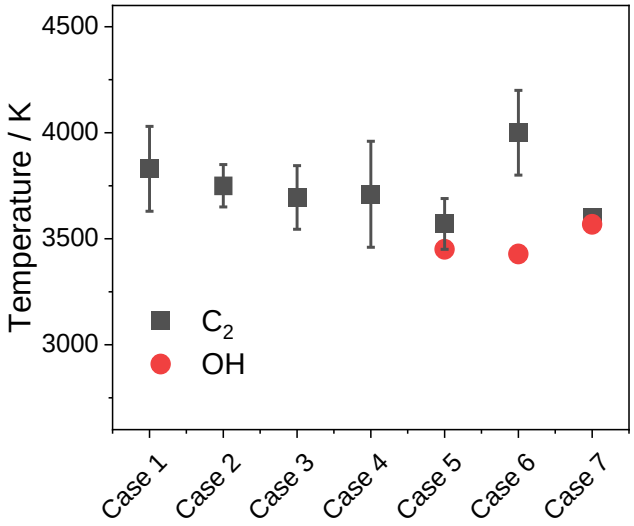

Figure 5-10: Comparison between the temperatures obtained by the Boltzmann plot method for C_2 and OH for Cases 1–7.

When comparing the values for the C_2 rotational temperature or the OH obtained temperatures prior to C_2H_4 injection, only a small deviation can be observed. The rotational temperatures for OH seem to be overall slightly lower compared to those of C_2. The observed species in the OES spectra are compared to the predicted species generated by chemical equilibrium calculations (Figure 9-17 in Section 9.5.4) for the calculated/assumed plasma temperature. The comparison reveals that the observed emitting species match the predicted ones and the gas composition can be considered to be in or near equilibrium and the reactants are (almost) fully dissociated towards their atomic constituents at ~3800 K. For the addition of H_2O, >99 % of water molecules are dissociated at such temperature and the concentrations of atomic hydrogen and oxygen are reaching a plateau. Similarly, when adding C_2H_4 as hydrocarbon reactant (with or without water being present), or adding C_2H_5OH, the concentrations for atomic carbon and hydrogen are in a constant state. Furthermore, for all experimental cases, similar temperatures are observed independent on whether the specific cases form carbon particle mixtures which are abundant in soot-like particles or FLG flakes.

Summarizing the results, it can be stated that the plasma temperature is not the main driving force behind the observation of different carbon particle mixtures in the investigated experimental cases, as the temperature values are almost the same for every experimental case, the reactants are fully dissociated into their atomic constituents, and no mechanistic changes in the PAHs formation and growth processes are expected.

5.3.2 FTIR

To further analyze the process, potential changes of the species gas-phase concentrations are monitored by *in situ* infrared absorption spectroscopy (4000–400 cm^{-1}) for the Cases 1, 2, and 5–7. These measurements were performed together with Stanislav Musikhin at Reactor B (Table 3-1) by guiding the infrared beam through a ~0.6 m long straight tube in the plasma reactor effluent. Figure 5-11 does show exemplary the obtained FTIR spectra for the pristine plasma, Case 1, Case 2, and Case 7.

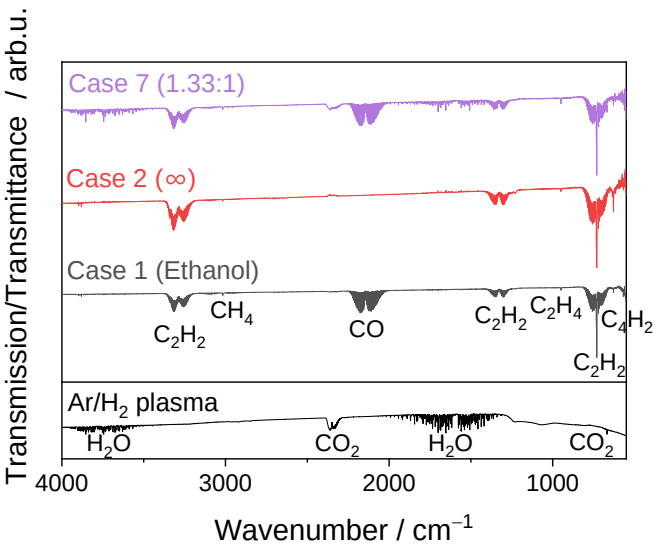

Figure 5-11: FTIR transmission/transmittance measurement of the plasma off-gas with ~0.6 m absorption length plotted between 4000 and 550 cm^{-1} [175]. For the base plasma the transmission is shown in the lower part and for Cases 1, 2, and Case 7 (C/O = 1.33:1) transmittance in the upper part.

For the pristine plasma, the transmission spectrum of the beam through parts of the laboratory and the reactor is shown. Several absorption bands can be recognized and assigned to water vapor (~3700, ~1600 cm^{-1}) and carbon dioxide (~2300, ~670 cm^{-1}) originating from the laboratory air. The plasma only consists of H_2 and Ar, which do not absorb significantly in the given wavenumber range. For the displayed transmittance spectra, these signals are also weakly visible, because flushing the IR-light path with dry nitrogen did not lead to completely stable results. When C_2H_5OH (Case 1) is added into the plasma, the composition of the off-gas changes. For the transmittance, the appearance of C_2H_2 (~3250, ~1300, ~750 cm^{-1}), C_2H_4 (~950 cm^{-1}), CH_4 (~3000 cm^{-1}), and also CO (~2150 cm^{-1}), can be observed. A weak feature at ~630 cm^{-1} can be attributed to C_4H_2. Case 2 shows the same hydrocarbon absorption lines but not CO, which is caused by the oxygen-free atmosphere. Also, the absorption of C_2H_2 and C_4H_2 is stronger for Case 2 compared to Case 1. Comparing these observations to results from literature, shows that the observation of these specific species matches with reported experimental work and reaction kinetical calculations (e.g., [23, 196-198]). For Case 7, the presence of CO can be observed while the absorption for the different hydrocarbon bands is reduced. Figure 5-12 compares the absorbance of C_2H_2, CO and C_4H_2 for Case 1, Case 2, and for Cases 5–7. The absorbance of the species is proportional to the concentration of the respective molecules. Therefore, observed trends are also indicative for quantitative changes in the species concentrations.

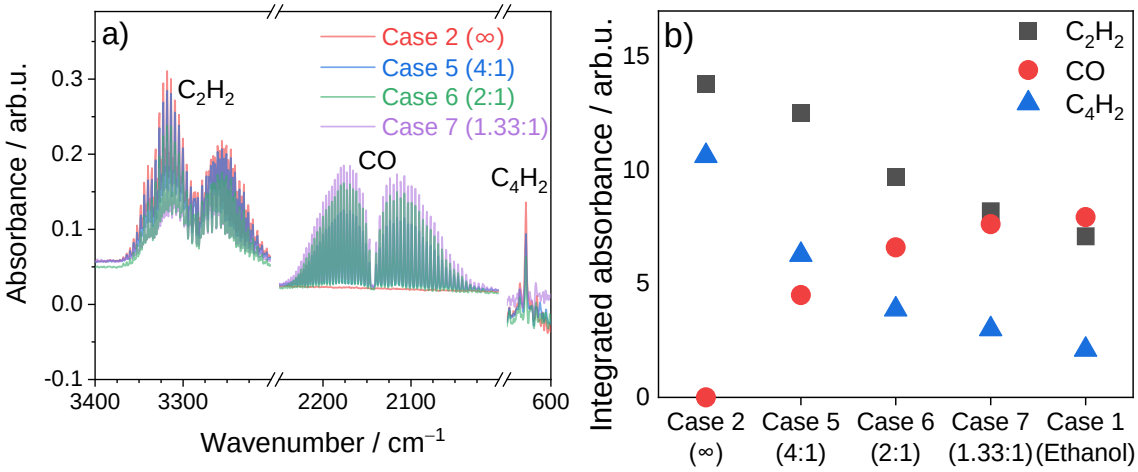

Figure 5-12: Variation of the FTIR spectra of C_2H_2, CO, and C_4H_2 for experiments using mixtures of ethylene and water at different input C/O ratios and their variation of the integrated absorbance [175]. The values for C_4H_2 are multiplied by a factor of 30 to scale.

Figure 5-12a shows the changes of the C_2H_2, CO, and C_4H_2 absorption bands for Case 2 and Cases 5–7. It can be seen that the CO absorption increases when the flowrate of water is increased. Simultaneously the absorption bands for C_2H_2 and C_4H_2 become weaker. Figure 5-12b compares the integrated absorption for these mentioned lines between Case 1, Case 2 and Cases 5–7. The measurements visualize the trend in Figure 5-12a and reveal that only Case 7 (C/O = 1.33:1) shows absorbances similar to Case 1 (C_2H_5OH, C/O = 2:1).

To summarize the FTIR results, the stable pyrolysis gases which are identified for all experimental cases are C_2H_2. C_2H_4, CH_4 and C_4H_2. When oxygen is supplied into the reactor either as part of a reactant (ethanol) or as additional separate molecule (H_2O), CO formation is observed. Decreasing C/O ratios by the addition of more H_2O (Cases 5–7) leads to the formation of increasingly more CO, while the concentrations of C_2H_2 and C_4H_2 are decreasing. The decrease in C/O ratio and resulting increase in CO formation correlates for Cases 2 and 5–7 with the decrease in yield of harvested carbon particles. Yet, absorbances and yields for Case 1 and 6 vary although the same C/O ratio is supplied.

5.4 Reaction kinetics modeling

To further aid in describing the experimental observations, simple 1D kinetics simulations are performed in collaboration with Xian Shi and Hai Wang (Stanford University) to simulate the concentration of different molecular species and their evolution along the plasma reactor at different HAN. The used chemical kinetic mechanism, assumptions, and boundary conditions are summarized in Section 2.5. Figure 5-13 displays the assumed temperature profile and the evolution of different species concentrations along the reactor axis for Case 1 and Case 2. For the purpose of visibility, only the most abundant predicted species and some intermediates are shown.

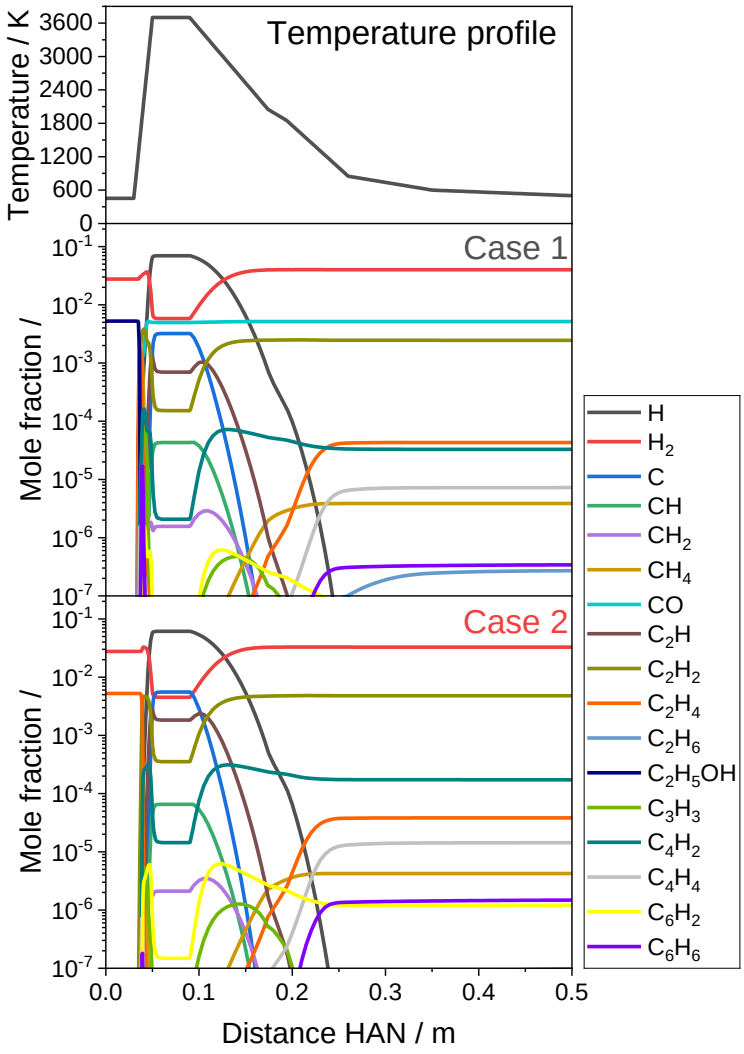

Figure 5-13: Simulated species concentration profiles along the reactor for Cases 1–2 and the temperature profile determined by *in situ* methods as a basis for the simulation.

Following the reaction coordinate, the species profiles can be separated in three different regions. In the first region the temperature increases fast and reaches the assumed plasma temperature of 3700 K. Caused by the increase in temperature, the reactants dissociate into their atomic components (C, H) or other simple and stable molecular fragments. Because the reactant mixture for Case 1 contains oxygen, CO is formed, which only start to dissociate at temperatures of >4000 K. The second region describes the plasma zone in which a constant temperature is assumed. All the species are in thermodynamic equilibrium meaning their fraction of dissociation is determined by their temperature stability. The third region is characterized by the drop in temperature from 3700 K at 0.09 m HAN to 600 K at 0.35 m HAN. In this region the concentration of different hydrocarbon fragments such as C_2H, CH, and C starts to decrease while more stable simple molecules are formed. The most abundantly formed species are H_2, C_2H_2, and C_2H_4. The species do reach a stable plateau below 1000 K (~0.25 m HAN).

Comparing the simulated stable species concentrations of Case 1 to Case 2 shows that Case 1 has lower concentrations for all and especially the most abundant hydrocarbon species. This also affects the relative ratio between the different hydrocarbon species as can be seen at the example of the C_4H_2 concentrations. In Case 2 its concentration (~1.7×10^{-4}) is larger in

comparison to C_2H_4 (~4×10^{-5}) while for Case 1 both the relative and absolute concentrations (~3×10^{-5}) change. The absolute concentration for C_2H_4 is mostly unaltered between both cases. The reason why C_4H_2 shows such a sensitivity to the presence of oxygen is probably related to its formation path which is directly linked to the concentration of C_2H_2. Because the concentration of C_2H_2 halves from Case 2 (~4.8×10^{-3}) to Case 1 (~2.4×10^{-3}), the concentration for C_4H_2 also drops.

The Chemkin simulation is investigated on how sensitive the species concentration profiles react to changes in the assumptions such as the peak gas temperature and the temperature decay rate. Figure 5-14 shows a comparison between assuming a different peak temperature (6000 instead of 3700 K) in the plasma region and artificially changing the residence time of the gas mixture to become larger by increasing the flow reactor model diameter (factor 5). For visual clarity, only a limited number of species (compared to Figure 5-13) is displayed.

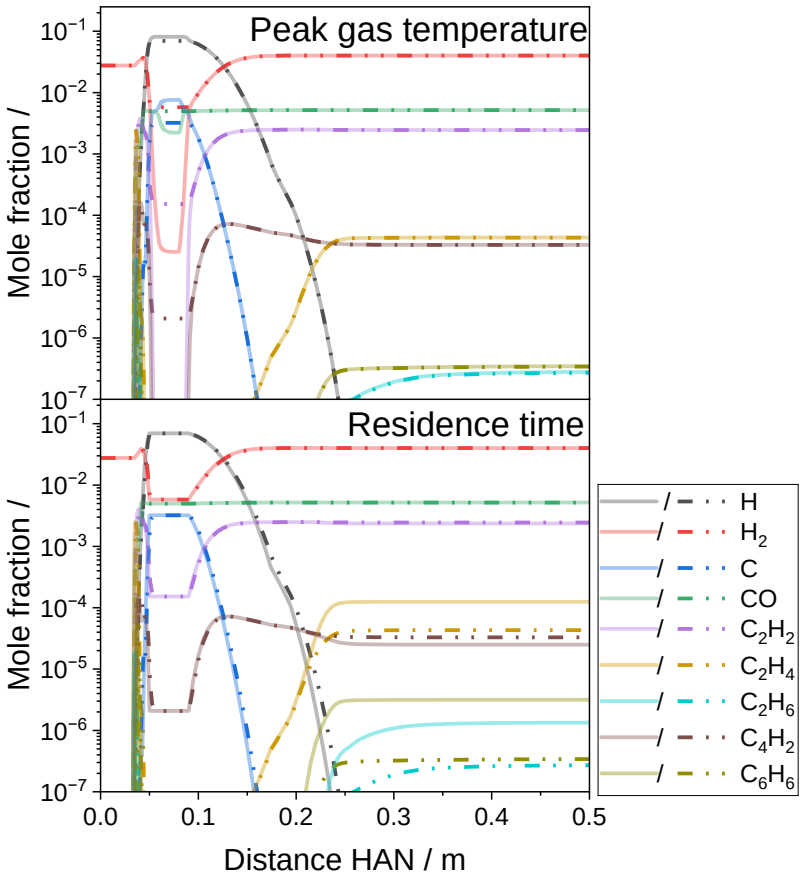

Figure 5-14: Analysis of the simulation sensitivity to different boundary conditions shown here for Case 1. The simulation on top assumes a higher peak gas temperature, while the plot on the bottom modifies the residence time. Dash-dotted lines refer to the pristine Case 1 while transparent solid lines represent the altered boundary conditions.

The comparison reveals that the simulated concentration profiles are sensitive to the overall residence time, while being mostly unaffected by the peak gas temperature assumed for the plasma. An increase in the peak temperature only slightly affects the overall plug-flow residence time (0.97 s) compared to the normal Case 1 (0.97 s) while reducing the residence time in the plasma (HAN 0.05–0.09 m) from 17 to 12 ms. Although the concentrations of stable species within the plasma are changing for a different temperature and more atomic fragments are

present, the concentration of the species formed at larger HAN is unchanged. An increase in residence time to in total 24.6 s, leads to the formation of different concentrations of molecular species from ~0.2 m HAN downstream. The dependence on the residence time which is equivalent to a different temperature decay rate indicates that the process is kinetically controlled in the third region of the temperature profile, because the species are not in equilibrium anymore. For equilibrium, the concentrations would reach the same values. Noticeable is the increase of the benzene concentration for the case in which the residence time is increased. This finding may imply that altering the residence time can be used to change the yield and the type of obtained solid carbon materials as more growing PAH molecules become available for solid carbon formation.

The by the simulation predicted different stable gas compositions can be analyzed regarding trends and compared to the FTIR observations. A comparison of the expected CO and C_2H_2 mole fractions for Cases 1, 2, and 5–7 is shown in Figure 5-15a. For the cases in which C_2H_4 as reactant is employed, similar trends to the FTIR absorbances are observed. The formation of CO is predicted to increase with increasing H_2O content (decreasing C/O ratio), while the concentration of generated hydrocarbons, most abundantly C_2H_2, decreases. Additionally, and similarly to the FTIR measurements, the amount of C_2H_2 when using pure C_2H_4 (Case 2) compared to ethanol (Case 1) is larger. Cases 1 and 6, which both share the same C/O ratio of 2:1, are predicted to form the similar absolute amounts of CO and C_2H_2 mole fractions. This prediction deviates from the experimental FTIR observation, as the amount of CO absorbance for Case 1 was measured to be larger and the corresponding C_2H_2 absorbance smaller.

Another aspect that can be extracted from the simulations is the amount of C6+ species (i.e., molecular species with six or more carbon atoms) generated. Species such as benzene are considered important precursors for the growth of solid carbon. Figure 5-15b shows the expected C6+ species concentration within the different experimental cases.

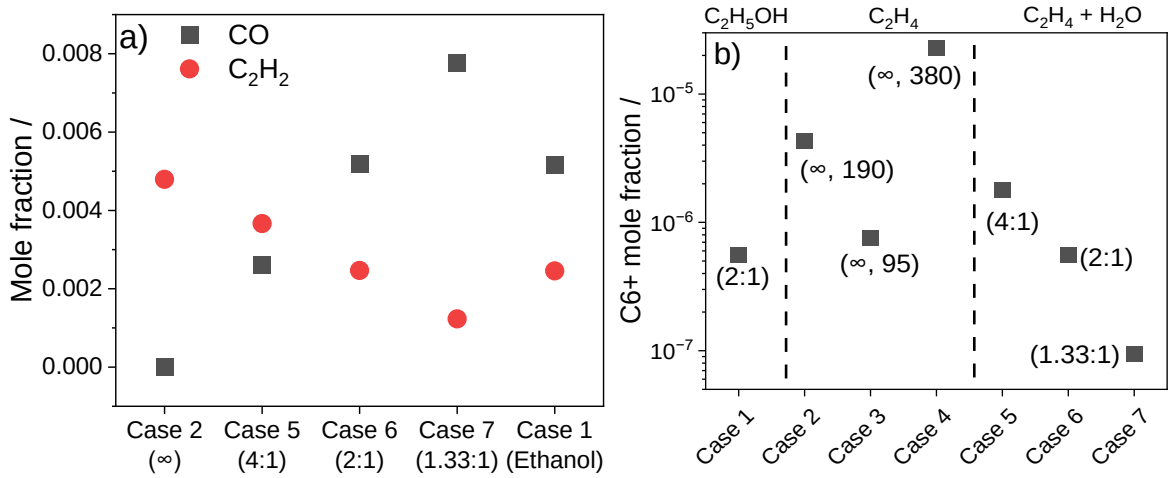

Figure 5-15: Evolution of critical species during the synthesis of different experimental Cases [175]. a) compares the evolution of C_2H_2 and CO for the experimental Cases of 1–2 and 5–7, b) displays the molar fraction of C6+ species generated for Cases 1–7.

Both decreasing the concentration of C_2H_4 reactant and an increase in the addition of water leads to a decrease of the expected C6+ species concentration. This behavior can be explained with the larger amounts of CO formed depending on the supplied C/O ratio, as it reduces the concentrations of the remaining hydrocarbon species which can form larger

molecules. Comparing the obtained carbon particle mixtures and their respective yields to the trends of C6+ species concentrations shows that FLG-rich carbon samples and their yields correlate with lower predicted C6+ concentrations. For Cases 2 and 5–7 the C6+ concentrations decrease, while purer FLG particle mixtures with smaller yields are obtained. A similar observation is also evident when altering the supplied C_2H_4 reactant concentration in Cases 2–4. However, the same concentrations are predicted for Cases 1 and 6 while the experimental observations show differences of the yield and composition in the obtained carbon particles.

Interestingly, the results are also almost independent on the amount of H_2 added to the gas mixture. Because H_2 is reported by some authors to be able to guide the process for the generation of tailored carbon materials (e.g., plasma processes or flames [94, 179, 199, 200]) by influencing at which rate hydrogen abstraction reactions on e.g. the growing PAHs edges take place during the growth process, this result is surprising. Increasing the H_2 content in the reaction mixture leads to a decrease in C6+ species while the formation of more simple hydrocarbons (e.g., C_2H_2) increases. When the concentration of H_2 is doubled from a H_2/C_2H_4 ratio of 5 to 10, changes in the species concentrations are observable but not as large compared to the addition of water (Figure 5-15b). Figure 5-16 shows the evolution of C6+ species with the content of hydrogen. Experiments in which the addition of H_2O to C_2H_4 is substituted with H_2 confirm the simulations. The corresponding details are shown in Section 9.5.1 of the appendix.

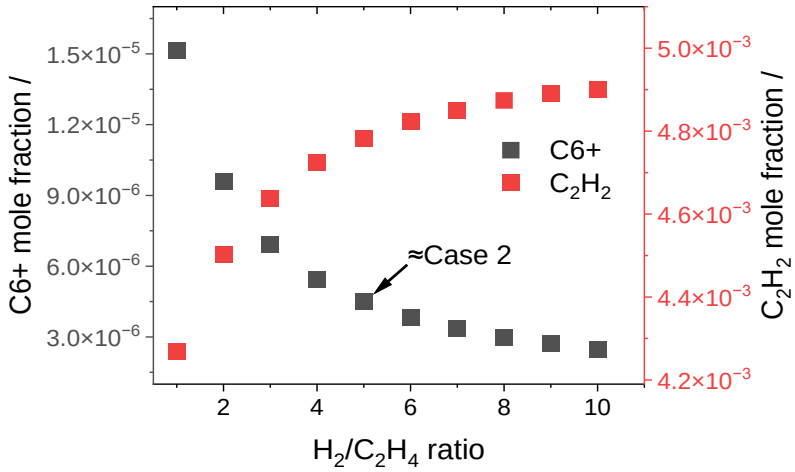

Figure 5-16: Evolution of the mole concentrations of C6+ species and C_2H_2 with different H_2/C_2H_4 ratios. A ratio of 5 is similar to the experiments for Case 2 as 1 slm of H_2 is added into the sheath gas and the used plug flow model assumes homogeneous mixing.

5.5 Conclusions

Summarizing the experimental results and the simulation, the results indicate that the addition of oxygen in the form of water reduces the overall yield of solid carbon phase while simultaneously the formation of FLG like materials is favored. Taking into account how the generated carbon nanoparticles differ when the concentration of C_2H_4 is altered, being more FLG-rich when using less reactant, indicates that the concentration of the gaseous carbon species which is supplied into the plasma is important to tailor the growing solid carbon phase. Oxygen supplied by water is fully converted to CO, which alters the concentration of gaseous carbon species which can grow into solid carbon, as evident by FTIR measurements and the simulations. With these results in mind, a regime diagram (Figure 5-17) for the employed experimental parameters can be constructed displaying quantitatively which conditions are favorable for the

growth of FLG dependent on the fraction of "available" carbon atoms ($x_C - x_O$) downstream of the plasma and the input C/O ratio used in the experiments. It needs to be stressed that the regime diagram is only valid for the experimental limit in which ethanol as reactant generates pure FLG (Case 1) and ethylene mixtures of different carbon particle types (Case 2).

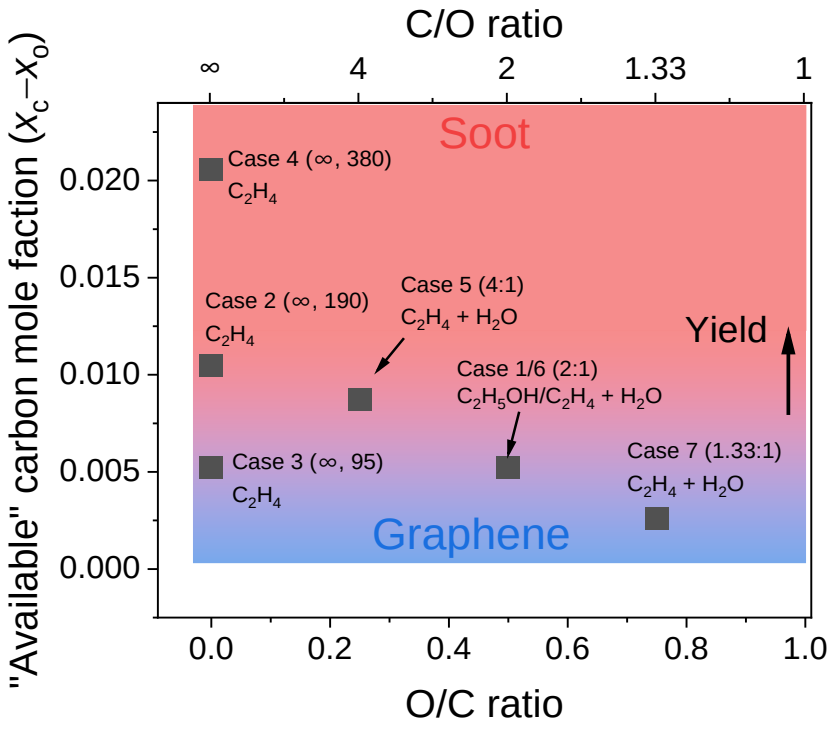

Figure 5-17: Regime diagram (inspired by the diagram of Xian Shi [175]) for the affinity of different experimental cases to form graphene (blue) and soot (red). It is displaying the mole fraction of carbon minus oxygen ($x_C - x_O$), the oxygen-to-carbon O/C input ratio at the bottom, and the carbon-to-oxygen C/O input ratio at the top. The "available" carbon fraction refers to the carbon species not consumed by CO formation and experiments with varying C_2H_4 concentrations contain information on their respective flowrate.

Looking at the generated regime plot shows that all experiments which reproduce the C/O ratio of ethanol should lead to graphene formation because the resulting elemental carbon fraction is in the same range. However, the experimental results for Case 6, when H_2O is added to C_2H_4 with a C/O ratio of 2:1, do not yield pure FLG materials. It is unclear whether kinetic effects play a role to explain this difference. Based on the simulation, which assumes homogeneous mixing, all the added water should be dissociated in the plasma region and no difference to Case 1 (C_2H_5OH) should be observed. This difference can imply that the given boundary conditions for the simulations are not valid and/or that there are more underlying processes which are not accounted for. One unknown is, e.g., whether there exists a significant coupling between the plasma and the reaction chemistry, because the simulation only looks at a purely thermal description of the process.

Another aspect that may play a role during the solid carbon formation is the reactivity of different oxygen species with carbon structures. This topic is traditionally studied more intensely in the context of soot oxidation. To describe soot oxidation, usually small PAH molecules are studied that describe the edge of a soot particle in terms of aromatic rings and then react with specific oxygen species for the determination of reaction kinetic constants. One example

where oxidation of a complete particle aerosol is modeled is the work by Frenklach et al. [76]. In this work the soot oxidation was modeled for low (1000 K) and high-temperature (2000 K) environments. A major result of this study was that the overall oxidation rate is limited by the concentration of atomic oxygen as reactant. The explanation for the important effect of atomic oxygen is that species such as OH and O_2 usually transform/oxidize a six-membered ring to a five-membered ring [74]. However, they are not able to attack a five-membered ring site efficiently and only atomic oxygen is reactive enough. Comparing the reaction rate of O_2 with a six-membered ring and O with a five-membered ring, shows that oxidation based on O is one order of magnitude faster in oxidizing the corresponding edge site. Hence, O should be able to selectively remove five-membered rings and prevent – as required for graphene formation – the out of plane growth, which can lead to the buildup of soot-like particles. Based on such consideration Leon et al. [77] generated a stability map that predicts the type of carbon nanomaterial grown in a flame (~1300 K) based on the type and concentration of different oxidizers (O_2 or O) present. Looking at the results, depending on the specific partial pressures of the respective oxidizer, FLG should be obtainable by such low-temperature flames if the partial pressures can realistically be supplied as most combinations are out of chemical equilibrium. The preferential transformation of six-membered rings to five-membered rings by O_2 has been experimentally observed by, e.g., Huang and coworkers in benzene diffusion flames [201]. They thermophoretically sampled soot nanoparticles in the flame at specific heights and compared their microstructure as a function of premixing benzene fuel with fractions of the diffusion flame oxidizer O_2. They observed that increased premixing ratios i.e., larger amounts of O_2 premixed with benzene, leads to soot particles with shorter and more curved graphitic fringes and linked it to the presence of more (curvature increasing) five-membered aromatic rings. For the presented experiments throughout this dissertation, all reactants are premixed prior to their decomposition, so similar effects with the observed oxygen species (OH, O) could occur as well.

In light of these remarks, however, it needs to be mentioned that the simulations predict the formation of CO already prior to the plasma meaning that all oxygen species should already be consumed at the beginning of the defined plasma region. The OES measurements are performed at a HAN distance of ~9 cm downstream of the resonator. No OES signals for OH or O are observed at the measurement position when hydrocarbon reactants are added to the experiments indicating that they are potentially already consumed by CO formation. However, CO could not be observed by OES in Sections 5 or 6, so the experimental proof for this specific result of the simulation is missing.

Still, the combination of experimental results with the applied inline and *in situ* methods allowed to generate a quantitative criterion for the input of reactants into the experiment to rationalize the growth of FLG in the used reactor system.

6 Effect of different oxygen carriers on graphene synthesis

6.1 Introduction

In the previous chapter, one of the main conclusions is that the C/O ratio in the reaction system mainly affects the concentration of 'available' carbon for growth as oxygen leads to the rapid formation of CO as the thermodynamically most stable species under the given high-temperature conditions. According to this analysis, the source of oxygen should not matter. Yet, some reports in literature suggest that this might not be true in all cases and beyond thermodynamic considerations, intermediate species also matter. For example, the formation of soot-like particles is observed even when high concentrations of CO_2 [202, 203] are added to the reactant mixture traveling into similar plasma reactors. Other authors also report that some reactants are more prone to the formation of soot-like particles even when they are supplied with the 'correct' concentration and C/O ratio. Fronczack and coworkers report the formation of soot-like particles when ethyl acetate is supplied while reactants with the same C/O ratio and similar concentrations (ethanol and butyric acid) only generate FLG [80].

To clarify the relevance of the chemical nature of the oxygen supplied, experiments are performed in which instead of water, different oxygen carriers are employed. Molecular oxygen (O_2, purity 4.8), nitrous oxide (N_2O, 5.0), and carbon dioxide (CO_2, 4.5) are used as oxygen sources to adjust various C/O ratios. Compared to the addition of water, the mixtures contain less hydrogen and do not fully reproduce the C/O/H ratio of C_2H_5OH. For the design of experiments, it is assumed that in O_2 and N_2O all oxygen atoms contribute to the reaction but CO_2 releases only one while the remaining CO is considered inert at the relevant peak gas-phase temperature of ~3700 K (it would require temperatures around 6000 K to dissociate 50 % of CO). Thus, the additional carbon and oxygen atom of CO_2 are neglected for calculating C/O ratios. The C/O ratio is varied from 4:1–1.33:1 for N_2O and O_2, for CO_2 only 2:1 and 1.33:1 is used. Table 6-1 summarizes the experimental cases.

Table 6-1: Oxygen-carrier type and volumetric flow rates.

Case	Oxygen carrier	Flow rate / sccm	Ar flow rate / slm	C/O ratio
8	None	0	5	∞
9–11	Oxygen (O_2)	47.5–142.5	5 – x	4:1–1.33:1
12–14	Nitrous oxide (N_2O)	95–285	5 – x	4:1–1.33:1
15–16	Carbon dioxide (CO_2)	190–285	5 – x	2:1–1.33:1

6.2 Reaction kinetics modeling and experimental comparison

To judge how the three considered reactants interact with C_2H_4, kinetics simulations are performed. The same temperature profile of the simulations in Section 5 is used as input and the resulting predicted species concentrations are analyzed. Because the FTIR apparatus was not available for these experiments, the simulated concentrations for the various gaseous species are compared to GC/MS measurements of the effluent gas composition performed by Jürgen

Herzler. Gas samples are taken during reactor operation by extracting gas samples into 3 l volume vacuum containers at a fixed position at ~0.8 m HAN (height above nozzle). Prior to sampling, the containers are purged with N_2 and evacuated multiple times. Then, the containers are filled with the gaseous sample up to approx. 800 mbar. Afterwards, the containers are transported, and the gas composition is measured with the GC/MS system. These measurements are performed for the reference Case 8 only using C_2H_4 and the cases employing C/O ratios of 1.33:1. Based on the simulations, no reactions should take place at temperatures below 1000 K (related to HAN ≈ 0.3 m), i.e., the species concentrations at the measurement locations are expected to have reached a stable state and therefore, the measurement results can be directly compared to the simulations. Figure 6-1 shows the temperature profile (top part) and examples for simulated (on the left ordinate), and GC/MS-measured concentrations (on the right ordinate) for Case 14 on two separate scales. The simulation results for the other experimental cases are shown in the Appendix Section 9.6.1.

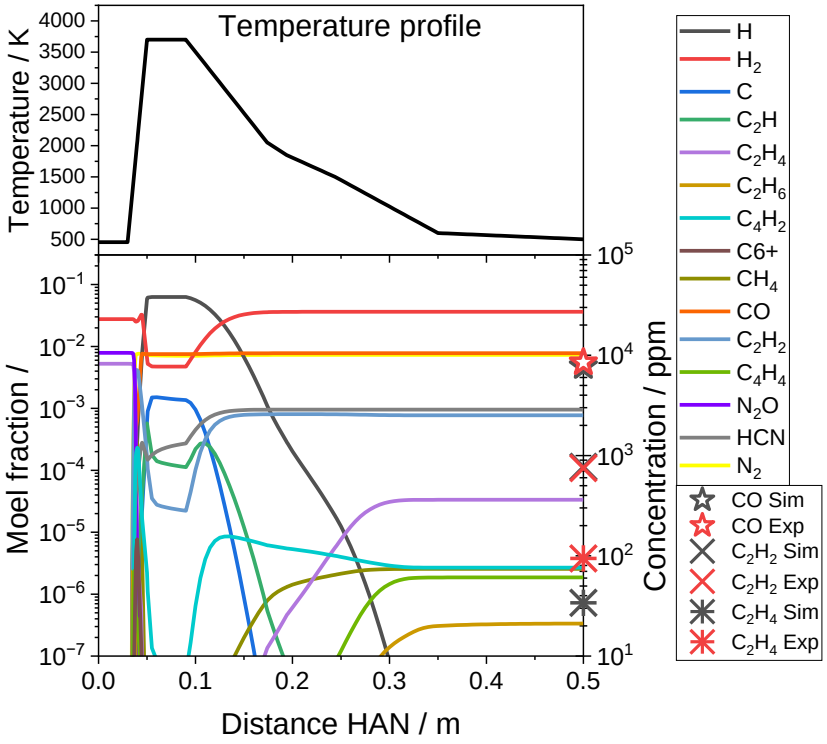

Figure 6-1: Temperature profile and kinetics simulation of the species formed in the reactor for Case 14 (C/O ratio of 1.33:1 with N_2O) as a function of height above the nozzle (HAN). The comparison between validation measurements by GC/MS in the reactor off-gas and the simulation is shown on the second ordinate on the right (axis uses a different scale).

Similar to the calculations in Section 5 – with the exception of Case 8 in which only C_2H_4 is employed – the formation of CO is predicted in all experimental cases with the concentration depending on the amount of oxygen carrier added. Comparing the measured and simulated gaseous species concentration for Case 14, they do partly agree. The C_2H_4 concentration is underpredicted significantly while both CO and C_2H_2 deviate within 25 % of their respective prediction. Figure 6-2 summarizes the comparison of the calculated (HAN = 0.5 m) and measured concentrations (HAN ≈ 0.8 m) for CO, C_2H_2, and C_2H_4. The exact numerical values for both the simulations and the measurements are shown in Table 9-1 of Section 9.6.3.

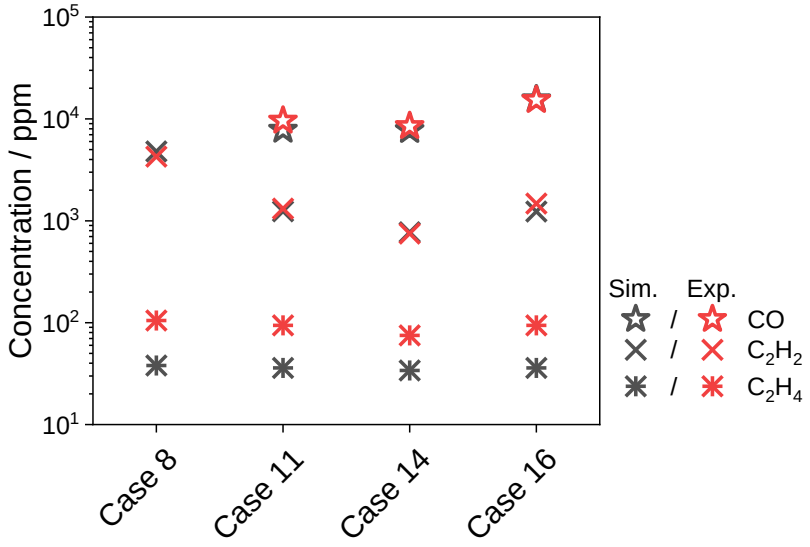

Figure 6-2: Comparison of measured and simulated concentrations of CO, C_2H_2, and C_2H_4 at the measurement position at HAN ≈ 0.8 m with a local temperature of T < 500 K.

It is found that for all Cases, the C_2H_4 concentrations are underpredicted by the simulation by a factor of 2–3. The C_2H_2 concentrations are well predicted (within 20 %) and similar results are observed for CO. For the addition of N_2O, all simulations predict the formation of HCN (Cases 12–14, shown in Section 9.6.1 or for Case 14 in Figure 6-1). HCN is also detected by GC/MS (Case 14) with concentrations similar to C_2H_2, but cannot be quantified because the GC signal for HCN is not calibrated. The differences in the predicted and assumed C_2H_4 concentration observed in Figure 6-2 are unlikely to originate from potentially undecomposed C_2H_4 introduced into the reactor for the experiments, because previous FTIR absorption measurements described in Sections 5 and 9.2 [175] show complete reactant decomposition at similar reactor conditions (microwave power, reactant flowrates, detection limit: ~1 ppm). Therefore, the difference is likely caused by inaccuracies in, e.g., the temperature profile or some of the other assumptions used for the simulation. Because the concentration of gaseous species in the reactor effluent strongly depends on the temperature decay, comparable results between simulation and experiment (C_2H_2 within 20 %, CO within 25 %) indicate that the assumptions are not completely accurate but decently describe the experimental conditions.

Figure 6-3 compares the simulated concentration of C6+ species in dependence of the different oxygen carriers. For comparison, the addition of H_2O investigated in Section 5 is also shown. In accordance to Section 5, the C6+ species concentration is thereby used as a marker on how many carbon particles are likely to be formed. Case 8 shows the largest amount of C6+ formed. When any oxygen carrier is added, the C6+ species concentrations decrease. For C/O ratios of 1.33:1, the concentrations decrease by almost two orders of magnitude compared to the oxygen-free case. Comparing the expected concentrations for the addition of H_2O with the other oxygen carriers reveals that all species show a similar decrease in C6+ species concentration and, hence, their ability to form solid carbon particles. As an outlier, the addition of N_2O is expected to reduce the concentration more, because it also forms HCN as a gaseous carbon sink next to CO.

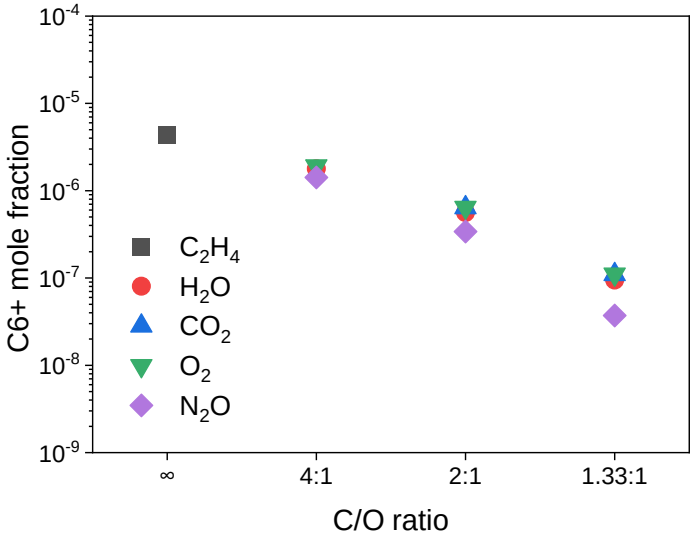

Figure 6-3: Mole fractions of C6+ species formed as extracted from kinetics simulations at 0.5 m HAN distance [204]. The mole fraction decreases for all experimental cases almost similarly, by the addition of oxygen carriers and lowering the C/O ratio. As a comparison to the previous section, the results for H_2O are also displayed.

In conclusion, the simulation results confirm the previous observation that the formation of CO can be linked to the C/O ratio with decreasing C/O ratios leading to a significant reduction of C6+ species. Therefore, all employed oxygen carriers should guide the carbon growth towards FLG with decreasing C/O ratios.

6.3 Experimental results: Powder analysis

The carbon nanomaterials collected from the reactor off-gas are analyzed with Raman spectroscopy. Figure 6-4 shows results of Raman spectroscopy from carbon materials synthesized at different C/O ratios and harvested from the fiber filter located at the end of the reactor. The Raman spectra for all experimental cases are displayed separately in Section 9.6.3. Case 8 represents the reference without any oxygen carrier added. Comparing Case 8 in which only C_2H_4 is employed to the previous one in Section 5 (Figure 5-1a, Case 2) reveals some changes in composition, because the relative intensity of the 2D band to the G band is larger (1.5 compared to 1.2). Such a change in the relative intensity suggests an FLG-richer particle mixture for Case 8 and potential reasons are discussed in Sections 7.1 and 9.4. Case 8 shows a shoulder at ~1250 cm^{-1} indicative of the presence of soot-like particles and a 2D band intensity, which is lower than the G band. Similar properties are also observed when small amounts (4:1 C/O input ratio) of oxygen carriers are added (Case 9 and Case 12). For Cases 11 and 14, when the amount of oxygen carrier is increased to a C/O ratio of 1.33:1, the relative 2D peak intensity increases while the shoulder of the D peak disappears. This may be associated to few-layer graphene samples with less impurities such as soot-like particles. The stacking order is based on the description of the 2D bands with a single Lorentzian line shape (FWHM of ~55 cm^{-1}, $A_{2D/G}$ ratio >1.8) – similar to Section 5 – considered to be turbostratic.

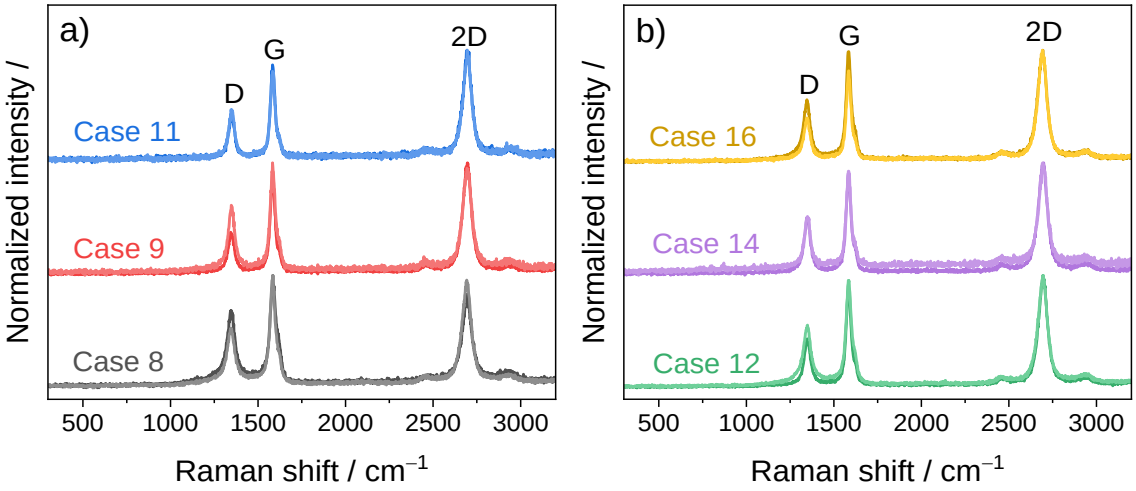

Figure 6-4: Raman spectra for selected samples in the 300–3200 cm^{-1} range [204].

The measured spectrum for Case 16 (CO_2, 1.33:1) also appears similar to the spectra for Case 11 and Case 14, i.e., it should only contain FLG particles. However, it is observed that the Raman spectra for some cases vary significantly between different measurement positions on the respective samples making it difficult to clearly characterize whether the corresponding sample possesses a mixture of allotropes or pure FLG. Thus, TEM images are required to confirm or refute the presence of non-FLG particles in the samples. Figure 6-5 shows illustrative TEM images of the same cases as shown in Figure 6-4 while more images are shown in Section 9.6.

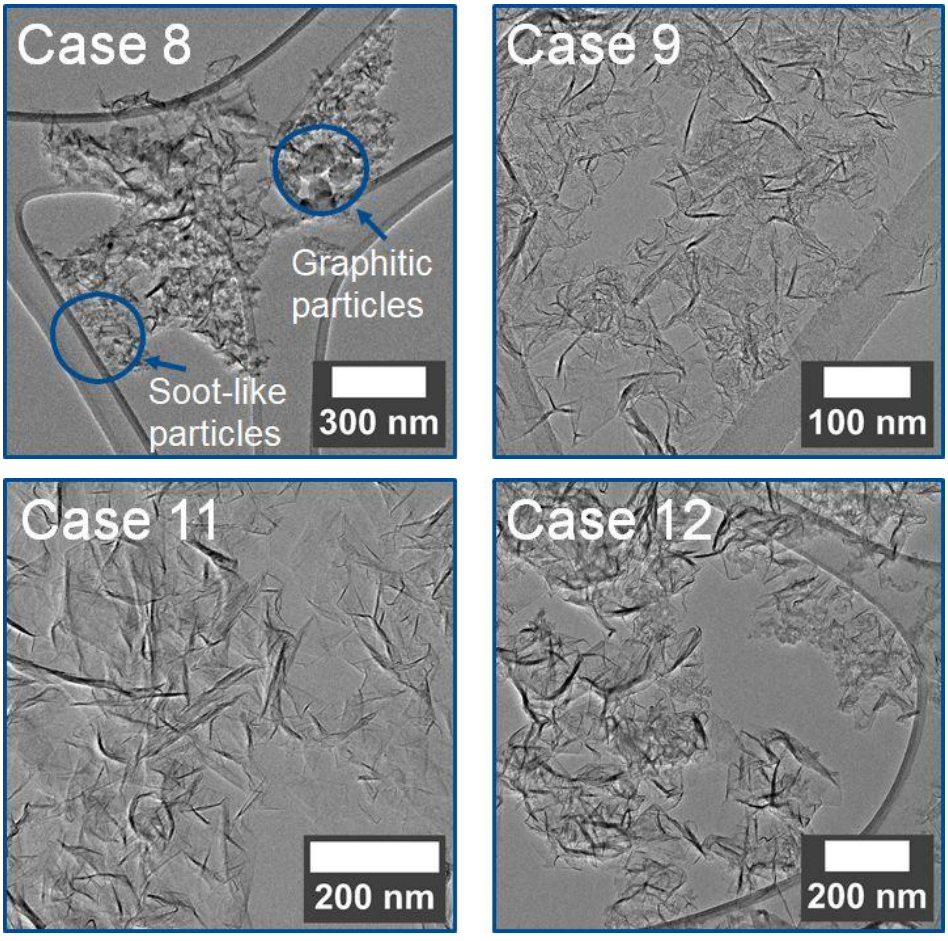

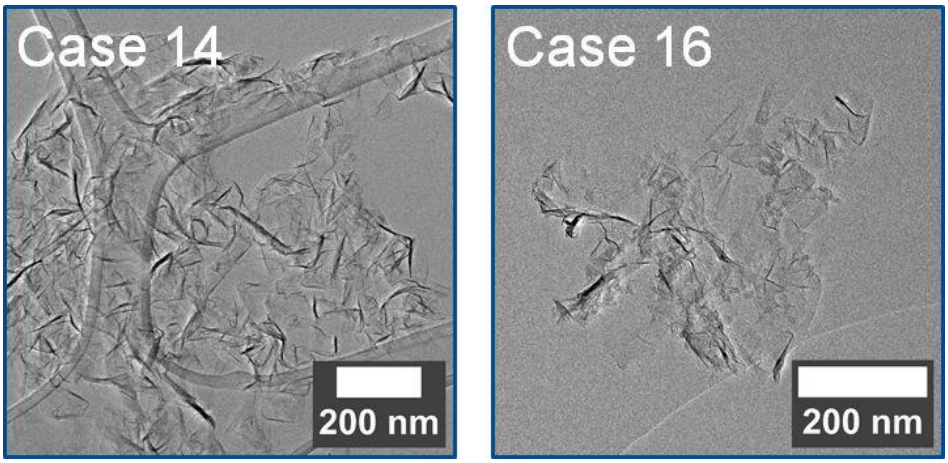

Figure 6-5: TEM images of on the filter collected powders [204]. By reactants: Pure ethylene (Case 1); addition of O_2 at C/O ratios of 4:1 and 1.33:1 (Cases 2 and 4); addition of N_2O at C/O ratios of 4:1 and 1.33:1 (Cases 5 and 7); addition of CO_2 at a C/O ratio of 2:1.

Depending on the oxygen carrier, different effects are observed. For O_2 (Case 9) and N_2O (Case 12), experiments with C/O ratios of 4:1 qualitatively lead to partial suppression of the formation of soot-like and graphitic particles. Only for the C/O ratio of 1.33:1 no formation of soot-like or graphitic particles is observed. Both observations match the visible changes in the Raman spectra. When employing CO_2 with the same C/O ratios, the formation of soot-like particles is not fully suppressed and they are present for both Case 15 and Case 16 (C/O ratios of 2:1 and 1.33:1, respectively). The yield of harvested carbon particles decreases from 6.6 wt.% (Case 8) to values between 1.1–1.8 wt.% for C/O ratios of 1.33:1, including the experiment with CO_2.

To investigate whether the *ex situ* observed differences in the grown carbon allotropes are already present in the near-plasma region, thermophoretic sampling for Case 8 and cases with a C/O ratio of 1.33:1 is performed. The reasoning for these experiments is that the carbon nanoparticles alter their morphology along the reactor axis [168] as discussed in Section 4 and therefore is of interest if the alteration depends on the nature and concentration of oxygen carriers. TEM images are shown in Figure 6-6 for a sampling height of HAN ≈ 15 cm.

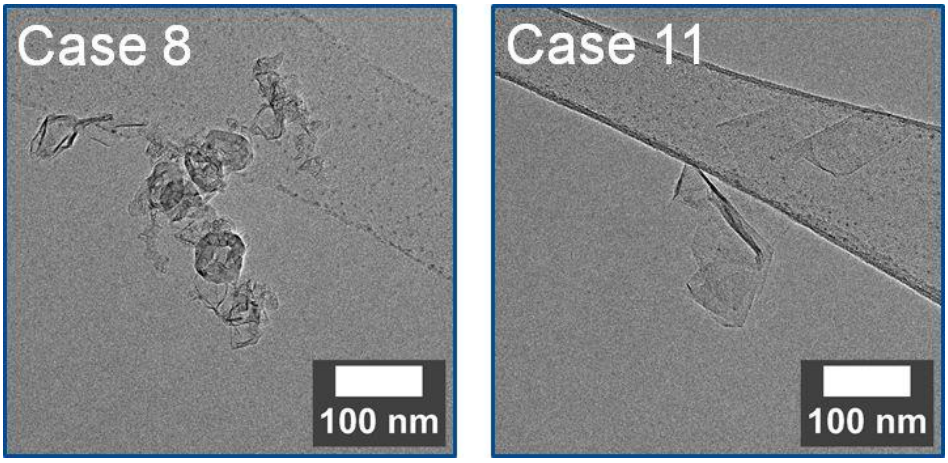

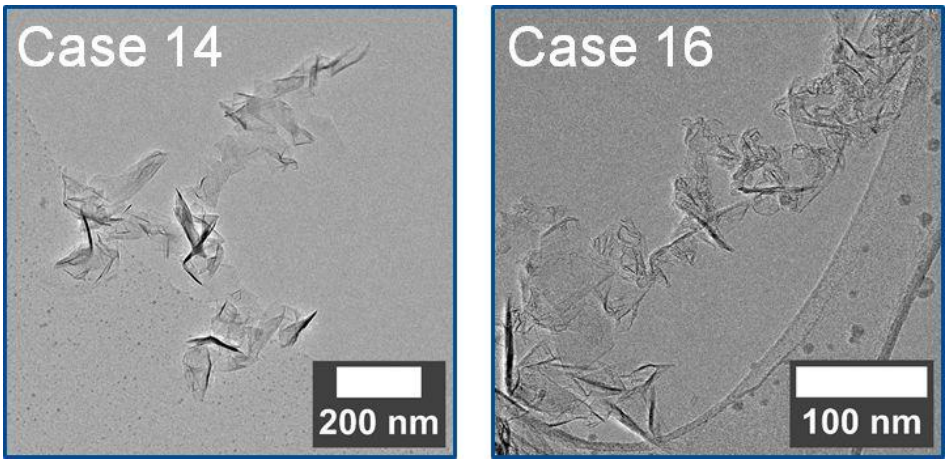

Figure 6-6: TEM images of thermophoretically sampled materials collected on TEM grids at HAN ≈ 15 cm [204].

Comparing the images in Figure 6-6 to the results from Figure 6-5 indicates that the growing carbon allotropes are already defined and present early in the near-plasma region. No qualitative difference is observed for the various oxygen carriers. Case 11 and Case 14 generate FLG, while Cases 8 and 16 also show the presence of soot-like and graphitic carbon particles.

For a more quantitative analysis, thermogravimetric measurements are used to estimate the amount of different carbon allotropes present in the powder samples which are harvested from the filter. Figure 6-7 shows exemplary the TG results for Case 8 and cases employing N_2O as oxygen carrier (Cases 12–14).

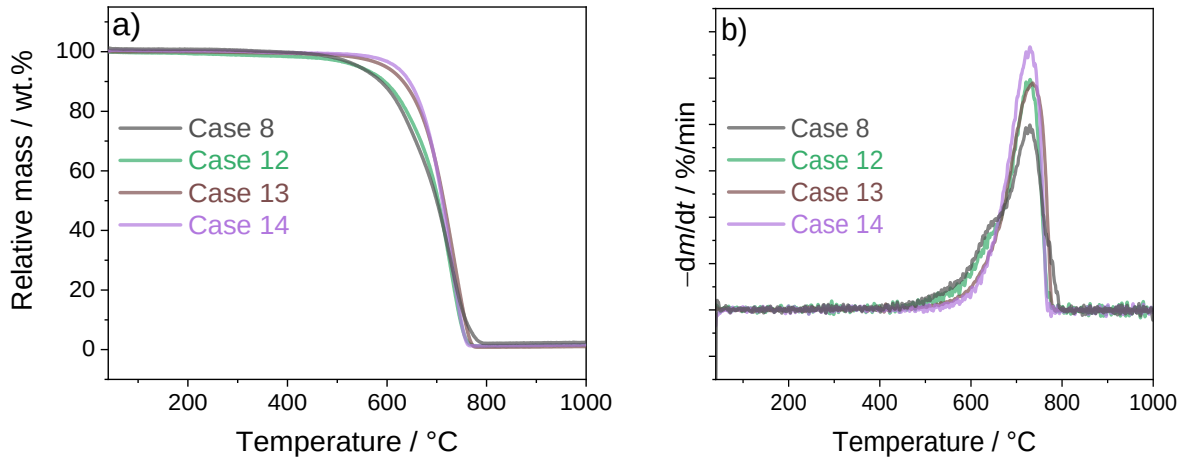

Figure 6-7: a) TG and b) DTG measurements from samples prepared from Cases 8 and 12–14.

When N_2O is added to C_2H_4, the onset of the mass loss (Figure 6-7a) shifts to slightly higher temperatures for decreasing C/O ratios. Taking into account the discussion in Section 5 and the reference measurements described in the Appendix 9.1, this is an indication that the samples prepared with lower C/o ratios possess a lower amount of soot-like particles as the peak of the low-temperature oxidizable carbon phase vanishes (Figure 6-7b). Because the samples with C/O ratios of 2:1 (for all oxygen carriers) are not distinguishable from the pure FLG samples anymore, the TG/QMS data are used to estimate the soot-like particle content. As discussed in Section 9.1, the QMS data is more sensitive to small fractions of particles than the

DTG plots. The result of this analysis is shown in Table 6-2. The measurements including the TG, DTG, and QMS data are shown for every case in the Appendix Section 9.6.5.

Table 6-2: Content of soot like particles in wt.% determined by thermogravimetric measurements.

Experiment	Oxygen carrier	C/O ratio	Soot particle fraction / wt.%	FLG fraction / wt.%
Case 8	–	∞	~25	~75
Case 9	O_2	4:1	~5–10	~90–95
Case 10	O_2	2:1	<5	>95
Case 11	O_2	1.33:1	~0	~100
Case 12	N_2O	4:1	~13	~87
Case 13	N_2O	2:1	~5	~95
Case 14	N_2O	1.33:1	~0	~100
Case 15	CO_2	2:1	~5	~95
Case 16	CO_2	1.33:1	<5	>95

Summarizing the results, decreasing C/O ratios lead to a smaller fraction (wt.%) of soot-like particles in the samples. For the addition of CO_2 (Cases 15 and 16), however, the formation of soot-like particles is not completely suppressed.

Because oxygen- and nitrogen-containing reactants are added into the reactor and intermediates such as CN are predicted to form, some of the respective atoms may end up bonded to the carbon lattice. Such results have been reported for the synthesis of, e.g., nitrogen-doped FLG in a similar process [205]. To analyze the chemical purity of the carbon particle samples with slightly below ~1 at.% sensitivity, XPS is used. Figure 6-8 shows XPS measurements for Case 1 and the cases prepared with the addition of C/O ratios 1.33:1 as they contain the most amount of oxygen carrier added into the reactant mixture.

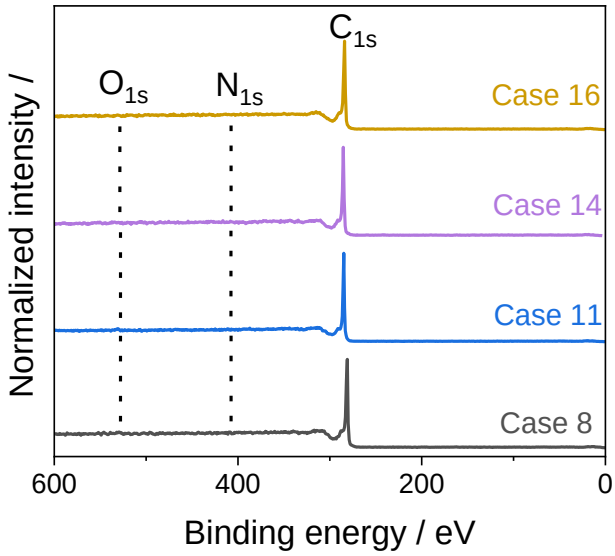

Figure 6-8: XPS measurements taken of samples which are prepared with C/O ratios of 1.33:1 (O_2: Case 11, N_2O: Case 14, CO_2: Case 16) and the reference Case 8 [204].

All samples mostly consist of carbon (≥99 at.%) as determined by integrating the atomic lines of the survey scan. Comparing the obtained oxygen content for the different samples, no observable difference is detected. For all cases, the oxygen content is below 1 at.% and slight differences are not considered to be significant. Furthermore, no nitrogen bonding (at ~400 eV) within the resolution limit of XPS is detected. Therefore, effects which may be caused by doping or heterogeneous reactions between the solid carbon phase and nitrogen-containing gaseous molecules can be neglected. However, it has to be mentioned that the probed area for the XPS measurements is similar to the Raman measurements which showed variations between different measurement positions. Therefore, the measurements have similar drawbacks and e.g., the independent determination of soot/FLG ratio by analyzing the C_{1s} carbon line becomes challenging (Section 9.6.6). Yet, fitting the high-resolution region with model line shapes of the C_{1s} spectra shows changes in the relative ratio of soot like particles to FLG matching the other experimental observations (Figure 9-26).

To summarize the powder analysis, the experimental results partly contradict the expected results from the reaction kinetics simulations. All oxygen carriers should suppress the formation of C6+ species and hence, of carbon particles other than FLG similarly well. Similar to Section 5, a decrease in yield of harvested carbon particles is observed for all cases when the C/O ratio decreases. Furthermore, the measured concentrations of the most abundant gas-phase species are comparable to the expected ones obtained from the gas kinetics simulations. However, for the case in which CO_2 is used as oxygen carrier, the formation of soot-like particles is not fully suppressed and differences in carbon particle composition can already be observed close to the plasma, i.e., immediately after particle inception as shown in Figure 6-6. Because the first formed carbon particles already show differences in composition, the region of particle inception needs to be probed as their have to be differences which promote soot-like particle growth when using CO_2. Therefore, OES is used to inquire whether significant differences in gas-phase temperature or generated molecular fragments can be observed when employing CO_2 compared to O_2 or N_2O as oxygen carrier.

6.4 Optical emission spectroscopy

Firstly, Figure 6-9 compares low-resolution scans of the emission spectra for the admixture of the different oxygen carriers but without the addition of ethylene. Compared to the pristine plasma containing Ar and H_2 only, the admixture of all investigated oxygen carriers leads (similarly to the addition of water in Section 5) to the formation of OH (~310 nm) and atomic oxygen (~777 and 833 nm). For experiments performed with N_2O, the formation of NH (~335 nm [196, 206]) is observed, which implies that N_2 generated by N_2O decomposition is partly dissociated. However, CO_2 additionally shows the formation of atomic carbon (~250 nm) and C_2 (~516 nm). The fact that CO_2 can fully dissociate and form pure carbon species has been reported and discussed for microwave plasmas above 100 mbar by, e.g. Carbone et al. and Miotk et al. [197, 207]. The simultaneous presence of carbon and oxygen species is surprising, because only the presence of (stable) CO molecules would be expected in the chemical equilibrium calculations at the assumed gas temperature of 3700 K. While for N_2O and O_2 addition the observed species match those predicted from chemical equilibrium calculations, for CO_2, the observed species imply the presence of a nonequilibrium formation processes.

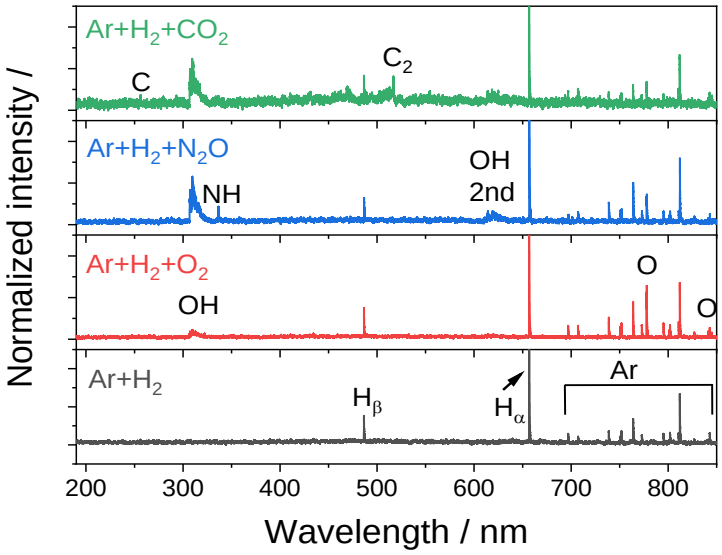

Figure 6-9: Comparison of measured OES spectra for the addition of the different oxygen carriers (O_2, N_2O, and CO_2) to the Ar + H_2 plasma [204].

The spectra obtained when C_2H_4 is added to the reactor are similar to the ones reported in Section 5. The emission lines generated from the different oxygen carriers (O, OH, NH) vanish and the spectra become dominated by the C_2 Swan band emission and several other hydrocarbon fragments. However, the addition of N_2O also leads to the detection of intense CN violet band lines (~380 nm [208]). Figure 6-10 compares the emission spectrum measured for Case 8 and Case 14.

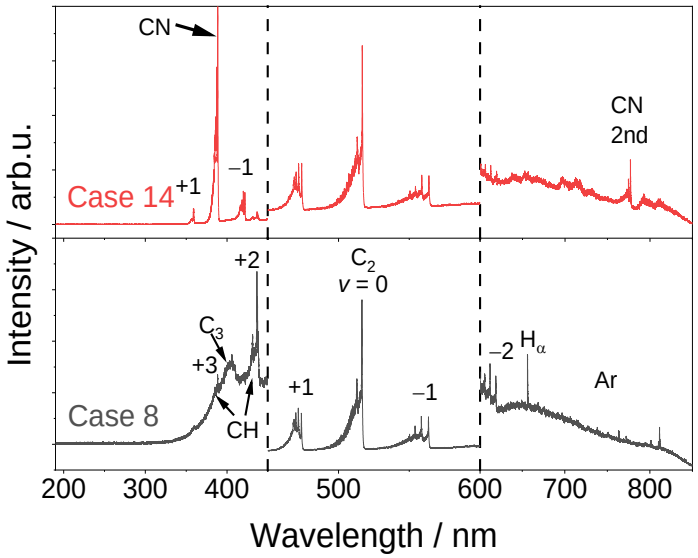

Figure 6-10: Comparison of OES spectra in the range of 190–520 nm obtained for Cases 8 and 14 For better visibility, the graphs are separated in three different regions [204].

Similar to the analysis presented in Section 5, the observed C_2 and OH (prior to the C_2H_4 addition) spectra are used to calculate (rotational) temperatures. For all experimental cases, at least four different spectra are recorded for the determination of temperature; three for C_2 and one for OH. When CO_2 is added into the reactant mixture, additional measurements are performed to record the C_2 emission observed prior to the addition of C_2H_4. For the C_2 emission lines, two spectra in the range of 510–520 nm and one in the range of 480–520 nm are recorded. Two different methods are applied to extract temperature values of the C_2 spectra. The Boltzmann-plot method is applied to all three measurements for the emission lines in the region of 510–520 nm. Additionally, the full recorded spectrum in the range of 480–520 nm is fitted with the PGOPHER software. For obtaining temperatures from the OH emission lines, only a single spectrum is recorded in the range of 300–320 nm and analyzed by the Boltzmann plot method.

Comparing the temperatures obtained from C_2 and OH for the different experimental cases – before and after the addition of C_2H_4 – similar values are observed. The temperature values are depicted in Figure 6-11 and are in the range of 3200–3900 K.

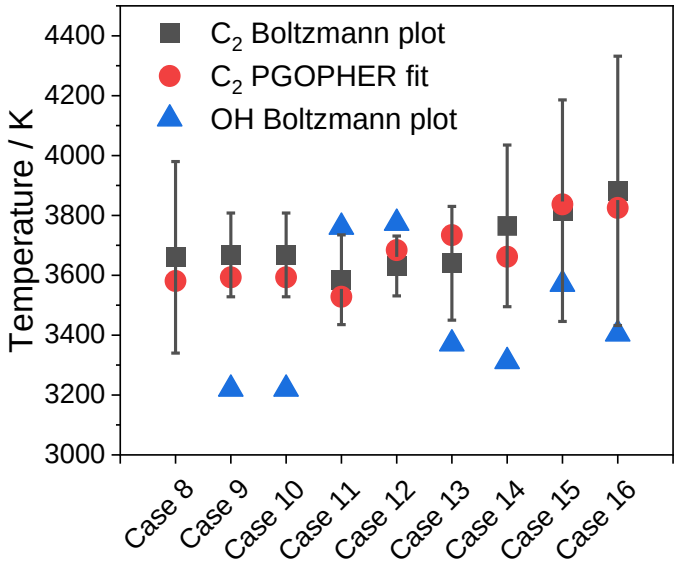

Figure 6-11: Comparison of temperature values calculated by either the Boltzmann-plot method or fits with PGOPHER for C_2 and OH emission spectra [204].

The resulting temperature values are similar to those presented in Section 5. The only exception from these temperature values is observed for Cases 15 and 16, employing CO_2 as oxygen carrier, by analyzing the C_2 emission present prior to C_2H_4 injection. For, e.g., Case 15 in Figure 6-12, the derived C_2 rotational temperature is ~6100 K while the OH temperature is in the expected range of ~3570 K (both are calculated with the Boltzmann plot method). Such a high value for the C_2 temperature would not be surprising in a thermal process as temperatures above 4000 K are required to thermally dissociate CO into atomic carbon and oxygen. But because this effect is exclusively observed for CO_2 addition it is more likely that the hot C_2* originates from chemiluminescence.

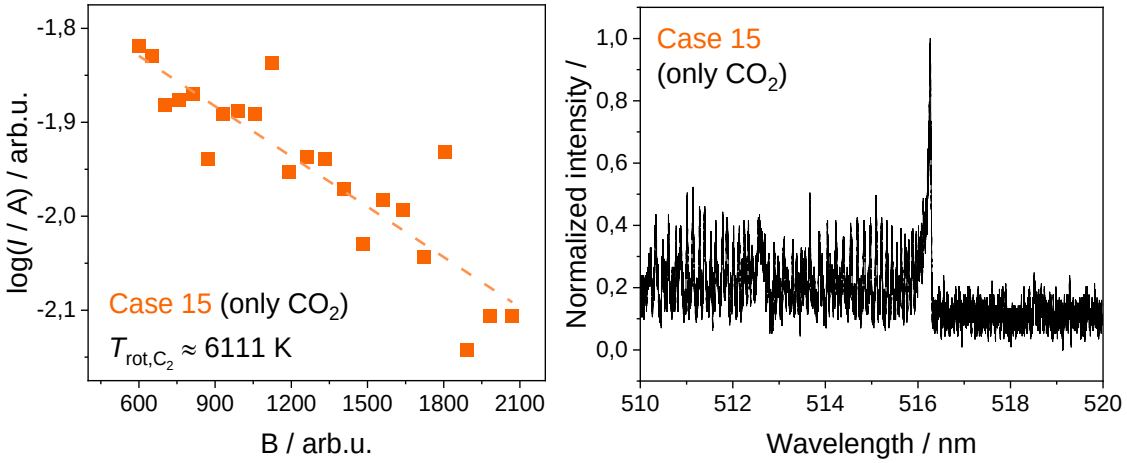

Figure 6-12: High-resolution scan of the C_2 region for Case 15 when only CO_2 is added, i.e., prior to C_2H_4 addition [204].

6.5 Summary

Summarizing the results and revisiting the discussion at the start of this section, one question based on the results described in Section 5 was whether the source for oxygen can play a role in the formation of carbon nanomaterials. Some results in literature suggest that there are

some extreme cases in which soot-like particles form although the supplied reactant concentration is in a regime (Figure 5-17), where pure FLG as product would be expected. Based on the model and the simulations, no impact was expected, because all reactant should, upon reaching the plasma, decompose into their atomic constitutes and reassemble into similar species (concentrations) downstream of the plasma. The experimental results refute this assumption by showing that although all tested oxygen carriers (O_2, N_2O, CO_2) reduce the amount of solid carbon harvested, CO_2 did not fully suppress the formation of soot-like particles at the same concentration of expected formed atomic oxygen. This difference is already observed in materials harvested by thermophoretically sampling close to the plasma effluent. It might imply that the formation of soot-like particles is directly linked to a localized effect. Comparison of the expected species concentrations to GC/MS measurements matching within 25 %. OES reveals that while all (decomposed) oxygen carriers generate OH and O species in the plasma, CO_2 apparently also leads to the formation of atomic carbon and C_2. Therefore, CO_2 not only needs to be considered as a source of net one oxygen atom, but also (locally) as a source for carbon. The unexpected release of additional carbon species by CO_2 might then be able to influence the first nucleation and growth of solid carbon species in a similar way to larger ethanol concentrations which also lead to soot-like particle formation [23, 83].

7 Summary

The thesis investigates the growth of carbon particles, focusing on FLG in a microwave plasma reactor by the means of *ex situ* material characterization, different *in situ* and inline analysis techniques, and gas-phase CHEMKIN simulations.

The questions which are formulated and addressed in this thesis are:

- How does the FLG structure formation happen and proceed in the employed experimental setup?
- What is the effect of oxygen on the selectivity of the synthesis to generate FLG?

The first question is addressed by employing thermophoretic sampling aided by laser based *in situ* diagnostics (performed by Stanislav Musikhin and Muhammad Asif) as discussed in Section 4. Studying the particle formation provides experimental proof on how the carbon particle growth for FLG likely proceeds within the plasma reactor and can be visualized with the sketch presented in Figure 7-1.

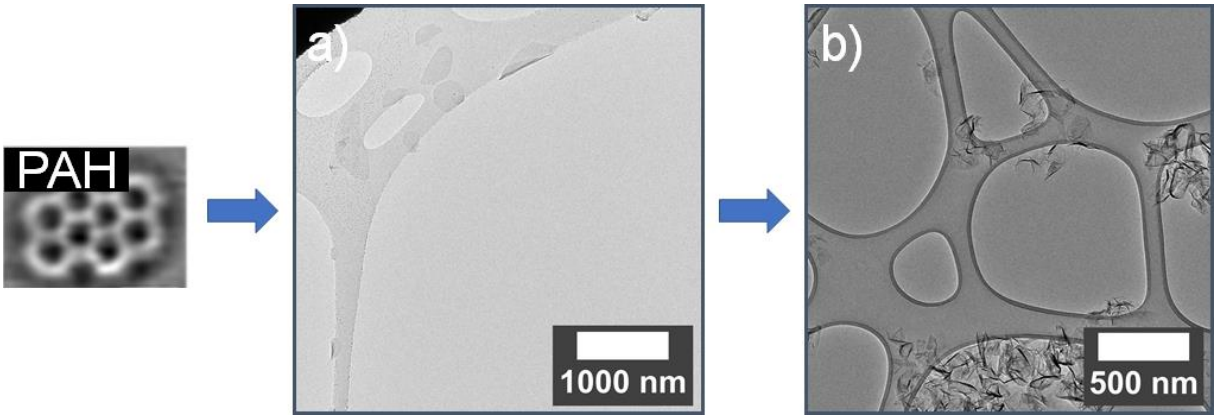

Figure 7-1: TEM images depicting the likely evolution of FLG particles during the growth process, starting from a PAH molecule (image taken from literature [57]). (a) Graphene particles showing mostly rounded shapes and starting to fold or crumple; (b) End result of crumpled FLG sheets.

At first, PAH molecules are formed and undergo heterogeneous growth at their edges towards larger rounded flakes. Later on, the flakes become unstable and start to fold/crumple into more dense structures (Figure 7-1a). It is possible that the folding occurs in a 'nice' way showing well-defined folds or arbitrary arrangements. The folding and crumpling of structures may be induced by several external effects, which can induce corrugations and reduce stability of the unfolded and uncrumpled flakes. At the same time, flakes can also continue their edge growth into the direction of the respective fold. It is also possible that some flakes start to agglomerate before reaching the filter. In all the cases, FLG flakes will finally agglomerate at the collection filter where they are harvested (Figure 7-1b).

The second question on how oxygen affects the growth of carbon particles is addressed in two parts (Sections 5 and 6) by synthesizing materials with specific variations of the experimental parameters. Literature results suggest that specific C/O ratios (2:1) in the input gas mixture can favor the formation of FLG. The effect of the C/O ratio is studied in Section 5 by using different reactants (ethanol and C_2H_4) and reactant mixtures (C_2H_4 admixed with different amounts of H_2O), it has been possible to form carbon particle mixtures which contain different amounts of distinguishable carbon allotropes (soot-like/graphitic particles and FLG). The

yield/amount of harvested carbon particles thereby correlates with the abundance of different carbon allotropes in the particle mixtures, i.e., syntheses with larger yields are richer in soot-like and graphitic particles while lower yields show FLG-rich mixtures. Estimations of the gas-phase temperatures in the plasma by OES do not show differences when different carbon particle mixtures are synthesized. FITR absorption measurements of the gas-phase composition in the effluent show that when H_2O is added to C_2H_4, increasing amounts of CO are formed while the concentration of hydrocarbon species (most abundantly C_2H_2) decreases. Reaction kinetics simulations which employ a generated temperature profile and are based on a reduced combustion mechanism are able to reproduce the observed trends in gas-phase composition. Because the temperatures are not varying between the different experiments and all reactants should be decomposed to the same degree before growing into carbon structures, the effect that FLG is formed when an input C/O ratio of 2:1 is used is most likely only related to the carbon concentration available for growth. Oxygen thereby depletes the concentrations of carbon species by CO formation and generates a chemical environment in which the growth of few PAH molecules into larger graphene sheets is favored.

Section 6 investigates the effect of C/O ratio on the selectivity of the syntheses further by evaluating whether the source of oxygen can have an impact on the obtained carbon particles. The motivation for this study is that some literature results suggest influences when specific reactants, e.g., CO_2 are used. For the investigation, H_2O is substituted by O_2, N_2O, or CO_2. Employing reaction kinetics simulations to predict the gas-phase composition in comparison to Section 5 and considering that the reactants are fully decomposed, no different influence on the particle growth is expected and all oxygen carriers should yield the same carbon particle product. The simulations are compared to GC/MS measurements of the off-gas and similarities in absolute concentrations are found. Yet when using *ex situ* characterization to analyze the obtained carbon particle mixtures, experiments show a different behavior as CO_2 leads to the formation of soot-like particles even when low C/O ratios (1.33:1) are used. N_2O and O_2 show similar results to H_2O in favoring the formation of FLG at a C/O ratio of 1.33:1, however, all reactants – including CO_2 – show decreasing yields of harvested particles when larger amounts are admixed. Thermophoretic sampling in the syntheses in which C/O ratios of 1.33:1 are employed. When using O_2 and N_2O as oxygen carrier only FLG is observed while utilization of CO_2 shows the presence of FLG mixed with other carbon particles. The results show that the specific difference in carbon particle mixture composition are already present close to the plasma after the first particle formation. OES measurements of the plasma on the different reactant mixtures prior to the introduction of C_2H_4 show that in case of using CO_2 also C_2 and atomic carbon as a decomposition product is formed. Because the absolute concentration of CO formed and a similar (to the other oxygen carriers) decrease in particle yield is observed, it is likely that carbon species formed by the CO_2 decomposition influence the first particle nucleation following the plasma and need to be accounted for when using CO_2 as oxygen carrier.

The results can be compiled into a short conceptual description of the carbon growth. Simple PAH molecules are formed. The conditions in which the PAH molecules form and continue to grow is given by the concentration of reactive species as supplied into the reactor by employing specific experimental parameters including C/O ratio and residence time. The requirement is to prevent the random attachment of PAH molecules to each other as it induces a formation path leading to soot-like particle formation. The PAH molecules grow into large monolayer

graphene sheets which then self-fold, crumple, and agglomerate into their final morphology when harvested from the particle filter

7.1 Outlook

Independent of the questions that have been addressed in this work, i.e., of the experimental conformation on how the growth of FLG particles proceeds and which conditions are favorable for their formation, little is known in detail about the growth of PAH molecules towards graphene. The gas-phase chemistry and observed concentrations and trends which are measured in the effluent can be well described as purely thermal processes by combustion mechanisms. Yet, when trying to implement a model to describe the carbon particle growth, the growth rates are significantly underpredicted and may indicate that some formation pathways are unaccounted for and/or the used assumptions might be lacking. One influencing factor is likely to be the use of mechanisms that do not fully represent the plasma reaction environment as these mechanisms do not contain reactions that involve electrons or ionized species. Studies focusing on the PAH growth in space (e.g., [209-211]) show altering discharge induced formation pathways, however, the conditions are hard to compare to present experiments. Indication that reactions of plasma chemistry may play a role comes from the observation that CO_2 likely dissociates towards C_2 via a nonequilibrium pathway, which would not be expected for the assumed temperature profile. Hence, one goal should be to investigate the plasma chemistry on a more detailed level by the means of more characterization techniques to determine the properties of the plasma itself and identify PAH hydrocarbon species fragments which are formed.

One approach in doing so might be to improve the accessibility for optical diagnostic methods which will be one major challenge which needs to be tackled. A way to improve the accessibility might be to switch to plasma systems which generate an extended plasma torch in the downstream region. In such case the temperature gradients leading to formation of the condensed phase are easier to reach. Figure 7-2 compares the current plasma system to a Muegge atmospheric plasma torch. As can be seen from the comparison, the currently employed version only possesses a very localized plasma torch that does not extend into the effluent (Figure 7-2a) and only the added thermocouple does indicate the hot gas flow. Contrary, Figure 7-2c shows the formation of a torch towards large HAN distances. When a reactant is added, the current plasma system leads to the formation of a hot particle flow downstream (Figure 7-2b). In case of the other plasma system in Figure 7-2d, the particle nucleation seems to happen at the boundary between the luminescent plasma torch and the surrounding colder gas. Thus, the particle and PAH formation zones may be accessed more easily.

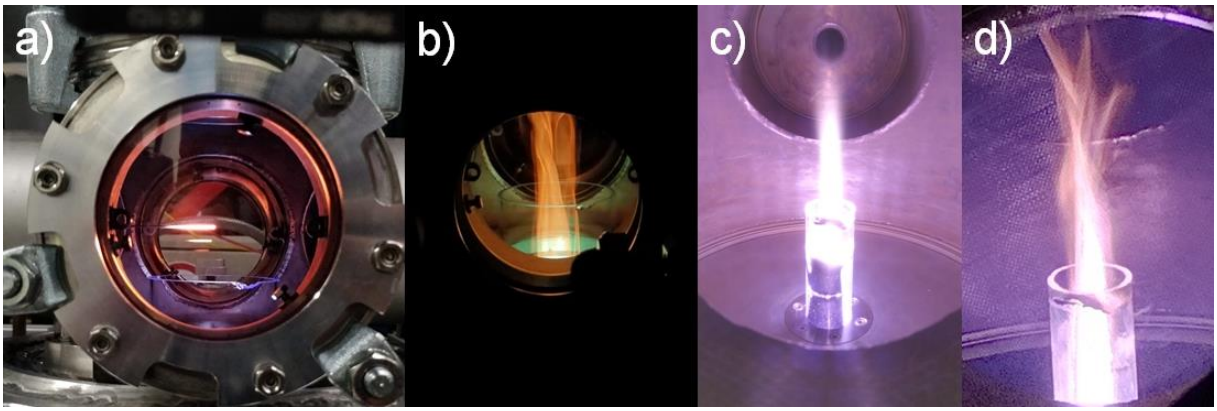

Figure 7-2: Comparison of the currently employed CYRANNUS plasma source (a, b) with a different one from Muegge (c, d). In both cases the operation of just the plasma is shown (a, c) and compared to the situation when a hydrocarbon reactant is added (b, d).

The materials sampling processes would also benefit from further improvement. Classically, sampling probes are added into the reaction zone to extract quenched gas or aerosol samples for further analysis. As an example, the images of molecules displayed in Figure 2-3 and data-points in Figure 2-4 are generated from samples which are extracted by a hole-in-a-tube nozzle from flames. In the current experimental setup, the reactions of interest happen very early, as the formation of monolayer graphene flakes is already observed at very low distances from the plasma zone. Therefore, the introduction of probes is partly hindered by the limited accessibility and the extreme conditions. A possible solution could be to purely rely on and improve the thermophoretic sampling process to analyze the simultaneously adsorbed molecular fragments. An example in which such an approach is used is the work of Apicella and coworkers [212]. They employ laser desorption time-of-flight mass spectrometry on materials harvested via thermophoretic sampling to analyze differently volatile carbon species formed.

8 References

[1] A. Bogaerts, E.C. Neyts, Plasma Technology: An Emerging Technology for Energy Storage, ACS Energy Letters, 3 (2018) 1013-1027.

[2] R. Zhou, Y. Zhao, R. Zhou, T. Zhang, P. Cullen, Y. Zheng, L. Dai, K. Ostrikov, Plasma-electrified up-carbonization for low-carbon clean energy, Carbon Energy, 5 (2023) e260.

[3] P.J. Bruggeman, M.J. Kushner, B.R. Locke, J.G.E. Gardeniers, W.G. Graham, D.B. Graves, R.C.H.M. Hofman-Caris, D. Maric, J.P. Reid, E. Ceriani, D. Fernandez Rivas, J.E. Foster, S.C. Garrick, Y. Gorbanev, S. Hamaguchi, F. Iza, H. Jablonowski, E. Klimova, J. Kolb, F. Krcma, P. Lukes, Z. Machala, I. Marinov, D. Mariotti, S. Mededovic Thagard, D. Minakata, E.C. Neyts, J. Pawlat, Z.L. Petrovic, R. Pflieger, S. Reuter, D.C. Schram, S. Schröter, M. Shiraiwa, B. Tarabová, P.A. Tsai, J.R.R. Verlet, T. von Woedtke, K.R. Wilson, K. Yasui, G. Zvereva, Plasma–liquid interactions: a review and roadmap, Plasma Sources Science and Technology, 25 (2016) 053002.

[4] D. Palma, C. Richard, M. Minella, State of the art and perspectives about non-thermal plasma applications for the removal of PFAS in water, Chemical Engineering Journal Advances, 10 (2022) 100253.

[5] M.J. Gallagher, A. Fridman, Chapter 8 - Plasma Reforming for H_2-Rich Synthesis Gas, in: D. Shekhawat, J.J. Spivey, D.A. Berry (Eds.) Fuel Cells: Technologies for Fuel Processing, Elsevier, Amsterdam, 2011, pp. 223-259.

[6] C.K. Kiefer, R. Antunes, A. Hecimovic, A. Meindl, U. Fantz, CO_2 dissociation using a lab-scale microwave plasma torch: An experimental study in view of industrial application, Chemical Engineering Journal, 481 (2024) 148326.

[7] I. Tsonev, C. O'Modhrain, A. Bogaerts, Y. Gorbanev, Nitrogen Fixation by an Arc Plasma at Elevated Pressure to Increase the Energy Efficiency and Production Rate of NOx, ACS Sustainable Chemistry & Engineering, 11 (2023) 1888-1897.

[8] P. Lamichhane, N. Pourali, E.V. Rebrov, V. Hessel, Energy Intensified Nitrogen Fixation Through Fast Modulated Gas Discharge from Pyramid-shaped Micro-electrode, Plasma Chemistry and Plasma Processing, (2023).

[9] E.C. Neyts, K. Ostrikov, M.K. Sunkara, A. Bogaerts, Plasma Catalysis: Synergistic Effects at the Nanoscale, Chemical Reviews, 115 (2015) 13408-13446.

[10] Z. Cui, S. Meng, Y. Yi, A. Jafarzadeh, S. Li, E.C. Neyts, Y. Hao, L. Li, X. Zhang, X. Wang, A. Bogaerts, Plasma-Catalytic Methanol Synthesis from CO_2 Hydrogenation over a Supported Cu Cluster Catalyst: Insights into the Reaction Mechanism, ACS Catalysis, 12 (2022) 1326-1337.

[11] U.R. Kortshagen, R.M. Sankaran, R.N. Pereira, S.L. Girshick, J.J. Wu, E.S. Aydil, Nonthermal Plasma Synthesis of Nanocrystals: Fundamental Principles, Materials, and Applications, Chemical Reviews, 116 (2016) 11061-11127.

[12] D.V. Szabó, S. Schlabach, Microwave Plasma Synthesis of Materials—From Physics and Chemistry to Nanoparticles: A Materials Scientist's Viewpoint, Inorganics 2(2014) 468-507.

[13] N. Sánchez-Bastardo, R. Schlögl, H. Ruland, Methane Pyrolysis for CO2-Free H2 Production: A Green Process to Overcome Renewable Energies Unsteadiness, Chemie Ingenieur Technik, 92 (2020) 1596-1609.

[14] S. Schneider, S. Bajohr, F. Graf, T. Kolb, State of the Art of Hydrogen Production via Pyrolysis of Natural Gas, ChemBioEng Reviews, 7 (2020) 150-158.

[15] J. Diab, L. Fulcheri, V. Hessel, V. Rohani, M. Frenklach, Why turquoise hydrogen will Be a game changer for the energy transition, International Journal of Hydrogen Energy, 47 (2022) 25831-25848.

[16] J.R. Fincke, R.P. Anderson, T.A. Hyde, B.A. Detering, Plasma Pyrolysis of Methane to Hydrogen and Carbon Black, Industrial & Engineering Chemistry Research, 41 (2002) 1425-1435.

[17] H. Okuno, E. Grivei, F. Fabry, T.M. Gruenberger, J. Gonzalez-Aguilar, A. Palnichenko, L. Fulcheri, N. Probst, J.-C. Charlier, Synthesis of carbon nanotubes and nano-necklaces by thermal plasma process, Carbon, 42 (2004) 2543-2549.

[18] O. Jašek, M. Eliáš, L. Zajíčková, V. Kudrle, M. Bublan, J. Matějková, A. Rek, J. Buršík, M. Kadlečíková, Carbon nanotubes synthesis in microwave plasma torch at atmospheric pressure, Materials Science and Engineering: C, 26 (2006) 1189-1193.

[19] K.S. Kim, A. Moradian, J. Mostaghimi, Y. Alinejad, A. Shahverdi, B. Simard, G. Soucy, Synthesis of single-walled carbon nanotubes by induction thermal plasma, Nano Research, 2 (2009) 800-817.

[20] A. Dato, V. Radmilovic, Z. Lee, J. Phillips, M. Frenklach, Substrate-Free Gas-Phase Synthesis of Graphene Sheets, Nano Letters, 8 (2008) 2012-2016.

[21] S. Musikhin, P. Fortugno, T. Endres, T. Dreier, K.J. Daun, C. Schulz, Elemental carbon and hydrogen concentrations as the main factors in gas-phase graphene synthesis: Quantitative fourier-transform infrared spectroscopy study, Carbon, 202 (2023) 47-60.

[22] N. Bundaleska, J. Henriques, M. Abrashev, A.M. Botelho do Rego, A.M. Ferraria, A. Almeida, F.M. Dias, E. Valcheva, B. Arnaudov, K.K. Upadhyay, M.F. Montemor, E. Tatarova, Large-scale synthesis of free-standing N-doped graphene using microwave plasma, Scientific Reports, 8 (2018) 12595.

[23] A. Casanova, R. Rincón, J. Muñoz, C.O. Ania, M.D. Calzada, Optimizing high-quality graphene nanoflakes production through organic (bio)-precursor plasma decomposition, Fuel Processing Technology, 212 (2021) 106630.

[24] M. Rahaman, R. Theravalappil, S. Bhandari, L. Nayak, P. Bhagabati, 4 - Electrical conductivity of polymer-graphene composites, in: M. Rahaman, L. Nayak, I.A. Hussein, N.C. Das (Eds.) Polymer Nanocomposites Containing Graphene, Woodhead Publishing 2022, pp. 107-139.

[25] Y. Fu, J. Hansson, Y. Liu, S. Chen, A. Zehri, M.K. Samani, N. Wang, Y. Ni, Y. Zhang, Z.-B. Zhang, Q. Wang, M. Li, H. Lu, M. Sledzinska, C.M.S. Torres, S. Volz, A.A. Balandin, X. Xu, J. Liu, Graphene related materials for thermal management, 2D Materials, 7 (2020) 012001.

[26] T. Wejrzanowski, M. Grybczuk, M. Chmielewski, K. Pietrzak, K.J. Kurzydlowski, A. Strojny-Nedza, Thermal conductivity of metal-graphene composites, Materials & Design, 99 (2016) 163-173.

[27] H. Zhang, J. Mischke, W. Mertin, G. Bacher, Graphene as a Transparent Conductive Electrode in GaN-Based LEDs, Materials, 15 (2022) 2203.

[28] E. Bertin, A. Münzer, S. Reichenberger, R. Streubel, T. Vinnay, H. Wiggers, C. Schulz, S. Barcikowski, G. Marzun, Durability study of platinum nanoparticles supported on gas-phase synthesized graphene in oxygen reduction reaction conditions, Applied Surface Science, 467-468 (2019) 1181-1186.

[29] M. Pahlevaninezhad, E.E. Miller, L. Yang, L.S. Prophet, A. Singh, T. Storwick, M. Pahlevani, M.A. Pope, E.P.L. Roberts, Exfoliated Graphene Composite Membrane for the All-Vanadium Redox Flow Battery, ACS Applied Energy Materials, 6 (2023) 6505-6517.

[30] A. Ali, F. Liang, J. Zhu, P.K. Shen, The role of graphene in rechargeable lithium batteries: Synthesis, functionalisation, and perspectives, Nano Materials Science, (2022).

[31] S.P. Surwade, S.N. Smirnov, I.V. Vlassiouk, R.R. Unocic, G.M. Veith, S. Dai, S.M. Mahurin, Water desalination using nanoporous single-layer graphene, Nature Nanotechnology, 10 (2015) 459-464.

[32] M.A. Zafar, Y. Liu, F.C.R. Hernandez, O.K. Varghese, M.V. Jacob, Plasma-Based Synthesis of Freestanding Graphene from a Natural Resource for Sensing Application, Advanced Materials Interfaces, 10 (2023) 2202399.

[33] M. Šiškins, M. Lee, D. Wehenkel, R. van Rijn, T.W. de Jong, J.R. Renshof, B.C. Hopman, W.S.J.M. Peters, D. Davidovikj, H.S.J. van der Zant, P.G. Steeneken, Sensitive capacitive pressure sensors based on graphene membrane arrays, Microsystems & Nanoengineering, 6 (2020) 102.

[34] K. Kohse-Höinghaus, Combustion in the future: The importance of chemistry, Proceedings of the Combustion Institute, 38 (2021) 1-56.

[35] A. Münzer, Untersuchungen zur Gasphasen-Synthese von Graphen, PhD Thesis, Department of Mechanical and Process Engineering, University of Duisburg-Essen, Duisburg ; Essen, 2020.

[36] A. Dato, M. Frenklach, Substrate-free microwave synthesis of graphene: experimental conditions and hydrocarbon precursors, New Journal of Physics, 12 (2010) 125013.

[37] M. Fronczak, P. Fazekas, Z. Károly, B. Hamankiewicz, M. Bystrzejewski, Continuous and catalyst free synthesis of graphene sheets in thermal plasma jet, Chemical Engineering Journal, 322 (2017) 385-396.

[38] I. Langmuir, Oscillations in Ionized Gases, Proceedings of the National Academy of Sciences, 14 (1928) 627-637.

[39] C. Tendero, C. Tixier, P. Tristant, J. Desmaison, P. Leprince, Atmospheric pressure plasmas: A review, Spectrochimica Acta Part B: Atomic Spectroscopy, 61 (2006) 2-30.

[40] J. Kopecki, Entwicklung und spektroskopische Untersuchung eines Mikrowellen-Plasmabrenners für die Schichtabscheidung aus Pulvern, PhD Thesis, Fakultät Mathematik und Physik, Universität Stuttgart2012.

[41] M. Jiménez, R. Rincón, A. Marinas, M.D. Calzada, Hydrogen production from ethanol decomposition by a microwave plasma: Influence of the plasma gas flow, International Journal of Hydrogen Energy, 38 (2013) 8708-8719.

[42] M. Snirer, J. Toman, V. Kudrle, O. Jašek, Stable filamentary structures in atmospheric pressure microwave plasma torch, Plasma Sources Science and Technology, 30 (2021) 095009.

[43] M. Snirer, V. Kudrle, J. Toman, O. Jašek, J. Jurmanová, Structure of microwave plasma-torch discharge during graphene synthesis from ethanol, Plasma Sources Science and Technology, 30 (2021) 065020.

[44] Y. Kabouzi, M.D. Calzada, M. Moisan, K.C. Tran, C. Trassy, Radial contraction of microwave-sustained plasma columns at atmospheric pressure, Journal of Applied Physics, 91 (2002) 1008-1019.

[45] F. Bakhtar, J.B. Young, A.J. White, D.A. Simpson, Classical Nucleation Theory and Its Application to Condensing Steam Flow Calculations, Proceedings of the Institution of Mechanical Engineers, Part C: Journal of Mechanical Engineering Science, 219 (2005) 1315-1333.

[46] H. Wang, M. Frenklach, A detailed kinetic modeling study of aromatics formation in laminar premixed acetylene and ethylene flames, Combustion and Flame, 110 (1997) 173-221.

[47] R.L. Vander Wal, A.J. Tomasek, Soot oxidation: dependence upon initial nanostructure, Combustion and Flame, 134 (2003) 1-9.

[48] T.A. Sipkens, A. Boies, J.C. Corbin, R.K. Chakrabarty, J. Olfert, S.N. Rogak, Overview of methods to characterize the mass, size, and morphology of soot, Journal of Aerosol Science, 173 (2023) 106211.

[49] G.A. Kelesidis, E. Goudeli, S.E. Pratsinis, Morphology and mobility diameter of carbonaceous aerosols during agglomeration and surface growth, Carbon, 121 (2017) 527-535.

[50] U. Trivanovic, T.A. Sipkens, M. Kazemimanesh, A. Baldelli, A.M. Jefferson, B.M. Conrad, M.R. Johnson, J.C. Corbin, J.S. Olfert, S.N. Rogak, Morphology and size of soot from gas flares as a function of fuel and water addition, Fuel, 279 (2020) 118478.

[51] A. Khabazipur, N. Eaves, Development of a Fully Reversible PAH Clustering Model, Proceedings of the Combustion Institute, 39 (2023) 919-927.

[52] N.A. Eaves, S.B. Dworkin, M.J. Thomson, The importance of reversibility in modeling soot nucleation and condensation processes, Proceedings of the Combustion Institute, 35 (2015) 1787-1794.

[53] K. Bowal, J.W. Martin, M. Kraft, Self-assembly of curved aromatic molecules in nanoparticles, Carbon, 182 (2021) 70-88.

[54] A. Menon, J.W. Martin, J. Akroyd, M. Kraft, Reactivity of Polycyclic Aromatic Hydrocarbon Soot Precursors: Kinetics and Equilibria, The Journal of Physical Chemistry A, 124 (2020) 10040-10052.

[55] M.R. Kholghy, N.A. Eaves, A. Veshkini, M.J. Thomson, The role of reactive PAH dimerization in reducing soot nucleation reversibility, Proceedings of the Combustion Institute, 37 (2019) 1003-1011.

[56] J.W. Martin, M. Salamanca, M. Kraft, Soot inception: Carbonaceous nanoparticle formation in flames, Progress in Energy and Combustion Science, 88 (2022) 100956.

[57] L.-A. Lieske, M. Commodo, J.W. Martin, K. Kaiser, V. Benekou, P. Minutolo, A. D'Anna, L. Gross, Portraits of Soot Molecules Reveal Pathways to Large Aromatics, Five-/Seven-Membered Rings, and Inception through π-Radical Localization, ACS Nano, 17 (2023) 13563-13574.

[58] J.W. Martin, R.I. Slavchov, E.K.Y. Yapp, J. Akroyd, S. Mosbach, M. Kraft, The Polarization of Polycyclic Aromatic Hydrocarbons Curved by Pentagon Incorporation: The Role of the Flexoelectric Dipole, The Journal of Physical Chemistry C, 121 (2017) 27154-27163.

[59] J.W. Martin, D. Hou, A. Menon, L. Pascazio, J. Akroyd, X. You, M. Kraft, Reactivity of Polycyclic Aromatic Hydrocarbon Soot Precursors: Implications of Localized π-Radicals on Rim-Based Pentagonal Rings, The Journal of Physical Chemistry C, 123 (2019) 26673-26682.

[60] T. Kirschbaum, F. Rominger, M. Mastalerz, A Chiral Polycyclic Aromatic Hydrocarbon Monkey Saddle, Angewandte Chemie International Edition, 59 (2020) 270-274.

[61] K. Kawasumi, Q. Zhang, Y. Segawa, L.T. Scott, K. Itami, A grossly warped nanographene and the consequences of multiple odd-membered-ring defects, Nature Chemistry, 5 (2013) 739-744.

[62] K.J. Putman, M.R. Rowles, N.A. Marks, C. de Tomas, J.W. Martin, I. Suarez-Martinez, Defining graphenic crystallites in disordered carbon: Moving beyond the platelet model, Carbon, 209 (2023) 117965.

[63] A. Sharma, K.M. Mukut, S.P. Roy, E. Goudeli, The coalescence of incipient soot clusters, Carbon, 180 (2021) 215-225.

[64] M. Commodo, K. Kaiser, G. De Falco, P. Minutolo, F. Schulz, A. D'Anna, L. Gross, On the early stages of soot formation: Molecular structure elucidation by high-resolution atomic force microscopy, Combustion and Flame, 205 (2019) 154-164.

[65] R. Whitesides, M. Frenklach, Detailed Kinetic Monte Carlo Simulations of Graphene-Edge Growth, The Journal of Physical Chemistry A, 114 (2010) 689-703.

[66] L.B. Tuli, A.M. Mebel, M. Frenklach, Bay capping via acetylene addition to polycyclic aromatic hydrocarbons: Mechanism and kinetics, Proceedings of the Combustion Institute, 39 (2023) 969-977.

[67] G. Leon, A. Menon, L. Pascazio, E.J. Bringley, J. Akroyd, M. Kraft, Kinetic Monte Carlo statistics of curvature integration by HACA growth and bay closure reactions for PAH growth in a counterflow diffusion flame, Proceedings of the Combustion Institute, 38 (2020) 1449-1457.

[68] A.S. Semenikhin, A.S. Savchenkova, I.V. Chechet, S.G. Matveev, M. Frenklach, A.M. Mebel, Transformation of an Embedded Five-Membered Ring in Polycyclic Aromatic Hydrocarbons via the Hydrogen-Abstraction–Acetylene-Addition Mechanism: A Theoretical Study, The Journal of Physical Chemistry A, 125 (2021) 3341-3354.

[69] A.D. Abid, N. Heinz, E.D. Tolmachoff, D.J. Phares, C.S. Campbell, H. Wang, On evolution of particle size distribution functions of incipient soot in premixed ethylene–oxygen–argon flames, Combustion and Flame, 154 (2008) 775-788.

[70] H. Böhm, D. Hesse, H. Jander, B. Lüers, J. Pietscher, H.G.G. Wagner, M. Weiss, The influence of pressure and temperature on soot formation in premixed flames, Symposium (International) on Combustion, 22 (1989) 403-411.

[71] S. Dasappa, J. Camacho, Deposition of graphenic nanomaterials from elevated temperature premixed stagnation flames, Applications in Energy and Combustion Science, 15 (2023) 100178.

[72] J. Bonpua, Y. Yagües, A. Aleshin, S. Dasappa, J. Camacho, Flame temperature effect on sp^2 bonds on nascent carbon nanoparticles formed in premixed flames ($T_{f,max}$ > 2100 K): A Raman spectroscopy and particle mobility sizing study, Proceedings of the Combustion Institute, 37 (2019) 943-951.

[73] S. Dasappa, J. Camacho, Evolution in size and structural order for incipient soot formed at flame temperatures greater than 2100 K, Fuel, 291 (2021) 120196.

[74] R.I. Singh, A.M. Mebel, M. Frenklach, Oxidation of Graphene-Edge Six- and Five-Member Rings by Molecular Oxygen, The Journal of Physical Chemistry A, 119 (2015) 7528-7547.

[75] R. Singh, M. Frenklach, A mechanistic study of the influence of graphene curvature on the rate of high-temperature oxidation by molecular oxygen, Carbon, 101 (2016) 203-212.

[76] M. Frenklach, Z. Liu, R.I. Singh, G.R. Galimova, V.N. Azyazov, A.M. Mebel, Detailed, sterically-resolved modeling of soot oxidation: Role of O atoms, interplay with particle nanostructure, and emergence of inner particle burning, Combustion and Flame, 188 (2018) 284-306.

[77] G. Leon, J.W. Martin, E.J. Bringley, J. Akroyd, M. Kraft, The role of oxygenated species in the growth of graphene, fullerenes and carbonaceous particles, Carbon, 182 (2021) 203-213.

[78] N. Arjun, P.S. Gajendra, N.F. Bret, C.M. Sorensen, One-step synthesis of graphene via catalyst-free gas-phase hydrocarbon detonation, Nanotechnology, 24 (2013) 245602.

[79] J.P. Wright, S. Sigdel, S. Corkill, J. Covarrubias, L. LeBan, A. Nepal, J. Li, R. Divigalpitiya, S.H. Bossmann, C.M. Sorensen, Synthesis of turbostratic nanoscale graphene via chamber detonation of oxygen/acetylene mixtures, Nano Select, 3 (2022) 1054-1068.

[80] M. Fronczak, A.M. Keszler, M. Mohai, B. Jezsó, A. Farkas, Z. Károly, Facile and continuous synthesis of graphene nanoflakes in RF thermal plasma, Carbon, 193 (2022) 51-67.

[81] R.R. Kumal, A. Gharpure, V. Viswanathan, A. Mantri, G. Skoptsov, R. Vander Wal, Microwave Plasma Formation of Nanographene and Graphitic Carbon Black, C, 6 (2020) 70.

[82] A. Wu, H. Chen, J. Zheng, J. Yang, X. Li, C. Du, Z. Chen, A. Xu, J. Qiu, Y. Xu, J. Yan, Conversion of coalbed methane surrogate into hydrogen and graphene sheets using rotating gliding arc plasma, Plasma Science and Technology, 21 (2019) 115501.

[83] P. Fortugno, Untersuchungen zur Herstellung von Graphen in einem Mikrowellen-Plasmareaktor, MSc Thesis, Department of Mechanical and Process Engineering, University of Duisburg-Essen, Duisburg ; Essen, 2018.

[84] T. Aissou, F. Casteignau, N. Braidy, J. Veilleux, Synthesis and Growth of Onion-Like Polyhedral Graphitic Nanocapsules by Thermal Plasma, Plasma Chemistry and Plasma Processing, 43 (2023) 413-427.

[85] C. Wang, Z. Lu, J. Ma, X. Chen, C. Yang, W. Xia, Pressure-dependent synthesis of graphene nanoflakes using $Ar/H_2/CH_4$ non-thermal plasma based on rotating arc discharge, Diamond and Related Materials, 111 (2021) 108176.

[86] R. Pristavita, J.-L. Meunier, D. Berk, Carbon Nano-Flakes Produced by an Inductively Coupled Thermal Plasma System for Catalyst Applications, Plasma Chemistry and Plasma Processing, 31 (2011) 393-403.

[87] E. Tatarova, J. Henriques, C.C. Luhrs, A. Dias, J. Phillips, M.V. Abrashev, C.M. Ferreira, Microwave plasma based single step method for free standing graphene synthesis at atmospheric conditions, Applied Physics Letters, 103 (2013) 134101.

[88] J. Toman, O. Jasek, M. Snirer, V. Kudrle, J. Jurmanova, On the interplay between plasma discharge instability and formation of free-standing graphene nanosheets in a dual-channel microwave plasma torch at atmospheric pressure, Journal of Physics D: Applied Physics, 52 (2019) 265205.

[89] C. Wang, M. Song, X. Chen, D. Li, W. Xia, Synthesis of few-layer graphene flakes by magnetically rotating arc plasma: effects of input power and feedstock injection position, Applied Physics A, 126 (2020) 210.

[90] J. Toman, O. Jašek, M. Šnírer, D. Pavliňák, Z. Navrátil, J. Jurmanová, S. Chudják, F. Krčma, V. Kudrle, J. Michalička, On the transition of reaction pathway during microwave plasma gas-phase synthesis of graphene nanosheets: From amorphous to highly crystalline structure, Plasma Processes and Polymers, 18 (2021) 2100008.

[91] R. Rincón, C. Melero, M. Jiménez, M.D. Calzada, Synthesis of multi-layer graphene and multi-wall carbon nanotubes from direct decomposition of ethanol by microwave plasma without using metal catalysts, Plasma Sources Science and Technology, 24 (2015) 032005.

[92] M.B. Shavelkina, E. Filimonova, R.H. Amirov, Effect of helium/propane-butane atmosphere on the synthesis of graphene in plasma jet system, Plasma Sources Science and Technology, 29 (2019) 025024.

[93] Z. Lu, D. Li, C. Wang, X. Chen, W. Xia, Effects of hydrogen/carbon molar ratio on graphene nano-flakes synthesis by a non-thermal plasma process, Diamond and Related Materials, 108 (2020) 107932.

[94] X. Chen, C. Wang, M. Song, J. Ma, T. Ye, W. Xia, The morphological transformation of carbon materials from nanospheres to graphene nanoflakes by thermal plasma, Carbon, 155 (2019) 521-530.

[95] M. Singh, A. Sengupta, K. Zeller, G. Skoptsov, R.L. Vander Wal, Effect of hydrogen concentration on graphene synthesis using microwave-driven plasma-mediated methane cracking, Carbon, 143 (2019) 802-813.

[96] F. Casteignau, T. Aissou, C. Allard, C. Ricolleau, J. Veilleux, R. Martel, N. Braidy, Synthesis of Carbon Nanohorns by Inductively Coupled Plasma, Plasma Chemistry and Plasma Processing, 42 (2022) 465-481.

[97] P.J. Larkin, Infrared and Raman spectroscopy: principles and spectral interpretation, Second edition. ed., Elsevier, Amsterdam, Netherlands, 2018.

[98] Jorio, Raman Spectroscopy in Graphene Related Systems, 1 ed., John Wiley & Sons, Inc 2011.

[99] J.-B. Wu, M.-L. Lin, X. Cong, H.-N. Liu, P.-H. Tan, Raman spectroscopy of graphene-based materials and its applications in related devices, Chemical Society Reviews, 47 (2018) 1822-1873.

[100] R. Beams, L. Gustavo Cançado, L. Novotny, Raman characterization of defects and dopants in graphene, Journal of Physics: Condensed Matter, 27 (2015) 083002.

[101] L.M. Malard, M.A. Pimenta, G. Dresselhaus, M.S. Dresselhaus, Raman spectroscopy in graphene, Physics Reports, 473 (2009) 51-87.

[102] L. Gustavo Cançado, M. Gomes da Silva, E.H. Martins Ferreira, F. Hof, K. Kampioti, K. Huang, A. Pénicaud, C. Alberto Achete, R.B. Capaz, A. Jorio, Disentangling contributions of point and line defects in the Raman spectra of graphene-related materials, 2D Materials, 4 (2017) 025039.

[103] J. Ribeiro-Soares, M.E. Oliveros, C. Garin, M.V. David, L.G.P. Martins, C.A. Almeida, E.H. Martins-Ferreira, K. Takai, T. Enoki, R. Magalhães-Paniago, A. Malachias, A. Jorio, B.S. Archanjo, C.A. Achete, L.G. Cançado, Structural analysis of polycrystalline graphene systems by Raman spectroscopy, Carbon, 95 (2015) 646-652.

[104] A.C. Ferrari, J.C. Meyer, V. Scardaci, C. Casiraghi, M. Lazzeri, F. Mauri, S. Piscanec, D. Jiang, K.S. Novoselov, S. Roth, A.K. Geim, Raman Spectrum of Graphene and Graphene Layers, Physical Review Letters, 97 (2006) 187401.

[105] J.E. Lee, G. Ahn, J. Shim, Y.S. Lee, S. Ryu, Optical separation of mechanical strain from charge doping in graphene, Nature Communications, 3 (2012) 1024.

[106] K. Kim, S. Coh, L.Z. Tan, W. Regan, J.M. Yuk, E. Chatterjee, M.F. Crommie, M.L. Cohen, S.G. Louie, A. Zettl, Raman Spectroscopy Study of Rotated Double-Layer Graphene:

Misorientation-Angle Dependence of Electronic Structure, Physical Review Letters, 108 (2012) 246103.

[107] J.-S. Hwang, Y.-H. Lin, J.-Y. Hwang, R. Chang, S. Chattopadhyay, C.-J. Chen, P. Chen, H.-P. Chiang, T.-R. Tsai, L.-C. Chen, K.-H. Chen, Imaging layer number and stacking order through formulating Raman fingerprints obtained from hexagonal single crystals of few layer graphene, Nanotechnology, 24 (2013) 015702.

[108] D.R. Lenski, M.S. Fuhrer, Raman and optical characterization of multilayer turbostratic graphene grown via chemical vapor deposition, Journal of Applied Physics, 110 (2011) 013720.

[109] C. Cong, T. Yu, Evolution of Raman *G* and *G'* (2*D*) modes in folded graphene layers, Physical Review B, 89 (2014) 235430.

[110] J.A. Garlow, L.K. Barrett, L. Wu, K. Kisslinger, Y. Zhu, J.F. Pulecio, Large-Area Growth of Turbostratic Graphene on Ni(111) via Physical Vapor Deposition, Scientific Reports, 6 (2016) 19804.

[111] R. Rao, R. Podila, R. Tsuchikawa, J. Katoch, D. Tishler, A.M. Rao, M. Ishigami, Effects of Layer Stacking on the Combination Raman Modes in Graphene, ACS Nano, 5 (2011) 1594-1599.

[112] C. Cong, T. Yu, R. Saito, G.F. Dresselhaus, M.S. Dresselhaus, Second-Order Overtone and Combination Raman Modes of Graphene Layers in the Range of 1690−2150 cm^{-1}, ACS Nano, 5 (2011) 1600-1605.

[113] C. Casiraghi, A. Hartschuh, H. Qian, S. Piscanec, C. Georgi, A. Fasoli, K.S. Novoselov, D.M. Basko, A.C. Ferrari, Raman Spectroscopy of Graphene Edges, Nano Letters, 9 (2009) 1433-1441.

[114] B. Krauss, P. Nemes-Incze, V. Skakalova, L.P. Biro, K.v. Klitzing, J.H. Smet, Raman Scattering at Pure Graphene Zigzag Edges, Nano Letters, 10 (2010) 4544-4548.

[115] E. Picheau, A. Impellizzeri, D. Rybkovskiy, M. Bayle, J.-Y. Mevellec, F. Hof, H. Saadaoui, L. Noé, A.C. Torres Dias, J.-L. Duvail, M. Monthioux, B. Humbert, P. Puech, C.P. Ewels, A. Pénicaud, Intense Raman D Band without Disorder in Flattened Carbon Nanotubes, ACS Nano, 15 (2021) 596-603.

[116] A.K. Gupta, C. Nisoli, P.E. Lammert, V.H. Crespi, P.C. Eklund, Curvature-induced D-band Raman scattering in folded graphene, Journal of Physics: Condensed Matter, 22 (2010) 334205.

[117] P. Parent, C. Laffon, I. Marhaba, D. Ferry, T.Z. Regier, I.K. Ortega, B. Chazallon, Y. Carpentier, C. Focsa, Nanoscale characterization of aircraft soot: A high-resolution transmission electron microscopy, Raman spectroscopy, X-ray photoelectron and near-edge X-ray absorption spectroscopy study, Carbon, 101 (2016) 86-100.

[118] A.C. Ferrari, J. Robertson, Interpretation of Raman spectra of disordered and amorphous carbon, Physical Review B, 61 (2000) 14095-14107.

[119] A. Sadezky, H. Muckenhuber, H. Grothe, R. Niessner, U. Pöschl, Raman microspectroscopy of soot and related carbonaceous materials: Spectral analysis and structural information, Carbon, 43 (2005) 1731-1742.

[120] F. Herziger, R. Mirzayev, E. Poliani, J. Maultzsch, In-situ Raman study of laser-induced graphene oxidation, physica status solidi (b), 252 (2015) 2451-2455.

[121] Y. Leng, Transmission Electron Microscopy, Materials Characterization 2008, pp. 79-119.

[122] R. Brydson, Aberration-corrected analytical transmission electron microscopy, 1st ed., Wiley, Hoboken, 2011.

[123] S.D. Berger, D.R. McKenzie, P.J. Martin, EELS analysis of vacuum arc-deposited diamond-like films, Philosophical Magazine Letters, 57 (1988) 285-290.

[124] P.K. Chu, L. Li, Characterization of amorphous and nanocrystalline carbon films, Materials Chemistry and Physics, 96 (2006) 253-277.

[125] P.G. Laye, S.B. Warrington, G. Thermal Methods, G.R. Heal, D.M. Price, R. Wilson, Principles of Thermal Analysis and Calorimetry, The Royal Society of Chemistry2002.

[126] Gabbott, Principles and Applications of Thermal Analysis, 1 ed., John Wiley & Sons, Inc 2008.

[127] E. Picheau, S. Amar, A. Derré, A. Pénicaud, F. Hof, An Introduction to the Combustion of Carbon Materials, Chemistry – A European Journal, 28 (2022) e202200117.

[128] F. Hagen, F. Hardock, S. Koch, N. Sebbar, H. Bockhorn, A. Loukou, H. Kubach, R. Suntz, D. Trimis, T. Koch, Why Soot is not Alike Soot: A Molecular/Nanostructural Approach to Low Temperature Soot Oxidation, Flow, Turbulence and Combustion, 106 (2021) 295-329.

[129] R. Niessner, The Many Faces of Soot: Characterization of Soot Nanoparticles Produced by Engines, Angewandte Chemie International Edition, 53 (2014) 12366-12379.

[130] D.S. Su, R.E. Jentoft, J.O. Müller, D. Rothe, E. Jacob, C.D. Simpson, Ž. Tomović, K. Müllen, A. Messerer, U. Pöschl, R. Niessner, R. Schlögl, Microstructure and oxidation behaviour of Euro IV diesel engine soot: a comparative study with synthetic model soot substances, Catalysis Today, 90 (2004) 127-132.

[131] C. Russo, A. Ciajolo, S. Cimino, V. La Matta, A. La Rocca, B. Apicella, Reactivity of soot emitted from different hydrocarbon fuels: Effect of nanostructure on oxidation kinetics, Fuel Processing Technology, 236 (2022) 107401.

[132] F. Farivar, P. Lay Yap, R.U. Karunagaran, D. Losic, Thermogravimetric Analysis (TGA) of Graphene Materials: Effect of Particle Size of Graphene, Graphene Oxide and Graphite on Thermal Parameters, C, 7 (2021) 41.

[133] F. Farivar, P.L. Yap, K. Hassan, T.T. Tung, D.N.H. Tran, A.J. Pollard, D. Losic, Unlocking thermogravimetric analysis (TGA) in the fight against “Fake graphene” materials, Carbon, 179 (2021) 505-513.

[134] P.L. Yap, F. Farivar, Å.K. Jämting, V.A. Coleman, S. Gnaniah, E. Mansfield, C. Pu, S.M. Landi, M.V. David, E. Flahaut, M. Aizane, M. Barnes, M. Gallerneault, M.D. Locatelli, S. Jacquinot, C.G. Slough, J. Menzel, S. Schmölzer, L. Ren, A.J. Pollard, D. Losic, International Interlaboratory Comparison of Thermogravimetric Analysis of Graphene-Related Two-Dimensional Materials, Analytical Chemistry, 95 (2023) 5176-5186.

[135] J. Toman, M. Šnírer, R. Rincón, O. Jašek, D. Všianský, A.M. Raya, F.J. Morales-Calero, J. Muñoz, M.D. Calzada, On the gas-phase graphene nanosheet synthesis in atmospheric microwave plasma torch: Upscaling potential and graphene nanosheet-copper nanocomposite oxidation resistance, Fuel Processing Technology, 239 (2023) 107534.

[136] J.U. Keller, R. Staudt, Gas Adsorption Equilibria: Experimental Methods and Adsorption Isotherms, 1. Aufl. ed., Springer Science + Business Media 2005.

[137] F. Schüth, K.S.W. Sing, J. Weitkamp, Handbook of Porous Solids, 1 ed., John Wiley & Sons, Inc 2008.

[138] M. Thommes, K. Kaneko, A.V. Neimark, J.P. Olivier, F. Rodriguez-Reinoso, J. Rouquerol, K.S.W. Sing, Physisorption of gases, with special reference to the evaluation of surface area and pore size distribution (IUPAC Technical Report), 87 (2015) 1051-1069.

[139] S. Brunauer, P.H. Emmett, E. Teller, Adsorption of Gases in Multimolecular Layers, Journal of the American Chemical Society, 60 (1938) 309-319.

[140] Y. Leng, Electron Spectroscopy for Surface Analysis, Materials Characterization 2013, pp. 221-251.

[141] P. Van der Heide, X-ray photoelectron spectroscopy: an introduction to principles and practices, Wiley-Blackwell, Hoboken N.J, 2012.

[142] H. Estrade-Szwarckopf, XPS photoemission in carbonaceous materials: A “defect” peak beside the graphitic asymmetric peak, Carbon, 42 (2004) 1713-1721.

[143] D.J. Morgan, Comments on the XPS Analysis of Carbon Materials, C, 7 (2021) 51.

[144] B.P. Reed, S. Marchesini, G. Chemello, D.J. Morgan, N. Vyas, T. Howe, J. Radnik, C.A. Clifford, A.J. Pollard, The influence of sample preparation on XPS quantification of oxygen-functionalised graphene nanoplatelets, Carbon, 211 (2023) 118054.

[145] N. Fairley, V. Fernandez, M. Richard-Plouet, C. Guillot-Deudon, J. Walton, E. Smith, D. Flahaut, M. Greiner, M. Biesinger, S. Tougaard, D. Morgan, J. Baltrusaitis, Systematic and collaborative approach to problem solving using X-ray photoelectron spectroscopy, Applied Surface Science Advances, 5 (2021) 100112.

[146] G. Herzberg, K.-P. Huber, Molecular spectra and molecular structure. 1. Spectra of diatomic molecules / by Gerhard Herzberg, 2. ed. ed., Van Nostrand Reinhold, New York [u.a], 1950.

[147] R.K. Hanson, R.M. Spearrin, C.S. Goldenstein, Spectroscopy and Optical Diagnostics for Gases, 1st 2016 ed., Springer International Publishing, Cham, 2016.

[148] P.F. Bernath, Spectra of atoms and molecules, 2. ed., Oxford Univ. Press, Oxford [u.a, 2005.

[149] R.K. Hanson, R.M. Spearrin, C.S. Goldenstein, Electronic Spectra of Atoms, in: R.K. Hanson, R.M. Spearrin, C.S. Goldenstein (Eds.) Spectroscopy and Optical Diagnostics for Gases, Springer International Publishing, Cham, 2016, pp. 149-159.

[150] S.S. Harilal, B.E. Brumfield, N.L. LaHaye, K.C. Hartig, M.C. Phillips, Optical spectroscopy of laser-produced plasmas for standoff isotopic analysis, Applied Physics Reviews, 5 (2018) 021301.

[151] R.K. Hanson, R.M. Spearrin, C.S. Goldenstein, Spectral Lineshapes, in: R.K. Hanson, R.M. Spearrin, C.S. Goldenstein (Eds.) Spectroscopy and Optical Diagnostics for Gases, Springer International Publishing, Cham, 2016, pp. 131-148.

[152] I.H. Hutchinson, Electromagnetic radiation from bound electrons, Principles of plasma diagnostics, Cambridge Univ. Press, Cambridge [u.a], 2005, pp. 217-272.

[153] C.O. Laux, T.G. Spence, C.H. Kruger, R.N. Zare, Optical diagnostics of atmospheric pressure air plasmas, Plasma Sources Science and Technology, 12 (2003) 125.

[154] C.M. Western, PGOPHER: A program for simulating rotational, vibrational and electronic spectra, Journal of Quantitative Spectroscopy and Radiative Transfer, 186 (2017) 221-242.

[155] C. Western, https://pgopher.chm.bris.ac.uk/index.html, 2022.

[156] Y. Leng, Vibrational Spectroscopy for Molecular Analysis, Materials Characterization 2013, pp. 283-332.

[157] J.H. Seinfeld, S.N. Pandis, Atmospheric chemistry and physics: from air pollution to climate change, 2. ed., Wiley, Hoboken, NJ, 2006.

[158] A. Wiedensohler, An approximation of the bipolar charge distribution for particles in the submicron size range, Journal of Aerosol Science, 19 (1988) 387-389.

[159] A.B. Murphy, Transport Coefficients of Hydrogen and Argon–Hydrogen Plasmas, Plasma Chemistry and Plasma Processing, 20 (2000) 279-297.

[160] S. Yu, J. Wang, G. Xia, L. Zong, Thermophoretic force on nonspherical particles in the free-molecule regime, Physical Review E, 97 (2018) 053106.

[161] S.K. Friedlander, Smoke, dust, and haze: fundamentals of aerosol dynamics, 2. ed., Oxford Univ. Press, New York [u.a], 2000.

[162] E. Bayer, Einleitung, in: E. Bayer (Ed.) Gas-Chromatographie, Springer Berlin Heidelberg, Berlin, Heidelberg, 1962, pp. 1-8.

[163] G. Wiegleb, Separationsverfahren, in: G. Wiegleb (Ed.) Gasmesstechnik in Theorie und Praxis: Messgeräte, Sensoren, Anwendungen, Springer Fachmedien Wiesbaden, Wiesbaden, 2016, pp. 279-327.

[164] R.J. Kee, E. Coltrin Michael, P. Glarborg, Chemically reacting flow: theory and practice, Wiley-Interscience, New York, 2003.

[165] H. Wang, X. You, A.V. Joshi, S.G. Davis, A. Laskin, F. Egolfopoulos, C.K. Law, USC mech version II: High-temperature combustion reaction model of H_2/CO/C1-C4 Compounds, https://ignis.usc.edu:80/Mechanisms/USC-Mech%20II/USC_Mech%20II.htm, (2007).

[166] G. Bagheri, E. Ranzi, M. Pelucchi, A. Parente, A. Frassoldati, T. Faravelli, Comprehensive kinetic study of combustion technologies for low environmental impact: MILD and OXY-fuel combustion of methane, Combustion and Flame, 212 (2020) 142-155.

[167] G.P. Smith, D.M. Golden, M. Frenklach, N.W. Moriarty, B. Eiteneer, M. Goldenberg, C.T. Bowman, R.K. Hanson, S. Song, W. Gardiner Jr, V.V. Lissianski, Z. Qin, GRI-Mech 3.0, URL: http://www.me.berkeley.edu/gri_mech/.

[168] C.-F. López-Cámara, P. Fortugno, M. Asif, S. Musikhin, C. Prindler, H. Wiggers, T. Endres, N. Eaves, K.J. Daun, C. Schulz, Evolution of particle size and morphology in plasma synthesis of few-layer graphene and soot, Combustion and Flame, 258 (2023) 112713.

[169] V. Hopfe, R. Spitzl, I. Dani, G. Maeder, L. Roch, D. Rogler, B. Leupolt, B. Schoeneich, Remote Microwave PECVD for Continuous, Wide-Area Coating Under Atmospheric Pressure, Chemical Vapor Deposition, 11 (2005) 497-509.

[170] N. Petermann, T. Schneider, J. Stötzel, N. Stein, C. Weise, I. Wlokas, G. Schierning, H. Wiggers, Microwave plasma synthesis of Si/Ge and Si/WSi2 nanoparticles for thermoelectric applications, Journal of Physics D: Applied Physics, 48 (2015) 314010.

[171] A. Münzer, L. Xiao, Y.H. Sehlleier, C. Schulz, H. Wiggers, All gas-phase synthesis of graphene: Characterization and its utilization for silicon-based lithium-ion batteries, Electrochimica Acta, 272 (2018) 52-59.

[172] I. Belov, V. Vermeiren, S. Paulussen, A. Bogaerts, Carbon dioxide dissociation in a microwave plasma reactor operating in a wide pressure range and different gas inlet configurations, Journal of CO2 Utilization, 24 (2018) 386-397.

[173] J. Engemann, M. Walter, Modelling of microwave plasma sources: potential and applications, Plasma Physics and Controlled Fusion, 41 (1999) B259.

[174] F. Kunze, S. Kuns, M. Spree, T. Hülser, C. Schulz, H. Wiggers, S.M. Schnurre, Synthesis of silicon nanoparticles in a pilot-plant-scale microwave plasma reactor: Impact of flow rates and precursor concentration on the nanoparticle size and aggregation, Powder Technology, 342 (2019) 880-886.

[175] P. Fortugno, S. Musikhin, X. Shi, H. Wang, H. Wiggers, C. Schulz, Synthesis of freestanding few-layer graphene in microwave plasma: The role of oxygen, Carbon, 186 (2022) 560-573.

[176] S. Suleiman, M. Nanjaiah, I. Skenderovic, T. Rosenberger, F. Kunze, I. Wlokas, F.E. Kruis, H. Wiggers, C. Schulz, Atmospheric-pressure particle mass spectrometer for investigating particle growth in spray flames, Journal of Aerosol Science, 158 (2021) 105827.

[177] S. Kuns, Synthesis of Silicon Nanoparticles in a Microwave Plasma Reactor at Pilot Scale, MSc Thesis, Department of Mechanical and Process Engineering and Institute of Energy and Environmental Technology e.V., University of Duisburg-Essen, Duisburg ; Essen, 2017.

[178] S. Deng, V. Berry, Wrinkled, rippled and crumpled graphene: an overview of formation mechanism, electronic properties, and applications, Materials Today, 19 (2016) 197-212.

[179] S. Ahmad, K. Mustonen, B. McLean, H. Jiang, Q. Zhang, A. Hussain, A.T. Khan, E.-X. Ding, Y. Liao, N. Wei, M.R.A. Monazam, A.G. Nasibulin, J. Kotakoski, A.J. Page, E.I. Kauppinen, Hybrid Low-Dimensional Carbon Allotropes Formed in Gas Phase, Advanced Functional Materials, 30 (2020) 2005016.

[180] Y. Liao, Z. Li, L. Chen, A.B. Croll, W. Xia, Crumpling Defective Graphene Sheets, Nano Letters, 23 (2023) 3637-3644.

[181] T.A. Sipkens, J. Menser, T. Dreier, C. Schulz, G.J. Smallwood, K.J. Daun, Laser-induced incandescence for non-soot nanoparticles: recent trends and current challenges, Applied Physics B, 128 (2022) 72.

[182] T.B. Limbu, J.C. Hernández, F. Mendoza, R.K. Katiyar, J.J. Razink, V.I. Makarov, B.R. Weiner, G. Morell, A Novel Approach to the Layer-Number-Controlled and Grain-Size-Controlled Growth of High Quality Graphene for Nanoelectronics, ACS Applied Nano Materials, 1 (2018) 1502-1512.

[183] J.C. Meyer, A.K. Geim, M.I. Katsnelson, K.S. Novoselov, T.J. Booth, S. Roth, The structure of suspended graphene sheets, Nature, 446 (2007) 60-63.

[184] C.-F. López-Cámara, P. Fortugno, M. Heidelmann, H. Wiggers, C. Schulz, Graphene self-folding: Evolution of free-standing few-layer graphene in plasma synthesis, Carbon, 218 (2024) 118732.

[185] A. Kramida, Y. Rachelko, J. Reader, NIST ASD Team, NIST Atomic Spectra Database (version 5.10), National Institute of Standards and Technology, Gaithersburg, MD2022.

[186] V. Milosavljević, M. Donegan, P.J. Cullen, D.P. Dowling, Diagnostics of an O_2–He RF Atmospheric Plasma Discharge by Spectral Emission, Journal of the Physical Society of Japan, 83 (2013) 014501.

[187] C.-K. Chen, J. Phillips, Impact of aerosol particles on the structure of an atmospheric pressure microwave plasma afterglow, Journal of Physics D: Applied Physics, 35 (2002) 998-1009.

[188] G.H. Dieke, H.M. Crosswhite, The ultraviolet bands of OH Fundamental data, Journal of Quantitative Spectroscopy and Radiative Transfer, 2 (1962) 97-199.

[189] J.S.A. Brooke, P.F. Bernath, T.W. Schmidt, G.B. Bacskay, Line strengths and updated molecular constants for the C_2 Swan system, Journal of Quantitative Spectroscopy and Radiative Transfer, 124 (2013) 11-20.

[190] A. Brockhinke, M. Letzgus, S. Rinne, K. Kohse-Höinghaus, Energy Transfer in the $d^3\Pi_g$−$a^3\Pi_u$ (0−0) Swan Bands of C_2: Implications for Quantitative Measurements, The Journal of Physical Chemistry A, 110 (2006) 3028-3035.

[191] M. Kraus, W. Egli, K. Haffner, B. Eliasson, U. Kogelschatz, A. Wokaun, Investigation of mechanistic aspects of the catalytic CO_2 reforming of methane in a dielectric-barrier discharge using optical emission spectroscopy and kinetic modeling, Physical Chemistry Chemical Physics, 4 (2002) 668-675.

[192] K. Haris, A. Kramida, Critically Evaluated Spectral Data for Neutral Carbon (C_I), The Astrophysical Journal Supplement Series, 233 (2017) 16.

[193] J. Oliver, N. Bharadwaj, T. Sizyuk, Laser-induced fluorescence of C_2 and C_3 in colliding carbon plasma, Journal of Applied Physics, 125 (2019) 073301.

[194] S. Acquaviva, M.L.D. Giorgi, High-resolution investigations of C_2 and CN optical emissions in laser-induced plasmas during graphite ablation, Journal of Physics B: Atomic, Molecular and Optical Physics, 35 (2002) 795.

[195] J.P.P. Gore, E.J.D. Mahoney, J.A. Smith, M.N.R. Ashfold, Y.A. Mankelevich, Imaging and Modeling C_2 Radical Emissions from Microwave Plasma-Activated Methane/Hydrogen Gas Mixtures: Contributions from Chemiluminescent Reactions and Investigations of Higher-Pressure Effects and Plasma Constriction, The Journal of Physical Chemistry A, 125 (2021) 4184-4199.

[196] R. Rincón, A. Marinas, J. Muñoz, C. Melero, M.D. Calzada, Experimental research on ethanol-chemistry decomposition routes in a microwave plasma torch for hydrogen production, Chemical Engineering Journal, 284 (2016) 1117-1126.

[197] R. Miotk, B. Hrycak, D. Czylkowski, M. Dors, M. Jasinski, J. Mizeraczyk, Liquid fuel reforming using microwave plasma at atmospheric pressure, Plasma Sources Science and Technology, 25 (2016) 035022.

[198] D. Tsyganov, N. Bundaleska, E. Tatarova, C.M. Ferreira, Ethanol reforming into hydrogen-rich gas applying microwave 'tornado'-type plasma, International Journal of Hydrogen Energy, 38 (2013) 14512-14530.

[199] B. Bekdüz, Y. Beckmann, J. Meier, J. Rest, W. Mertin, G. Bacher, Relation between growth rate and structure of graphene grown in a 4″ showerhead chemical vapor deposition reactor, Nanotechnology, 28 (2017) 185601.

[200] H. Hong, G. Xiong, Z. Dong, B.H. Kear, S.D. Tse, Open-atmosphere flame synthesis of monolayer graphene, Carbon, 182 (2021) 307-315.

[201] C.-H. Huang, R.L. Vander Wal, Partial premixing effects upon soot nanostructure, Combustion and Flame, 168 (2016) 403-408.

[202] F. Hof, K. Kampioti, K. Huang, C. Jaillet, A. Derré, P. Poulin, H. Yusof, T. White, K. Koziol, C. Paukner, A. Pénicaud, Conductive inks of graphitic nanoparticles from a sustainable carbon feedstock, Carbon, 111 (2017) 142-149.

[203] J. Ma, X. Chen, M. Song, C. Wang, W. Xia, Study on formation mechanism of three types of carbon nanoparticles during ethylene pyrolysis in thermal plasmas, Diamond and Related Materials, 117 (2021) 108445.

[204] P. Fortugno, C.-F. López-Cámara, F. Hagen, H. Wiggers, C. Schulz, Relevance of C/O ratios in the gas-phase synthesis of freestanding few-layer graphene, Applications in Energy and Combustion Science, 15 (2023) 100180.

[205] D. Tsyganov, N. Bundaleska, A. Dias, J. Henriques, E. Felizardo, M. Abrashev, J. Kissovski, A.M.B. do Rego, A.M. Ferraria, E. Tatarova, Microwave plasma-based direct synthesis of free-standing N-graphene, Physical Chemistry Chemical Physics, 22 (2020) 4772-4787.

[206] C. Melero, R. Rincón, J. Muñoz, G. Zhang, S. Sun, A. Perez, O. Royuela, C. González-Gago, M.D. Calzada, Scalable graphene production from ethanol decomposition by microwave argon plasma torch, Plasma Physics and Controlled Fusion, 60 (2018) 014009.

[207] E. Carbone, F. D'Isa, A. Hecimovic, U. Fantz, Analysis of the C_2 Swan bands as a thermometric probe in CO_2 microwave plasmas, Plasma Sources Science and Technology, 29 (2020) 055003.

[208] J.S.A. Brooke, R.S. Ram, C.M. Western, G. Li, D.W. Schwenke, P.F. Bernath, Einstein A coefficients and oscillator stenghts for the $A^2\Pi–X^2\Sigma^+$ (red) and $B^2\Sigma^+–X^2\Sigma^+$ (violet) systems and rovibrational transitions in the $X^2\Sigma^+$ state of CN, The Astrophysical Journal Supplement Series, 210 (2014) 23.

[209] Z.D. Levey, B.A. Laws, S.P. Sundar, K. Nauta, S.H. Kable, G. da Silva, J.F. Stanton, T.W. Schmidt, PAH Growth in Flames and Space: Formation of the Phenalenyl Radical, The Journal of Physical Chemistry A, 126 (2022) 101-108.

[210] A.K. Lemmens, D.B. Rap, S. Brünken, W.J. Buma, A.M. Rijs, Polycyclic aromatic hydrocarbon growth in a benzene discharge explored by IR-UV action spectroscopy, Physical Chemistry Chemical Physics, 24 (2022) 14816-14824.

[211] A.K. Lemmens, D.B. Rap, J.M.M. Thunnissen, B. Willemsen, A.M. Rijs, Polycyclic aromatic hydrocarbon formation chemistry in a plasma jet revealed by IR-UV action spectroscopy, Nature Communications, 11 (2020) 269.

[212] B. Apicella, C. Russo, A. Carpentieri, A. Tregrossi, A. Ciajolo, PAHs and fullerenes as structural and compositional motifs tracing and distinguishing organic carbon from soot, Fuel, 309 (2022) 122356.

[213] J.F. Alder, J.M. Mermet, A spectroscopic study of some radio frequency mixed gas plasmas, Spectrochimica Acta Part B: Atomic Spectroscopy, 28 (1973) 421-433.

[214] A. Tanabashi, T. Hirao, T. Amano, P.F. Bernath, The Swan System of C_2 : A Global Analysis of Fourier Transform Emission Spectra, The Astrophysical Journal Supplement Series, 169 (2007) 472-484.

[215] P.W.J.M. Boumans, Inductively coupled plasma emission spectroscopy. 2. Applications and fundamentals, Wiley, New York 1987.

[216] I. Ishii, A. Montaser, A tutorial discussion on measurements of rotational temperature in inductively coupled plasmas, Spectrochimica Acta Part B: Atomic Spectroscopy, 46 (1991) 1197-1206.

[217] A.Y. Nikiforov, C. Leys, M.A. Gonzalez, J.L. Walsh, Electron density measurement in atmospheric pressure plasma jets: Stark broadening of hydrogenated and non-hydrogenated lines, Plasma Sources Science and Technology, 24 (2015) 034001.

[218] A. Remigy, S. Kasri, T. Darny, H. Kabbara, L. William, G. Bauville, K. Gazeli, S. Pasquiers, J. Santos Sousa, N. De Oliveira, N. Sadeghi, G. Lombardi, C. Lazzaroni, Cross-comparison of diagnostic and 0D modeling of a micro-hollow cathode discharge in the stationary regime in an Ar/N_2 gas mixture, Journal of Physics D: Applied Physics, 55 (2022) 105202.

[219] M. A. Gigosos, V. Cardeñoso, New plasma diagnosis tables of hydrogen Stark broadening including ion dynamics, Journal of Physics B: Atomic, Molecular and Optical Physics, 29 (1996) 4795.

[220] D. Briggs, Surface analysis of polymers by XPS and static SIMS, Cambridge University Press, Cambridge, 1998.

[221] D.-Q. Yang, E. Sacher, Carbon 1s X-ray Photoemission Line Shape Analysis of Highly Oriented Pyrolytic Graphite: The Influence of Structural Damage on Peak Asymmetry, Langmuir, 22 (2006) 860-862.

9 Appendix

9.1 Thermogravimetric analysis of particle samples and reference measurements

Thermogravimetric (TG) measurements (O_2 in Ar) are performed to analyze the fraction of distinguishable carbon allotropes present in samples from the different experimental cases. Pure soot and FLG samples serve as reference. As shown in Figure 9-1, the thermal stability strongly differs between soot-like particles and graphene flakes. In graphene flakes, oxidation starts at higher temperatures. In the DTG plots, FLG shows a single peak at ~700 °C only, while soot-like particles show multiple peaks with varying intensity already at lower temperatures. A simultaneous analysis of the off-gases by quadrupole mass spectrometry (QMS) also shows the shift to lower temperatures and the multi-peak structure in the CO_2 (m/z = 44) signal for soot-like particles.

To further evaluate how well the materials can be distinguished and how well the concentrations can be determined, different mixtures of both materials with fixed content are measured. Down to concentrations of 10 wt.% soot in FLG, a clear second peak at lower temperatures as a shoulder is observed in the DTG plots. Below this concentration however (5 wt.%), it is difficult to distinguish. The CO_2 QMS data however (not shown), shows a small shoulder which allows one to detect the particles. For even lower concentrations (<5 wt.%), the measurement as they are performed here cannot visualize the presence of soot-like particles anymore.

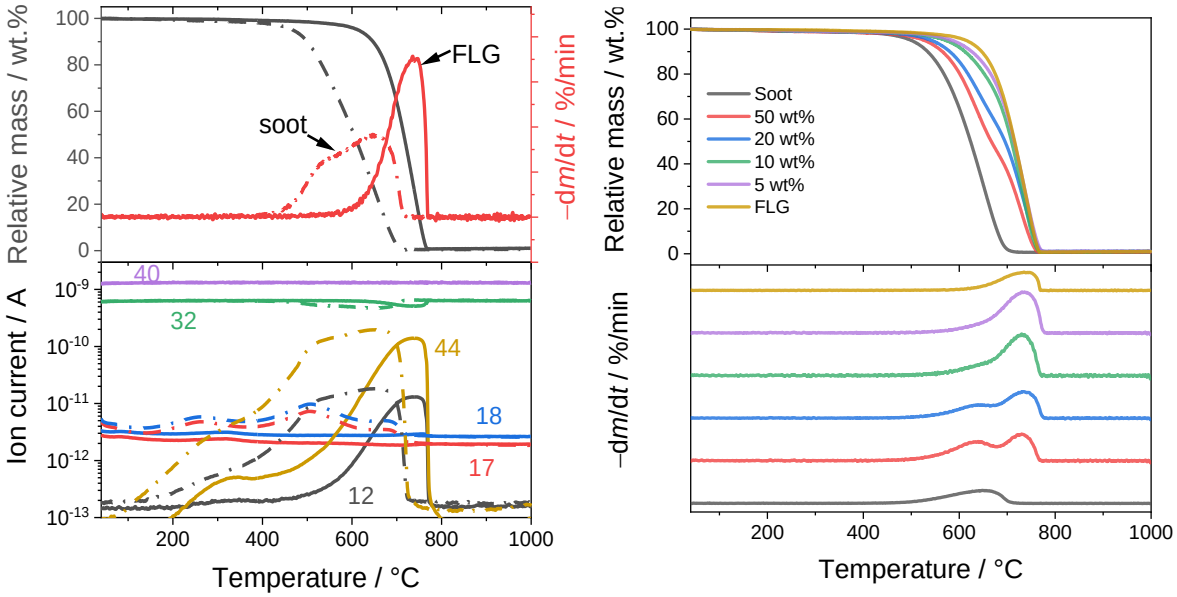

Figure 9-1: Left: TG measurements on powder synthesized with ethanol (solid lines) and toluene (dash-dotted lines). Below: Corresponding QMS measurements. Right: TG measurements of different soot-like particles/FLG mixtures. Below: Corresponding mass changes.

To further test the hypothesis that the shoulder at 540 and 650 °C specifically refers to soot-like particles, the material from Case 1 (cf. Section 6) was heated up to 660 °C to selectively remove the fraction of low oxidizing carbon. Figure 9-2 shows that for this material, the thermal treatment leads to a loss of ~30 wt.% of carbon.

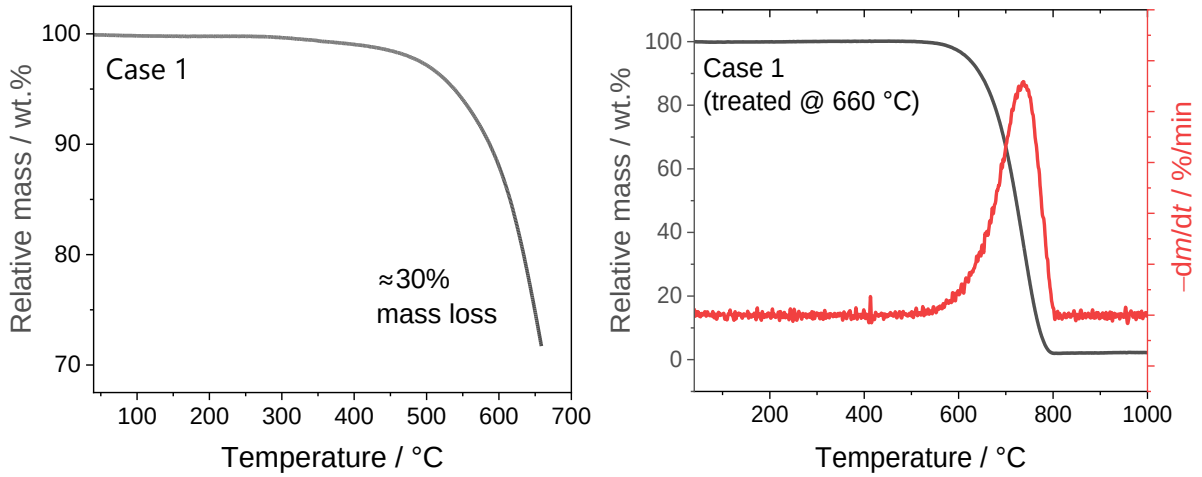

Figure 9-2: TG measurements performed for C_2H_4 to evaluate the selective removal of soot-like particles. Left: Thermal treatment up to 660 °C removes 30 wt.% of material. Right: TG measurement following the treatment.

Following this pretreatment with a normal measurement (heating up to 1000 °C), the shape of the DTG profile is transformed and the low-temperature multi-peak structure seen in samples without the pretreatment has disappeared. TEM measurements reveal (not shown), that after the heat treatment, the sample still contains particles, but their number is reduced, matching the TG results. Although this indicates that the selective removal is not 'optimized', it also confirms the peak assignment together with the calibration curves in Figure 9-1.

The oxidation of carbon materials measured by TGA depends on the specific reaction conditions. Thus, the effect of different oxygen concentrations in the reaction atmosphere and different heating rates are examined to investigate how they modify the TG and DTG curves (Figure 9-3). For the variation of reaction conditions, the sample prepared by Case 8 (Section 6) is used.

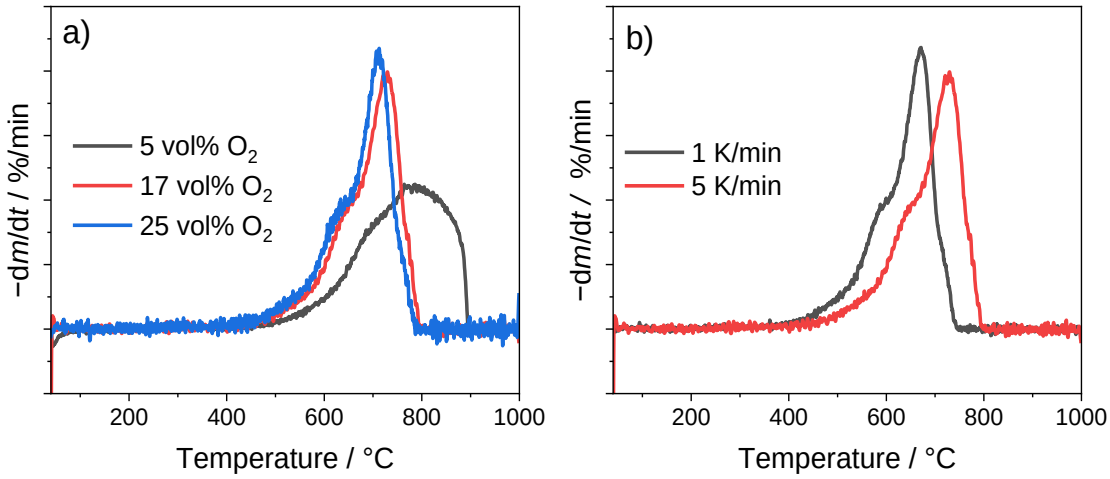

Figure 9-3: DTG plots obtained by performing TGA on powder generated by Case 8 while varying the reaction conditions. In a) the oxygen content in the gas mixture is varied while in b), the heating rate changes.

For the DTG plots in Figure 9-3a, it is observed that an increase in relative oxygen content in the supplied gas mixture shifts the DTG signals slightly towards lower temperatures. Contrary,

lower oxygen contents shift the signals to larger temperatures and the peaks become flatter and merge. The effect of different heating rates seems to be limited to shifting the entire curve to higher or lower temperatures, while maintaining the overall shape.

9.2 IR absorption measurements of ethanol vapor

Figure 9-4 displays three infrared absorption measurements that only measure the Ar + H_2 plasma, ethanol vapor diluted in Ar and H_2, and ethanol added to the Ar + H_2 plasma. When only a plasma consisting of Ar and H_2 is ignited, no significant absorption is observed. Adding ethanol vapor to the Ar + H_2 gas mixture without igniting the plasma shows absorption lines for ethanol. Thus, monitoring the ethanol absorption lines can give information whether ethanol is completely decomposed in the plasma process. When igniting the plasma and adding ethanol again (Case 1), the specific ethanol lines vanish and instead, CO, C_2H_2, and C_2H_4 is observed. Therefore, full conversion of ethanol towards solid carbon particles and gaseous molecular products is assumed. For the measurements presented in Section 5, mostly the transmittance instead of the transmission is used. The transmittance spectra show the relative change of the measured spectrum in respect to the background Ar + H_2 plasma. Hence, only new or absorption lines with different intensities are visible allowing to monitor trends more easily.

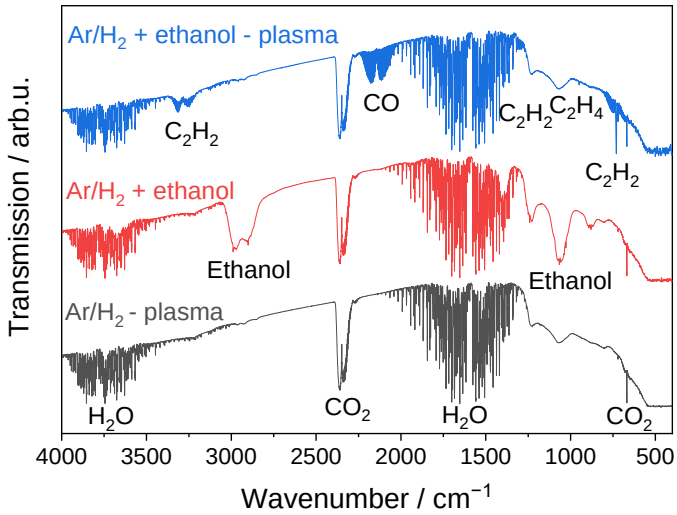

Figure 9-4: Recorded FTIR transmission spectra for experiments with ethanol as example hydrocarbon reactant inside of the reactor. Spectra include the pristine plasma (black), the plasma gases with ethanol but without plasma ignition (red), and the case but with running plasma and ethanol added (blue) [175].

9.3 OES measurements

9.3.1 Constraints by process stability and spectrometer system properties

For analyzing the optical emission spectroscopy (OES) measurements in the plasma zone, many aspects need to be considered. As already mentioned in Section 3.2 a steady state over the duration of each measurement is assumed. Such an assumption becomes necessary, as the measurements can take up to 20–30 minutes for one spectrum and the relative emission intensity of specific lines has to be stable for the full measurement duration. Figure 9-5 display two different plots with focus on the signal stability.

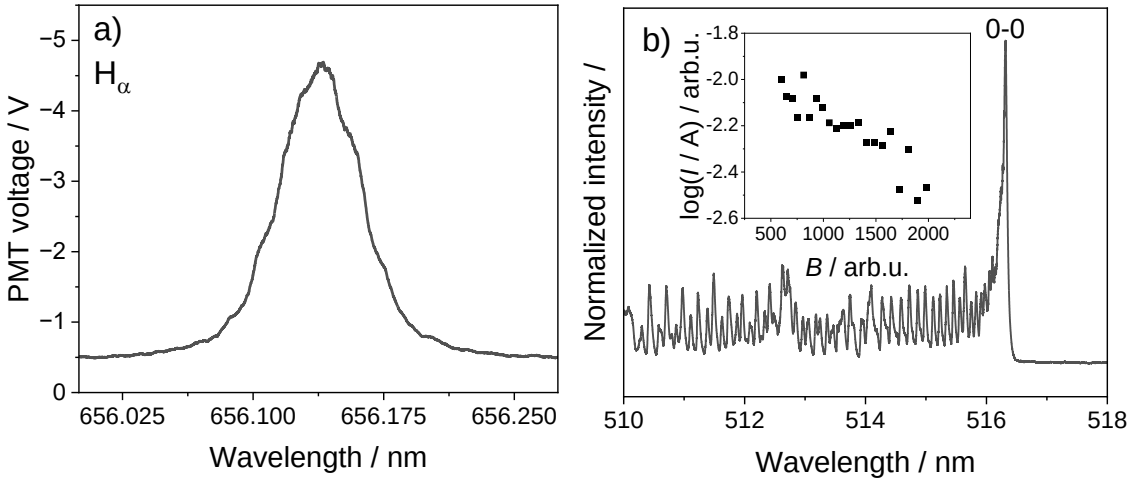

Figure 9-5: Example OES measurements showcase intensity fluctuations of the recorded spectra. a) Highly resolved scan (0.1 Å/s) of the H_α line, b) Scan of the C_2 Swan region between 510–518 nm (0.2 Å/s) recorded for experimental conditions in which water (2:1.5) is added to C_2H_4 (Case 7). The inset in b) shows the corresponding Boltzmann plot [175].

The shape of the H_α emission line in Figure 9-5a shows that the signal intensity slightly fluctuates during the measurements and has a small offset (~1.5 Å) to the emission wavelength (656.27 nm). The steadiness is experimentally directly linked to the plasma stability. Experiments with large amounts of H_2O lead to noticeable less stable operation. Figure 9-5b shows this effect for the C_2 emission lines in the 510–520 nm range. As a result, the Boltzmann plot leads to less accurate results.

Fitting the C_2 emission lines in the 480–520 nm range with PGOPHER requires a measured instrument function for the spectrometer system. Figure 9-6 shows the spectra obtained and generated to create the instrument function necessary for the intensity correction. Smoothing is applied to remove artifacts. Figure 9-6a shows the high sensitivity of spectrometer and detector in the visible range (350–650 nm), while UV and wavelengths >650 nm are detected with lower sensitivity. The grating is blazed for 400 nm, meaning that the detection efficiency will decrease towards shorter and longer wavelengths. Similarly, the response for the PMT is also the highest for 400 nm. The molecular lines used for temperature determination are detected with different efficiency (Figure 9-6b). The region of the OH emission lines (300–320 nm) is detected inefficiently and signal below 300 nm are measured with large error only. The region for C_2 (480–520 nm) shows significantly higher sensitivity.

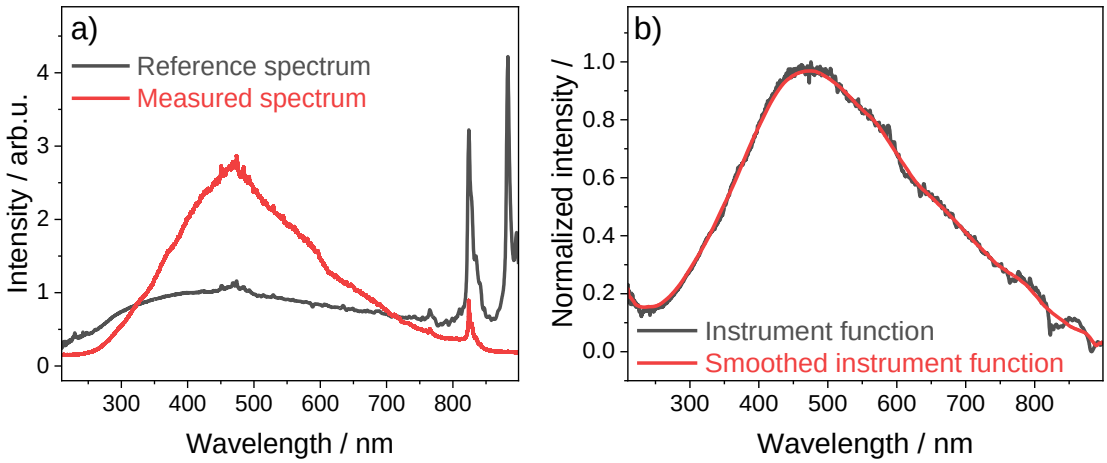

Figure 9-6: a) Comparison of a reference spectrum (measured at the PTB Braunschweig) and the measured spectrum of the employed spectrometer system. b) The generated instrument function (i.e., the spectral sensitivity) before and after smoothing.

The spectral resolution of the spectrometer system is detected with a Hg/Ar light source (LOT QuantumDesign). Figure 9-7 displays the corresponding emission spectra of the lamp with the spectrometer operated with a 40 µm slit width. In Figure 9-7a, the full emission spectrum is shown in the range of 200–600 nm indicating several atomic lines which can be assigned to Hg. The highest intensity line in Figure 9-7b at ~435 nm is then used to estimate the instrument broadening by using a Gauss fit. The Lorentzian broadening of Hg is negligibly small (<1 pm) and can be neglected. Hence, the instrument broadening is determined as ~0.03 nm.

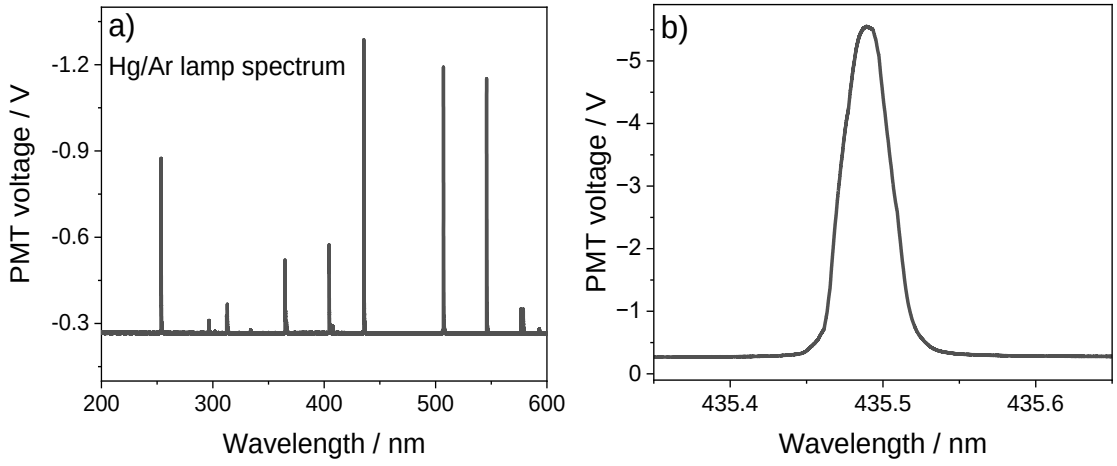

Figure 9-7: a) Emission spectrum of a Hg/Ar light source in the 200–600 nm range. b) Main Hg emission line at ~435 nm.

9.3.2 Details on the temperature determination from OES

As described in Section 2.4.1.1, two different approaches are used to obtain values for the rotational temperature (T_{rot}). In one case, the Boltzmann plot method is employed for both C_2 and OH emission while the obtained temperatures are only validated for C_2 with fitting against simulations. For C_2 the P_i branch (every line is a triplet) of lines near the 0–0 band is used, while for OH the Q_1 branch near 0–0 is employed. To understand in the following the simplified formula used for analyzing the C_2 emission, first a new formulism has to be introduced. The transition probability for spontaneous emission (A_{nm}, see Eq. 2-4) can be rewritten in different

forms which introduces one parameter known as Hönl-London factor (S_{nm}). The factor describes the intensity variation for different rotational lines. After including it and neglecting other influences, the relationship in Eq. 9-1 can be obtained.

$$I_{nm} \propto S_{nm} \exp\left[E_n / k_B T_{rot}\right] \qquad \text{Eq. 9-1}$$

Putting in a formalism for the specific P branch transitions instead of S_{nm}, rearranging, converting units, and assuming that the energy term can be described by the rigid rotor model, leads to the formula given as Eq. 9-2 presented in the work of Alder et al [213].

$$\log\left(\frac{I_{nm}\,(K^n{+}1)}{(K^n{+}1)^2 - 1}\right) \approx \text{ const. } - \frac{B_v\, h\, c}{k_B\, T_{rot}\, \log_e(10)}\, K^n\,(K^n{+}1) \qquad \text{Eq. 9-2}$$

K^n is the rotational quantum number of the excited state, which in case for the lines analyzed in this thesis are K^n = 24–44. B_v is the related molecular constant for the corresponding state ($d^3\Pi_g$, v = 0, B_v = 1.7455695 cm^{-1} [214]). The value defined as constant includes a dependence of the frequency or wavelength of each transition. As long as lines are analyzed for a small bandwidth only (here 3 nm, relative error less than 2 %) this constancy assumption holds and the wavenumber dependence can be neglected. This equation can be further simplified by combining the rotational quantum numbers and all the constants according to the formalism of Jimenez et al. [41] in which B equals K^n (K^n+1) and A is the corresponding factor in the argument of the logarithm on the left side.

$$\log\left(\frac{I}{A}\right) = \text{const.} - \frac{1.09}{T_{rot}}\, B \qquad \text{Eq. 9-3}$$

The OH emission was analyzed using data and formalism from literature [187, 215, 216] which originates from the work of Dieke et al. [188]. The used formalism is shown in Eq. 9-4 and is similar to Eq. 2-5 in Section 2.4.1.1.

$$I_{nm} = a\, A_{nm}\, h\, \frac{c}{\lambda_{nm}} \exp\left(\frac{-E_n\, h\, c}{k_B\, T_{rot}}\right) \qquad \text{Eq. 9-4}$$

a is a constant for Hund's cases a) or b), λ_{nm} is the emission wavelength. Rearranging this equation and combining constants leads to a simplified version (Eq. 9-5).

$$\log\left(\frac{I_{nm}\,\lambda_{nm}}{A_{nm}}\right) = \text{const. } - \frac{0.625}{T_{rot}}\, E_n \qquad \text{Eq. 9-5}$$

9.3.1 Limitation of hydrogen concentration measurements

With the obtained instrument function and estimated temperature values, the electron density can be calculated from the H_β line. The lower limit of electron densities required to obtain sufficient line broadening is usually assumed to be 10^{19} m^{-3} [217]. Here, the formalism described in the work of Remigy and coworkers [218] is employed to calculate an expected FWHM for the H_β line similar to the strategy presented by Laux et al. [153]. In this specific formulism by Remigy, the overall lineshape of the H_β line is described as a convolution of several broadening mechanism. These include the instrument broadening, Doppler broadening, Van der Waals broadening, and Stark broadening. Resonance broadening and natural lifetime broadening are

neglected as they are much smaller than the other broadening mechanisms. The calculation of the different broadening mechanisms requires an input for the conditions of the experiments. For the Van der Waals and Doppler broadening a temperature of 3000 K and partial pressure of ~950 kPa for Ar (neglecting other perturbers) is assumed. Figure 9-8 showcases the variation for the FWHM of the H_β line as a function of electron density for the given assumptions of temperatures and partial pressures. As additional simplification, the increase in electron density is assumed to have no impact on the broadening mechanisms other than Stark broadening. The figure shows that the instrument broadening is the largest contribution to the overall line broadening up to electron densities of ~6×10^{19} m^{-3}. Furthermore, the equations used for describing the Stark broadening originate from interpolating tabulated data, e.g., the table of Gigosos et al. [219] for electron densities in the range of 10^{20}–10^{24} m^{-3}. Hence, the measured values of ~49 pm of FWHM for the H_β line are deemed too small for a reliable electron density determination.

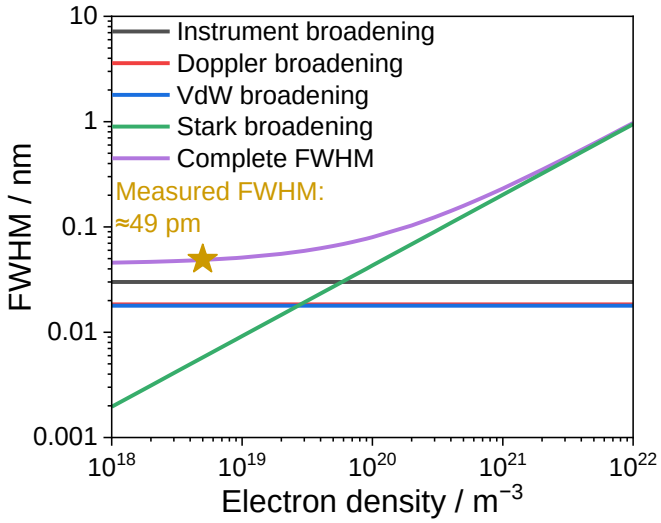

Figure 9-8: Expected FWHM calculated from the formulism presented by Remigy et al. [218] based on the experimental conditions ($T_g \approx 3000$ K and $p_{Ar} \approx 950$ kPa) in dependence of the electron density.

9.4 Discussion on quantitative differences particle composition between Cases 2 and 8

Comparing by TGA the cases in Sections 5 and 6 in which 190 sccm of C_2H_4 as reactant are used reveals that the sample in Section 6 is richer in FLG. Hence, all samples prepared in Section 6 with the addition of different oxygen carriers are also richer in FLG compared to their Section 5 counterparts in which H_2O was added. Still, the same qualitative trends are observed, i.e., a specific amount of oxygen carrier (2:1.5) needs to be added to reach or go below a similar specific threshold of carbon concentration to prevent growth of soot-like particles. However, it needs to be answered where the differences between the samples prepared in both sections originate from. The kinetics simulations revealed that the synthesis seems to be kinetically controlled because variations of the residence time influence the expected stable species concentrations at the end of the reactor. It implies that the flow rate of gases through the reactor affects the experimental outcome. As the experiments in Sections 5 and 6 are performed a reasonable time apart, unaccounted/noticed changes in a MFC calibration might lead

to different results. To check whether this hypothesis is true, another experiment was performed in which the flow rate through the central nozzle was reduced by an arbitrary value of 0.5 slm. To put the altered flowrate into more context, the overall flowrate through the central nozzle is 5.19 slm, so a reduction of 0.5 slm accounts to a relative change of less than 10 %. The comparison between these three samples by TGA (DTG) and Raman is shown in Figure 9-9.

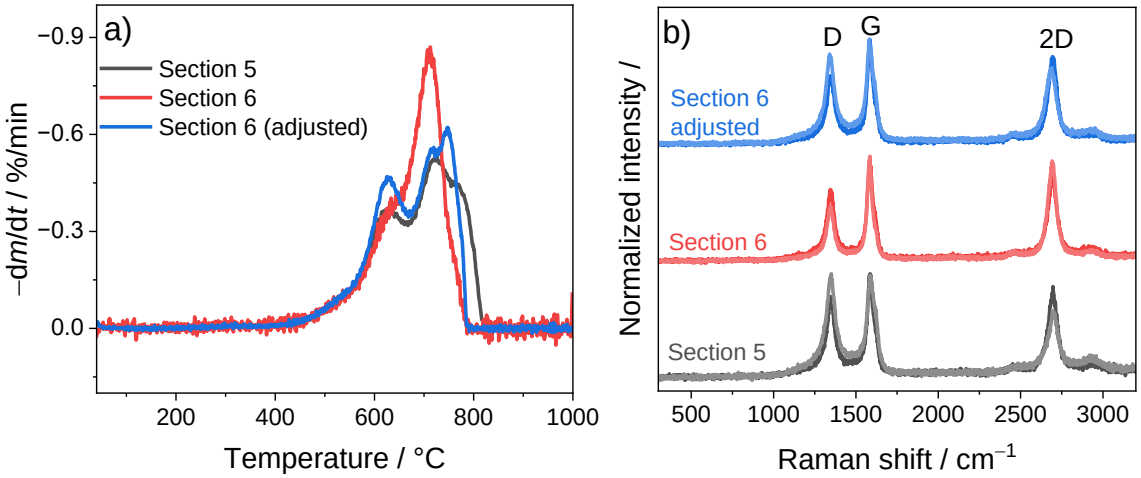

Figure 9-9: Comparison of samples prepared with 190 sccm of C_2H_4 presented in Sections 5 and 6, and with an adjusted flowrate following Section 6. a) shows DTG plots obtained by TGA and b) refers to Raman measurements.

The DTG plots reveal that artificially reducing the flowrate through the central nozzle influences the composition of the generated nanocarbons. Compared to the sample generated in Section 6, the adjusted sample quantitatively shows a smaller fraction of FLG and is in relation richer in soot-like/graphitic particles. It does not fully reproduce the sample described in Section 5 but becomes comparable. Similarly, to the DTG results, Raman spectroscopy also shows changes in the obtained spectra. The 2D band intensity of the Section 6 (adjusted) sample becomes smaller and the D-band intensity increases. Therefore, relative changes can be observed, albeit they do not fully reproduce the Section 5 sample. To confirm that the experimental impact of oxygen discussed in Section 5 can still be observed, experiments with H_2O addition are compared by TGA in Figure 9-10. The cases refer to the experimental conditions described in Table 5-1. The relative mass changes displayed in Figure 9-10a show a slight shift of the mass loss to larger temperatures. Such shift translates into a decreasing oxidation peak (~630 °C) indicative for the presence of soot-like particles in Figure 9-10b. Similarly, the CO_2 formation measured by QMS also shows a narrowing towards a single peak representing FLG. Comparing the measured lines in DTG and QMS to the observed measurements in Section 5, shows that the new samples are richer in FLG and more comparable to the composition observed in Section 6. Case 5 shows a clear presence of soot-like particles while for Case 6 and 7 the resolution limit of the method is reached and only qualitative estimations are possible. Thus, the trends are qualitatively reproduced and the addition of H_2O leads to more FLG-rich carbon particle mixtures.

As a consequence, the discussed criteria in terms of carbon concentration and specific C/O ratios need to be expanded to more precisely define reaction conditions including the residence time or flowrate.

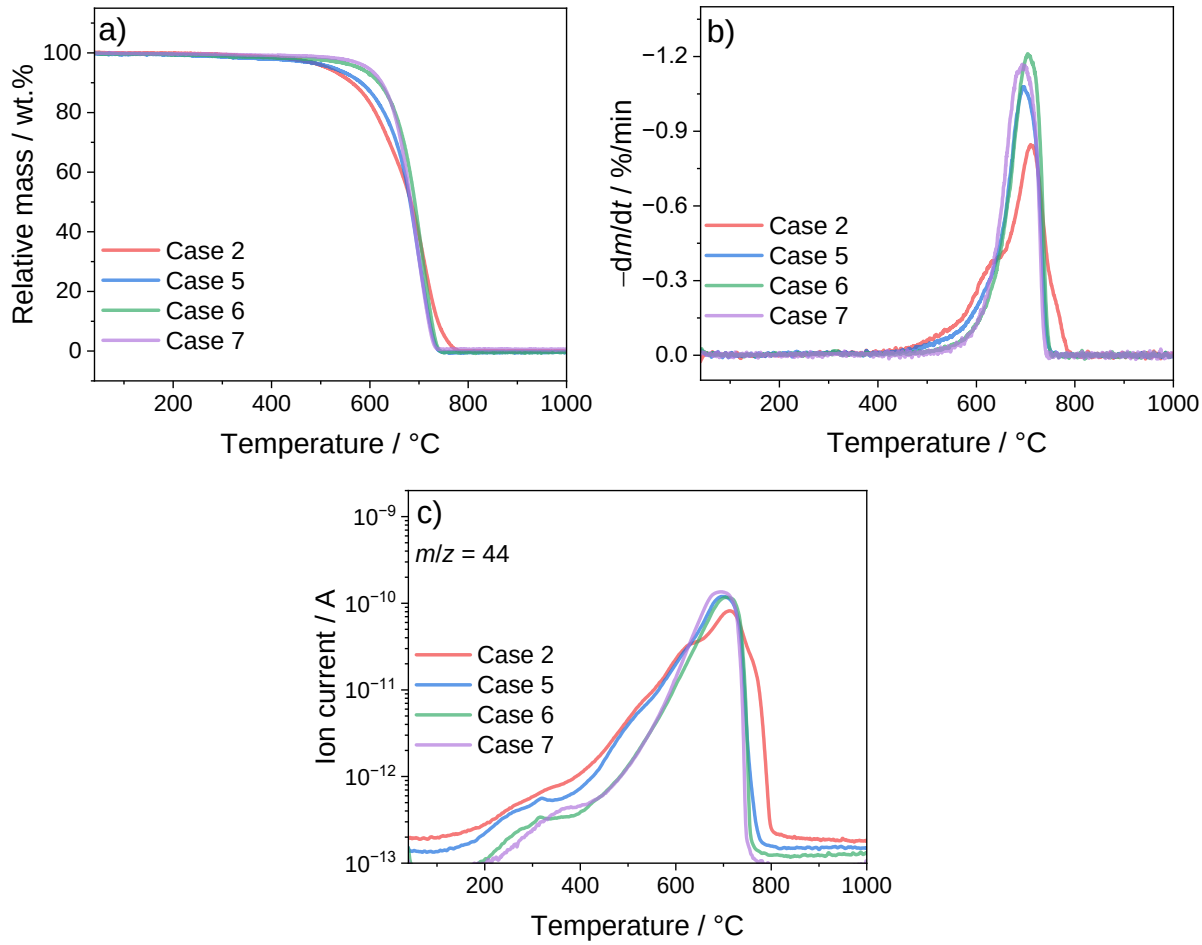

Figure 9-10: TGA results obtained from new samples reproducing the addition of H_2O to C_2H_4 in Section 5. a) Mass variation, b) Corresponding DTG data, c) QMS signal for CO_2 (m/z = 44).

9.5 Additional material on section 5

The following subsections include r more analysis or simulation results which are not already presented in the main body of the thesis. For Section 5 the additional results include the measured TGA QMS data, XPS measurements on the generated powders, Chemkin simulation results for the equilibrium gas compositions and the not already shown gas species profiles.

9.5.1 Hydrogen addition as reactant

Some of the kinetics simulations (Figure 5-16) in Section 5.4 suggest that the addition of H_2 has little effect on the growth of carbon particles. To validate this result for the given experimental conditions, experiments are performed in which the H_2/C_2H_4 ratio is increased to six and seven by the introduction of additional 190 and 380 sccm of H_2 through the central nozzle. TGA and Raman results are displayed in Figure 9-11. The results have to be referenced to Case 1 in Section 6 which shows a lower relative fraction of soot-like particles compared to the same sample in Section 5. Both the DTG and QMS in Figure 9-11a and b show a multipeak structure which indicates the presence of different forms of carbon particles. Similarly, the Raman spectra in Figure 9-11c show a low 2D band intensity while a shoulder at ~1250 cm^{-1} can be identified. Both results are indicative for the presence of soot-like particles, confirming the expectation based on the kinetic simulation that H_2 is not as effective as H_2O in suppressing

soot-like particle formation. Comparing the TGA results between the addition of both H_2 flowrates shows that there is little quantitative difference between the samples in terms of their composition of different oxidizable carbon phases.

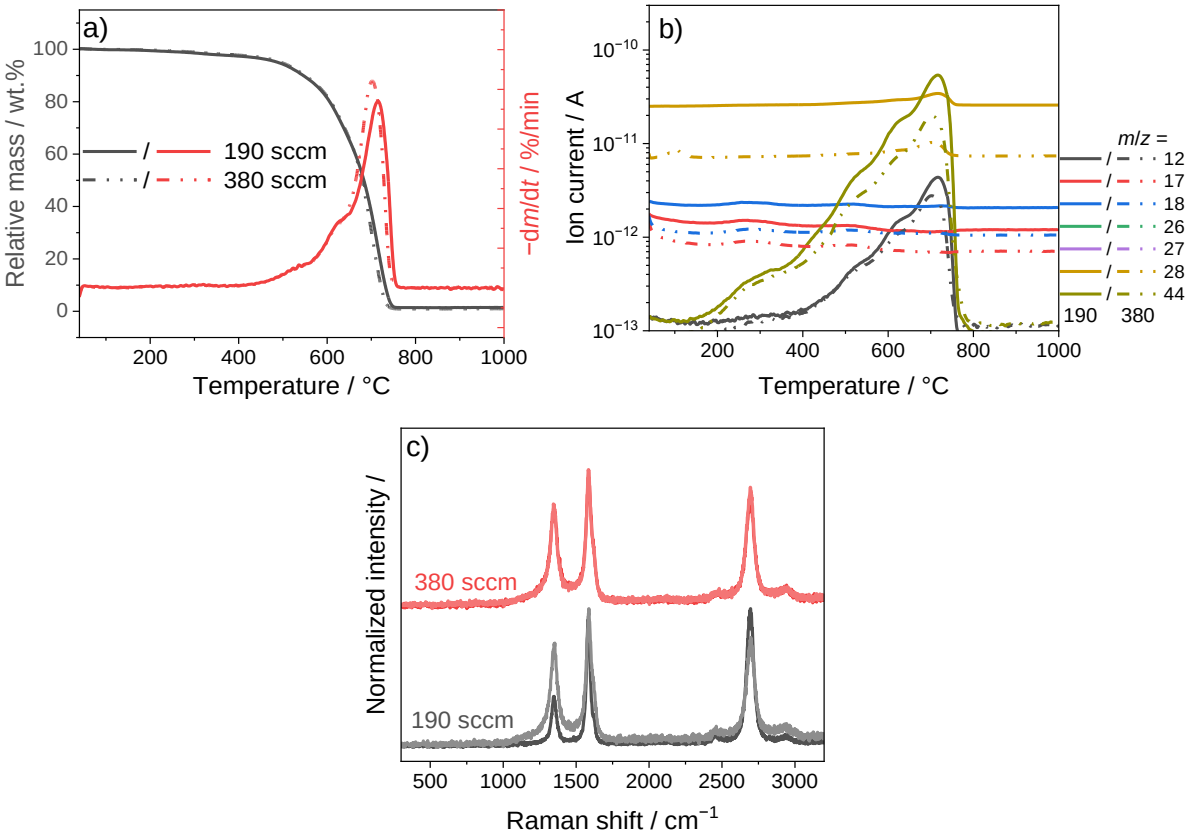

Figure 9-11: In a) and b) TGA results are whom while c) displays Raman results. Results are obtained for carbon particles gathered from experimental conditions in which additional H_2 is introduced into the central nozzle.

For additional confirmation, particle samples are analyzed with TEM. Figure 9-12 depicts examples of images when either 190 (Figure 9-12a and b) or 380 sccm (Figure 9-12c and d) of H_2 is added to C_2H_4. For both samples, blue arrows highlight non-FLG carbon particles. Soot-like particles are observed in both cases confirming the result by TGA and Raman.

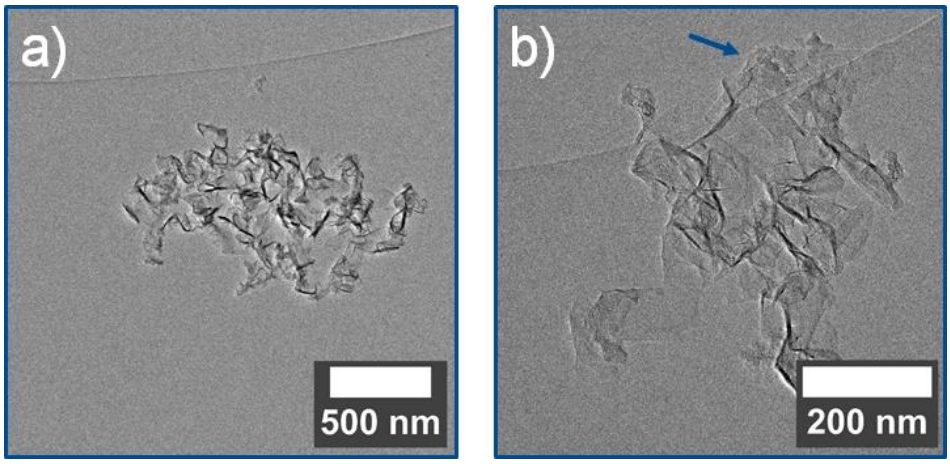

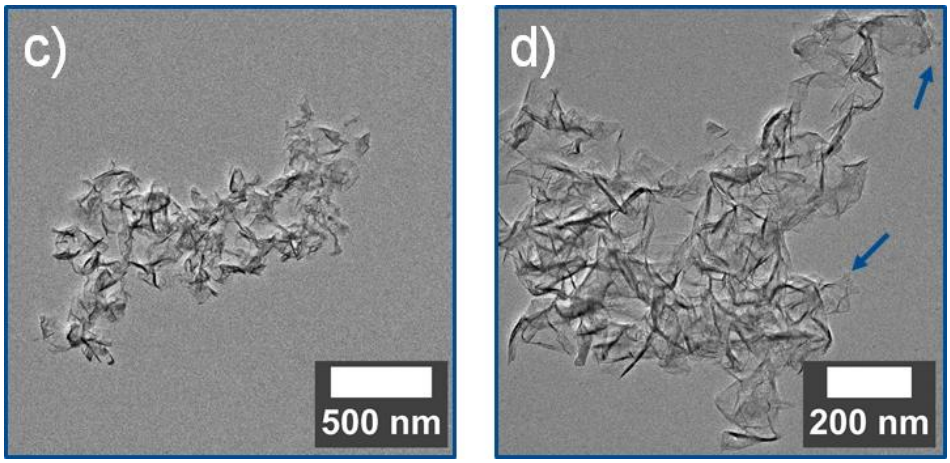

Figure 9-12: TEM images of samples which are prepared by the addition of either 190 (a, b) or 380 sccm of hydrogen (c, d). Carbon particle structures other than FLG are indicated with blue arrows.

9.5.2 Complete set of measured TGA QMS data

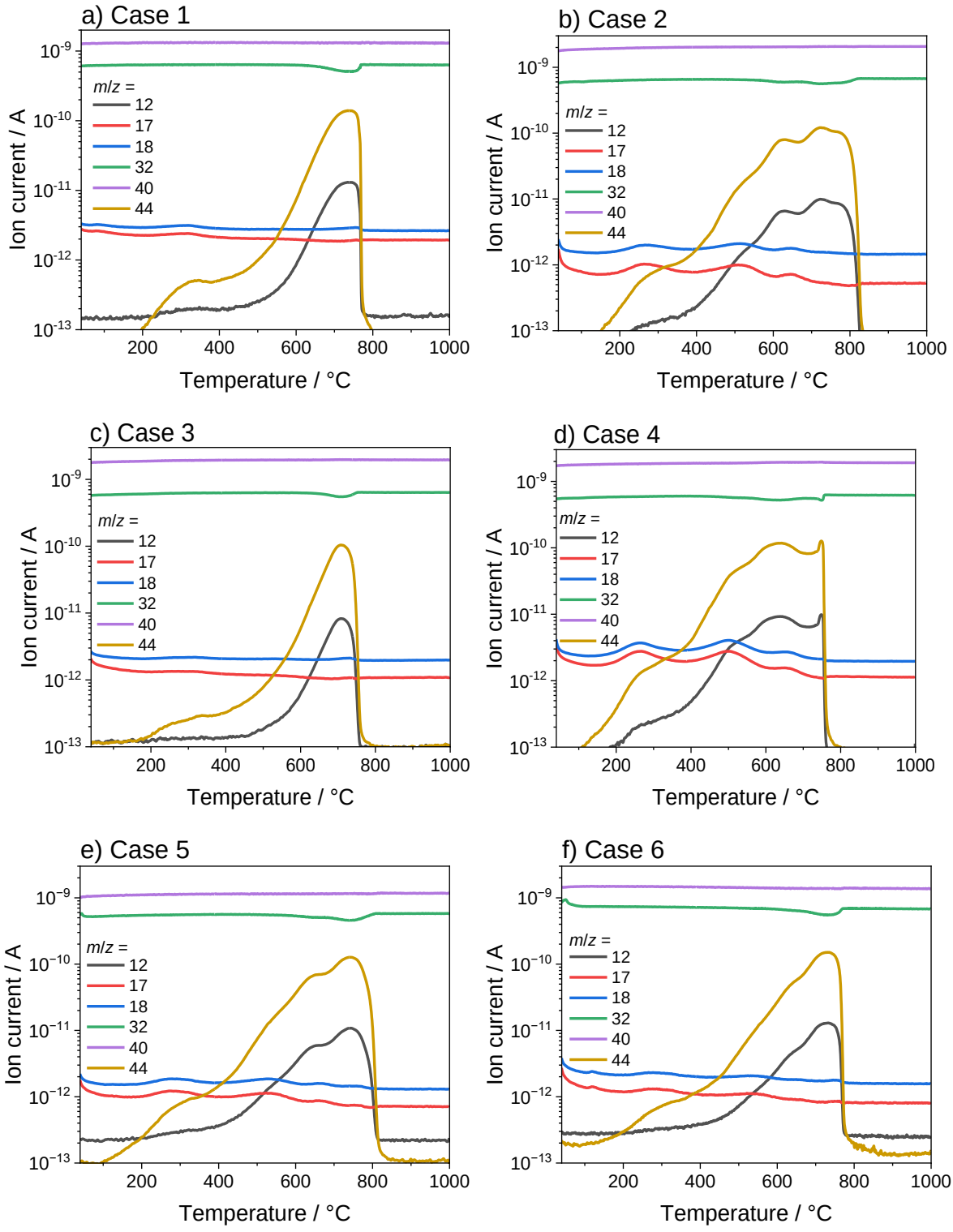

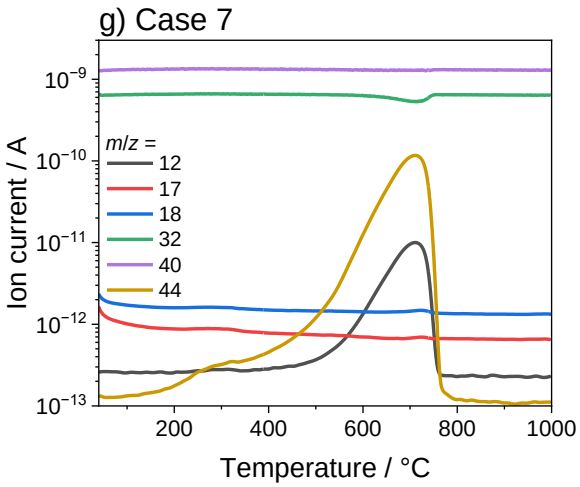

Figure 9-13: QMS measurements simultaneously obtained during the TGA measurements for Cases 1–7. The evolution of the *m*/*z* = 44 signal (CO_2) shows similar trends compared to the DTG plots; thus, it is also employed to distinguish between different carbon particle types.

9.5.3 XPS measurements performed on Cases 1–7

Figure 9-14 displays XPS measurements for powders collected from the experimental Cases 1–7. For each case as survey scan and the fitted C_{1s} region is shown. The fits include two carbon particle types that possess a different sp^2/sp^3 ratio i.e., FLG or soot-like particles. It is known that sp^2- and sp^3-hybridized carbon bonds possess different binding energies [220]. Additionally, sp^2-carbon lines are typically asymmetric while sp^3-carbon ones are symmetric [142, 221]. FLG and soot-like particles contain a mixture of both hybridizations. The mixture ("sp^2-to-sp^3 ratio") will be characteristic for the specific nanostructure i.e., FLG will be richer in sp^2-carbon compared to the soot-like particles (previous work based on the analysis of the C_{KKL} Auger peak suggest that the FLG materials are >90 % sp^2-hybridized [171]). Therefore, for cases where the samples only contain either pure FLG or pure soot-like particles, the line-shape for the respective nanostructure can be defined and used to distinguish between both types of materials in a mixture of both carbon allotropes. The lineshapes for the different carbon particle types are taken from the thesis of Münzer [35]. As a requirement, it is assumed that the FLG and soot-like particles do not change their microstructural properties within the performed set of experiments. Furthermore, this approach neglects the presence of graphitic particles present for Case 2, which may show similar amounts of sp^2-hybridization compared to FLG.

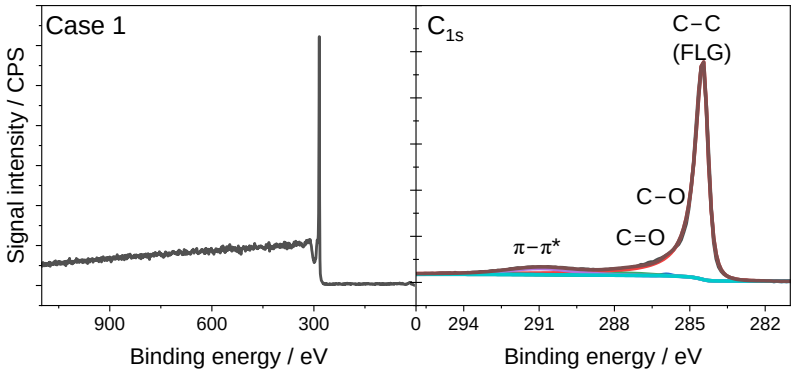

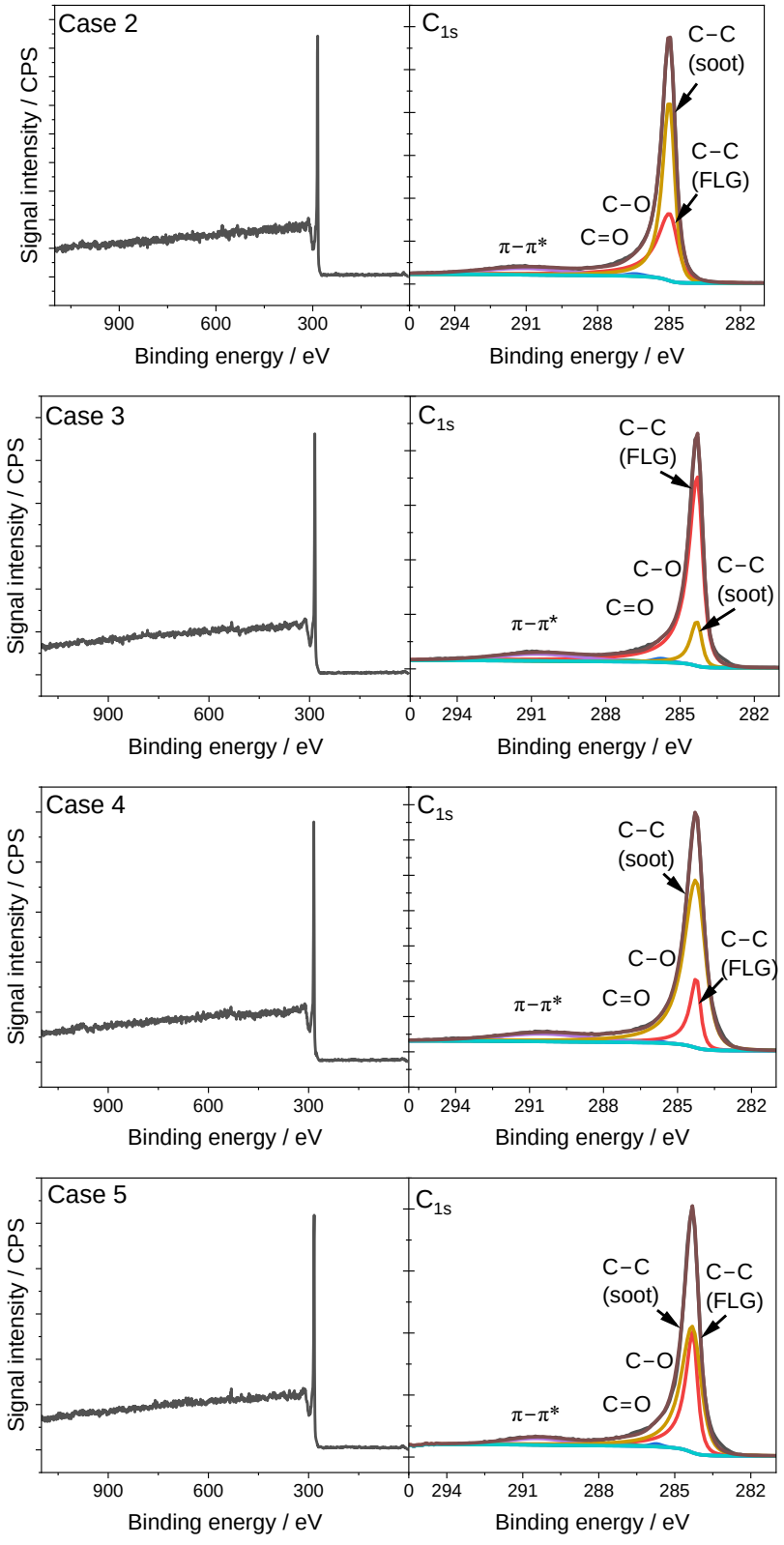
Case 2
C1s
C−C (soot)
C−C (FLG)
C−O
C=O
π−π*
Signal intensity / CPS
900
600
300
0
294
291
288
285
282
Binding energy / eV
Case 3
C1s
C−C (FLG)
C−O
C−C (soot)
C=O
π−π*
Signal intensity / CPS
900
600
300
0
294
291
288
285
282
Binding energy / eV
Case 4
C1s
C−C (soot)
C−O
C−C (FLG)
π−π*
C=O
Signal intensity / CPS
900
600
300
0
294
291
288
285
282
Binding energy / eV
Case 5
C1s
C−C (soot)
C−C (FLG)
C−O
π−π*
C=O
Signal intensity / CPS
900
600
300
0
294
291
288
285
282
Binding energy / eV

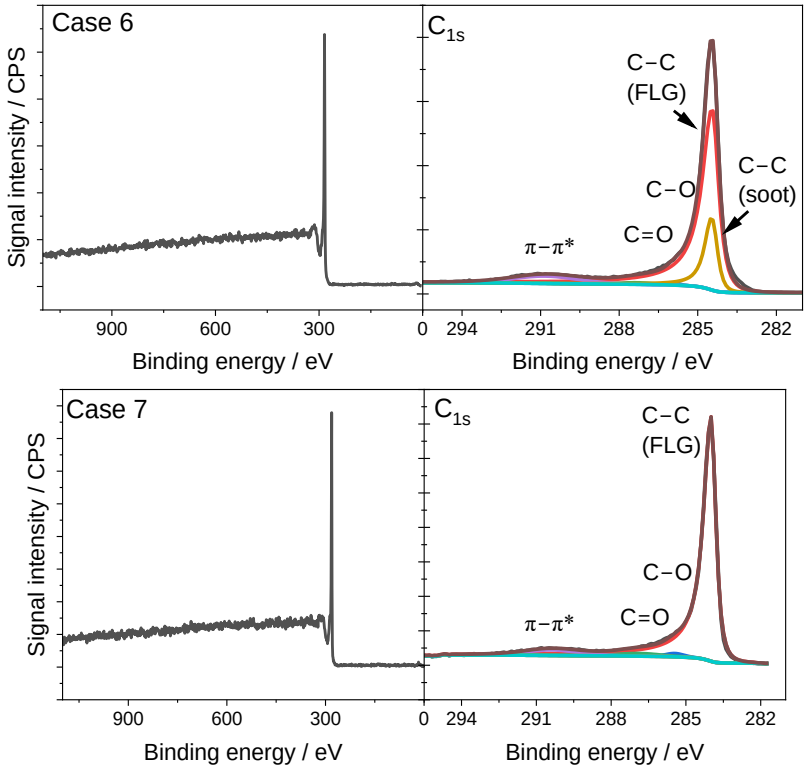

Figure 9-14: XPS measurements showing a survey scan and a high-resolution scan of the C_{1s} region of samples prepared by the Cases 1–7.

The results suggest different contents of FLG or soot-like particles depending on the specific experimental case. Overall, the fits can reproduce the other analysis results by e.g., TGA, Raman, and TEM.

9.5.4 Simulation of chemical equilibrium compositions and gas species profiles

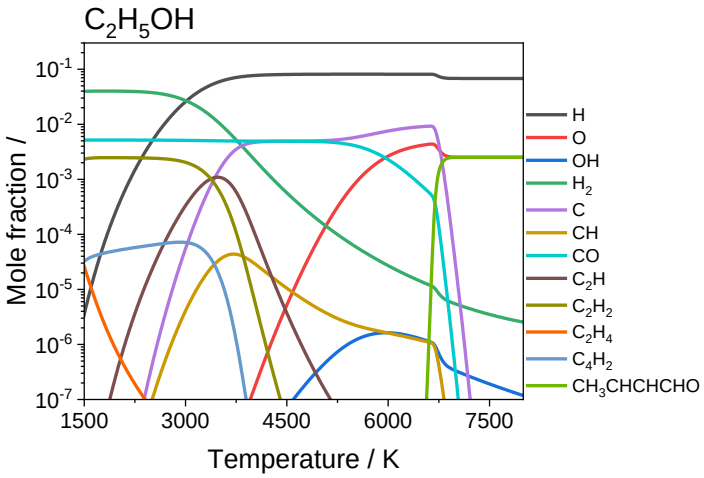

Figure 9-15: Temperature-dependent gas composition in chemical equilibrium for the addition of ethanol to the Ar + H_2 plasma

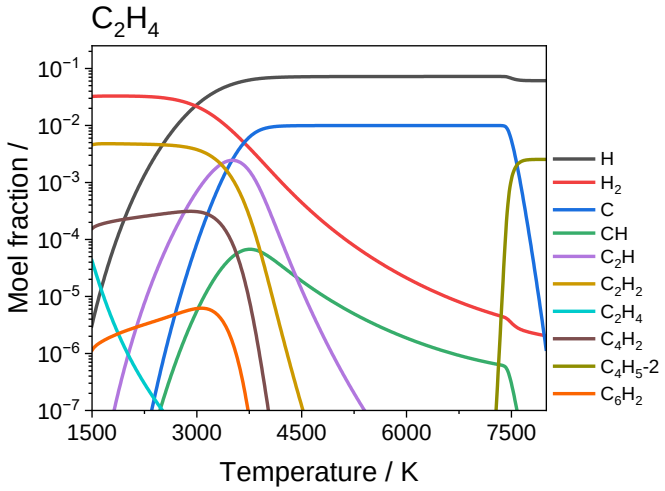

Figure 9-16: Temperature-dependent gas composition in chemical equilibrium for the addition of C_2H_4 into the plasma for a C/O ratio of ∞.

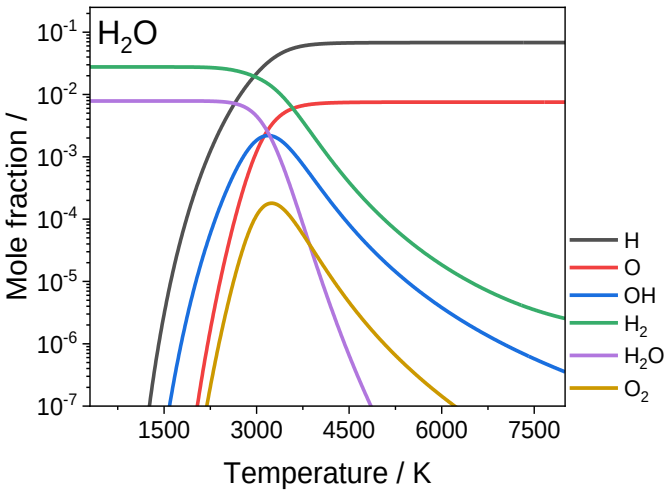

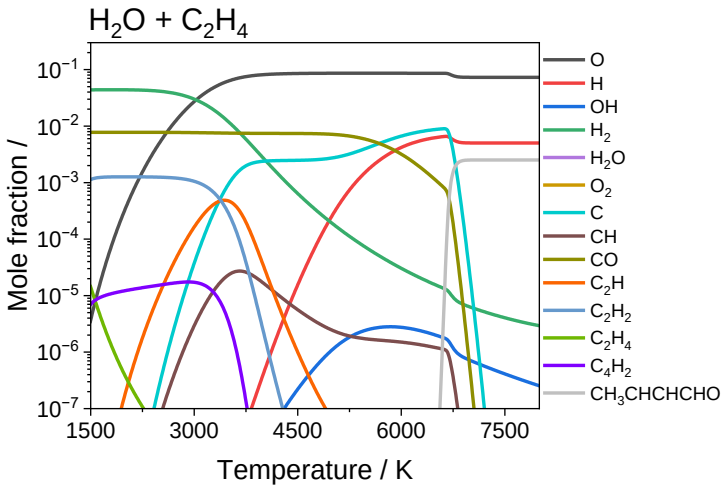

Figure 9-17: Temperature-dependent gas composition in chemical equilibrium for the addition of H_2O or H_2O and C_2H_4 (Case 7 equivalent C/O = 1.33:1) to the Ar/H_2 plasma.

Figure 9-18 presents the computed species spatial profiles of all cases that are not shown in the main text. A consistent pattern of hydrocarbon species profiles is observed across different test cases.

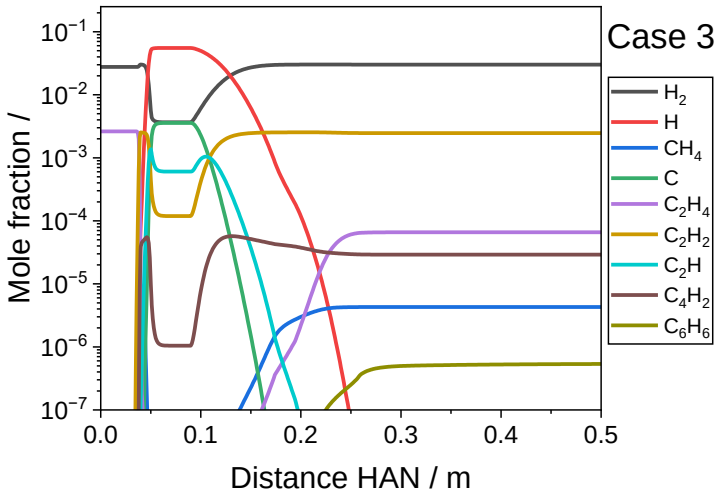

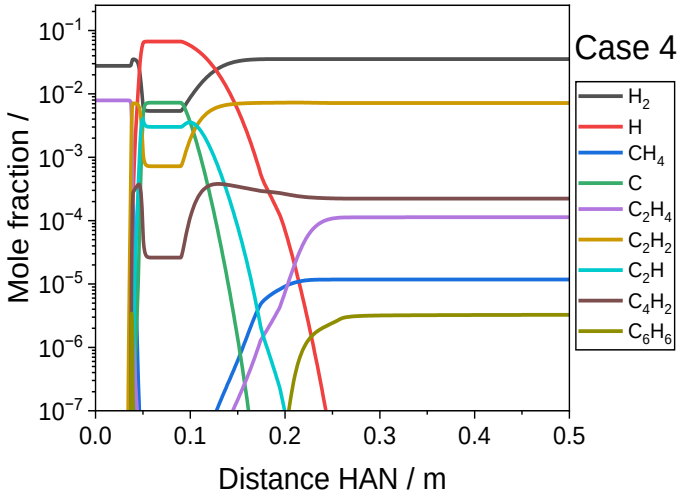

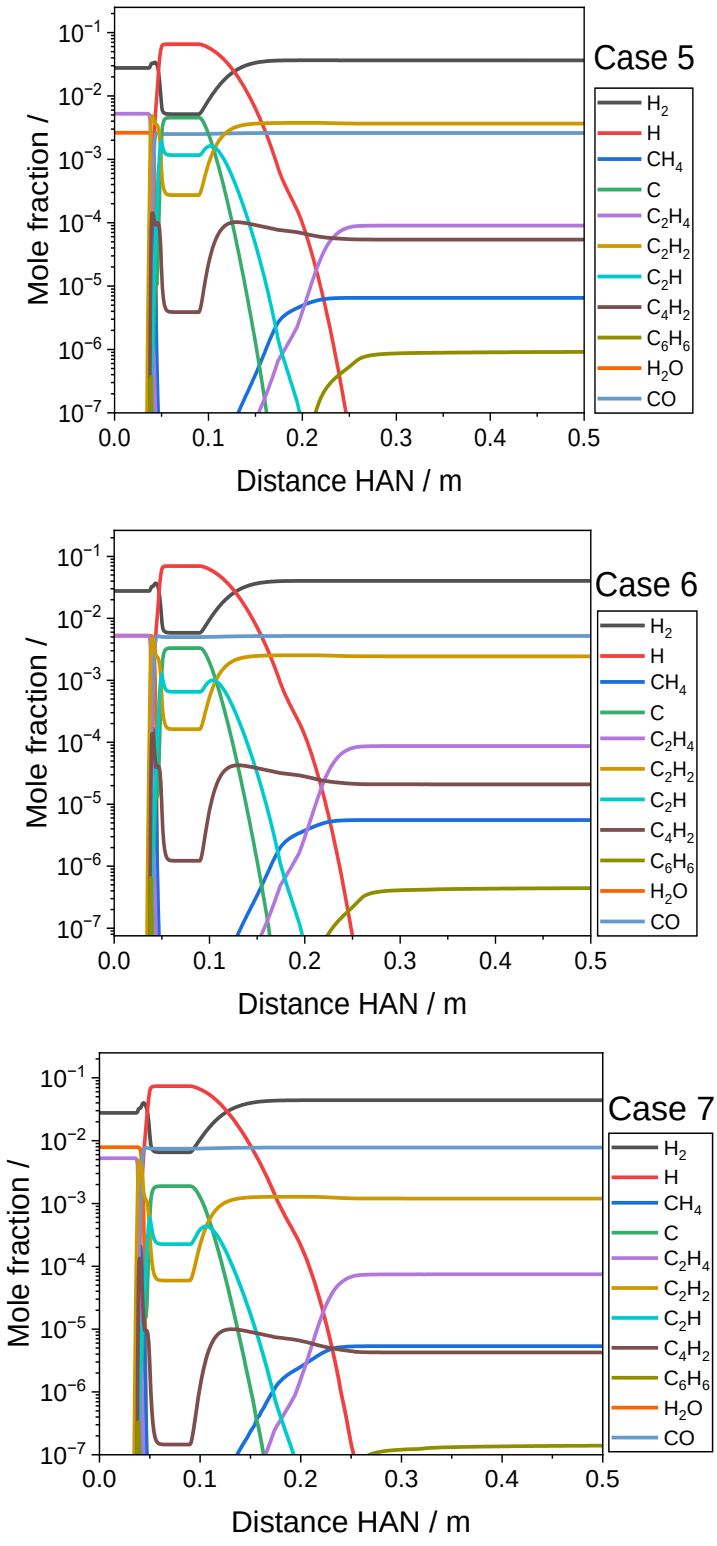

Figure 9-18. Computed gas species profiles for the experimental Cases 3–7. For better visibility, only a limited number of species is shown.

9.6 Additional material on Section 6

The following subsections include more analysis or simulation results which are not already presented in the main body of the thesis. For Section 6 at first the Chemkin simulations for the equilibrium gas composition when adding O_2, N_2O, or CO_2 (with and without ethylene) into the plasma are presented. Furthermore, gas species profiles for Cases 9–16 are shown. Afterwards qualitative TEM images for all experimental cases are shown, as the main body of the thesis only displays selected examples. TEM images are followed up by exact numerical values obtained from the GC/MS validation measurements which are only presented as a figure (Figure 6-2) in the main text. Next all of Cases 8–16 measured Raman spectra are displayed and the analysis result on peak ratios, linewidths, and FWHM are tabulated. At the end of the section, all recorded TGA results and the fitted XPS spectra are shown.

9.6.1 Chemkin simulations of the gas-phase species

The results for the Chemkin simulations referring to experimental Cases 9–16 are shown in the following figures and the results are discussed separately. Case 8 is not shown again as the result are the same as for Case 2. Figure 9-19–Figure 9-21 display results for chemical equilibrium calculations in which each of the oxygen carriers is added into the plasma (C/O ratio of 0) and when C_2H_4 as hydrocarbon reactant is added (C/O ratio of 1.33:1 and ∞). The quality of the results is limited by the thermochemical data used in the related chemistry mechanism because the utilized combustion mechanisms only contain a small number of species and some of the species' properties are estimated. As a consequence, at high temperatures (> 6000 K), unrealistic results are observed in which, e.g., the crotonaldehyde radical (CH_3–CH=CH–$CO^{\bullet}$) is stable. Comparing the results for main species to OES measurements is in first order approximation possible.

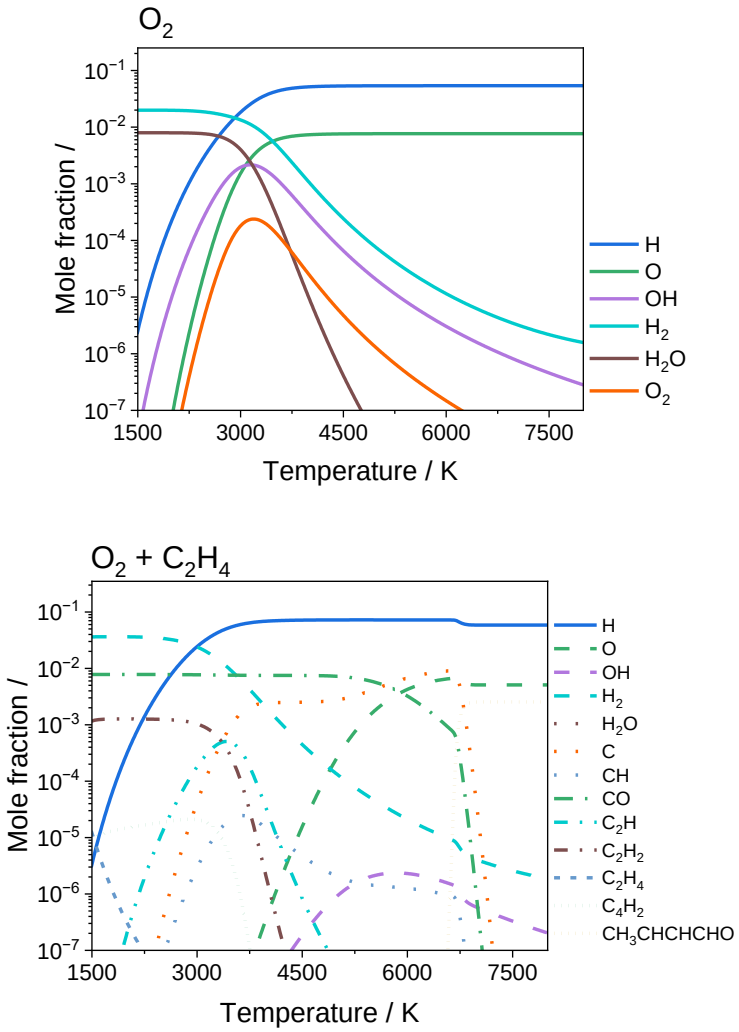

Figure 9-19: Chemical equilibrium calculations when using O_2 as oxygen carrier. a) No carbon-containing species, b) C/O ratio = 2:1.5.

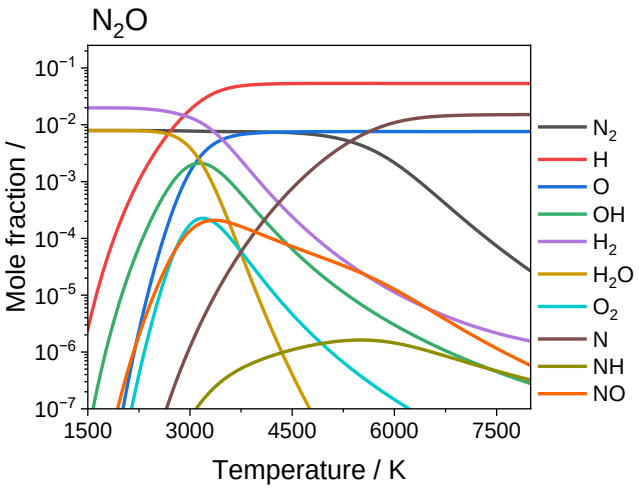

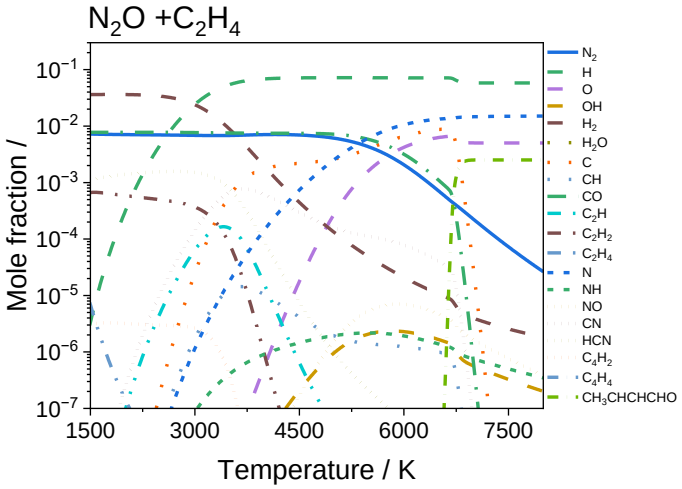

Figure 9-20: Chemical equilibrium calculations for cases that use N_2O as oxygen carrier [204].

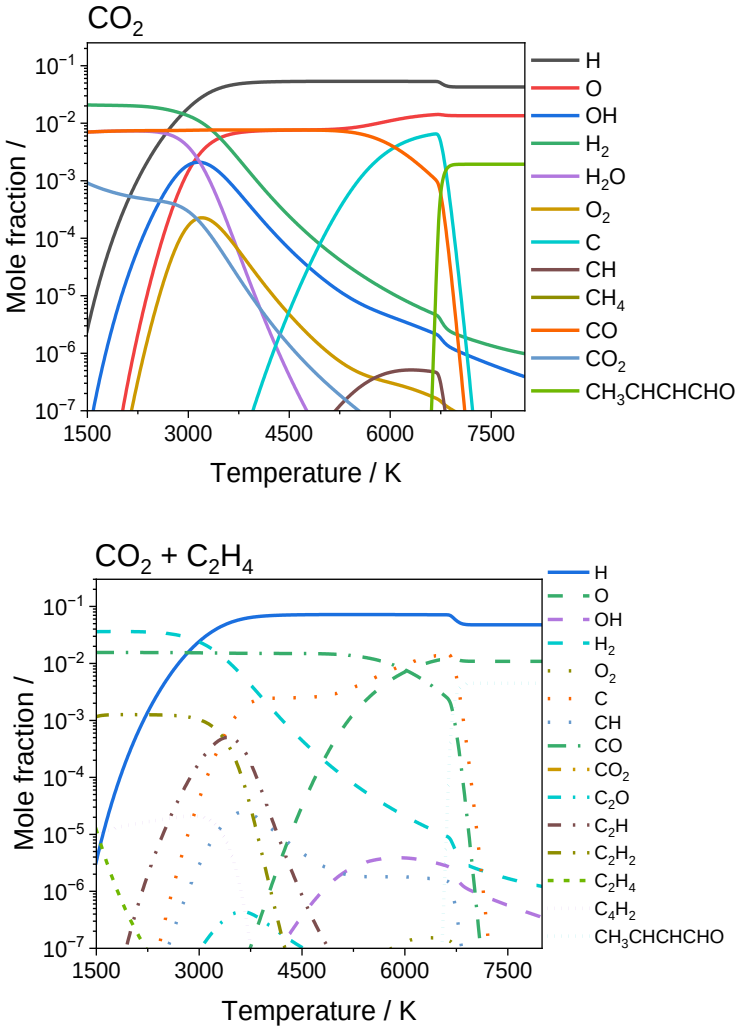

Figure 9-21: Chemical equilibrium calculation when using CO_2 as oxygen carrier [204].

The results for the Chemkin simulations referring to all experimental Cases are shown in Figure 9-22. When decreasing the C/O ratio, the concentration of CO is predicted to increase for all oxygen carriers, while the concentration of grown free hydrocarbons (mostly acetylene) decreases.

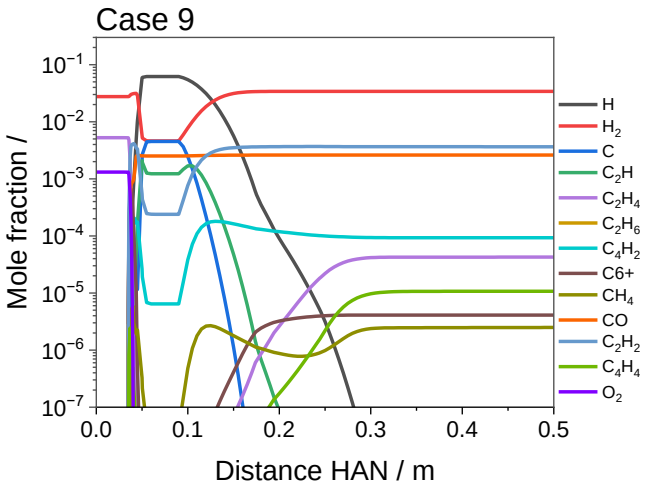
Case 9
Mole fraction /
Distance HAN / m
H
H2
C
C2H
C2H4
C2H6
C4H2
C6+
CH4
CO
C2H2
C4H4
O2

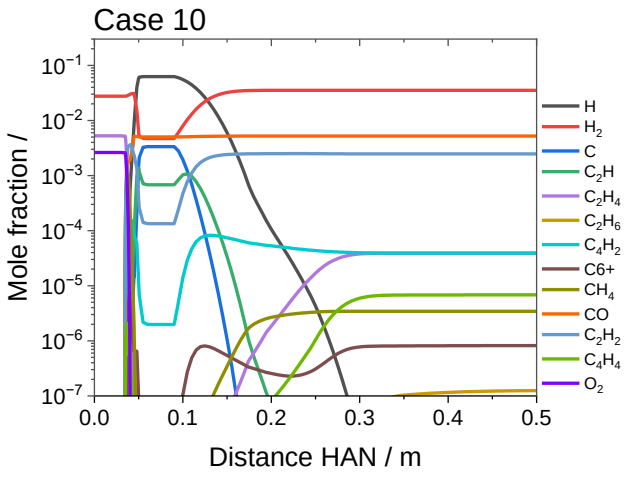
Case 10
Mole fraction /
Distance HAN / m
H
H2
C
C2H
C2H4
C2H6
C4H2
C6+
CH4
CO
C2H2
C4H4
O2

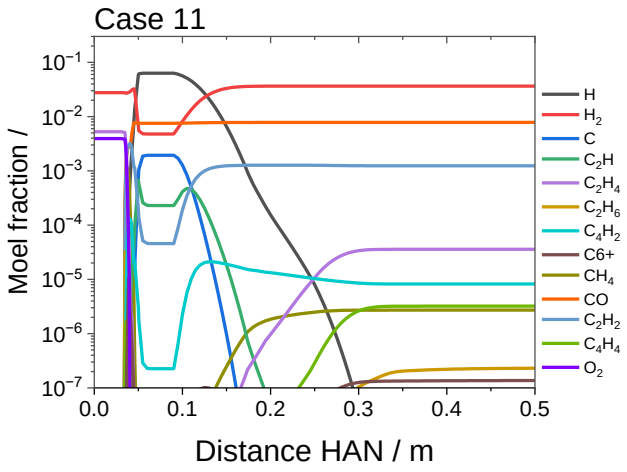
Case 11
Moel fraction /
Distance HAN / m
H
H2
C
C2H
C2H4
C2H6
C4H2
C6+
CH4
CO
C2H2
C4H4
O2

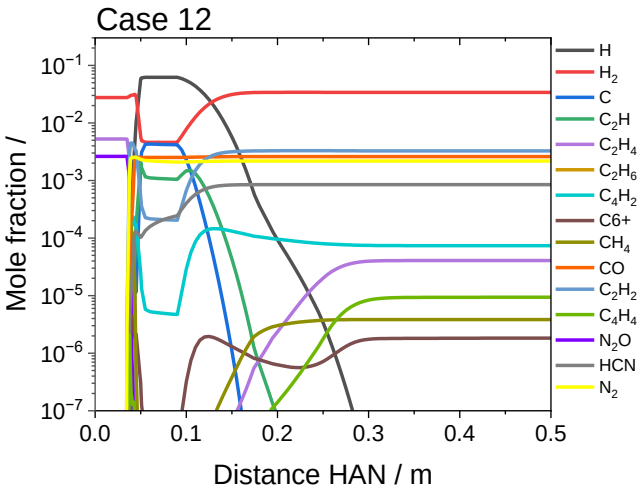
Case 12
Mole fraction /
Distance HAN / m
H
H2
C
C2H
C2H4
C2H6
C4H2
C6+
CH4
CO
C2H2
C4H4
N2O
HCN
N2

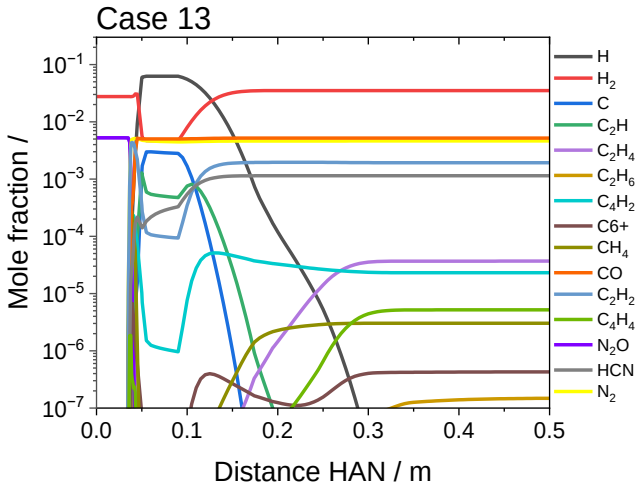
Case 13
Mole fraction /
Distance HAN / m
H
H2
C
C2H
C2H4
C2H6
C4H2
C6+
CH4
CO
C2H2
C4H4
N2O
HCN
N2

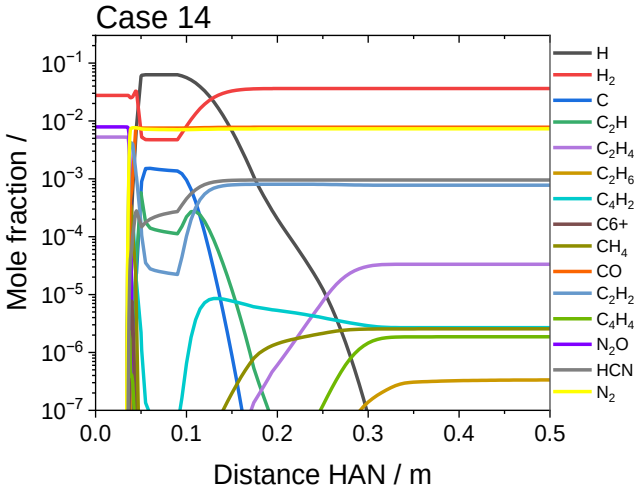
Case 14
Mole fraction /
Distance HAN / m
H
H2
C
C2H
C2H4
C2H6
C4H2
C6+
CH4
CO
C2H2
C4H4
N2O
HCN
N2

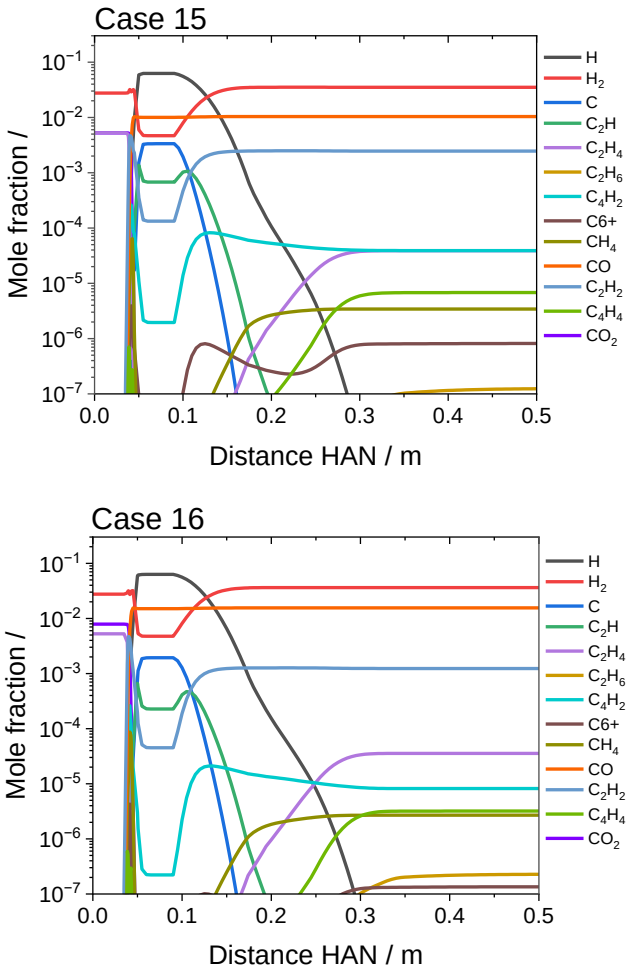

Figure 9-22: Kinetics simulations obtained with CHEMKIN for various experimental cases [204].

9.6.2 TEM images of all discussed experimental cases

In the main body of this work, only TEM images of a few selected samples are shown. Thus, Figure 9-23 additionally presents an overview of the type of carbon nanoparticle mixtures collected for Cases 8–16.

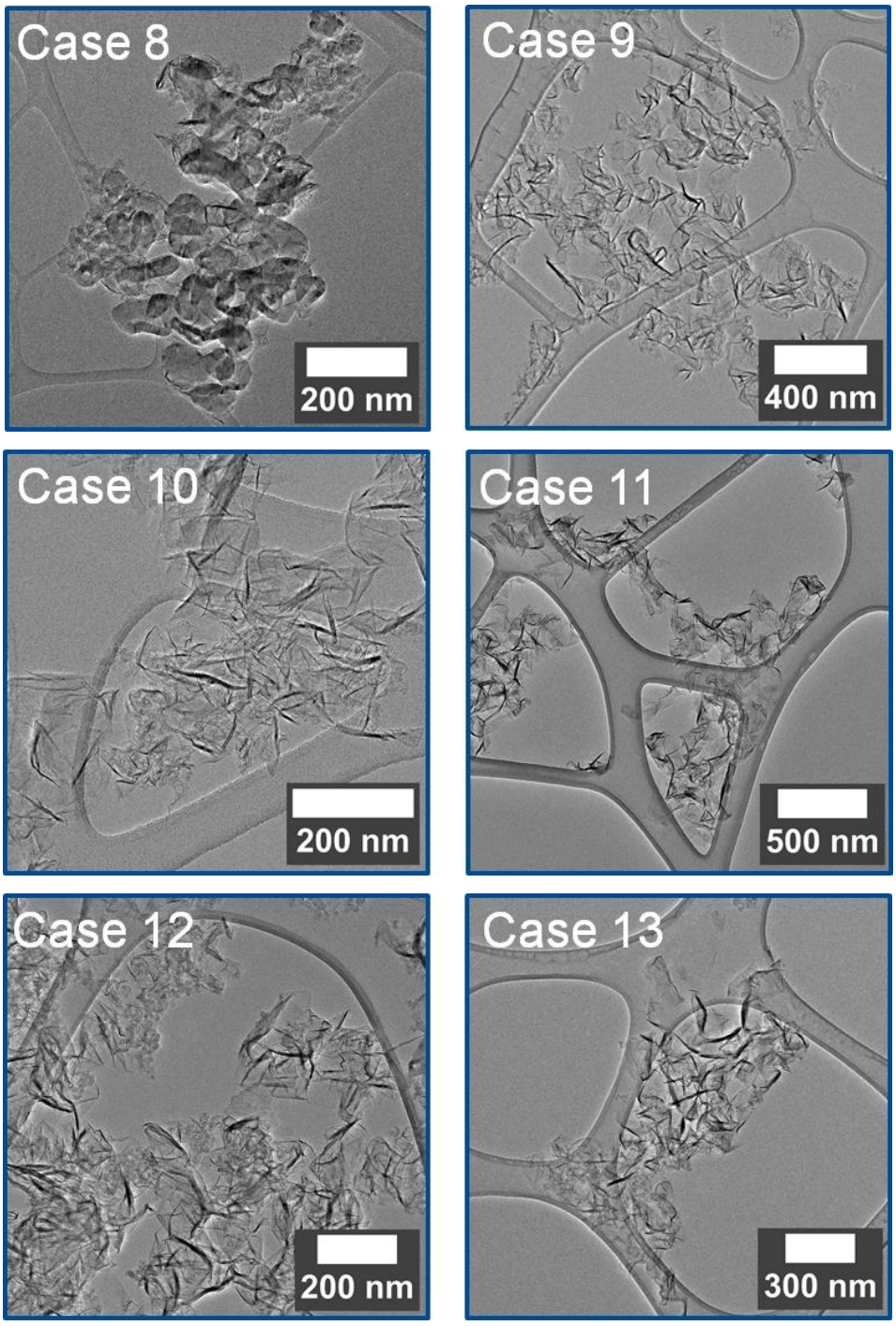

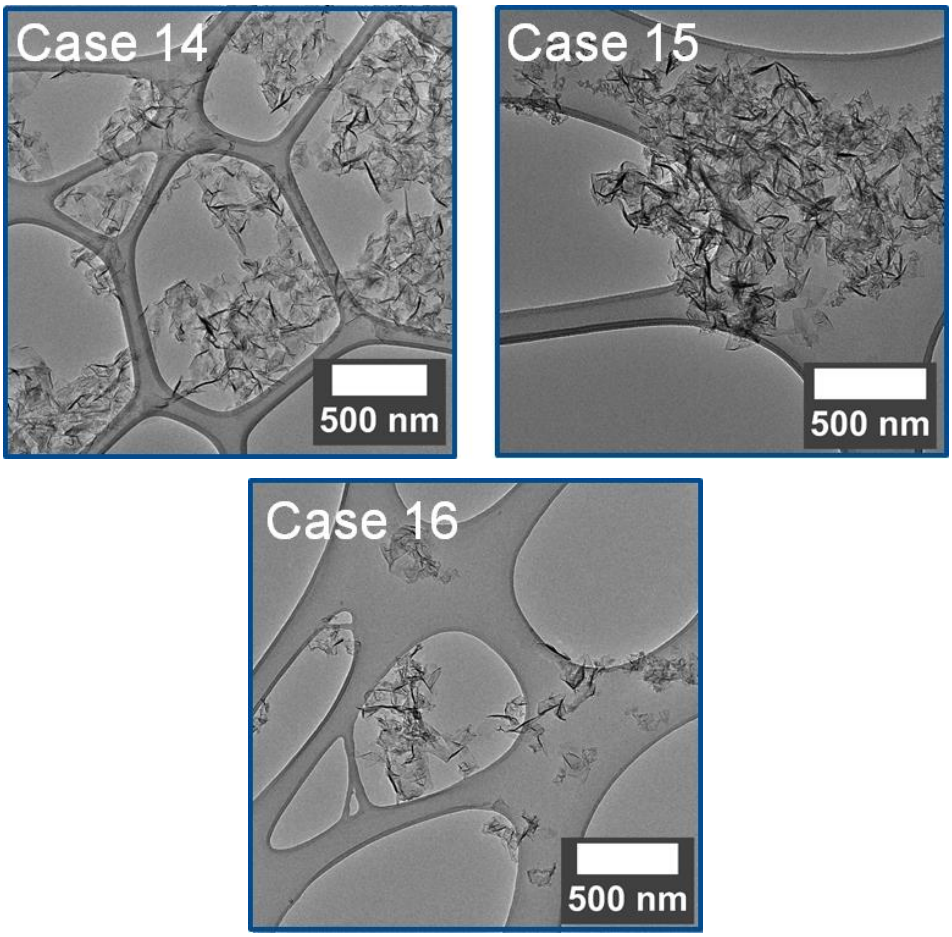

Figure 9-23: TEM images of prepared samples harvested for Cases 8–16 [204].

9.6.3 GC/MS validation measurements of the effluent gas composition

Table 9-1 shows the exact numerical values for the GC/MS validation measurements which are compared to the gas kinetics simulations of Section 6.2. Overall, the relative error between the simulation predicted and GC/MS measured concentrations for CO and C_2H_2 is at most ~25 % for all the considered experimental cases. The concentration of C_2H_4 is always under-predicted by a factor of ~2–3.

Table 9-1: Comparison of measured and simulated concentrations of CO, C_2H_2, and C_2H_4 at the measurement position at HAN ≈ 0.8 m with a local temperature of T < 500 K [204].

Species	Simulation / ppm				Experiment / ppm			
	Case 8	Case 11	Case 14	Case 16	Case 8	Case 11	Case 14	Case 16
CO	0	7803	7773	15546	~0	~9600	~8500	~15300
C_2H_2	4794	1239	772	1234	~4263	~1318	~750	~1477
C_2H_4	38	36	34	36	~105	~94	~75	~94

9.6.4 Raman spectra obtained from synthesis and their analysis

The Raman spectra of all experimental cases are shown in Figure 9-24. The spectra were fitted and analyzed based on their respective peak ratios and widths. For the fitting procedure, the region of the D and G peak (1150–1700 cm^{-1}) was either fitted by five or three peaks depend on how well the fitted performed, but it was only qualitatively evaluated. For the five-peak fit, the strategy of Sadezky et al. was followed [119]. A summary for these results is shown in Table 9-2.

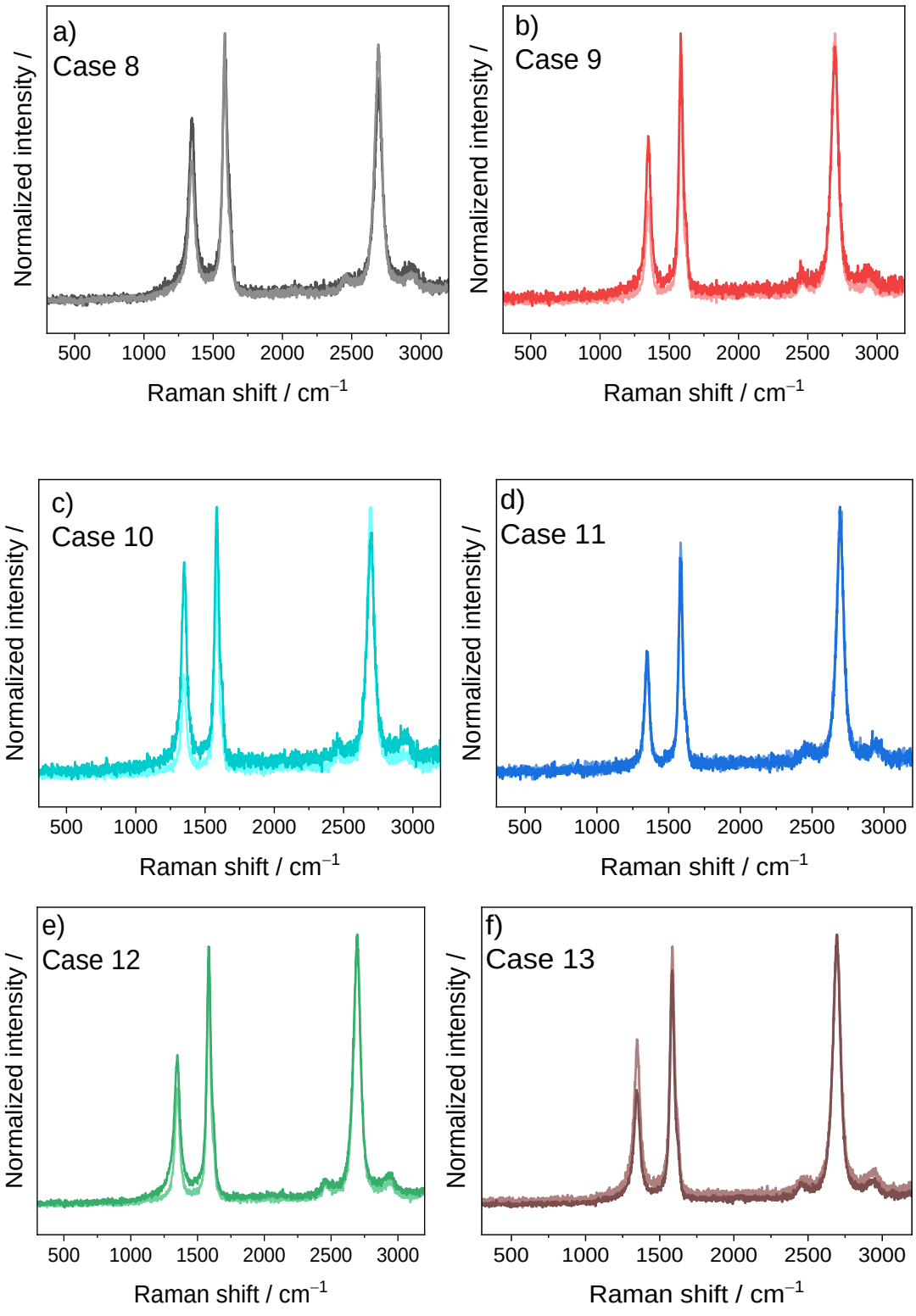

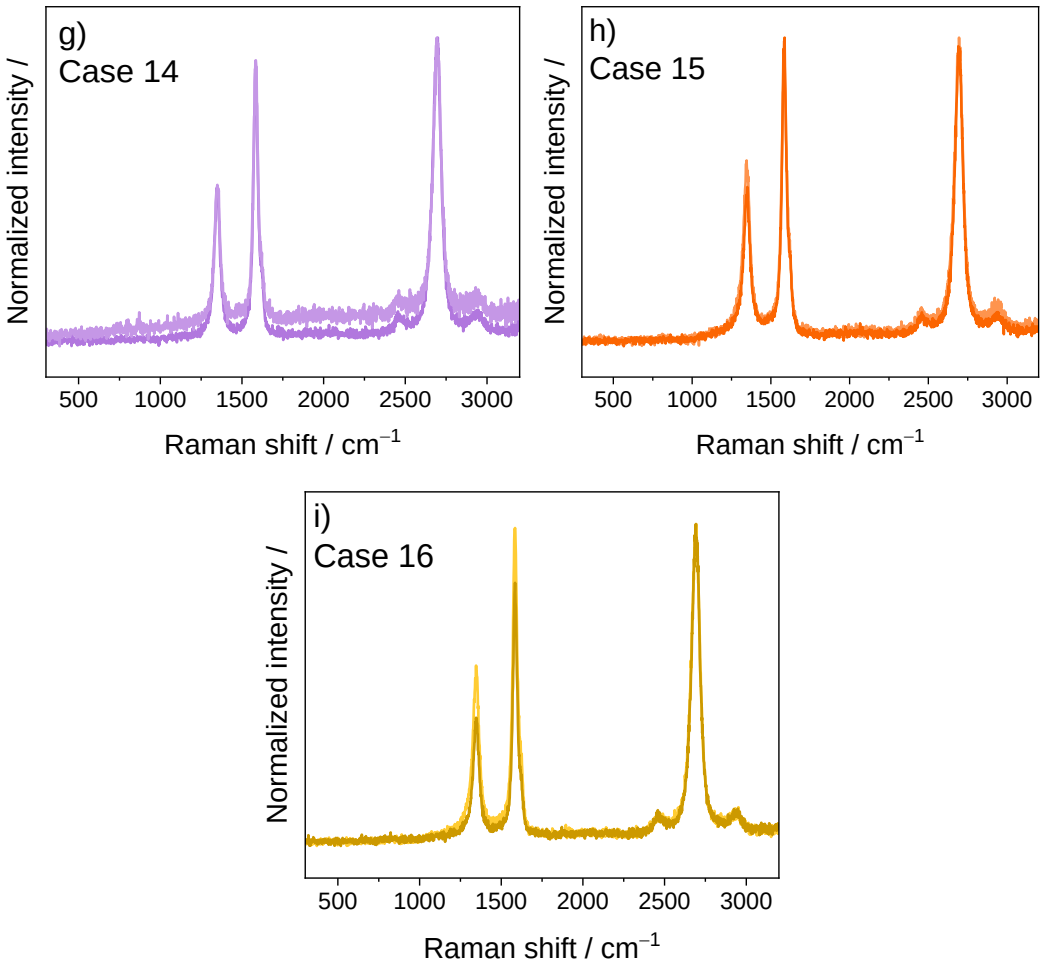

Figure 9-24: Raman spectra measured of materials prepared by Cases 8–16 [204].

The results displayed in Table 9-2 show how the material properties change when the C/O ratio is decreased. For their calculation, the average of the two measurements displayed in Figure 9-24 for each case were used. It can be observed in Figure 9-24 that, on average, the 2D peak intensity increases with decreasing C/O ratio. Therefore, the $A_{2D/G}$ ratio, determined by the fits, increases.

Table 9-2: Results obtained for fitting the Raman spectra displayed in Figure 9-24 *[204]*

Sample	$FWHM_G$	$FWHM_{2D}$	$A_{2D/G}$	$A_{D/G}$
Case 8	~37	~61	~1.5	~0.9
Case 9	~32	~56	~1.8	~0.7
Case 10	~36	~58	~1.7	~0.7
Case 11	~35	~55	~2	~0.6
Case 12	~33	~58	~1.8	~0.7
Case 13	~34	~59	~1.9	~0.7
Case 14	~32	~56	~1.9	~0.7
Case 15	~35	~59	~1.7	~0.7
Case 16	~31	~58	~2	~0.7

9.6.5 TGA measurement results for Cases 8–16

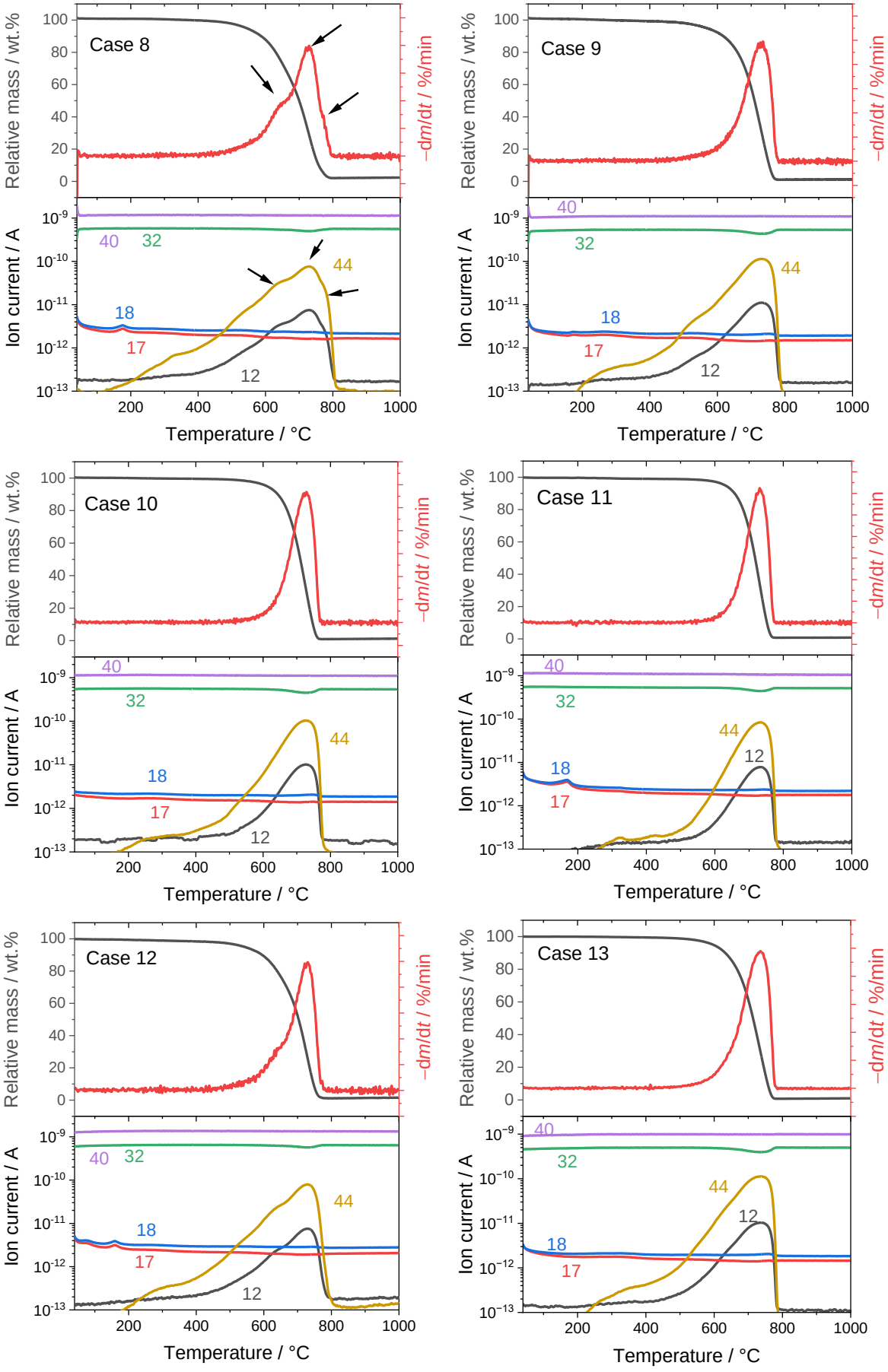

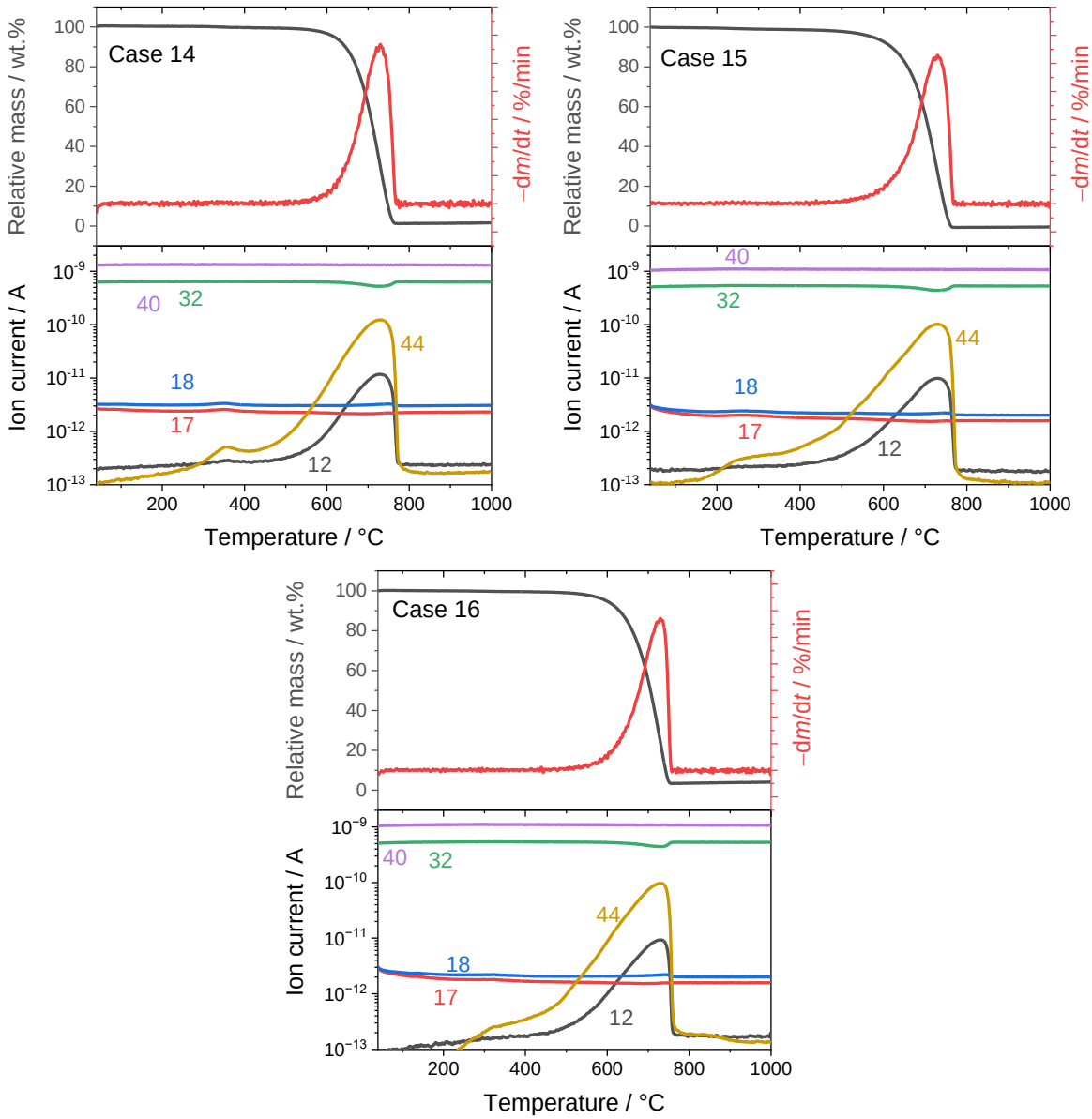

Figure 9-25: TG measurements performed for all the experiment Cases 8–16.TG and DTG data is shown in the top for each Case, while the corresponding QMS measurements are shown below.

9.6.6 XPS measurements of the synthesized nanopowders

The XPS spectra measured for the nanomaterials prepared by different cases are shown in Figure 9-26. For the analysis of the C_{1s} high-resolution scans, five different components were chosen, while the O_{1s} region is only described by two components. The lines used for the analysis of the C_{1s} region include two different lineshapes located at the same binding energy to describe two different carbon nanostructures (FLG and soot-like particles), C-O and C=O bonds, and the π-π* transition. The use of two different lineshapes to describe the carbon nanostructure is justified by the difference between sp^2- and sp^3-bonded carbon in XPS.

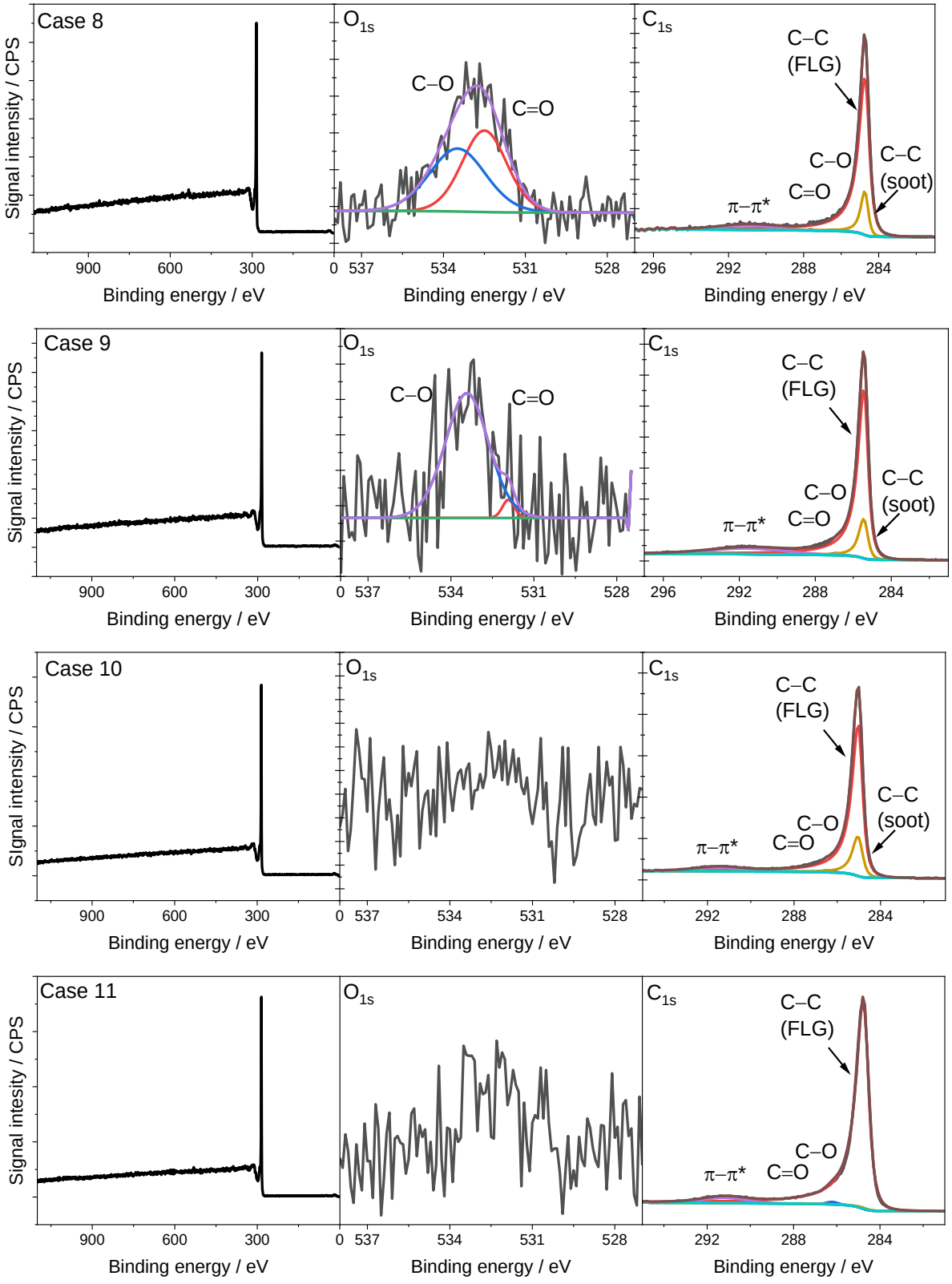
Case 8
O1s
C1s
C–O
C=O
C–C
(FLG)
C–O
C=O
C–C
(soot)
π–π*
Signal intensity / CPS
Binding energy / eV
Case 9
Case 10
SIgnal intensity / CPS
Case 11
Signal intesity / CPS

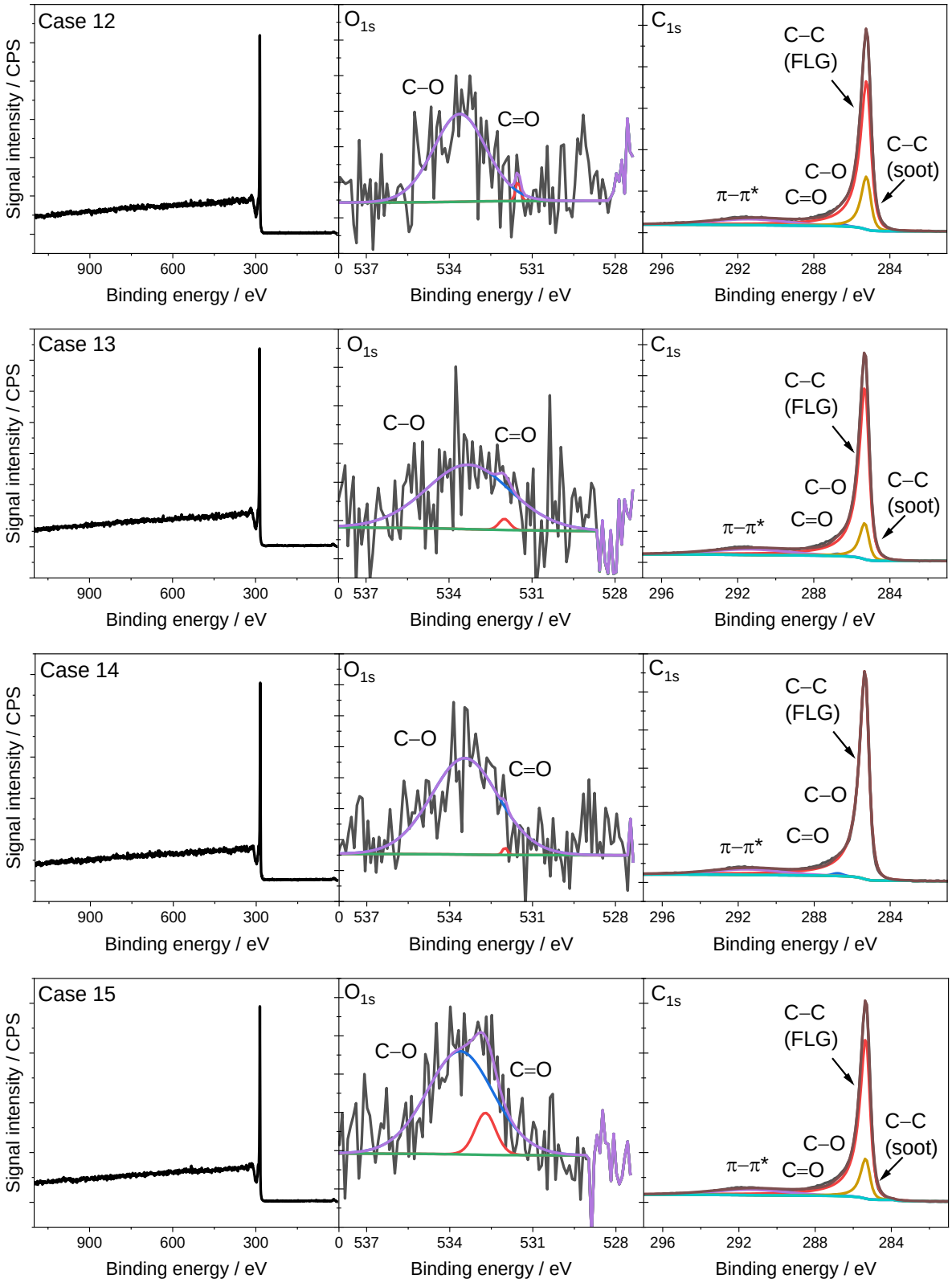
Case 12
Case 13
Case 14
Case 15
Signal intensity / CPS
O1s
C1s
C–O
C=O
C–C
(FLG)
C–C
(soot)
π–π*
900
600
300
0
537
534
531
528
296
292
288
284
Binding energy / eV

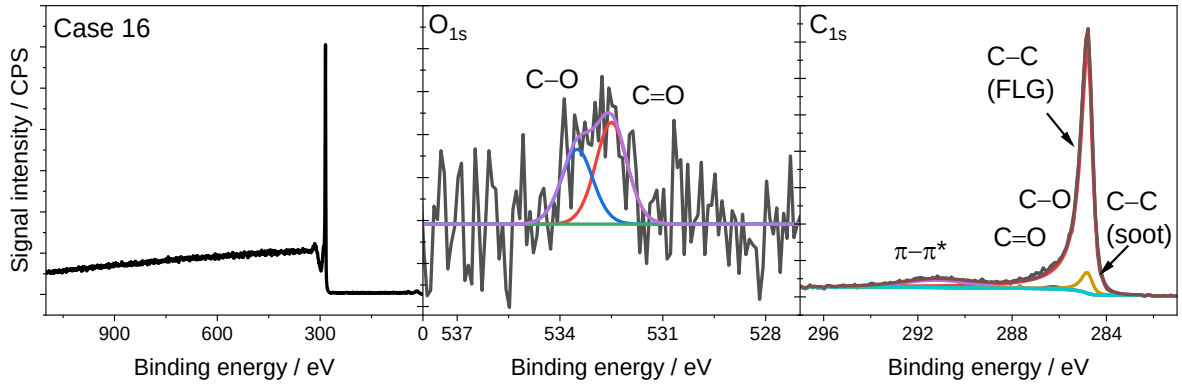

Figure 9-26: XPS measurements of sample prepared for Cases 8–16. For each Case the survey scan and the high-resolution scans of the C_{1s} and O_{1s} region are shown [204].

The fit suggests that most samples contain a small fraction of soot-like particles, and only Cases 11 and 14 did not show the presence of a secondary phase confirming qualitatively the results by TEM and TGA. However, for Case 8, the fraction of soot-like particles is small compared to the quantitative TG results. The small fraction of soot-like particles may be caused by the limited probe volume which may not fully represent the sample, as observed from time to time in the Raman measurements.

10 Acknowledgment

I would like to first acknowledge all the current and former PIs at the Institute for Energy and Materials Processes–Reactive Fluids for fostering a great research environment, their continuous support, and patience. The environment allowed me to progress in my own speed and grow as a person. Furthermore, I would like to thank Ferdi Schüth for accepting me as external PhD student and insightful comments/discussions.

I'm especially grateful to all coworkers who made the last ~10 years at the institute a wonderful time. Especially during my PhD, I cannot think of a better place to work, discuss, and celebrate achievements with my colleagues. It includes the technical and administrative staff, all current and former scientific coworkers, the workshop, and the ICAN and NETZ team. I'm glad to have met so many smart and ambitious people during my time at the university and in the different projects I contributed to (FOR2284, SPP2289, and IMPRS SurMat). It made me learn and experience a wide range of topics, personalities, and different points of view.

DOI: 10.17185/duepublico/82221
URN: urn:nbn:de:hbz:465-20240813-083044-6